

# Thermal fluctuations in disordered superconductors

By

**Sabyasachi Tarat**

PHYS08200804004

**Harish-Chandra Research Institute, Allahabad**

*A thesis submitted to the  
Board of Studies in Physical Sciences*

*In partial fulfillment of requirements  
For the degree of*

**DOCTOR OF PHILOSOPHY**

*of*

**HOMI BHABHA NATIONAL INSTITUTE**



**September, 2014**



## STATEMENT BY AUTHOR

This dissertation has been submitted in partial fulfillment of requirements for an advanced degree at Homi Bhabha National Institute (HBNI) and is deposited in the Library to be made available to borrowers under rules of the HBNI.

Brief quotations from this dissertation are allowable without special permission, provided that accurate acknowledgement of source is made. Requests for permission for extended quotation from or reproduction of this manuscript in whole or in part may be granted by the Competent Authority of HBNI when in his or her judgment the proposed use of the material is in the interests of scholarship. In all other instances, however, permission must be obtained from the author.



Sabyasachi Tarat



## DECLARATION

I, hereby declare that the investigation presented in the thesis has been carried out by me. The work is original and has not been submitted earlier as a whole or in part for a degree / diploma at this or any other Institution / University.

*Sabyasachi Tarat*

Sabyasachi Tarat



## List of Publications arising from the thesis

### Journal

1. Pairing fluctuations, the BCS-BEC crossover and strong disorder in superconductors, Pinaki Majumdar and Sabyasachi Tarat, *J. Supercond. Nov. Magn.*, **2013**, 26, 1787-1793.
2. Charge dynamics across the disorder driven superconductor-insulator transition, Sabyasachi Tarat and Pinaki Majumdar, *Europhys. Lett.*, **2014**, 105, 67002p1-67002p6
3. A real space auxiliary field approach to the BCS-BEC crossover, Sabyasachi Tarat and Pinaki Majumdar, *Eur. Phys. J. B*, **2015**, 88, 1-10

### Others

1. Tunneling spectroscopy across the superconductor-insulator thermal transition, Sabyasachi Tarat and Pinaki Majumdar, arXiv:1406.5423, **2014**.
2. Dense magnetic impurities in a s-wave superconductor: thermal and strong coupling effects beyond Abrikosov-Gorkov theory (in preparation), Sabyasachi Tarat and Pinaki Majumdar.



*To*  
*My Parents*



# Acknowledgements

First and foremost, I would like to express my profound gratitude towards my advisor and mentor, Prof. Pinaki Majumdar, for his continuous support during my Ph.D. years. His guidance, patience (immense!), motivation and deep knowledge have proved invaluable to me in my struggle to make the very difficult transition from a student to a researcher.

I am grateful to Prof. Prasenjit Sen, Prof. Sumathi Rao and Prof. G. V. Pai for their continuous encouragement, support and help. I am thankful to the members of my thesis advisory committee for their support in letting me continue my research without any obstructions. I would like to thank Prof. A. Raychaudhuri and Prof. J. K. Bhattacharjee for giving me an opportunity to work at HRI. I express my deep gratitude towards Prof. Ashoke Sen, Prof. Rajesh Gopakumar, Prof. Sudhakar Panda, Prof. L. Sriram Kumar, Prof. V. Ravindran, Prof. Satchidananda Naik and Prof. Ashesh Krishna Datta for their stellar courses on basic (and not so basic) physics.

The administration at HRI has always been very helpful and efficient, and I would like to thank Ravindra Singh, Yashpal Singh Bhadouriya, Archana Singh, Ajay Srivastava, Manish Sharma, Sanjay Verma, Anju Verma, Umakant Dwivedi, Dharmendra Malhotra, Amit Roy, Raj Gulati, Archana Tandon, Seema Agrawal, Rachna Pareek, Ananthi, Sumitra, Amit Khulve, Pradeep, Sushant, and Sadhu for their help and support during my stay. I am thankful for the HPC clusters at HRI, on which all the numerical calculations relevant to this thesis were done.

My life at HRI would never have been the same without the many friendships that I have forged here. Thank you Sayantanidi, Arjunda, Subhoda, Shamikda, Joydeepda, the two Sanjoydas (Biswas and Datta), Anirbanda, Atri, Ipsita, Satya, Dhiraj, Sourav (Mitra), Saurabh (Niyogi), Saurabh (Pradhan), Ujjal, Arunabha, Ushoshi, Manoj, Anushree, Vikas, Viveka Nand, Rajarshi, Madhuparna, Akansha, Nyayabanta, Dibya, Arijit, both Abhisheks (Joshi and Chowdhury), Sauri, Swapnamay, Masud, Avijit, Shrobona, Animesh, Shankha, Taushif, Aritra, Nabarun, Titas, Tanu-moy and Madhumita for making my stay at HRI so memorable. Special thanks are due to all my football partners, especially Niyogi, Pallab, Bibek, Samrat, Asheshda, Sanjoyda, Ramesh, Subhronel, Sarif, Ritabrata, Manabendra, Soumyarup, Mithun, Himadri and Rishabh with whom I spent some of the happiest hours of my life playing football at the HRI ground.

I am deeply grateful to my parents for loving and supporting me throughout my life, and nurturing my interest in physics and mathematics. My father, in particular, has always been more of a

friend than a guardian, and has deeply influenced me with his sincerity, honesty, intellect and above all, his wacky, self-deprecating sense of humour.

Finally, none of this would have been possible without my constant companion, dearest friend and wife, Paromita. Thank you for being the bedrock of my existence at HRI and enriching my life incomparably, indelibly, with your unconditional love and understanding. To me, you represent all that is good in this world.

# CONTENTS

SYNOPSIS	v
----------	---

LIST OF FIGURES	ix
-----------------	----

LIST OF TABLES	xxi
----------------	-----

<b>1 Introduction</b>	<b>1</b>
1.1 Basic concepts of superconductivity . . . . .	2
1.1.1 Zero resistivity . . . . .	2
1.1.2 Meissner effect . . . . .	3
1.1.3 London equations . . . . .	4
1.1.4 Flux penetration . . . . .	4
1.1.5 Landau-Ginzburg theory . . . . .	6
1.1.6 BCS theory . . . . .	7
1.2 Disorder in metals . . . . .	9
1.2.1 Drude theory . . . . .	10
1.2.2 The quantum approach . . . . .	10
1.2.3 Anderson localization . . . . .	11
1.2.4 Scaling theory . . . . .	11
1.3 Disordered superconductors . . . . .	13
1.3.1 Historical overview . . . . .	13
1.3.2 Thin films of Be and NbN . . . . .	14
1.3.3 InO <sub>x</sub> and TiN films . . . . .	17
1.3.4 3D NbN films . . . . .	21
1.3.5 Summary and discussion . . . . .	22

1.4	Magnetic impurities in superconductors . . . . .	24
1.4.1	Single impurity . . . . .	25
1.4.2	Many impurities . . . . .	27
1.4.3	Summary and further work . . . . .	30
<b>2</b>	<b>Theoretical work, model and methods</b>	<b>33</b>
2.1	From BCS theory to BCS-BEC crossover . . . . .	34
2.1.1	The BCS-BEC crossover . . . . .	34
2.1.2	Continuum and lattice . . . . .	35
2.1.3	Diagrammatic approaches . . . . .	37
2.1.4	Functional methods . . . . .	40
2.1.5	Summary and conclusions . . . . .	42
2.2	Disordered superconductors . . . . .	42
2.2.1	Extending BCS theory . . . . .	42
2.2.2	The ‘fermionic’ mechanism . . . . .	43
2.2.3	The ‘bosonic’ mechanism . . . . .	46
2.2.4	Numerical methods . . . . .	49
2.3	Model and methods . . . . .	56
2.3.1	Choice of model . . . . .	56
2.3.2	Auxiliary fields . . . . .	57
2.3.3	Bogolyubov transformation . . . . .	59
2.3.4	Monte Carlo protocol . . . . .	62
2.3.5	Calculating thermal averages . . . . .	63
2.3.6	Computing observables . . . . .	64
2.3.7	Approximations, benchmarking . . . . .	68
<b>3</b>	<b>The BCS-BEC crossover</b>	<b>73</b>
3.1	Earlier work . . . . .	74
3.2	Model and method . . . . .	76
3.3	Results . . . . .	77
3.3.1	Thermodynamic indicators . . . . .	77
3.3.2	Background fields . . . . .	78
3.3.3	Density of states . . . . .	79
3.3.4	Spectral functions . . . . .	81
3.4	Discussion . . . . .	84
3.4.1	Accuracy of $T_c$ estimate . . . . .	84
3.4.2	Effective classical functional . . . . .	85

3.4.3	Role of the ‘density’ field . . . . .	87
3.4.4	Handling inhomogeneity . . . . .	87
3.4.5	Quantum fluctuations . . . . .	88
3.5	Conclusions . . . . .	89
<b>4</b>	<b>Charge dynamics across the superconductor-insulator transition</b>	<b>91</b>
4.1	Background to the problem . . . . .	91
4.1.1	Summary of experiments . . . . .	92
4.1.2	Summary of current theory . . . . .	93
4.2	Model, parameters, and main results . . . . .	95
4.2.1	Recapitulation of method . . . . .	95
4.2.2	Parameters . . . . .	96
4.2.3	Summary of main results . . . . .	97
4.3	Results . . . . .	97
4.3.1	Phase diagram . . . . .	97
4.3.2	Resistivity . . . . .	100
4.3.3	Density of states . . . . .	101
4.3.4	Optical conductivity . . . . .	102
4.4	Discussion . . . . .	104
4.4.1	Numerical checks on transport . . . . .	105
4.4.2	The microscopic picture . . . . .	105
4.4.3	Interaction effects on localization . . . . .	107
4.4.4	Thermal transition and vortex physics . . . . .	108
4.4.5	Limitations of our method . . . . .	109
4.4.6	Comparison to experiments . . . . .	110
4.5	Conclusions . . . . .	111
<b>5</b>	<b>Tunneling spectroscopy across the superconductor-insulator transition</b>	<b>113</b>
5.1	Background to the problem . . . . .	114
5.2	Model, methods and main results . . . . .	114
5.2.1	Methods and parameters . . . . .	115
5.2.2	Main results . . . . .	115
5.3	Results . . . . .	116
5.3.1	Tunneling maps . . . . .	116
5.3.2	Spatial character at strong disorder . . . . .	117
5.3.3	Spatial character at moderate disorder . . . . .	118
5.3.4	Gap and coherence peak distributions . . . . .	121

5.3.5	Hills, valleys and LDOS . . . . .	122
5.4	Discussion . . . . .	123
5.4.1	$T = 0$ cluster pattern . . . . .	123
5.4.2	Multiple scales . . . . .	124
5.4.3	Effective Landau-Ginzburg functional . . . . .	126
5.4.4	Estimating the new scales . . . . .	127
5.4.5	Comparison with experiments . . . . .	127
5.5	Conclusions . . . . .	128
<b>6</b>	<b>Dense magnetic impurities in a <math>s</math>-wave superconductor</b>	<b>129</b>
6.1	Background and model . . . . .	130
6.1.1	Earlier work and limitations . . . . .	130
6.1.2	Model and parameter space . . . . .	131
6.2	Single impurity . . . . .	132
6.3	Multiple impurities . . . . .	133
6.3.1	Phase diagrams . . . . .	134
6.3.2	$T = 0$ results . . . . .	136
6.4	Thermal properties . . . . .	139
6.4.1	Density of states . . . . .	140
6.4.2	Spatial character . . . . .	141
6.5	Discussion . . . . .	142
6.5.1	Inhomogeneities and gapless phase . . . . .	143
6.5.2	Nature of thermal transition . . . . .	143
6.5.3	Effect of spin dependent auxiliary fields . . . . .	144
6.5.4	Extensions . . . . .	144
6.6	Conclusions . . . . .	144

# SYNOPSIS

Superconductivity is a striking example of macroscopic quantum behaviour driven by attractive interaction between electrons. While the ideas of pairing and phase coherence that emerged from the Bardeen-Cooper-Schrieffer (BCS) theory continue to be relevant to later discoveries in superconductivity, many of their specific predictions need to be modified when one encounters situations involving (a) strong interaction between electrons, (b) the presence of significant potential scattering, leading to a superconductor-insulator transition (SIT), (c) the coupling to magnetic impurities, and, for example, (d) the proximity to other ordered phases. Quite generally, these may require us to handle inhomogeneous ground states (which in principle can occur within the BCS scheme itself) and quantum and thermal fluctuations of the ‘order parameter’.

The primary focus of this thesis is on understanding the role of strong disorder in superconducting systems, in particular the thermal fluctuation effects that occur on the inhomogeneous background. We would want to study these effects in the presence of ‘scalar’ disorder as well as magnetic impurities. However, to get to these relatively less explored problems we needed to first benchmark our method in the context of a well studied problem - the BCS to BEC crossover with increasing pairing interaction in a fermi system. Following this logic, the chapters of the thesis are organised as below.

**Chapter 1.** presents a review of the experimental situation. It starts with a quick summary of superconductivity and disordered metals. We then review the experimental results on disordered superconductors, in the context of materials like (i) thin films of Be and NbN, (ii) amorphous films of  $\text{InO}_x$  and TiN and, (iii) three dimensional NbN films. We focus on:

- Resistivity and its dependence on temperature, disorder and magnetic field.
- Spectral functions, as inferred from scanning tunneling spectroscopy (STS) and their detailed evolution with temperature and disorder.
- More recent tunneling spectroscopy results, hinting at the inhomogeneity of the underlying superconducting state.

This is followed by a brief description of available data on magnetic impurities in superconductors including a short summary of results on the gapless phase and spectral functions.

**Chapter 2.** reviews the theory tools available, and our own method. It starts with a general review of ‘post BCS’ theoretical methods and a discussion of their results in the context of the BCS-BEC crossover. We then move to disordered superconductors, classifying the theory work into three groups:

- ‘Fermionic’ theories, which include Coulomb repulsion and explore the destruction of superconductivity due to suppression of the effective pairing interaction.
- Bosonic theories, which assume ‘preformed’ bosonic pairs and study how phase fluctuations can drive a superconductor-insulator transition.
- Numerical approaches, which start with an attractive fermion lattice model and use methods like Hartree-Fock-Bogoliubov-de-Gennes (HFBdG) mean field theory, quantum Monte Carlo (QMC), *etc.*, without assuming any preformed pairs.

We then discuss the appropriateness of the attractive Hubbard model (AHM) in treating the problem of SIT. We go beyond mean field theory by using an auxiliary field approach, using a pairing field  $\Delta_i$  and a ‘charge’ field  $\phi_i$ , that retains all the thermal fluctuations in the problem. Our AHM derived effective model has the look:

$$\mathcal{H}_{eff} = \mathcal{H}_0 + \sum_i (\Delta_i c_{i\uparrow}^\dagger c_{i\downarrow}^\dagger + h.c.) - \sum_{i\sigma} \phi_i c_{i\sigma}^\dagger c_{i\sigma} + \frac{1}{U} \sum_i (|\Delta_i|^2 + \phi_i^2) + \mathcal{H}_{dis}$$

$\mathcal{H}_0$  above is the kinetic energy and  $\mathcal{H}_{dis}$  incorporates the disorder in the system. For non-magnetic disorder,  $\mathcal{H}_{dis} = \sum_i V_i c_{i\sigma}^\dagger c_{i\sigma}$ , where  $V_i$  is a random number between  $[-V, V]$ . Magnetic impurities are included via  $\mathcal{H}_{dis} = J \sum_i S_i \cdot \sigma_i$ , where  $\sigma_i$  is the electron spin and  $S_i$  are classical moments modelling impurity spins. We describe in detail the Monte Carlo algorithm that generates the equilibrium configurations  $\{\Delta_i, \phi_i\}$  in the disordered background, and the computation of electronic properties thereon.

**Chapter 3.** revisits the well studied BCS-BEC problem. This is a prototype of weak to strong coupling evolution in many body physics. While extensive numerical results are available, and several approximate methods have been developed, none of these schemes are formulated in real space and as a result cannot handle spatial inhomogeneity. We solve the BCS-BEC problem in two dimensions using our auxiliary field based Monte Carlo. Our approach reproduces the HFBdG ground state, and leads to a  $T_c$  scale that agrees with quantum Monte Carlo estimates to within a few percent. We discuss results on the  $T_c$ , amplitude and phase fluctuations, density of states, and the momentum resolved spectral function, over the entire interaction and temperature window. We compare our results to those from full QMC and other semi-analytic approaches whenever possible.

**Chapter 4.** discusses the ‘global’ properties of a superconductor as it is driven towards the SIT. While the evolution of the superconducting *ground state* with disorder is now well understood, thermal effects and transport have remained mostly out of reach. Using our auxiliary field based MC we describe the disorder driven SIT at finite temperature. We track the  $T_c$ , the resistivity, the

global density of states (DOS) and the optical conductivity with increasing disorder. Our results on the resistivity suggest that beyond moderate disorder the low temperature superconducting state can arise out of an ‘insulating’ normal state. We observe a prominent pseudogap in the normal state DOS that deepens with increasing disorder, and a divergence of the  $T_c$  and the gap vanishing temperature beyond moderate disorder. We also find that the low frequency weight in the density of states and optical conductivity are non monotonic in disorder, with a maximum near critical disorder, and their high temperature value correlate with the superconducting fraction in the disordered ground state. We compare our results to recent experimental data.

**Chapter 5.** describes the spatially resolved response of the disordered superconductor near the SIT. Advances in scanning tunneling spectroscopy have revealed the presence of superconducting nanoregions well past the bulk thermal transition in strongly disordered superconductors. We first discuss how the disorder landscape provides ‘favourable’ regions where superconductivity can exist, interspersed with ‘unfavourable’ regions where it is suppressed. We use our method to study the spatially differentiated amplitude and phase fluctuations in this background and establish spatial maps of the coherence peak as the superconductor is driven through the thermal transition. Analysis of the local density of states reveals that superconducting regions shrink and fragment with increasing temperature, but survive in small clusters to a temperature  $T_{clust} \gg T_c$ . The gap (or pseudogap) in the spectrum survives in general to another independent scale,  $T_g$ , depending on the strength of interaction. We discuss the physical origin of these multiple scales, suggest a Ginzburg-Landau scheme that provides a phenomenological classical description of the situation, and compare our results in detail to experiments.

**Chapter 6.** investigates the effect of magnetic impurities on superconductivity. Magnetic impurities break time reversal invariance, and hence can suppress and eventually destroy superconductivity even at very small concentration. The presence of such impurities can create subgap levels in a superconductor, eventually closing the gap completely, leading to the famous gapless phase. We investigate the problem at fixed interaction for various impurity spin coupling  $J$ . We present phase diagrams showing the gapped, gapless and non-superconducting phases in the  $J - T$  window, and analyze their dependence on  $J$ . We provide detailed results on the density of states showing the formation of subgap impurity levels. Our results reveal that the gapless phase increases in size with increasing  $J$ . Additionally, we find that at large  $J$ , the lowest energy wavefunctions are concentrated near the impurity positions, which also act as nucleation centres for the loss of SC with increasing temperature.



# LIST OF FIGURES

1.1	The resistivity of Hg [8] as measured by Kammerlingh Onnes, showing a superconducting transition at 4.2K. . . . .	3
1.2	A cartoon illustrating the Meissner effect. The magnetic field lines penetrating the material at $T > T_c$ are expelled outside the body for $T < T_c$ [10]. . . . .	3
1.3	A schematic diagram illustrating the different response of Type I and Type II superconductors to an external magnetic field [12]. . . . .	5
1.4	Interfaces of Type I ( $\lambda \ll \xi$ ) and Type II ( $\lambda \gg \xi$ ) superconductors. The first has positive interface energy, favouring a uniform state, while the second, with negative energy, favours the mixed vortex state of Type II superconductors [14]. . . . .	5
1.5	The temperature dependence of the order parameter $\Delta$ and the density of states, according to BCS theory (from the internet). . . . .	8
1.6	The scaling function $\beta(g)$ for $d = 1, 2$ and $3$ [26,28]. Shows the existence of a critical conductance signalling a metal-insulator transition (MIT) in 3D, while for $d \leq 2$ , $\beta < 0$ always, showing that all states are localized. . . . .	12
1.7	Resistivity $R(T)$ with increasing disorder for Be [35] and NbN films [38] respectively. . . . .	15
1.8	Resistivity $R(T)$ with increasing disorder for Be [36,37] and NbN [38] films respectively. . . . .	15
1.9	Top: Thermal evolution of tunneling spectra [38] of two thin films with thickness $2.33nm$ and $2.16nm$ respectively, showing decreasing coherence peaks, smaller gaps, and a broad Coulomb interaction induced background feature. Bottom: Spatial maps of tunneling conductance near the coherence peaks of the same films, indicating considerable inhomogeneity in the superconducting state . . . . .	17

1.10	Resistance vs temperature curves for 3 films of $\text{InO}_x$ [45] and 4 films of TiN [51]. The latter clearly shows the sharpness of the transition, and the insulating nature of the critical curve. . . . .	18
1.11	Magnetoresistance of $\text{InO}_x$ [46] at a fixed disorder and varying temperatures and of $\text{TiN}$ films [52] at fixed temperature close to the critical point. The saturation resistance at high field $\sim R_Q$ , and the overall behaviour is very similar in the superconducting and insulating samples (shown for $\text{TiN}$ films).	19
1.12	The evolution of density of states of three TiN films with increasing disorder [55]. The plots show a very deep pseudogap which survives to an increasingly large temperature at strong disorder. . . . .	19
1.13	The top figure [47] shows the contrasting thermal evolution of the local density of states of two regions in an $\text{InO}_x$ film at strong disorder. Bottom [56] left shows the inhomogeneities in a map of the gap $\Delta$ , while bottom right shows the variation in spectra measured along a straight line in disordered TiN films.	20
1.14	Left: Intensity plots [60] of tunneling spectra for 6 samples with increasing disorder. With increasing disorder, the depression in the middle survives to a disorder independent scale $T^* \sim 7K$ . Right: Phase diagram [60] showing the superconducting, normal, pseudogapped and insulating states extracted from the tunneling data. . . . .	22
1.15	Thermal evolution [61] of the zero bias tunneling conductance in a disordered sample with $T_c \sim 2.9K$ , showing the shrinking of the superconducting regions, which finally disappear at $T_{clust} \sim T^*$ . . . . .	23
1.16	Schematic figure [6] showing the intragap impurity state formed due to the presence of a single impurity in the density of states. The features at positive and negative parts show the respective weights of the electronic and hole components of the states respectively. Depending on the density, the contributions could in general be different, explaining the asymmetry of the diagram. . . .	26
1.17	Local density of states far from (top) and over an isolated magnetic Mn impurity in a single crystal Nb(110) sample used by Yazdani <i>et. al.</i> [71]. While the top plot is perfectly fitted by the BCS form, the bottom figure clearly shows the presence of intragap features, reflecting the intragap state formed due to the presence of the impurity. . . . .	27

1.18	Left: Schematic picture [6] of the quantum phase transition, showing the unpolarized initial ground state, and the polarized final ground state beyond the transition, where a spin is extracted from the condensate to form a singlet with the impurity spin. Right: The level crossing between the initial ground state $\Psi_0$ and the final one, $\Psi_1$ with increasing coupling $W$ . . . . .	28
1.19	Left: Comparison of the dependence of $T_c$ with impurity concentration $n_{imp}$ of several samples [76]. with the theoretical curve, showing a close match. Right: The evolution of the density of states [6] with increasing impurity scattering time $\tau_s^{-1} \sim n_{imp} J^2$ according to the Abrikosov-Gorkov theory [77]. The impurity states are always produced at the gap edge and below the critical point, there is always a hard gap in the system. . . . .	29
1.20	The contrasting evolution of the density of states for weak coupling (right) and strong coupling (left) with increasing concentration [6]. At weak coupling, the extra subgap states are formed close to the gap edge and slowly close the density of states until it is gapless. At strong coupling, the impurity states form a band inside the gap, and if the coupling strength is large enough, the bottom of the band reaches the Fermi surface before the top reaches the continuum to the right, and the gapless regime is enhanced. . . . .	30
2.1	Basic thermal scales of the BCS-BEC crossover [4]. Left: Schematic diagram for the crossover in continuum, from a Fermi liquid to the left to a Bose liquid to the right, where the $T_c$ increases initially and gradually saturates as pairs form with mass $2m$ . The dashed line shows the evolution of the pairing scale $T^*$ . Right: BCS-BEC crossover on a lattice, where $T_c \propto (1/U)$ at strong coupling (see text). Basic physics arises due to the competition between two scales, the pairing scale $T_{pair} = T^*$ and the stiffness scale $T_{phase}$ . . . . .	35
2.2	Schematic diagram of the self consistency loop [112]. An initial guess of the Green's function provides the susceptibility $\chi$ , which is then used to calculate the T-matrix $T$ , which leads to the self energy $\Sigma$ , which is used to calculate the Green's function again, completing the loop. DFT is discrete Fourier transform. . . . .	39
2.3	Left: $T_c$ and other thermal scales calculated using the method of Ref [114]. in two dimensions. Right: Density of states data calculated using the method of Ref [113] , showing accurate match with QMC data (dashed lines). . . . .	40

2.4	Schematic diagram [121] of the physics of the competition between the Coulomb repulsion and the attractive interaction induced by electron-phonon interactions in a clean superconductor. The repulsive interaction (red dashed line) is defined at the Fermi energy $E_F$ and is renormalized down. The attractive interaction (blue dashed dotted line) is defined at the Debye energy $\omega_D$ and its strength increases with decreasing energy, diverging at a nominal temperature $T_c^a$ . The combined interaction (orange line), if attractive at $\omega_D$ , becomes stronger under further renormalization until it diverges at the true $T_c$ of the system. Disorder changes this physics, strengthening the Coulomb interaction, and hence decreases the overall attraction. . . . .	44
2.5	Left: Results from perturbation calculations in Ref. [122], showing the strong decrease at large disorder (x axis is proportional to $R_\square$ . Right: Renormalization group calculations of Ref. [123] compared to experimental data, showing a very good match. Note the slower fall at stronger disorder, contrary to the perturbation calculations. . . . .	45
2.6	Schematic figure [131] of the evolution of superconductivity with increasing disorder as postulated by the fermionic mechanism. The superconductor consists of coherent pairs with finite order parameter $\Delta$ and stiffness $D_s$ . With increasing disorder both $\Delta$ and $D_s$ decrease due to increasing Coulomb repulsion, until they vanish at the critical point. Beyond this, all pairs are broken, and the system properties are determined by free fermions in a disordered system. . . . .	46
2.7	Left: Schematic resistivity from bosonic mechanism [133], showing the horizontal critical line, along with the universal value, and other resistivity lines diverging from it. Right: Experimental data from Ref. [132], in agreement with this theory. . . . .	48
2.8	Schematic picture of optical conductivity calculated from Mattis-Bardeen theory (left) [136] and results from QMC calculation using the quantum XY model in Ref. [134] (right). Top right plot is at weak disorder, far from the critical region, middle right is near the critical region, clearly showing enhanced low frequency weight, which again decreases as one goes beyond it into the insulator (bottom right). This is in contrast to the mean field theory results, which show zero conductivity between $\omega = 0$ and the single particle gap $2\Delta$ . . . .	49

2.9	Schematic figure [131] of the evolution of superconductivity with increasing disorder as postulated by the bosonic mechanism. The superconductor consists of coherent pairs with finite order parameter $\Delta$ and stiffness $D_s$ . With increasing disorder, increasing phase fluctuations results in a decrease in $D_s$ , while the gap parameter $\Delta$ remains the same. The disorder causes the bosonic pairs to lose long range coherence, and increased phase fluctuations among these pairs drives the system insulating. In the insulating regime, the bosonic pairs are incoherent, but the single particle gap remains (the variation shown in the single particle gap is determined from calculations using fermionic models, see numerical methods section). . . . .	50
2.10	Left: Map of $\Delta_i$ at strong disorder from BdG calculations [85], showing clusters with large $\Delta_i$ embedded in regions with very small $\Delta_i$ . Right: Density of states at $T = 0$ at three different disorder strengths [85], showing the persisting gap even at high disorder, and decreasing coherence peaks with disorder. . . . .	51
2.11	Phase correlation between edges (red) and order parameter $\Delta$ with increasing magnetic flux $\phi/\phi_0$ at weak disorder (top) and strong disorder (bottom) [87]. While the top shows a suppression of both the order parameter and phase correlation, both of which vanish at the transition point, the bottom one shows that the order parameter remains finite, but enhanced phase fluctuations drive the transition, causing the phase correlations to vanish. . . . .	52
2.12	Phase diagram from QMC calculations [88]. Blue line shows the $T_c$ degradation with disorder $V$ , vanishing at $V_c \sim 1.6t$ . Single particle gap $\omega_{dos}$ persists through the transition, while a two particle correlation gap $\omega_{pair}$ vanishes as one goes from the insulator to the superconductor. . . . .	53
3.1	(a). Temperature dependence of the $\mathbf{q} = \{0, 0\}$ component of the pairing field correlation for different $U/t$ . The onset locates the superconducting $T_c$ . (b). The $T_c$ inferred from the structure factor result. This is compared to QMC results at the end of the paper. (c). Ratio of $T = 0$ gap $2\Delta_0$ to $T_c$ . In the BCS limit the ratio would be $\sim 3.5$ . (d). The ‘phase diagram’ in terms of the low frequency behaviour of the density of states. The high temperature normal state has three regimes, ungapped (UG), pseudogapped (PG) and gapped (G), while for $T < T_c$ the system is a gapped superconductor (SC) exact definitions of these phases are given in the text. . . . .	77

- 3.2 Maps of amplitude fluctuation and phase correlation for single configurations at  $U/t = 2$  (top),  $U/t = 6$  (middle) and  $U/t = 10$  (bottom) at three temperatures:  $T = 0.1T_c$ ,  $T = T_c$  and  $T = 2T_c$  (left to right). For each set, the upper row shows the amplitude  $|\Delta_i|$  (normalised by the  $T = 0$  mean field value  $\Delta_0$ ) for a MC configuration, while the lower row shows the phase correlation:  $\Phi_i = \cos(\theta_i - \theta_0)$ , where  $\theta_0$  is the phase at a site  $\mathbf{R}_0$  near the center. . . . . 79
- 3.3 (a)-(c). The distribution  $P(|\Delta|)$  of the magnitude,  $|\Delta|$ , of the pairing field. The x-axis is normalised by the mean field value  $\Delta_0$  at  $T = 0$ . The results are for  $T = 0.1T_c$ ,  $0.5T_c$ ,  $1.0T_c$ ,  $2.0T_c$ . (a).  $U/t = 2$ , (b).  $U/t = 6$ , (c).  $U/t = 10$ . At  $U/t = 2$  there is a prominent increase in the mean and width of  $P(|\Delta|)$  with  $T$ . This  $T$  dependence weakens with growing  $U/t$ . (d). The growth of the mean value  $\langle|\Delta|\rangle$  and width  $\omega_\Delta$  with  $T$ . Both are normalized by the  $T = 0$  mean value of  $\Delta$ . The firm lines denote the mean  $|\Delta|$ , while the dot-dashed lines show the corresponding width. . . . . 80
- 3.4 Temperature dependence of the DOS,  $N(\omega)$  at different couplings. Panels (a)-(c) have the same legends. (a).  $U/t = 2$ , (b).  $U/t = 6$ , and (c).  $U/t = 10$ . The oscillations in the DOS in panel (a) are finite size artifacts (even on a  $24 \times 24$  lattice). At  $U/t = 2$  the gap essentially vanishes at  $T \sim T_c$ , while at  $U/t = 6$  a small ‘hard gap’ persists to  $T_c$  and above, although lorentzian broadening gives the impression of a pseudogap at the highest  $T$ . For  $U/t = 10$  a ‘hard gap’ persists to  $T \sim 0.5$  although with a clear reduction with increasing temperature. (d). Variation in the single particle gap, normalised by its  $T = 0$  value. . . . . 81
- 3.5 Plot of  $A(\mathbf{k}, \omega)$ . The rows, left to right, are for  $U/t = 2, 6$  and  $10$ . Columns, top to bottom, correspond to  $0.1T_c$ ,  $T_c$  and  $2T_c$ . The momentum, on the x-axis, is scanned as  $(0,0) \rightarrow (0,\pi) \rightarrow (\pi,\pi)$  and back through  $(\pi/2,\pi/2)$  to  $(0,0)$  along the diagonal. These points are labelled as A, B, C and D respectively. The gaps are lowest around  $(\pi/2, \pi/2)$  and  $(\pi, 0)$ , where the Fermi-surface of the free system intersects our path in k-space. Increasing temperature causes broadening and a decrease of the gaps, which close in the case of  $U = 2t$ . The increasing symmetry of the low  $T$  graphs with increasing  $U$  signals the participation of states far from the FS in pairing. . . . . 82

- 3.6 Spectral function  $A(\mathbf{k}, \omega)$ . The panels in the top row are for  $\mathbf{k} = \{\pi, \pi\}$ . (a).  $U/t = 2$ , (b).  $U/t = 6$ , (c).  $U/t = 10$ . Bottom row,  $\mathbf{k} = \{\pi/2, \pi/2\}$ , and interaction strengths: (d).  $U/t = 2$ , (e).  $U/t = 6$  and (f).  $U/t = 10$ . For each  $U$  we show data at  $T = 0.5T_c$ ,  $T_c$  and  $2T_c$ . The frequency axis is normalised by the  $\mathbf{k}$  dependent mean field energy  $E_{\mathbf{k}}^0$  at  $T = 0$ . For  $\mathbf{k} = \{\pi, \pi\}$ , which is outside the non interacting Fermi surface, the basic structure consists of large peak at positive energies  $\omega \sim E_{\mathbf{k}}^0$ , a broad negative energy feature at  $\omega \gtrsim -E_{\mathbf{k}}^0$ , and for  $T < T_c$  a remnant of the quasiparticle peak at  $\omega = -E_{\mathbf{k}}^0$ . Beyond weak coupling the survival of a two peak structure even for  $T > T_c$  indicates ‘incoherent pairs’. For  $\mathbf{k} = \{\pi/2, \pi/2\}$  the features are similar to what we observe at  $\mathbf{k} = \{\pi, \pi\}$ , except the quasiparticle peak is no longer separately visible. . . . . 83
- 3.7 (a) Comparison of our  $T_c$  (labelled SAF) with QMC [165] on a  $10 \times 10$  lattice, and the semi-analytic method employing the fluctuation exchange approximation (FEA) [151]. DMFT results [166] overestimate the  $T_c$  significantly, and also the location of peak  $T_c$ , and have not been included in the same plot. (b) Size dependence of our result, showing that the  $T_c$  estimate is almost size independent beyond  $L = 16$ . . . . . 84
- 3.8 Parameters defining the phenomenological model. (a) The parameter  $a(T, U)$ , (b). the parameter  $b(T, u)$ , and (c). the stiffness  $J(T, U)$  of the effective XY model for the phase degrees of freedom.  $a$  and  $b$  are normalised to their  $T = 0$  values. Notice the essential flatness of  $a(T)$  and  $b(T)$  at  $U = 10t$ , the weak  $T$  dependence at  $U = 6t$ , and the dramatic variation with  $T$  at  $U = 2t$ .  $J$  similarly is only weakly  $T$  dependent for  $U \gtrsim 6t$  and varies strongly with  $T$  at weak coupling. . . . . 85
- 3.9 (a) Comparison of  $T_c$  with and without  $\phi$  fields and corresponding QMC results at size  $10 \times 10$  [165]. Inclusion of  $\phi$  fields brings  $T_c$  in closer correspondence with QMC. (b), (c) and (d) compare the density of states for the same two cases at  $U/t = 2, 6$  and  $10$  respectively, at  $T/T_c = 0, 1.0$  and  $2.0$  respectively. The firm lines show the two fields results, while the circles of same colour show the single field results. There are small differences, but on the whole, they are very similar to each other. . . . . 88

- 4.1 The disorder dependence of resistivity calculated using QMC [141] for  $U/t = 3, 4$  and  $6$ . Shows that  $d\rho/dt$  changes sign at the critical disorder  $V_c$  at all coupling values, going from metallic ( $d\rho/dt > 0$ ) to insulating ( $d\rho/dt < 0$ ). Does not manage to capture the interesting behaviour at intermediate disorder seen in experiments. . . . . 94
- 4.2 (a): Phase diagram for  $U = 2t$  showing the superconducting (SC), and the following non superconducting phases: gapped (G), ungapped (UG) and pseudogapped (PG). The SC  $T_c$  is determined from the behaviour of  $S(q = 0)$ , whose temperature dependence at various disorder is shown in (b). We take the critical disorder  $V_c \sim 2t$ . The tail shows the exponentially small superconducting  $T_c$  surviving beyond  $V_c$ . A normal state pseudogap shows up for  $V \gtrsim 0.25V_c$  and for  $V \gtrsim 0.75V_c$  the  $T \gtrsim T_c$  phase actually has a hard gap. The crossover between pseudo-gapped and notionally ungapped phase is shown by the green area. The blue dashed line shows the transition from an ‘insulating’ ( $d\rho/dT < 0$ ) to ‘metallic’ regime, which lies within the broad crossover. . . . 98
- 4.3 (a) The resistivity,  $\rho(T)$ , measured in units of  $\rho_0 = \hbar/(\pi e^2)$ , evolving from metallic to insulating behaviour in the normal state with growing disorder. For  $V \lesssim 0.25V_c$ , it is metallic, between  $0.25V_c \lesssim V \lesssim 0.75V_c$ , it is mixed, showing a thermal transition from ‘insulating’ at low  $T$  to weakly ‘metallic’ at larger  $T$ . Beyond  $V = 0.75V_c$ , the low  $T$  behaviour is exponential  $\rho(T) \propto e^{\Delta_g/T}$ , with  $\Delta_g$  increasing with  $V$ . This is highlighted in (b), where we see that such a fit ceases to be valid below  $V \sim 0.75V_c$ . . . . . 99
- 4.4 Density of states at  $U = 2$ . (a) The DOS at low temperature, showing the persistence of a gap at all  $V$ , while the coherence peaks are difficult to discern beyond  $V \sim 0.75V_c$ . (b) Temperature dependence of the DOS for  $V = 0.5V_c$ , already showing a noticeable pseudogap for  $T > T_c$ . (c) Same as (b) but for  $V \sim V_c$ , where the system is insulating at all temperature. (d) Temperature dependence of  $N(0)$ , the DOS at the Fermi level, for different disorder. . . . 101

4.5	Optical conductivity and low frequency optical spectral weight. (a) The behaviour of $\sigma(\omega)$ , measured in units of $\sigma_0 = \pi e^2/\hbar$ , over a wide frequency range for disorder varying across the SIT. The temperature is $T = 0.2T_c^0$ . (b) The low frequency behaviour of $\sigma(\omega)$ for varying $V$ (same legends as in panel (a)), at $T = 0.2T_c^0$ . (c) Same as in (b), now at $T = 0.7T_c^0$ . Notice the absence of any gap, and the low frequency upturn, in samples with $V = 0.25V_c$ and $V = 0.5V_c$ which are still below their respective $T_c$ . (d) Disorder dependence of the low frequency optical spectral weight, $w(V, \Omega)$ , see text, at different $T$ . Inset shows low frequency weight of the single particle spectrum. . . . .	103
4.6	(a): Size dependence of clean resistivity. (b), (c) and (d): Dependence on the averaging interval $\Delta\omega$ at weak ( $V = 0.25V_c$ ), moderate ( $V = 0.5V_c$ ) and strong ( $V = 0.75V_c$ ) respectively. . . . .	106
4.7	Effective disorder $V_i^{eff} = V_i - \phi_i$ with increasing disorder. . . . .	107
4.8	Vortex density and structure factor with temperature for (a): $U/t = 2$ and (b): $U/t = 10$ . The black lines denote the results from our calculations while the red lines denote corresponding XY model results with the same $T_c$ . . . .	108
5.1	Maps of the tunneling conductance integrated over a narrow frequency window around the coherence peak feature in the LDOS (see text). Rows, top to bottom, $V = 0.2V_c, 0.5V_c, 0.9V_c$ . Columns, left to right, $T/T_c(V) = 0, 0.5, 1.0$ . Thermal average over 100 configurations. . . . .	116
5.2	Spatial maps at $V = 0.9V_c$ . 1st row: $\langle \Delta_i \rangle$ , 2nd row: phase correlation $\Phi_i$ , 3rd row: tunneling conductance $T_i^{gap}$ , 4th row: $T_i^{coh}$ . The notation is explained in the text. Columns, from left to right, are for $T = 0, T_c, 2T_c$ . The interpretation of these patterns is discussed in the text. . . . .	119
5.3	Spatial maps at $U = 2$ and $V = 0.5V_c$ . First row: $\langle \Delta_i \rangle$ , second row: phase correlation $\Phi_i$ (see text), third and fourth rows show the tunneling conductance averaged over two frequency (or bias) windows $\omega_{gap}$ and $\omega_{coh}$ . Along the row: temperatures $T = 0, 0.4T_{c0}$ and $0.8T_{c0}$ . $\langle \Delta_i \rangle$ at low $T$ forms phase correlated clusters, which shrink in size as $T$ is increased. $\langle \Delta_i \rangle$ is weakly inhomogeneous at low $T$ , and smoothens with increasing $T$ . $\Phi_i$ decrease with $T$ and vanishes almost homogeneously at $T_c$ (not shown, but between $0.5T_{c0}$ and $T_{c0}$ .) The subgap region lights up with increasing $T$ , due to the transfer of spectral weight to low frequency, while the plot for $\omega_{coh}$ loses intensity. . . . .	120
5.4	Thermal evolution of the gap and coherence peak height distribution. Top: Gap distribution for $V = 0.2V_c$ (left) and $0.9V_c$ (right). Bottom: Coherence peak height distribution at same $V$ . $T/T_c(V) = 0, 0.5, 1.0$ . . . . .	121

- 5.5 Local DOS on a typical ‘plateau’ site (top) and ‘hill’ site (bottom). The left panels (a) & (c) are at  $V = 0.2V_c$ , the right panels (b) & (d) are for  $V = 0.9V_c$ . In each panel the low energy DOS is shown for four temperatures  $T \approx 0, 0.5T_c, T_c, 2.0T_c$ . The curve at  $0.5T_c$  has been omitted in (b) for clarity. 122
- 5.6 Gap maps for 3 cases,  $T = 0$ . Left: Original calculation, showing patches with low gaps, identical to the correlated patches. Middle: With  $V_{bare}$ , scaled to lie between  $(-V - 2, V)$ , showing low gap patches with same basic structure; Right: with  $V_{eff}$ , increasing the contrast of the original  $V$ , gives similar map, with gaps of the insulating regions raised substantially. . . . . 124
- 5.7 Comparison of location of ‘plateau’ sites (see text) inside superconducting clusters (left) with the same outside clusters (middle) at  $V = 0.9V_c, T = 0$ . Right figure shows the spatial plot of  $|\Delta_i|$  for reference. ‘Plateau’ sites form a backbone over which the superconducting clusters are formed. In the insulating area, ‘hill’ or ‘valley’ sites (see text) predominate, ruling out the formation of SC clusters. . . . . 124
- 5.8 Left: Distribution of nearest neighbour  $J_{ij}$  at different disorder, showing successive broadening with disorder, but even at strong disorder, a finite number of sites have  $J \sim O(J_0)$ . Right: Spatial map of  $J_{ij}$ , at  $V = 0.9V_c$ , showing that the large values of  $J_{ij}$  correspond to the centres of the SC clusters. . . 125
- 5.9 Comparison of correlated patches for  $V = 0.8V_c$  for successive  $T$  points using the full Monte Carlo (top) and the simplified XY model (bottom). The basic phenomenon of an island pattern at low  $T$ , and shrinkage of these clusters with increasing temperature is well captured by the simplified model. . . . . 126
- 5.10 Phase diagrams showing superconducting (SC), gapped (G), pseudogapped (PG) and ungapped (UG) phases, and the cluster vanishing scale  $T_{clust}$  (green dashed lines) at  $U = 2$  and 4 (see text). . . . . 128
- 6.1 Top row: Spatial maps of left:  $|\Delta|$  and right: Phase correlation  $P_i$  (see text) at  $J = J_c = 1.2$ . Below  $J_c$  both are uniform, while after the phase transition has taken place,  $|\Delta|$  at the impurity site decreases in magnitude and changes phase by  $\pi$ . Bottom row shows the density of states for different  $J$ . As  $J$  increases, impurity level moves from edge of gap inwards, crossing  $\omega = 0$  at  $J_c$ . 132
- 6.2 Superconducting order parameter  $S(q = 0)$  -vs-  $T$  at  $J = 0.5, 0.75$  and  $1.0$  at various concentrations  $\eta$ , demonstrating the suppression and eventual destruction of superconductivity. The critical concentration  $\eta_{sc}(\%)$  is  $\sim 70, 40$  and  $30$  for the three  $J$  values respectively. . . . . 134

- 6.3  $\eta - T$  phase diagrams for  $J = 0.5, 0.75$  and  $1$ . G-SC, GL-SC/GL and N denote the gapped superconducting, gapless superconducting and normal phases respectively. As we increase  $J$ ,  $\eta_c$  decreases from around 80% for  $J \sim 0.5$  to 30% for  $J \sim 1$ . The gapless fraction increases substantially from  $\eta_g/\eta_c \sim 0.83$  for  $J = 0.5$  to 0.25 at  $J = 1$ . Bottom right shows a  $J$  vs.  $\eta$  phase diagram at low  $T$ , using data from the three  $J$  points and extrapolating them to the limits  $J \rightarrow \infty$  and  $\eta \rightarrow 100$  respectively. . . . . 135
- 6.4 Density of states for  $J = 0.25, 0.5, 0.75$  and  $1$  at various concentrations  $\eta$  at  $T = 0$ . At  $J = 0.25$ , there is a very small narrowing of the gap with increasing  $\eta$ , impurity levels are at the edge. As  $J$  increases, impurity levels move inwards and with increasing  $\eta$ , close the gap at some  $\eta_g(J)$  to form a gapless superconducting phase.  $\eta_g$  decreases from 60% at  $J = 0.5$  to only 8% at  $J = 1$ . . . . . 137
- 6.5 Spatial plots for for  $J = 1$  at  $\eta = 2\%, 12\%$  and  $30\%$  at  $T = 0$ . Upper panel shows the impurity positions. Middle panels show the thermally averaged  $|\Delta_i|$ , while bottom panels show the phase correlation (see text). At  $\eta = 2\%$ , the system is a uniform superconductor. At  $12\%$ ,  $\Delta_i$  are depressed in many impurity positions, however, the phase correlation seems uniform except for three sites. At  $\eta = 30\% \sim \eta_c$ ,  $\Delta_i$  is small at most sites, while the phases are randomly oriented, signalling the transition to a non superconducting metal. 138
- 6.6 Spatial plots for for  $J = 0.5$  at  $\eta = 12\%, 44\%$  and  $70\%$  at  $T = 0$ . Panels same as Fig.6.6. Shows much more homogeneous behaviour than  $J = 1$ , with the system being largely homogeneous and phase coherent even around  $\eta \sim 60\%$ , where the system becomes gapless. However, the eventual destruction at  $\eta = 70\%$  is brought about by almost complete suppression of all  $\Delta_i$ , just like at  $J = 1$ . . . . . 139
- 6.7 Density of states for  $J = 0.5$  and  $0.75$ , at two values of  $\eta$ , 32% and 60%, and 12% and 24% respectively. Four temperature values are given by  $0.1T_{c0}$ ,  $0.5T_{c0}$ ,  $T_{c0}$  and  $1.5T_{c0}$ , where  $T_{c0} \sim 0.07t$  is the clean transition temperature. The evolution is along expected lines starting from the  $T = 0$  values, with no outstanding features. . . . . 140

6.8	<p>Spatial signatures of thermal evolution for <math>J = 1</math> (top two rows) and <math>J = 0.5</math> (bottom two rows) at <math>\eta = 12\%</math>. The first snapshot shows the impurity positions. Next 5 snaps show the nearest neighbour phase correlation (see text) in steps of <math>T = 0.01</math> starting at <math>T_{min} = 0.005</math>. Shows low correlations at a few sites to begin with, which become larger with increasing <math>T</math>, while the correlations weaken at other impurity sites as well. Last 6 snaps show the correlations for <math>J = 0.5</math>, starting at <math>T_{min}</math> with steps of <math>T = 0.01</math>. Show negligible effects on phase correlation till <math>T \sim 0.35</math>, and even after that, the correlation is lost much more homogeneously. . . . .</p>	141
6.9	<p>Low temperature wavefunctions for <math>J = 1</math> at <math>\eta = 2\%, 6\%</math> and <math>12\%</math> respectively. Top row shows spatial impurity distribution at these concentrations. Middle and bottom rows show wavefunctions corresponding to the first and third excited states. Have large overlaps with impurity positions, avoiding regions with large <math>\Delta_i</math> (see text). . . . .</p>	143

# LIST OF TABLES

3.1	Comparison of available methods with our static auxiliary field approach for the two dimensional attractive Hubbard model. The expanded title for each method is given in the text. . . . .	75
-----	---	----



# INTRODUCTION

Superconductivity is a fascinating example of correlated quantum behaviour driven by an effective attractive interaction between electrons [1]. When cooled below a critical temperature  $T_c$ , which is usually very low, these materials show a remarkable set of properties, including vanishing electrical resistance and perfect diamagnetism. These fascinating properties have ensured that superconductivity has continued to be an active field of research since its discovery in 1911 by Kammerlingh Onnes.

The basic characteristics of a superconducting state are (i) the pairing of two electrons to form a bound state called a Cooper pair, and (ii) the condensation of these Cooper pairs to form a macroscopic, coherent quantum state. While the first phenomenon shows up as a finite gap in the single particle density of states, the formation of a coherent state leads to a finite phase stiffness, that is, a finite amount of energy is required to twist the phase of the condensate.

Decades of theoretical effort culminated in the development of the famous Bardeen-Cooper-Schreiffer (BCS) theory [2], which provided a satisfactory explanation of conventional superconductors. While the mean-field ideas of BCS continue to be relevant to later discoveries in superconductivity, many of their specific predictions need to be modified when one encounters situations involving

1. Strong interaction between electrons. This causes the well known BCS to Bose-Einstein condensate (BEC) crossover [3, 4], where the system evolves from the BCS state (of large overlapping pairs) to a BEC of strongly bound pairs that act as effective bosons.
2. Presence of significant potential scattering, which can suppress superconductivity and destroy it eventually, causing a superconductor-insulator transition (SIT) [5]. This is further accompanied by a metallic to insulating crossover in the high temperature resistivity, a suppression (pseudogap) in the single particle density of states near the Fermi energy, and considerable inhomogeneity in the underlying superconducting state.

3. Coupling to magnetic impurities [6], which can cause a rapid suppression and destruction of superconductivity, along with the presence of a window of gapless superconductivity.
4. Proximity to other ordered phases.

Quite generally, these may require us to handle inhomogeneous ground states (which in principle can occur within the BCS scheme itself) and quantum and thermal fluctuations of the ‘order parameter’.

This motivates the primary focus of the thesis: understanding the role of strong disorder in superconducting systems, in particular the thermal fluctuations that occur on the inhomogeneous background. We would want to study these effects in the presence of ‘potential’ disorder as well as magnetic impurities. However, to get to these relatively less explored problems we first benchmark our method on a well studied problem - the BCS to BEC crossover with increasing pairing interaction in a Fermi system.

In this chapter we first provide a basic review of superconductivity. This is followed by a discussion of disorder in metals, and a heuristic discussion of the phenomenon of Anderson localization. Finally, we move on to our main topic, disordered superconductors, and review the extensive body of experimental results that exists on the subject. We focus mainly on potential disorder, in view of the large body of work in this field, and considerable current interest driven by recent advances in scanning tunneling spectroscopy (STS) [7]. At the end, we provide a brief description of available data on magnetic impurities in superconductors.

## 1.1 Basic concepts of superconductivity

### 1.1.1 Zero resistivity

A superconductor is characterized by the unique property of zero resistance in the superconducting state. This was the basis for the discovery of superconductivity by Kammerlingh Onnes in 1911 [8].

While studying the resistance of Hg at very low temperatures, he observed the abrupt vanishing of the resistance at around  $T \sim 4.2K$ , as shown in Fig.1.1. In the ensuing decades, the same signature was observed in a number of materials, including Pb, NbB<sub>2</sub>, MgB<sub>2</sub> etc. While the critical temperature for the older superconductors was very low the discovery of ‘unconventional’ superconductivity in the cuprates increased the scale considerably. For mercury based cuprates it can be as high as 130K.

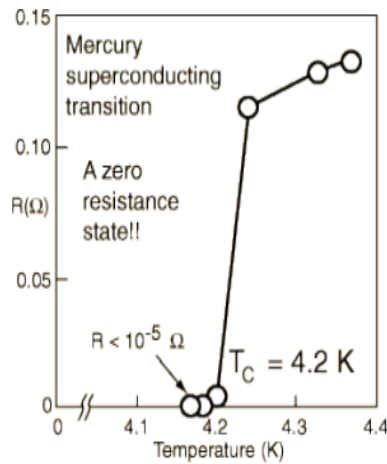


Figure 1.1: The resistivity of Hg [8] as measured by Kammerlingh Onnes, showing a superconducting transition at 4.2K.

### 1.1.2 Meissner effect

The other important property of all superconductors is perfect diamagnetism, that is, the ability to expel all magnetic field from its interior when placed in an external magnetic field. This was first noticed by W. Meissner and R. Ochsenfeld in 1933 [9]. As shown in Fig.1.2, when a superconducting material is cooled below its transition temperature in a small magnetic field, all the field lines inside the material are ejected outside. The magnetic field induces surface currents in the superconducting state, and the internal field produced by these exactly cancel the externally applied field inside the material, thus displaying a kind of perfect diamagnetism. The magnetic field is not strictly expelled from the whole body though, and manages to penetrate a small distance  $\lambda$  into the material, known as the penetration depth. The Meissner effect is an *additional attribute* of superconductors. A ‘non-superconducting’ perfect conductor (which also has zero resistivity) will not show this effect.

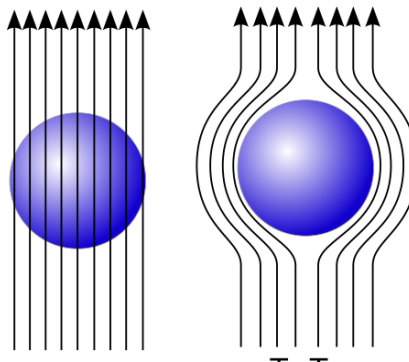


Figure 1.2: A cartoon illustrating the Meissner effect. The magnetic field lines penetrating the material at  $T > T_c$  are expelled outside the body for  $T < T_c$  [10].

While a superconductor shows perfect diamagnetism at weak fields, strong enough fields can destroy the superconducting state. Once the magnetic field reaches a critical value (say,  $H_c$ ), the superconducting state is destroyed abruptly in most elemental superconductors. This also gives us a measure of the energy of stability of the superconductor; since an external magnetic field increases the energy of the system by an amount  $H^2/8\pi$  per unit volume, it follows that the energy of the superconducting state is lower than that of the normal state by  $H_c^2/8\pi$ .

### 1.1.3 London equations

The London brothers provided the first phenomenological explanation of the twin properties of zero resistivity and perfect diamagnetism [11]. They proposed the equations

$$\begin{aligned}\partial J_s / \partial t &= (n_s e^2 / m) \vec{E} \\ \vec{\nabla} \times J_s &= -(n_s e^2 / m) \vec{B}\end{aligned}$$

Here,  $J_s$  is the superconducting current,  $\vec{E}$  and  $\vec{B}$  are the electric and magnetic fields inside the superconductor,  $e$  and  $m$  are respectively the electron charge and mass and  $n_s$  is a phenomenological ‘superfluid density’ characterizing the number density of superconducting carriers. Intuitively, the first equation simply says that the change in the supercurrent is proportional to the external electric field, as it should without any resistance in the superconducting state. The second, when combined with Maxwells’ equation  $\vec{\nabla} \times \vec{B} = \mu_0 J_s$ , gives

$$\nabla^2 \vec{B} = \vec{B} / \lambda$$

where  $\lambda = (m / \mu_0 n_s e^2)^{1/2}$ . The solution of this equation,  $B \sim B_0 \exp(-x/\lambda)$ , provides an ‘explanation’ of the Meissner effect and an estimate of the penetration depth  $\lambda$ .

### 1.1.4 Flux penetration

The abrupt destruction of superconductivity with increasing magnetic field happens for most elemental superconductors, but there is another important class of superconductors (comprised mainly of alloys and compounds) in which the process happens very differently. Here, the material shows perfect diamagnetism upto a lower critical field,  $H_{c1}$ , but beyond this the magnetic field starts to penetrate the material, giving rise to a unique vortex state where superconducting and normal regions exist side by side. As the field is increased further, the superconducting regions shrink, and beyond a second critical field,  $H_{c2}$ , superconductivity is destroyed completely. These two types are called Type I and Type II superconductors respectively. Fig.1.3 shows the contrasting behaviour of

the two classes under an external magnetic field.

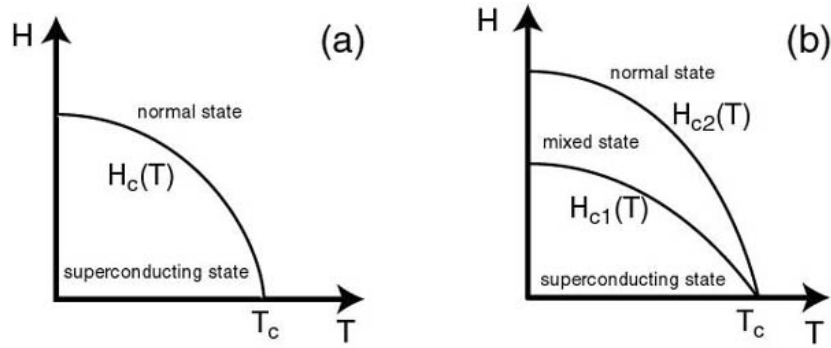


Figure 1.3: A schematic diagram illustrating the different response of Type I and Type II superconductors to an external magnetic field [12].

### Coherence length

The difference in the two types of superconductors is caused by the relative magnitude of two fundamental length scales, namely, the penetration depth  $\lambda$  that we discussed earlier, and the coherence length  $\xi$ , introduced first by Pippard [13] in a non-local generalization of the London equations. Pippard argued that the superconducting current at a point should depend on the superconducting wave function over a length scale  $\xi$ . He also provided a crude estimate for  $\xi$ : With  $\Delta E \sim kT_c$ , we get, for the momentum uncertainty,  $\Delta p \sim kT_c/v_F$  ( $v_F$  is the Fermi velocity), which gives a length scale  $\Delta x \sim \hbar v_F/kT_c$ . With the definition  $\xi \sim a\Delta x$ , where  $a \sim \mathcal{O}(1)$ , Pippard managed to fit his theory to a lot of experimental data that could not be understood from a local picture.

The two scales,  $\lambda$  and  $\xi$  provide us with an intuitive understanding of the contrasting behaviour of Type I and Type II superconductors. Fig.1.4 shows the interfaces for two cases,  $\lambda \ll \xi$  and  $\lambda \gg \xi$ . The first, corresponding to Type I superconductors, turns out to have positive interface

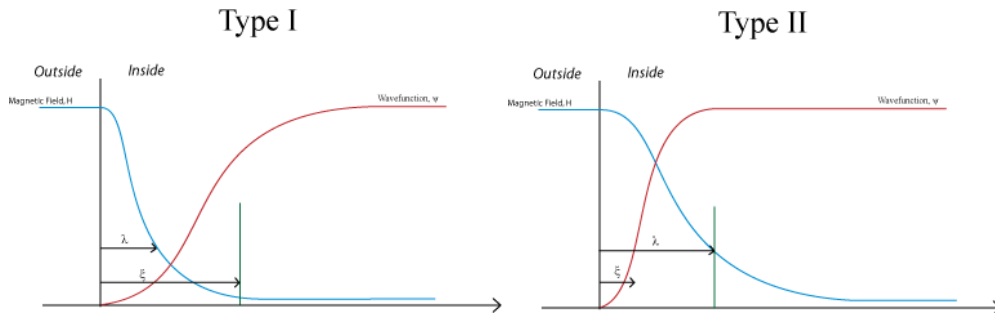


Figure 1.4: Interfaces of Type I ( $\lambda \ll \xi$ ) and Type II ( $\lambda \gg \xi$ ) superconductors. The first has positive interface energy, favouring a uniform state, while the second, with negative energy, favours the mixed vortex state of Type II superconductors [14].

energy which favours a uniform state until it is destroyed by the magnetic field, while the second has negative energy, which favours as many such interfaces as possible, resulting in the intermediate state of Type II superconductors.

### 1.1.5 Landau-Ginzburg theory

While the London equations provided an intuitive understanding of the Meissner effect and the infinite conductivity, it could not provide insight into the evolution of the superconducting property of the system in situations other than those involving electric and magnetic fields. Landau and Ginzburg developed a phenomenological theory [1, 15], based on Landau's concept of an order parameter, which was able to provide several results about the superconductor under varying conditions of temperature, field, *etc.*

The theory starts by defining an order parameter, a superconducting wavefunction  $\psi(x)$ , so that the superconducting electron density is given by

$$n_s = |\psi|^2$$

Now, in the regime where the order parameter value is small ( $\psi \ll 1$ ) and it varies slowly in space, the superconducting free energy of the system, in the presence of a magnetic field, can be written as an expansion in powers of the order parameter and its gradients:

$$f = f_0 + \alpha|\psi|^2 + \beta|\psi|^4 + (1/2m^*)|(-i\hbar\vec{\nabla} - e^*\vec{A})\psi|^2 + B^2/8\pi$$

Here,  $m^*$  and  $e^*$  are the effective mass and charges of the 'particle' corresponding to the wave function, which would turn out to be equal to twice those of an electron due to the formation of Cooper pairs. Here, as is usual for a Landau theory of second order transitions,  $\beta$  is assumed positive throughout while  $\alpha$  changes sign at the transition temperature  $T_c$ :

$$\alpha = \alpha_0(T/T_c - 1)$$

The minimization of energy with respect to  $\psi$  and  $B$  provide the Landau-Ginzburg equations. Since the functional incorporates the energy cost associated with a slowly varying wavefunction, this theory is especially suited for application to situations which involve inhomogeneities in the order parameter, corresponding to, for example, interfaces between superconducting and non-superconducting regions. Hence, one can work out the two basic length scales,  $\lambda$  and  $\xi$  in terms of the phenomenological parameters  $\alpha$  and  $\beta$  and thus also study the phenomena of Type I and II superconductors. In fact, the most remarkable achievement of this theory was the prediction by Abrikosov [16] of a vortex lattice in Type II superconductors. The deep intuition and success of

this theory was recognised by the award of the Nobel Prize to Ginzburg and Abrikosov in 2003.

### 1.1.6 BCS theory

While the London equations provided an intuitive understanding of zero resistivity and the Meissner effect, a satisfactory microscopic understanding was only achieved in 1957 with the BCS theory [2]. This triumph was built upon the crucial earlier work of many other scientists. The isotope effect [17] showed the importance of the electron-phonon interaction, which led to the work by Frohlich [18], showing that an effective attractive electron electron interaction can result from the electron phonon coupling in the material. Also, the presence of a critical field and experimental results [19] showing the exponential temperature dependence of the specific heat at low temperature pointed to the presence of a gap in the excitation spectrum [20], hinting at some form of binding in the superconductor. This focussed the attention on building a theory which included bound states between pairs of electrons, and macroscopic coherence among these states. This led to many unsuccessful attempts [21], including using the concept of Bose-Einstein condensation (BEC), before finally culminating in the development of the BCS theory.

#### Basic concepts

The basic ingredients of the BCS theory are the following:

1. There is an attractive interaction between electrons in the narrow range  $(\epsilon_F - \omega_D, \epsilon_F + \omega_D)$ , where  $\omega_D$  is the Debye frequency, mediated by electron phonon interactions. Cooper showed that the presence of such an interaction always causes a bound state, so that the Fermi sea becomes unstable to the formation of such bound pairs. The lowest energy states are made of pairs with zero total momentum, between states  $k \uparrow$  and  $-k \downarrow$ .
2. BCS argued that the large number of particles involved in the process in most real materials validates the use of a mean-field theory, where the occupancy of any pair depends only the average occupation of the other energy levels (in pairs), and fluctuations can be neglected. This leads to the BCS ground state wavefunction

$$|\Psi_0\rangle = \prod_k (u_k + v_k c_{k\uparrow}^\dagger c_{-k\downarrow}^\dagger) |0\rangle$$

3. The fact that oppositely paired bound states have lowest energies motivates the reduced BCS Hamiltonian:

$$\mathcal{H}_{BCS} = \sum_{k\sigma} \xi_k n_{k\sigma} + \sum_{kl} V_{kl} c_{k\uparrow}^\dagger c_{-k\downarrow}^\dagger c_{-l\downarrow} c_{l\uparrow}$$

## Solution and results

The parameters  $u_k$  and  $v_k$  can be determined via a variational approach. It also determines the order parameter  $\Delta$ , whose value characterizes the superconducting state. Since, the relevant energy range of the interaction is small,  $\sim \mathcal{O}(2\omega_D) \ll E_F$ ,  $V_{kl}$  is assumed to be a constant,  $V$ , in this range. The important results are the following:

1. The  $T = 0$  state is superconducting, and characterized by  $u_k^2 = (1/2)(1 - \xi_k/E_k)$ ,  $v_k^2 = 1 - u_k^2$ , with  $E_k = \sqrt{(\xi_k^2 + \Delta^2)}$ , where  $\Delta$  is an order parameter characterizing the superconducting state, obtained from a self consistency condition. At  $T = 0$ ,  $\Delta \equiv \Delta_0 \approx 2\hbar\omega_D e^{-1/N(0)V}$  in the so called ‘weak coupling’ regime where  $N(0)V \ll 1$ .
2. The superconducting ground state is lower in energy than the corresponding normal state by an amount  $(1/2)N(0)\Delta_0^2$ . An elementary excitation requires a minimum energy  $\Delta$  to be formed, implying a gap in the single particle spectra.
3. The single particle spectrum has square root singularities (called coherence peaks) at the gap edge, and this is a characteristic feature of BCS systems.
4. The transition temperature, where  $\Delta(T) \rightarrow 0$ , is given by  $kT_c = 1.13\hbar\omega_D e^{-1/N(0)V}$ . This implies  $\Delta_0/kT_c \sim 1.76$ , another characteristic of BCS systems.

## Bogolyubov-Valatin canonical transformation

To gain more insight into the physics of the mean field theory, we analyse the BCS solution from a slightly different, more modern, approach that does not require a variational ansatz for the ground

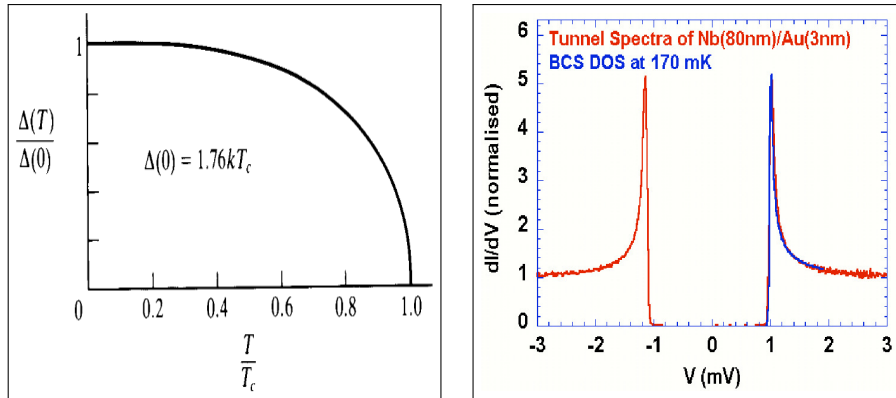


Figure 1.5: The temperature dependence of the order parameter  $\Delta$  and the density of states, according to BCS theory (from the internet).

state. This method was first utilized for the BCS case by Bogolyubov and Valatin [22], and emphasizes the mean field concept of ‘factorizing’ the interacting part of the Hamiltonian into an effective field times a quadratic combination of fermionic operators. We have,

$$\mathcal{H}_{BCS} = \sum_{k\sigma} \xi_k n_{k\sigma} + \sum_{kl} V_{kl} c_{k\uparrow}^\dagger c_{-k\downarrow}^\dagger c_{-l\downarrow} c_{l\uparrow}$$

Since the ground state is a coherent superposition of pairs  $|k \uparrow\rangle$  and  $|-k \downarrow\rangle$ , one expects that the expectation values  $\langle c_{-k\downarrow} c_{k\uparrow} \rangle$  will be non-zero, and the mean field treatment would further assume that the fluctuations would be small. This motivates us to express the product as

$$c_{-k\downarrow} c_{k\uparrow} = b_k + (c_{-k\downarrow} c_{k\uparrow} - b_k)$$

Here  $b_k$  denotes the non zero average of the product of the operators, while the term in parenthesis denotes the fluctuations. Since these fluctuations are small, one neglects terms  $\sim \mathcal{O}((c_{-k\downarrow} c_{k\uparrow} - b_k)^2)$  in the final expression. Thus, we have

$$\mathcal{H}_{BCS} = \sum_{k\sigma} \xi_k n_{k\sigma} + \sum_{kl} V_{kl} (c_{k\uparrow}^\dagger c_{-k\downarrow}^\dagger b_k + c_{-l\downarrow} c_{l\uparrow} b_k^* - b_k^* b_l)$$

Now, with the substitution  $\Delta_k = -\sum_l V_{kl} b_l$ , one gets

$$\mathcal{H}_{BCS} = \sum_{k\sigma} \xi_k n_{k\sigma} + \sum_k (\Delta_k c_{k\uparrow}^\dagger c_{-k\downarrow}^\dagger + \Delta_k^* c_{-k\downarrow} c_{k\uparrow}) + \sum_k \Delta_k b_k^*$$

Thus, the interacting part of the Hamiltonian is ‘factorized’ into a product of a mean field ( $\Delta_k$  here) and a quadratic combination of fermionic operators. This Hamiltonian, being quadratic, can now be solved by a canonical transformation to yield the BCS solution for a uniform, single  $\Delta$ .

Apart from successfully predicting all the basic characteristics listed above, BCS theory has also been applied to other situations [1], including acoustic and electromagnetic attenuation, nuclear spin relaxation, and a number of tunneling results. However, as mentioned earlier, it begins to fail when the coupling is comparatively large, or, more interestingly, when the system is highly disordered. Before describing disordered superconductors, however, we provide a basic introduction to disorder and its effects on normal metals in the next section.

## 1.2 Disorder in metals

A fundamental classification of materials is as metals or insulators. Metals have d.c conductivity,  $\sigma_{dc}$ , finite as  $T \rightarrow 0$ , while for insulators  $\sigma_{dc} \rightarrow 0$  as  $T \rightarrow 0$ . At finite  $T$ , metals have  $d\sigma_{dc}/dT < 0$ ,

while for insulators  $d\sigma_{dc}/dT > 0$ . An ideal metal has infinite conductivity at  $T = 0$  and is a perfect conductor. At finite temperatures, Umklapp processes can provide a scattering mechanism, resulting in a finite  $T$  dependent conductivity. However, real materials always contain disorder in the form of dislocations, impurities etc., that induce random scattering and can have profound implications on the conductivity of the material, especially when quantum interference effects are taken into account. This section presents a brief summary of disorder and its effects, including Drude's classical theory, the concept of localization and, finally, modern scaling theory arguments.

### 1.2.1 Drude theory

The first comprehensive theory of electrical transport in disordered metals was provided by Paul Drude in 1900 [23]. In his theory, electrons are assumed to be classical objects that are scattered randomly by the heavier immobile ions present in a solid. The collisions impart an instantaneous retarding force, and on an average, the electron travels through the material with a velocity  $v_{av}$ . The average time between collisions is  $\tau$ . Using this, Drude obtained

$$\vec{J} = (ne^2\tau/m)\vec{E}$$

Here,  $\vec{J}$  is the current due to an external electric field  $\vec{E}$ ,  $n$ ,  $e$  and  $m$  denote the number density, electronic charge and mass respectively. This implied that the conductivity  $\sigma$ , defined as  $J = \sigma\vec{E}$ , is given by  $\sigma = (ne^2\tau/m)$ .

### 1.2.2 The quantum approach

With the development of quantum mechanics, the idea of electrons as balls bouncing off heavy ions was invalidated. The perfect lattice structure of an ideal solid permits the classification of electronic eigenstates in terms of Bloch states [24], and a perfect lattice should have infinite conductivity. However, there is always disorder, in the form of impurities, dislocations and other irregularities in the crystal structure. When such disorder is low, the problem can be analysed in terms of scattering of Bloch waves by impurity potentials, and the concepts of Drude's theory can be carried over with a suitably defined  $\tau$ . This is true as long as the mean free path,  $l$ , of electrons in the material is much greater than the Fermi wavelength  $\lambda_F = 2\pi/k_F$ . In typical metals, where  $l \sim (10^4 - 10^6)\lambda_F$ , Drude's theory works very well. With increasing disorder, however,  $l$  decreases, and when  $l \sim \lambda_F$ , the quantum effects become crucial. This condition, which can be re-expressed as  $k_F l \sim \mathcal{O}(1)$ , is known as the Ioffe-Regel criterion. Further increase in disorder leads ultimately to localization of the electronic states.

### 1.2.3 Anderson localization

The concept of localization was first put forward by P. W. Anderson in 1958 [25, 26], to explain the absence of spin diffusion in certain disordered lattices. He showed that sufficiently strong disorder can profoundly alter the nature of the electronic wavefunctions in the material, and ultimately localize them completely, so that the modulus of the wavefunction decays exponentially with distance,  $|\psi(r)| \sim \exp(-r/\xi)$ , where  $\xi$  is a localization length.

An intuitive understanding of localization effects can be provided from an analysis of the path of an electron which starts from and returns to a given point  $r$ . From the principle of quantum mechanics, the total amplitude is given by the sum of all such paths. Now, since there is time reversal symmetry, the time reversed counterpart of any given path has the exact same magnitude and phase, and thus they interfere constructively, increasing the amplitude to return twofold compared to what we would expect classically. This is known as weak localization, and calculations reveal that the total conductivity is given by

$$\sigma = \sigma_0(1 - (1/2\pi k_F l) \ln(\tau_0/\tau))$$

Here,  $\tau_0$  is a cutoff provided by either inelastic scattering or the system size.

As the disorder is increased, we enter the regime of strong localization. In this situation, the electron eigenstates at the extremities of the band are localized, bound by deep fluctuations in the random potential profile. However, at moderate disorder, states near the centre of the band can be extended (in three dimensions), separated from the localized states by a mobility edge. With further increase of disorder, eventually, all states would get localized.

### 1.2.4 Scaling theory

The first ideas on scaling theory were advanced by Thouless [27], who considered putting blocks of a material of size  $L^d$  to build one of size  $2L^d$ , where  $d$  is the number of dimensions. He reasoned that the nature of the eigenstates in the final block will depend on (i) the level spacing  $\delta W$  in the initial blocks, and (ii) the overlap integral  $\delta E$ , typically equal to the band spread of an energy level when the original block is extended in one direction to form a periodic chain. Depending on whether the ratio  $\delta E/\delta W$  is large/small, the eigenstates of the final block will be extended throughout the system/localized in one of the original blocks, and thus determine the transport properties of the larger block. Thouless related this to the dimensionless quantity  $g = G/(e^2/\hbar)$ , where  $G$  is the conductance. This says that  $g$  is the single parameter that determines the behaviour of the system under scaling.

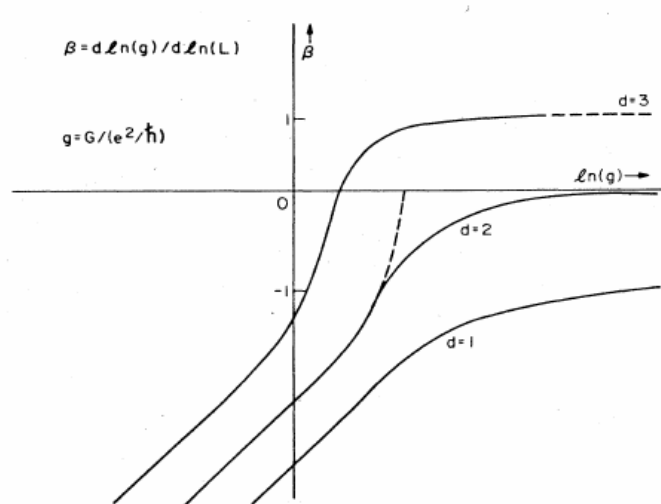


Figure 1.6: The scaling function  $\beta(g)$  for  $d = 1, 2$  and  $3$  [26, 28]. Shows the existence of a critical conductance signalling a metal-insulator transition (MIT) in 3D, while for  $d \leq 2$ ,  $\beta < 0$  always, showing that all states are localized.

Inspired by this, Abrahams, *et al.* [28], provided a single parameter scaling relation for  $g$ :

$$(d \ln g(L) / d \ln L) = \beta(g)$$

The nature of the scaling function  $\beta(g)$  can be determined from the limiting behaviour of the system. When conductance is large, one can use the Drude relations to get

$$\beta(g) = (d - 2)$$

In the opposite regime of small conductance, since  $g(L) \sim \exp(-L/\xi)$ , we have

$$\beta(g) = -\ln g$$

Using the two limits, one can get an idea of the behaviour of  $\beta(g)$ , shown in Fig.1.6. It shows the presence of a metal-insulator transition at a critical conductance  $g_c$  in 3D, above which the scaling function is positive (and hence the eigenstates are extended), while it is negative (eigenstates localized) below. On the other hand, for  $d \leq 2$ , *all* states are localized by arbitrary values of disorder.

## 1.3 Disordered superconductors

The contrasting transport properties of superconductors and disordered systems makes the problem of disordered superconductors an intriguing one. The inevitable presence of disorder in all materials also makes this a natural problem to study, and hence, this problem has been studied for a long time now. Depending on the type of disorder, the effect it has on superconductivity varies sharply. While superconductivity seems robust to moderate amounts of potential disorder, magnetic impurities can destroy superconductivity even at low concentration.

In this section, we provide a review of disordered superconductors, concentrating on the large body of experimental data that exists on the subject. In the first part we focus mainly on potential disorder, and describe the experimental results on the subject. We follow this up by a brief description of available data on magnetic impurities in superconductors including a short summary of results on the gapless phase.

### 1.3.1 Historical overview

The first experiments on disordered superconductors date from around the same time as the original discovery of superconductivity. These concluded that the effects of such disorder was negligible on the thermodynamic properties of the superconductor such as  $T_c$ . Several experiments down the line also seemed to lead to the same conclusion, hinting at a remarkable robustness of the superconducting state to non-magnetic disorder [29].

The first theoretical explanation was provided by Abrikosov and Gorkov [30], and followed up by an intuitive argument by Anderson [31]. He explained that one could redo the whole BCS pairing theory in terms of the exact eigenstates of the disordered material and their time reversed counterparts. While the exact nature of these complicated eigenstates cannot be determined, the *average* effect on thermodynamic properties such as  $T_c$  were shown to be negligible, as long as the superconducting order could be assumed to be uniform.

However, these were followed up by a large number of experiments over the last few decades which demonstrated the suppression and eventual destruction of superconductivity by strong disorder. They also revealed a metallic to insulating crossover in the normal state resistivity, a pseudogap in the density of states, and spatial inhomogeneity (inferred from scanning tunneling spectroscopy measurements [5]).

We expand on these observations below, in the context of materials like (i) thin films of Be [32–37] and NbN [38], (ii) amorphous films of InO<sub>x</sub> [39–48] and TiN [49–56] and, (iii) three dimensional NbN [57–62] films, focusing on:

- Resistivity and its dependence on temperature, disorder and magnetic field.

- Tunneling density of states, as inferred from STS, and their detailed evolution with temperature and disorder.
- More recent STS maps, hinting at the inhomogeneity of the superconducting state.

### 1.3.2 Thin films of Be and NbN

Thin films of a substance can be prepared by depositing it on a substrate material by several methods, including magnetron sputtering. One can typically perform this process in several steps, resulting in an array of films of different thicknesses, and make measurements on them. It is seen that as the thickness decreases, so does the mean free path  $l$ , and thus the effective disorder increases. This represents one of many different ways to control the disorder of a material. Other methods, including formation of vacancies in the deposited material, will be discussed separately. Depending on whether the thickness  $d$  is less than or greater than the coherence length  $\xi$ , the system can be considered effectively 2 or 3 dimensional, respectively. Here, we will consider Be and NbN thin films and mainly concentrate on the results in 2 dimensions (even though one can study the effect of dimensional crossover in these systems).

There is no conventional superconducting transition in two dimensions, following the Mermin-Wagner theorem [63]. However, there is a different type of transition called a Berezinski-Kosterlitz-Thouless (BKT) transition [64] at a temperature  $T_{BKT}$ , where the system enters into a state with algebraically decaying correlations instead of true long range order. This requires a little more care in determining the transition temperature from transport data or measurements of superfluid stiffness.

#### Transport

We begin with the electrical transport, one of the most important indicators of the properties of the underlying state. Fig.1.7 shows the zero magnetic field resistance  $R$  for different thicknesses of Be [35] and NbN [38] films respectively. All the Be films (thickness  $\lesssim 1nm$ ) and the NbN films with  $d \lesssim \xi \sim 5nm$  can be considered 2 dimensional. We find that

(i) Both films display a suppression of the superconducting  $T_c$  and ultimately  $T_c \rightarrow 0$ , and a simultaneous crossover from metallic (or weakly insulating) to insulating behaviour. This constitutes the most basic evidence of a disorder driven SIT.

(ii) The transition from superconducting to insulating is sharp, and there is almost certainly no metallic phase in between. The slight non-monotonicity in the curves near the critical disorder for Be are probably due to specific experimental factors like overheating of the sample, etc.

(iii) The insulating Be films show simple activated behaviour  $R(T) \propto \exp(T_a/T)$ , which crosses over to Efros-Shklovskii  $R(T) \propto \exp(T_{es}/T)^{1/2}$  at higher temperatures. The low tem-

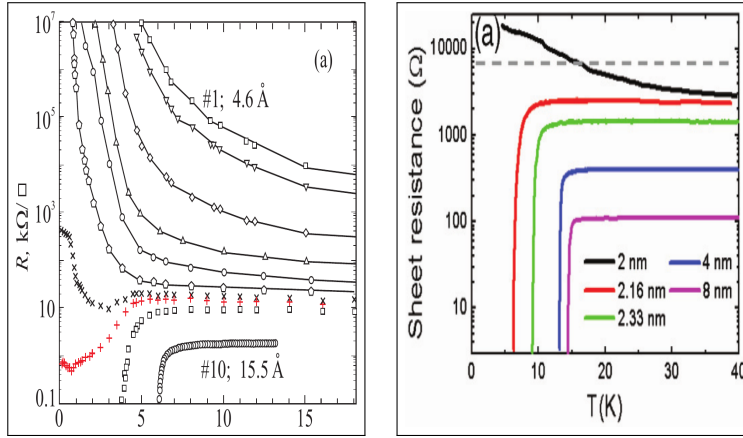


Figure 1.7: Resistivity  $R(T)$  with increasing disorder for Be [35] and NbN films [38] respectively.

perature fitting parameter  $T_a$  increases with increasing disorder.

While these observations point to a direct transition from a superconductor to an insulator due to increasing disorder, it does not provide any insight on the nature of the superconducting or insulating state close to the transition, apart from the activated nature of the transport. For more information, we show a magnetic field driven superconductor-insulator transition in Fig.1.7. (a) and (b) show  $R(T)$  curves for different magnetic fields  $B$  for Be [36,37] and NbN [38] respectively, on the superconducting side very near to the critical disorder, while (c) plots the variation of resistance at a fixed  $T = 100mK$  on the insulating side very near to the critical point. The basic observations are

(i) Both (a) and (b) show that the curves for different  $B$  begin to deviate from around the same temperature and turn insulating when superconductivity is destroyed completely. This temperature is slightly larger than the  $B = 0 T_c$  of the systems.

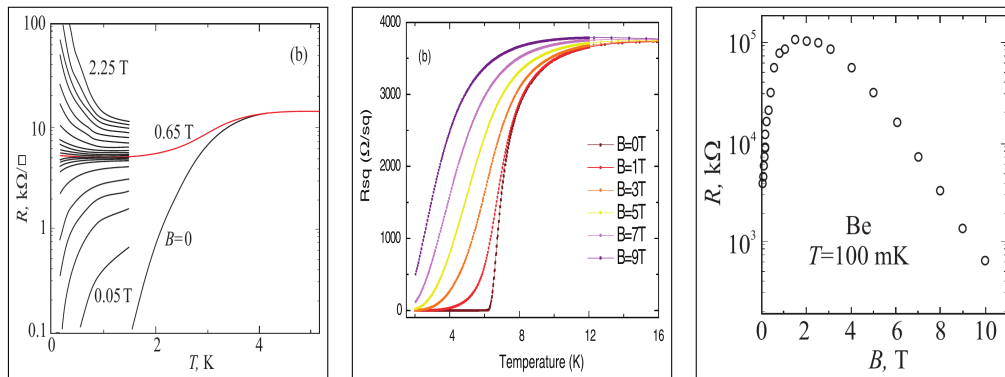


Figure 1.8: Resistivity  $R(T)$  with increasing disorder for Be [36,37] and NbN [38] films respectively.

(ii) In Be, the separatrix extrapolates to a value  $\sim R_Q = 4k\Omega$  at  $T = 0$ , but the curves saturate to a larger value  $\sim 10k\Omega$  at stronger magnetic fields.

(iii) A strong non-monotonicity is observed in the magnetoresistance in (c). This strongly hints at the fact that superconducting correlations survive in the insulating state, where the loss of phase coherence among superconducting regions leads to the initial increase, while the subsequent destruction of pairing leads to the decrease thereafter.

## Tunneling spectra

We have seen earlier that BCS theory has a characteristic density of states with a gap in the middle and two coherence peaks at the gap edge [1]. The strong suppression of superconductivity by disorder also hints at major changes in the underlying state, and the density of states can provide valuable information on that. STS data can be used to extract the required information by plotting the differential conductance,  $dI(V)/dV$  vs. the voltage  $V$  [7]. Fig.1.9 shows such data from two NbN films [38] with thickness  $2.33nm$  and  $2.16nm$  respectively, which are already at high disorder, compared to a clean film with thickness  $\sim 15nm$ . The salient features are:

(i) The density of states has small coherence peaks that decrease further with decreasing thickness, along with the gap in the middle. The zero bias conductance has a finite value that increases with disorder, suggesting a pair breaking mechanism. The overall profile is poorly fitted by a BCS formula broadened by a Dynes parameter  $\Gamma$ .

(ii) The  $\Delta/kT_c$  ratio extracted from the fitting above show very little change for all the films. However, it is unclear whether any firm conclusion can be drawn from this at strong disorder, since BCS fitting is no longer very accurate in that regime.

(ii) The spectral function rides on a background feature with a wide depression at the centre, probably caused by disorder enhanced Coulomb interactions. Thermal evolution causes further decrease of the gap and coherence peaks, and for the  $2.16nm$  film, there is a slight window above  $T_c$  where a pseudo gap is observed.

(iii) The spatial maps of the spectra near the coherence peak regions reveal considerable variation, hinting at an inhomogeneous superconducting state.

(iv) While one finds robust vortex lattices at weak disorder, they weaken considerably with increasing disorder, and vanish completely for the  $2.16nm$  film. This effect suggest weakened phase coherence in the films at strong disorder.

To summarize, the transport data provide strong hints that superconducting correlations are present even in the insulating side of the disorder driven transition. Even in the superconducting side, magnetic field weakens phase coherence among superconducting regions first, suggesting the presence of inhomogeneity at strong disorder. This is confirmed by tunneling data, which show

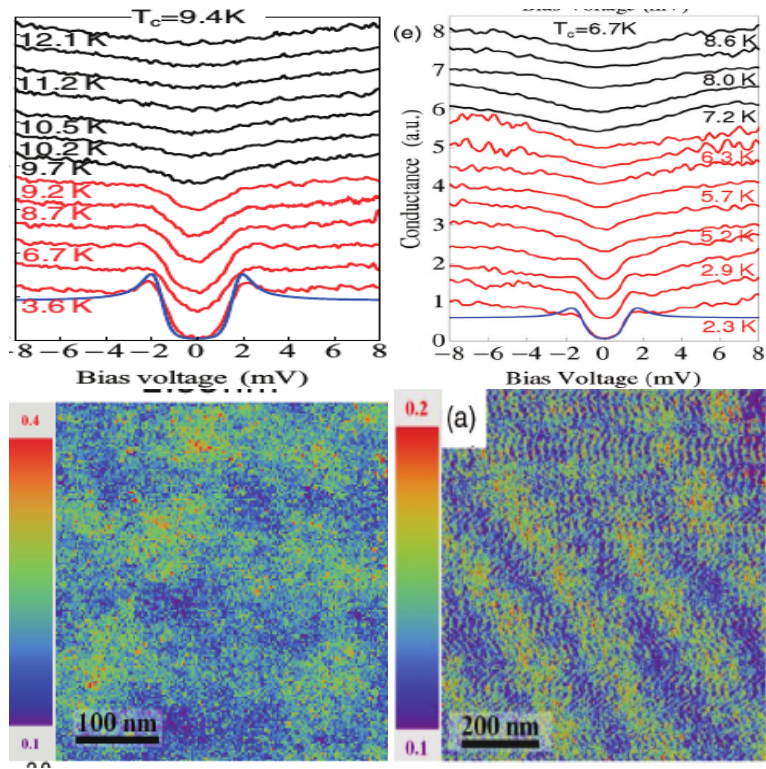


Figure 1.9: Top: Thermal evolution of tunneling spectra [38] of two thin films with thickness  $2.33\text{nm}$  and  $2.16\text{nm}$  respectively, showing decreasing coherence peaks, smaller gaps, and a broad Coulomb interaction induced background feature. Bottom: Spatial maps of tunneling conductance near the coherence peaks of the same films, indicating considerable inhomogeneity in the superconducting state

considerable inhomogeneity at strong disorder and a pseudogap above  $T_c$ . All of this hint towards a transition driven by possible phase fluctuations in an inhomogeneous superconducting background. We next move on to consider results on amorphous  $\text{InO}_x$  and thin TiN, where much recent work has been done, to shed more light on these issues.

### 1.3.3 $\text{InO}_x$ and TiN films

In this section, we review the experiments on materials with variable compositions, such as found in amorphous  $\text{InO}_x$  and polycrystalline TiN films. The properties of these films depend not only on the thickness, but also on the details of their formation and the chemical composition. Hence, the disorder in such films can be controlled by a variety of methods sensitively dependent on the procedure of formation.

Amorphous films of  $\text{InO}_x$  [39, 40] with thickness in the range  $20 - 40\text{nm}$  can be formed by depositing high purity  $\text{In}_2\text{O}_3$  on an  $\text{SiO}_2$  substrate by electron beam sputtering. These have a deficit of oxygen atoms, which cause vacancies in the system. The amount of the deficiency can

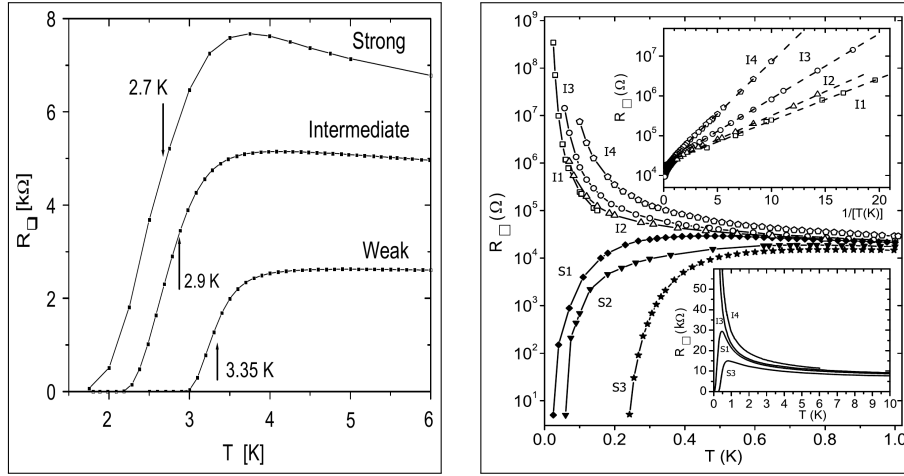


Figure 1.10: Resistance vs temperature curves for 3 films of  $\text{InO}_x$  [45] and 4 films of TiN [51]. The latter clearly shows the sharpness of the transition, and the insulating nature of the critical curve.

be controlled by a slow annealing process. The deficiency determines the concentration of active electrons that do not participate in chemical bonding, which in turn changes  $k_F l$ , the effective disorder of the film. Similarly, TiN films [49] with thickness of a few nanometres are formed by magnetron sputtering of a target from pure Ti in a nitrogen plasma. Here the resistivity depends on the excess concentration of N in the final film. Besides this, the thickness can also be varied to control the effective disorder. The form of disorder control doesn't seem to affect the salient results, and hence the experimental results are described in a unified manner, without worrying about the source of disorder.

## Transport

Fig.1.10 shows the transport results from two experiments done at zero magnetic field on  $\text{InO}_x$  [45] and TiN [51] respectively. The curves show qualitatively similar behaviour to that of the Be and NbN films. The superconductor-insulator transition (seen clearly in the TiN films) is sharp and the insulating films (not shown for  $\text{InO}_x$  here) follow a simple Arrhenius activation law at low temperature, which crosses over to Efros-Shklovskii behaviour for TiN (similar to Be and NbN), while the bulkier  $\text{InO}_x$  films follow Mott's hopping behaviour  $R(T) \propto \exp(T_M/T)^{1/4}$ . The TiN films also clearly show the insulating behaviour of the critical curve, which also does not extrapolate to the quantum of resistance for pairs,  $R_{Qp} \sim \hbar/4e^2$  expected from bosonic theories (discussed in more detail in the next chapter).

The magnetoresistance behaviour [46,52,53] shown in Fig.1.11 is also very similar to the earlier films, with a pronounced non-monotonicity at strong disorder, both on the superconducting and the insulating side. However, we take note of certain details and deviations:

- (i) The resistance shows activated behaviour at weak to moderate magnetic fields for both kinds

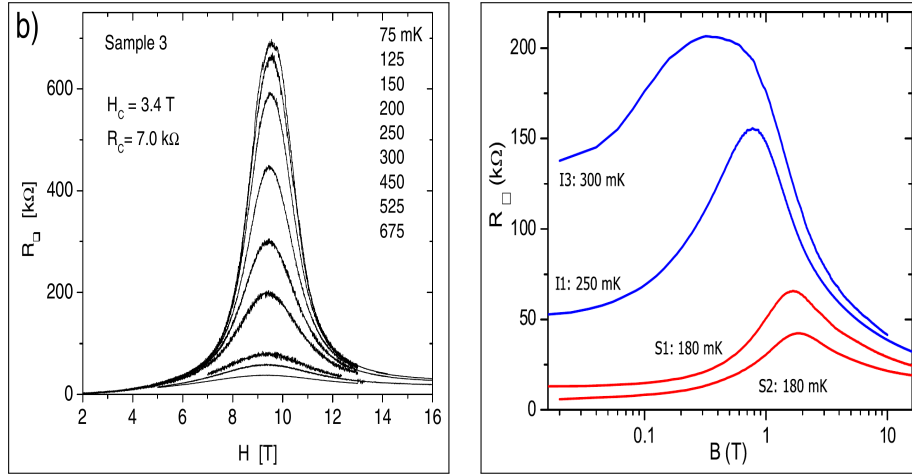


Figure 1.11: Magnetoresistance of  $\text{InO}_x$  [46] at a fixed disorder and varying temperatures and of  $\text{TiN}$  films [52] at fixed temperature close to the critical point. The saturation resistance at high field  $\sim R_Q$ , and the overall behaviour is very similar in the superconducting and insulating samples (shown for  $\text{TiN}$  films).

of films,  $R(T) \propto \exp(T_B/T)$ , with  $T_B$  following the non-monotonicity in the resistance.

(ii) At fixed disorder, the magnetoresistance peak decreases with increasing temperature, and at fixed temperature, increases with disorder. This is again consistent with the overall picture of inhomogeneous superconductivity at strong disorder.

(iii) The resistance at strong magnetic field saturates to a value much higher than the normal state resistance at that disorder, close to the quantum of resistance  $R_Q = \hbar/e^2 \sim 4k\Omega$ , indicating the formation of a novel correlated quantum metallic state at large fields.

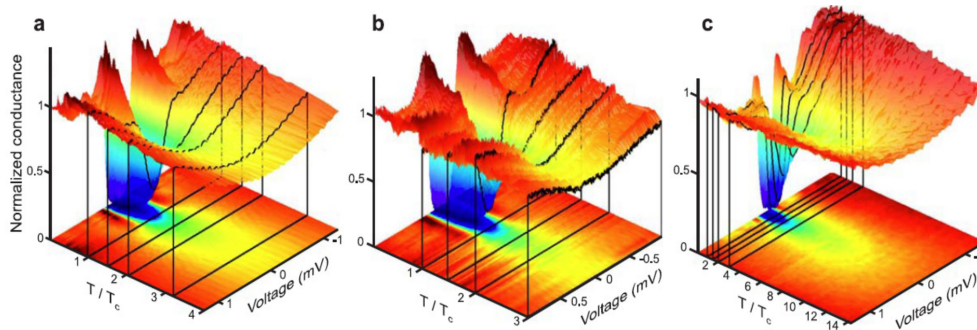


Figure 1.12: The evolution of density of states of three  $\text{TiN}$  films with increasing disorder [55]. The plots show a very deep pseudogap which survives to an increasingly large temperature at strong disorder.

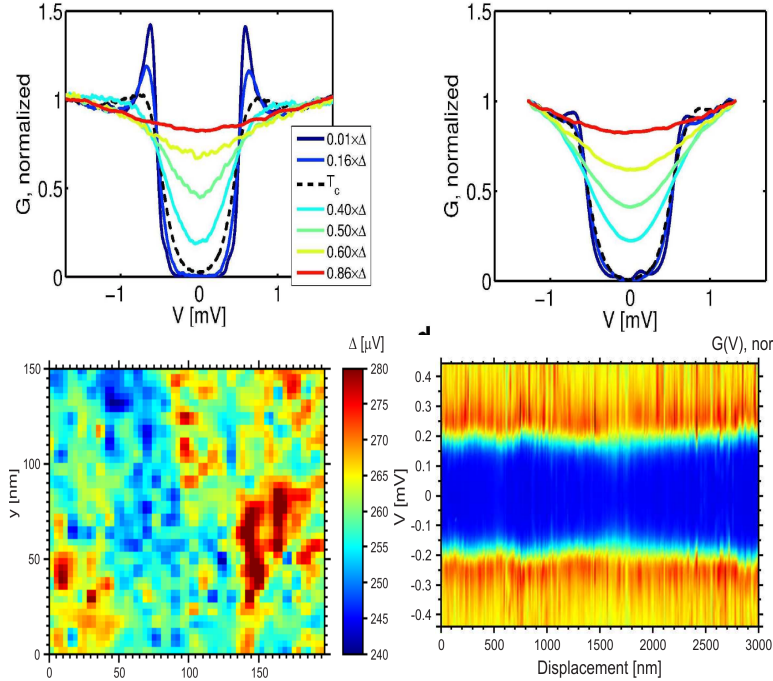


Figure 1.13: The top figure [47] shows the contrasting thermal evolution of the local density of states of two regions in an  $\text{InO}_x$  film at strong disorder. Bottom [56] left shows the inhomogeneities in a map of the gap  $\Delta$ , while bottom right shows the variation in spectra measured along a straight line in disordered TiN films.

## Tunneling spectra

Fig.1.12 shows the tunneling spectra for TiN [55] at three different disorders with temperature. Apart from the already observed trend of decreasing coherence peaks and suppressed gaps, one not only finds a very deep pseudogap at strong disorder, but the temperature at which it vanishes seems to *increase* with disorder. Thus at the strongest disorder shown, the suppression continues to be visible even around  $T \sim 6.3K \sim 14T_c$ , while it is only seen up to  $T \sim 3K \sim 3T_c$  for the sample in the middle. This is in contrast to earlier results on NbN films, which showed only a weak pseudogap above  $T_c$  over a very small range of temperatures.

Now we turn to the local inhomogeneities at strong disorder. The top plot [47] of Fig.1.13 shows the thermal evolution of the density of states at two different positions in a disordered  $\text{InO}_x$  film. The two families show very similar evolution upto  $T_c$ , with similar magnitudes of gap and a deep pseudogap. However, below  $T_c$ , one develops the characteristic coherence peaks of superconductivity, while the other doesn't, providing evidence of the presence of superconducting and non-superconducting regions at strong disorder.

The bottom [56] left shows a spatial map of the local  $\Delta$ , clearly showing the formation of nano-sized patches with larger gaps, interspersed with regions with smaller gaps. The right plot shows

the tunneling spectra along a line, showing considerable variations, but also a robust non zero gap everywhere. In fact, from the average  $\bar{\Delta}$  at different disorder, one finds that the ratio  $\bar{\Delta}/kT_c$  increases to anomalously large values at large disorder, indicating that the transition at  $T = 0$  takes place in a gapped system.

In conclusion, the similar transport behaviour as seen with Be and NbN films, the presence of a deep pseudogap in the spectral function at strong disorder, the considerable inhomogeneity observed across the films and the increasing  $\Delta/kT_c$  ratio all indicate the formation of a highly inhomogeneous ground state at large disorder, and an SIT driven by fluctuations among remnant superconducting regions.

We turn our attention now to experiments on thick 3 dimensional NbN films.

### 1.3.4 3D NbN films

We have seen earlier that NbN films have a superconducting coherence length of  $\xi \sim 5nm$ , hence films with thicknesses much larger than this would behave as three dimensional superconductors. Three dimensional NbN can be prepared by sputtering a Nb target on oriented single crystalline MgO substrates in a mixture of Ar/N<sub>2</sub> gas [57,58,60]. Depending on the sputtering power and ratio of N<sub>2</sub>, the number of Nb vacancies in the system can be controlled, and hence the effective disorder can be changed. These films have a thickness  $\sim 50nm$ , much larger than the coherence length, and the cleanest sample has a  $T_c \sim 17K$ .

Starting from the cleanest sample, increasing disorder suppresses superconductivity and  $T_c$  goes below measurement resolution around  $k_F l \sim 1$ . The transport characteristics are qualitatively similar to earlier results, with a direct transition and a slightly insulating critical curve, and a non-monotonic magnetoresistance at strong disorder in the insulating phase, so we skip these results and move on to the spectroscopy measurements.

#### Tunneling spectra

The tunneling spectra at low temperature is, again, qualitatively similar to that observed in the InO<sub>x</sub> and TiN films, with decreasing coherence peaks and gaps with increasing disorder, observations of two distinct kinds of spectra in different parts of the sample, and large inhomogeneity along a line in the sample. Thus, we concentrate on the thermal evolution and its change with disorder.

Fig.1.14, left, shows the intensity plots of tunneling spectra averaged over 32 points for 6 samples with increasing disorder [60]. We note that while the gap closes at  $T_c$  for the cleanest samples, with increasing disorder, it continues to persist beyond  $T_c$  to  $T^* \sim 7K$ , which remains roughly constant with further increase in disorder. This data is organized into a phase diagram [60] shown in Fig.1.14, right, which shows the superconducting, normal, pseudo-gap and insulating states in

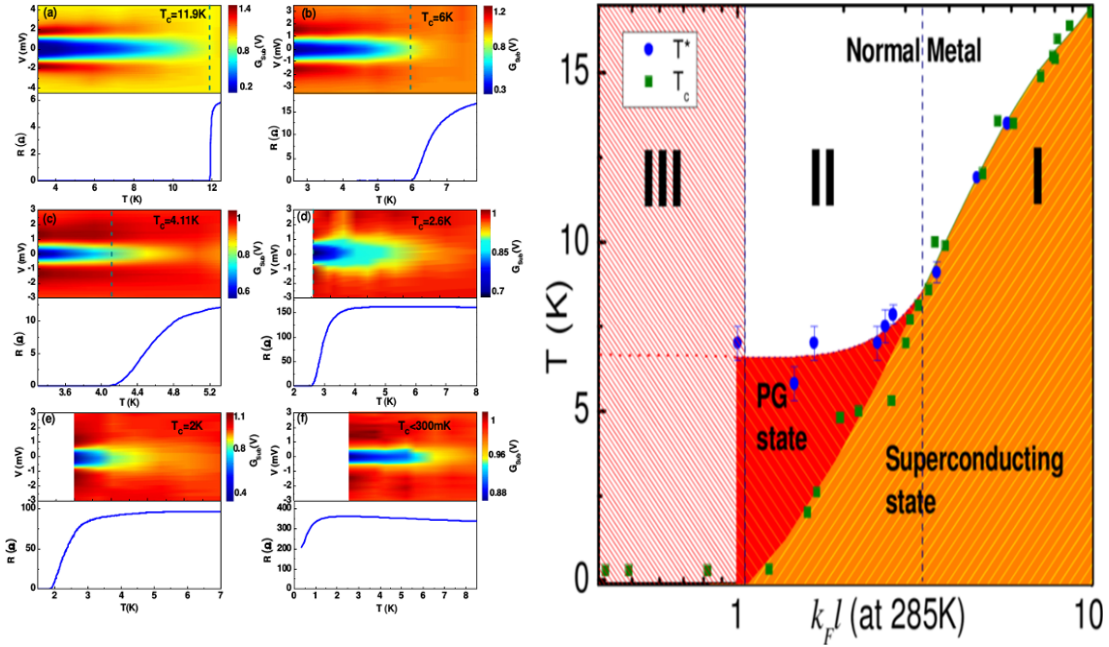


Figure 1.14: Left: Intensity plots [60] of tunneling spectra for 6 samples with increasing disorder. With increasing disorder, the depression in the middle survives to a disorder independent scale  $T^* \sim 7K$ . Right: Phase diagram [60] showing the superconducting, normal, pseudogapped and insulating states extracted from the tunneling data.

the disorder temperature plane.

Fig.1.15 shows the corresponding spatial evolution of the superconducting state [61]. It shows maps of the zero bias tunneling conductance (which was found to have an inverse correlation with the coherence peak height at a given site) for a highly disordered sample ( $T_c \sim 2.9K$ ) and their thermal evolution. The low temperature state shows nano clusters of superconducting regions, which shrink with increasing temperature and disconnect into independent clusters. However, these disappear completely only at  $T_{clust} \sim T^*$ , and hence the authors concluded that the two scales were equal.

In conclusion, results on three dimensional NbN films explicitly demonstrated the increasing inhomogeneity with increasing disorder, and confirmed the existence of different thermal scales ( $T_c$  diverging from  $T^* \sim T_{clust}$ ).

### 1.3.5 Summary and discussion

We examined the transport and tunneling data of a variety of materials including thin films of Be and NbN, amorphous films of  $\text{InO}_x$ , polycrystalline TiN films, and 3 dimensional NbN films. The disorder in these various materials is determined by various factors including the thickness, chemical composition, vacancies, *etc.* The resultant disorder in all of them is homogeneous, varying

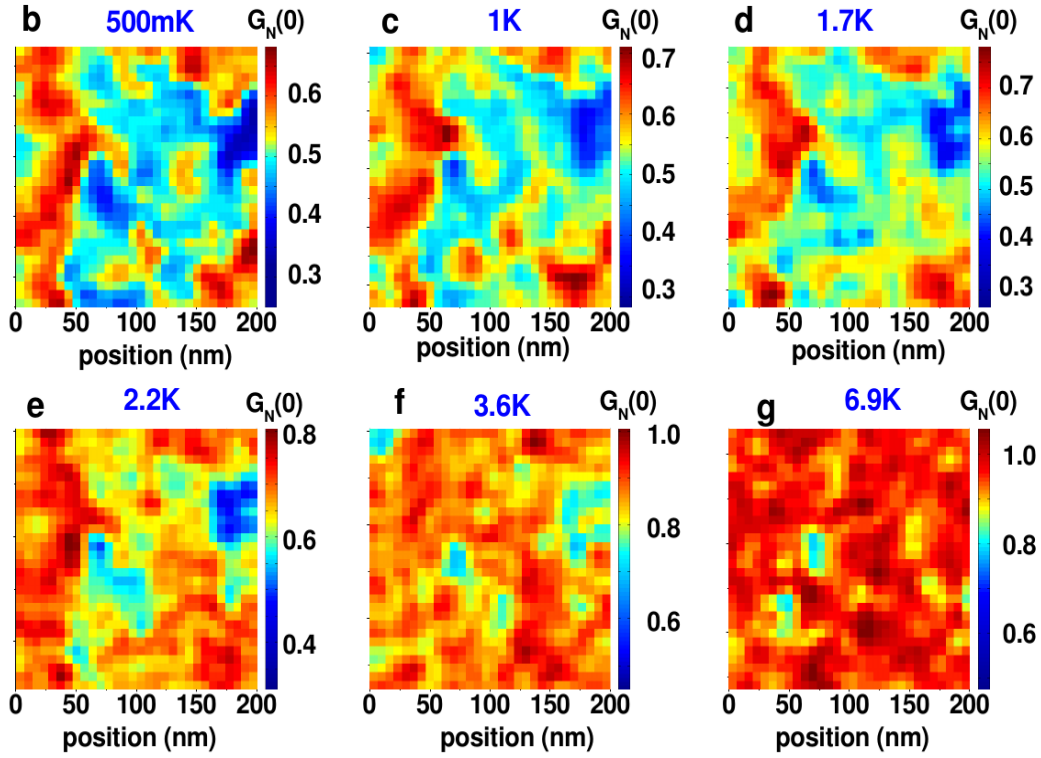


Figure 1.15: Thermal evolution [61] of the zero bias tunneling conductance in a disordered sample with  $T_c \sim 2.9K$ , showing the shrinking of the superconducting regions, which finally disappear at  $T_{clust} \sim T^*$ .

on an atomic scale, with no granularity. Despite the differing microscopic origins of disorder, several features seem to be ‘universal’, independent of such details. We list the most important ones below again, for convenience.

(i) Large potential disorder suppresses superconductivity, ultimately causing a transition to an insulating state. In most cases, the transition is direct and sharp, with no intervening metallic phase in between. This distinguishes these materials from other studied materials like amorphous  $Nb_xSi_{1-x}$ , which show an intermediate metallic phase.

(ii) The resistivity shows activated behaviour at low temperature in the insulating phase, which crosses over to Mott ( $InO_x$ ) or Efros-Shklovskii (Be, TiN) at higher temperatures. The separatrix is not horizontal but slightly insulating in most films, and its  $T = 0$  value does not necessarily extrapolate to either  $R_{Qp} \sim \hbar/4e^2$  or  $R_Q \sim \hbar/e^2$ . The next chapter will discuss this in more detail when comparisons with theory are done.

(iii) At strong disorder films on both sides of the transition show strong non-monotonic magnetoresistance, hinting at surviving superconducting correlations beyond the transition and possible inhomogeneities in the superconducting state at strong disorder.

(iv) The average tunneling spectra show reduced coherence peaks and generally reducing gaps at  $T = 0$ , while locally resolved spatial plots show increasing inhomogeneity with increasing disorder, with formation of nano-sized superconducting clusters at high disorder. Nevertheless, the local gap seems to persist through the disorder driven transition.

(v) The thermal evolution shows a persistent pseudogap whose vanishing temperature  $T^*$  diverges from  $T_c$  with increasing disorder. It seems to increase with disorder in 2 dimensional  $\text{InO}_x$  and  $\text{TiN}$ , but remains roughly constant in 3 dimensional  $\text{NbN}$ . Spatially resolved plots show thermal shrinking of the clusters, which vanish finally at  $T_{clust} \sim T^*$  in 3 dimensional  $\text{NbN}$ .

The general lesson from these is that the high disorder superconducting state is inhomogeneous in an essential way, and the  $T = 0$  transition is driven by fluctuations without complete destruction of superconductivity, as evidenced by the non-monotonic magnetoresistance in the insulating side. Clustering is seen at large disorder inspite of the disorder varying on an atomic scale. This distinguishes these materials from the so called granular superconductors, where the superconducting material is deposited in small grains on the surface which go superconducting at a fixed temperature, and the resultant properties of the system are determined by the coupling between these grains.

We will discuss these issues in more detail, along with comparisons of these results with previous theoretical work, and our numerical work, in the subsequent chapters. For now, we move on to a description of the existing results on magnetic impurities in superconductors.

## 1.4 Magnetic impurities in superconductors

When the condition of time reversal invariance does not hold, Anderson's theorem of pairing exact eigenstates and their time reversed counterparts is no longer valid. This is the case with magnetic impurities in a material. Thus, a very small concentration of such impurities can considerably suppress or even completely destroy superconductivity. The impurities also influence other properties profoundly, including the single particle density of states, resulting in the famous gapless phase of superconductivity, where the single particle gap is closed [6]. This section will review some of the basic physics of magnetic impurities in a superconducting material briefly, with emphasis on the primary concepts involved, rather than an exhaustive summary of the existing literature.

This simple premise of magnetic impurities in a superconductor can be generalized to include more important situations where the material can show both superconducting and magnetic ordering of some form. The interplay of the superconducting degrees of freedom and the magnetic ones can potentially result in very interesting physics, and many such materials have been investigated experimentally and theoretically. We will not describe these in any detail here, but later suggest ways in which our work can be generalized to include some physical effects similar to these.

## 1.4.1 Single impurity

### Theoretical picture

The first problem to illustrate the physics of magnetic impurities is to consider a single magnetic impurity in a superconductor. The magnetic moment of the impurity can interact with the electrons via either the orbital coupling or coupling with the electron's spin, and the coupling can be ferromagnetic or antiferromagnetic. Furthermore, in the antiferromagnetic case, the quantum nature of the spins placed in a metal results in the well known Kondo effect [65], and this is also expected to have important consequences in a superconductor. However, the basic physics of the suppression of superconductivity does not depend on these effects, and hence one can approximate the impurity spins as classical.

With this setup, the BCS equations with a magnetic impurity with coupling strength  $J$  and spin magnitude  $S$  were solved using various techniques by Yu, Rusinov, Shiba and others [66–69]. They found that the presence of the impurity creates an intragap state in the system, which is localized around the impurity site. The energy of the gap,  $E_0$ , is given by

$$(E_0/\Delta_0) = \frac{1 - (JS\pi N_0)^2}{1 + (JS\pi N_0)^2} \quad (1.1)$$

Here,  $\Delta_0$  is the superconducting gap parameter and  $N_0$  is the normal density of states at the Fermi energy. The above calculations also demonstrated that for a non-magnetic scattering potential there are no intragap states. Fig.1.16 shows a cartoon of the intra gap state in the overall density of states of the system.

### Experimental results

As explained in the context of disordered superconductors, STM methods are extremely valuable in probing the system at a microscopic level and providing local information about the spectral functions. Hence, such methods have proved very useful in studying the local changes in the density of states of superconductors with magnetic impurities. While signatures of subgap states were found in early planar junctions doped with magnetic impurities by Dumoulin, *et. al.* [70], a direct observation using STM was found much later in 1997 by Yazdani, *et. al.* [71]. They found that in contrast to non-magnetic impurity atoms such as Ag, magnetic Mn and Gd atoms showed intragap states localized around the impurity. Fig.1.17 shows their results for the local density of states, comparing the plots for a site away from a magnetic atom to one over it, clearly showing the presence of intragap states in the latter. A simple model of these states yielded results consistent with the theoretical predictions discussed above.

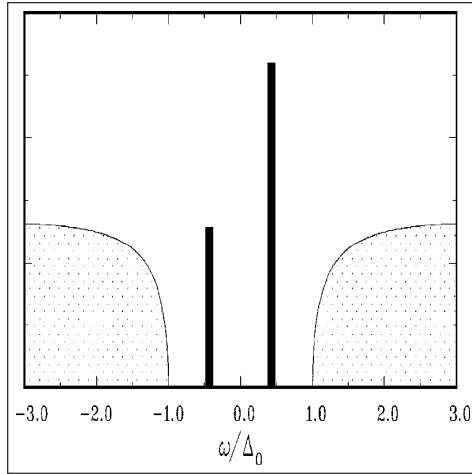


Figure 1.16: Schematic figure [6] showing the intragap impurity state formed due to the presence of a single impurity in the density of states. The features at positive and negative parts show the respective weights of the electronic and hole components of the states respectively. Depending on the density, the contributions could in general be different, explaining the asymmetry of the diagram.

Much theoretical and experimental work on intragap states [6] has been done on d-wave superconductors such as the high  $T_c$  cuprates, where the different pairing order implies that even potential scattering can cause resonance states around the impurities. However, since our focus will be on s-wave superconductivity, we will not describe these results, and instead move on to consider the effect of increasing coupling on these intragap states.

### Evolution with impurity strength

From the Eq. 1.1, one can clearly see that with increasing coupling strength  $J$ , the intragap state moves further inwards until at  $J = J_c = (1/\pi S N_0)$ , the intragap level goes to zero. This is associated with a quantum phase transition, whereby the original spin unpolarized ground state, with all electrons paired, no longer remains the lowest energy state of the system [72]. Instead, the impurity spin ‘removes’ an electron from the condensate to form a singlet (if the original interaction is antiferromagnetic), leading to a ground state with non zero spin polarization. Fig.1.18 demonstrates this effect with two cartoons showing the two states respectively, and the level crossing that takes place with increasing coupling. This is accompanied by an ill understood phenomenon, where the superconducting order parameter at the impurity site undergoes a phase change of  $\pi$ . While the reason behind this is not understood properly, it seems to be related to the  $\pi$ -shift superconducting junctions with tunneling barriers containing a magnetic impurity or a ferromagnetic layer [73].

Now we move on to the case of many impurities, and summarize the work done on this subject below.

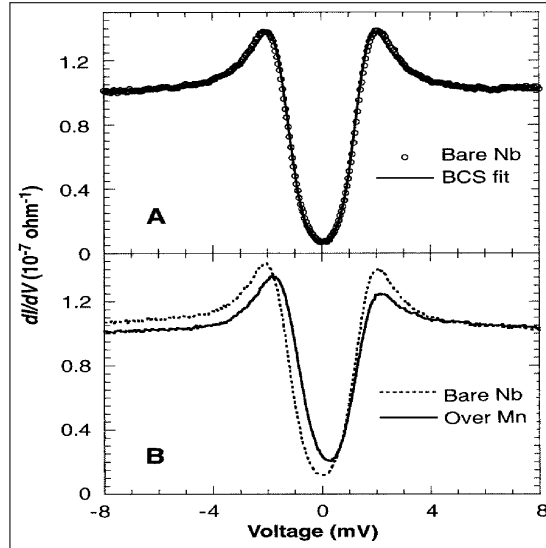


Figure 1.17: Local density of states far from (top) and over an isolated magnetic Mn impurity in a single crystal Nb(110) sample used by Yazdani *et. al.* [71]. While the top plot is perfectly fitted by the BCS form, the bottom figure clearly shows the presence of intragap features, reflecting the intragap state formed due to the presence of the impurity.

### 1.4.2 Many impurities

When the number of impurities is increased, multiple scattering effects from different impurities come into effect. This can result in complex interference effects due to scattering from the different impurity moments and cause considerable changes in the behaviour of the system. However, in the limit of dilute concentration, when the impurities are located far apart from each other, such interference effects are negligible (this is similar to the argument that quantum effects in transport are negligible at weak disorder). The method for dealing with such situations was first developed by Abrikosov, *et. al.* [74], who formulated the concept of impurity averaging, where the final result of any calculation was to be performed by taking the averages of the results from a single impurity distribution over all such possible configurations.

#### Abrikosov-Gorkov theory; gapless superconductivity

Abrikosov and Gorkov [75] applied this concept to the problem of non-magnetic impurities in superconductors and found that to second order of perturbation in the impurity potential, the transition temperature  $T_c$  did not change, which, as explained earlier, was reconfirmed by Anderson. In the case of magnetic impurities, however, they found that the  $T_c$  was suppressed by increasing impurity concentration until it was driven to zero when the characteristic energy scale associated with spin flip scattering,  $\alpha_s$ , became equal to half the superconducting gap,  $\Delta_0/2$ . Thus, superconductivity was destroyed when

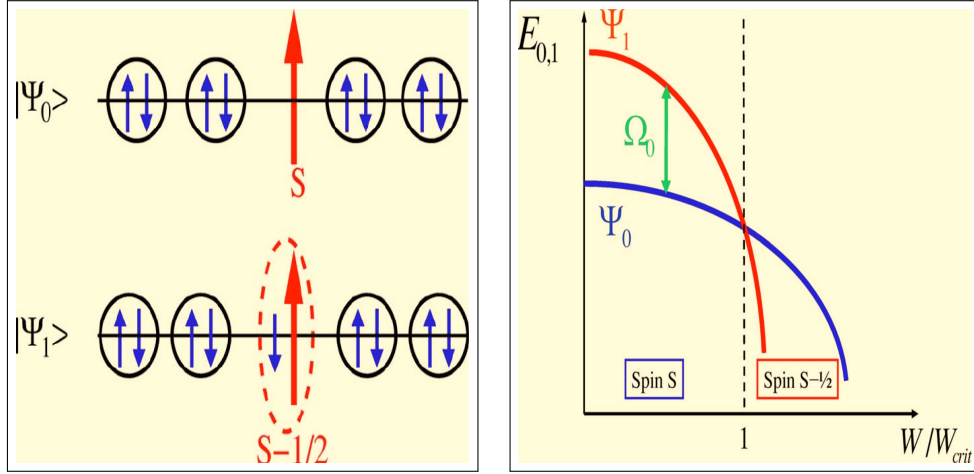


Figure 1.18: Left: Schematic picture [6] of the quantum phase transition, showing the unpolarized initial ground state, and the polarized final ground state beyond the transition, where a spin is extracted from the condensate to form a singlet with the impurity spin. Right: The level crossing between the initial ground state  $\Psi_0$  and the final one,  $\Psi_1$  with increasing coupling  $W$ .

$$\alpha_s = \tau_s^{-1} \sim n_{imp} N_0 J^2 S^2 = \alpha_{sc} = \Delta_0/2 \quad (1.2)$$

Here  $n_{imp}$  is the impurity concentration. Even more remarkably, they found that a little before this point, the single particle gap of the system vanished even though it was still superconducting. This is the famous gapless phase, given by

$$\alpha_s = \alpha_{sg} = \Delta_0 \exp(-\pi/4) \quad (1.3)$$

Thus, in the narrow interval between  $\alpha_{sg} \sim 0.912\alpha_{sc}$  and  $\alpha_{sc}$  the system showed gapless superconductivity. This prediction, first verified by Reiff and Wolfe, has since been reconfirmed by many experiments. Fig.1.19, left, shows a plot of the  $T_c$  dependence with  $n_{imp}$ , comparing the theory along with several experimental plots [76].

The evolution of the density of states that follows from this theory was studied in detail by many workers [77]. Fig.1.20, right, shows their main results schematically [6]. With increasing  $n_{imp}$ , the gap edge gradually moves inwards and the gap becomes smaller, but a hard gap persists until we reach the critical concentration for gapless superconductivity. This picture is contrary to what we would expect from an extrapolation of the single impurity case, where we saw that impurities created intragap states in the density of states. Below, we describe the limitations of the Abrikosov-Gorkov method that leads to this discrepancy, and the subsequent work that has been

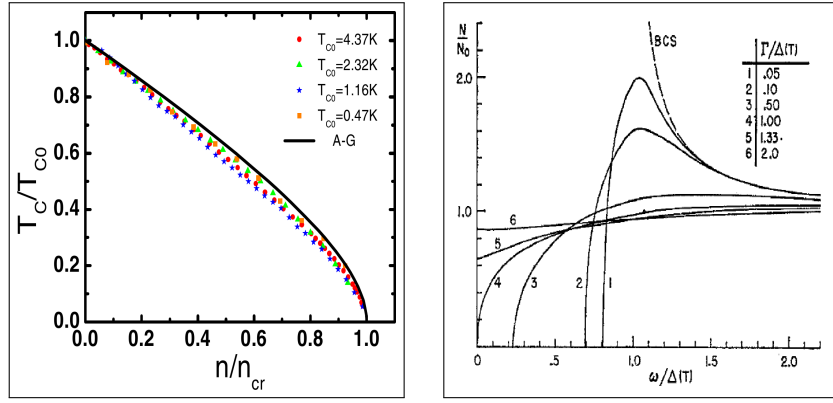


Figure 1.19: Left: Comparison of the dependence of  $T_c$  with impurity concentration  $n_{imp}$  of several samples [76]. with the theoretical curve, showing a close match. Right: The evolution of the density of states [6] with increasing impurity scattering time  $\tau_s^{-1} \sim n_{imp} J^2$  according to the Abrikosov-Gorkov theory [77]. The impurity states are always produced at the gap edge and below the critical point, there is always a hard gap in the system.

done to resolve this and extend the results beyond the Abrikosov-Gorkov regime.

### Generalization to stronger coupling

In spite of the success of the Abrikosov-Gorkov theory in explaining the destruction of superconductivity and the presence of the gapless phase, it is only strictly valid in the weak  $n_{imp}$ , weak  $J$  regime. This stems from the fact that in the Abrikosov-Gorkov theory, the parameters  $n_{imp}$  and  $J$  enter through the single combination  $\sim n_{imp} J^2$ , whereas in general they control different aspects of the impurity scattering. More general calculations [67, 68, 78] using more sophisticated self consistency methods (similar methods are described briefly in Chapter 2) were able to provide better results. These yielded the following relations:

$$\begin{aligned} \alpha_{sc} &= \Delta_0/2 \\ \alpha_{sg} &= 2\epsilon_0^2 \exp(-\pi\epsilon_0^2/2(1+\epsilon_0)) \end{aligned} \quad (1.4)$$

Thus the critical concentration for destruction of superconductivity remains the same, but the condition for gaplessness depends on the position of the intragap state  $E_0 = \Delta_0\epsilon_0$ . In the weak coupling limit, this is very close to the gap edge, and the evolution of the density of states is very close to the Abrikosov-Gorkov result. At stronger coupling, however, the intragap levels can be well inside the gap, and hence, the critical point for gaplessness,  $\alpha_{cg}$  can be much smaller, resulting in an enhancement of the gapless phase. As a result, hence the evolution of the density of states should also be quite different. Fig.1.20 shows the contrasting evolution in the two cases schematically.

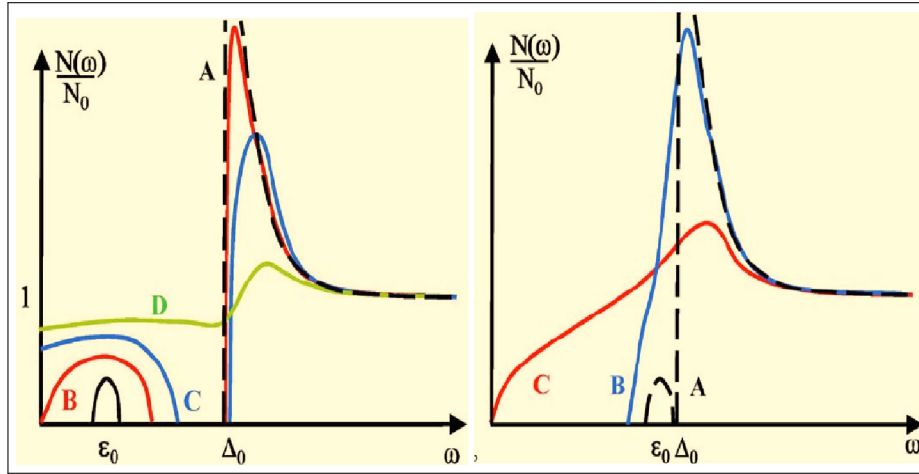


Figure 1.20: The contrasting evolution of the density of states for weak coupling (right) and strong coupling (left) with increasing concentration [6]. At weak coupling, the extra subgap states are formed close to the gap edge and slowly close the density of states until it is gapless. At strong coupling, the impurity states form a band inside the gap, and if the coupling strength is large enough, the bottom of the band reaches the Fermi surface before the top reaches the continuum to the right, and the gapless regime is enhanced.

### 1.4.3 Summary and further work

In this section, we summarize the results and achievements of the theoretical and experimental results and comment on the limitations of the analytical approaches that have been described so far. This sets the stage for our numerical analysis of the problem, the results of which will be described in detail in a later chapter.

#### Summary

The main results of the studies described so far are:

1. In contrast to a non-magnetic impurity, an intragap level is formed in the density of states in the presence of a magnetic impurity in an s-wave superconductor.
2. With increasing coupling, this level moves inwards, and causes a quantum transition from a spin unpolarized ground state to a polarized one at a critical coupling  $J_c$
3. With growing impurity concentration one first gets a ‘gapless’ superconductor, and then the destruction of superconductivity at a critical concentration,  $n_c$ . The window of gapless behaviour, and  $n_c$ , depends on the coupling strength.

In spite of these results, traditional methods have the following shortcomings:

1. Many of these assume the order parameter  $\Delta_0$  to be reasonably constant, while one expects that strong coupling could change it considerably, which would feed back to change the physics of the system, in particular, the range and extent of the gapless phase.
2. These theories are valid at weak concentration, and cannot deal with dense impurities because they neglect the interference effects from different closely situated impurities
3. These methods cannot provide a spatially resolved picture of the system as well as a satisfactory description at finite temperature where thermal fluctuations may play an important part.

These limitations call for the use of numerical methods to analyse this problem. Some work has been done using mean field methods with spin dependent disorder [79], where the authors have investigated the role of spatial inhomogeneity in determining the gapless regime. On the other hand, Sacramento, *et. al.* [80] have investigated the energetics of different magnetic domain structures inside a superconductor using similar numerical methods. However, a consistent study of the magnetic impurity problem over a large range of coupling strengths and temperature has been lacking. Our numerical method, described in detail in then next chapter, will allow us to take up this problem, whose results will be described in a later chapter.



# THEORETICAL WORK, MODEL AND METHODS

The formulation of the BCS theory and its subsequent success in explaining a huge body of experimental data [1,2] makes it one of the most remarkable achievements in condensed matter physics. Nevertheless, as we saw in the previous chapter, there are certain situations, involving strong coupling [3,4] and strong disorder [5] where a mean field approach is no longer sufficient to explain the underlying physics. This necessitates the development of theoretical approaches that modify and/or extend the BCS formulation to include the effects of (i) broken translational invariance, and (ii) fluctuations, within their framework. While the lack of translational invariance can be incorporated in the mean field framework itself [81], inclusion of fluctuations typically requires one to use statistical many body tools [74], either analytically using perturbation theory, self consistency, etc., or numerically by simulation of model systems.

This chapter will provide a summary of such methods. We start with a brief review of these methods in the context of the BCS-BEC crossover, leaving more detailed analysis to another chapter. Then we move to disordered superconductors, where the theory work can be classified broadly into three groups:

- ‘Fermionic’ theories, which include Coulomb repulsion and explore the destruction of superconductivity due to suppression of the effective pairing interaction [82].
- ‘Bosonic’ theories, which assume ‘preformed’ bosonic pairs and study [83] how phase fluctuations can drive a superconductor-insulator transition.
- Numerical approaches, which start with an attractive fermion lattice model and use methods like Hartree-Fock-Bogoliubov-de-Gennes (HFBdG) mean field theory, quantum Monte Carlo (QMC), *etc.*, without assuming any preformed pairs [84–88].

After reviewing each of these methods and their results briefly, we introduce our model, provide a description of the Monte Carlo algorithm we use for simulation, and describe the methods to compute the important electronic properties of our systems.

## 2.1 From BCS theory to BCS-BEC crossover

BCS theory is a mean field theory that ignores fluctuations. This is unimportant in the weak coupling limit, because fluctuations are suppressed by a factor  $T_c/\epsilon_F$  and are only important very close to  $T_c$ , so that they are usually unobservable in experiments. However, for the situations described above, one needs to include the effects of fluctuations at all temperatures. Below, we provide a description of such methods in the context of the BCS-BEC crossover, using simple model systems that capture the basic physics.

### 2.1.1 The BCS-BEC crossover

While the BCS equations provide a particular solution  $\Delta$  that minimizes the Hamiltonian, the general treatment of the system at finite temperatures should consist of fluctuations on top of the mean field state. Such a situation is presented in the problem of the BCS-BEC crossover [4] with increasing coupling  $U/t$ . At weak coupling, the system is a BCS superconductor, and as explained earlier, fluctuations are suppressed by a factor  $T_c/\epsilon_F$ . The transition is determined by the temperature at which these pairs form, and gives the BCS form for  $T_c$ . On the other hand, at strong coupling, the system is composed of tightly bound local pairs which form at a much higher temperature  $T^*$ , resulting in a gap in the single particle spectrum, while the superconducting transition is determined by the coherence of these pairs.

With increasing coupling the system interpolates smoothly from one limit to the other. The  $T = 0$  evolution is captured by the BCS wavefunction itself, with suitably defined coefficients, as shown by Leggett [89]. The thermal behaviour at arbitrary coupling is, however, governed by fluctuation effects, and mean field theory is insufficient. It captures the pairing scale  $T^*$  but not the real  $T_c$ . In the BCS limit, the  $T_c$  increases with increasing coupling  $U$ . In the BEC limit, it is stationary in the continuum case (determined by twice the mass of an electron) while in a lattice it goes as  $t^2/U$  due to virtual ionization of the pairs. Thus, the lattice systems show an intermediate coupling maximum in  $T_c$ , where the system consists of both bound pairs and fermions above  $T_c$ , resulting in a ‘pseudo-gap’, a pronounced depression at the centre of the single particle density of states. Fig.2.1 summarizes the basic physics and thermal scales for the continuum and lattice cases.

The realisation of BEC in ultracold Bose gases [90–92] opened a completely new avenue for experimentally realizing and testing various simple models of quantum matter in a controlled en-

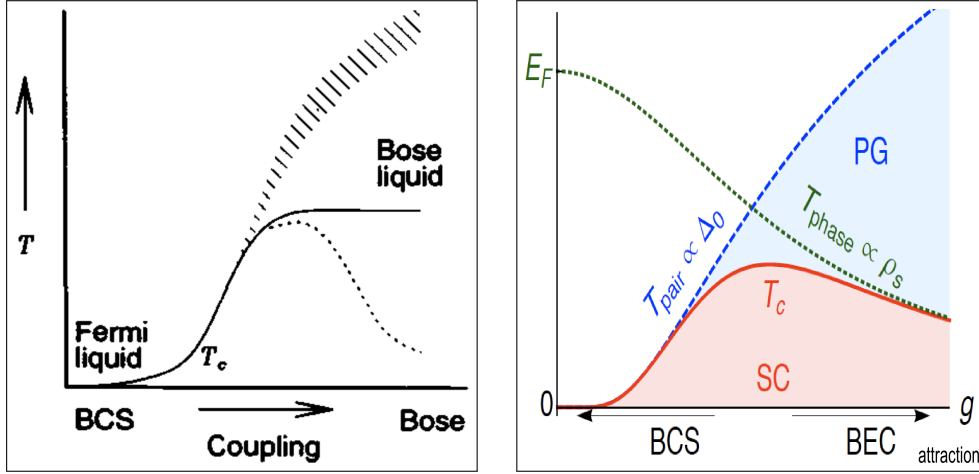


Figure 2.1: Basic thermal scales of the BCS-BEC crossover [4]. Left: Schematic diagram for the crossover in continuum, from a Fermi liquid to the left to a Bose liquid to the right, where the  $T_c$  increases initially and gradually saturates as pairs form with mass  $2m$ . The dashed line shows the evolution of the pairing scale  $T^*$ . Right: BCS-BEC crossover on a lattice, where  $T_c \propto (1/U)$  at strong coupling (see text). Basic physics arises due to the competition between two scales, the pairing scale  $T_{pair} = T^*$  and the stiffness scale  $T_{phase}$ .

vironment. For ultracold Fermi gases, the interparticle interaction can be tuned via a Feshbach resonance. For attractive interaction such systems exhibit superfluidity at low temperature and in  $\text{Li}^6$ ,  $\text{K}^{40}$  etc [93–96], one could study the BCS-BEC crossover. Since this is a translationally invariant system, the strong coupling  $T_c$  saturates to a value set by twice the atomic mass [97].

One can also generate optical lattices to mimic solid state systems [98]. Such systems provide an ideal playground for testing simple lattice models like the Hubbard model. On optical lattices one still has not attained temperatures that allow study of superfluidity [99]. Speckled laser patterns can be used to generate ‘disorder’ [100–103] further expanding the wide range of phenomena that can be studied in these systems.

## 2.1.2 Continuum and lattice

The BCS theory assumes a simple model where electron pairs have a constant attractive interaction between them in a small energy range around the Fermi energy. This corresponds to the simplest form of pairing, where the interaction acts between pairs at the same point in position space. Since the qualitative physics of the fluctuations do not depend on the detailed nature of pairing, we take this simplest form of pairing for our study of non-BCS effects. To this end, we introduce two such models, one in continuum and the other on a lattice. The continuum model [4] is given by

$$\mathcal{H} = \int d^d r (\bar{\Psi}_\sigma(\vec{r}) (-\nabla^2 - \mu) \Psi_\sigma(\vec{r}) - g \bar{\Psi}_\uparrow(\vec{r}) \bar{\Psi}_\downarrow(\vec{r}) \Psi_\downarrow(\vec{r}) \Psi_\uparrow(\vec{r})) \quad (2.1)$$

Here the first term denotes the kinetic energy of free electrons, while the second denotes the interaction term with a constant attractive constant  $g$ . The corresponding lattice model is given by

$$H = - \sum_{\langle ij \rangle \sigma} t \left( c_{i\sigma}^\dagger c_{j\sigma} + \text{h.c.} \right) - \mu \sum_i \hat{n}_i - U \sum_i \hat{n}_{i\uparrow} \hat{n}_{i\downarrow} \quad (2.2)$$

This is the negative  $U$  Hubbard model [104], defined on a square or cubic lattice in two and three dimensions respectively. The attractive coupling constant, denoted by  $U$ , acts on up and down spins on the same site, while the first term denotes nearest neighbour hopping of the electrons on the lattice with strength  $(-t)$ . There are two independent parameters, namely, the filling  $f$  and the coupling ratio  $U/t$ .

Since the basic form of the Hamiltonians is the same for both the continuum and the lattice cases, we will treat these two in a uniform manner in the subsequent discussions, inspite of some of the important physical differences between the two in specific limits. Furthermore, we will choose the lattice description to demonstrate specific equations to explain the methods. First, we look at the weak coupling BCS limit of these models, in which the lattice and continuum models behave identically.

### BCS limit

If we rewrite the negative  $U$  Hubbard model in  $k$  space, we get

$$H = \sum_{k\sigma} (\epsilon_k - \mu) n_{k\sigma} - U \sum_{kk'+q} c_{k+q\uparrow}^\dagger c_{k'+q\uparrow} c_{-k\downarrow}^\dagger c_{-k'\downarrow} \quad (2.3)$$

where  $\epsilon_k$  is given by the standard expression  $(-2t) \sum_i \cos(k_i a_i)$ . We get the same form with the continuum case, albeit with a different expression for  $\epsilon_k$ . The interaction term corresponds to scattering of a pair of electrons with opposite spins and total momentum  $q$ . The attractive interaction favours the formation of Cooper pairs, causing an instability in the normal state, which is reorganized to form a superconducting state of coherent Cooper pairs. The BCS reduced Hamiltonian retains only the terms with  $q = 0$ , since these give rise to the most stable pairs. As explained above, the ground state ansatz and self consistent solution corresponds to a mean field decomposition in the so called ‘pairing’ channel, where terms like  $\langle c_{-k\downarrow} c_{k\uparrow} \rangle$  are assumed to have a particular non-zero value corresponding to which the energy is minimum. The self consistent equations are given by

$$\begin{aligned} 1 &= (U/2N) \sum_k \tanh(\beta E_k/2) / E_k \\ n &= (U/N) \sum_k (1 - ((\epsilon_k - \mu)/E_k) \tanh(\beta E_k/2)) \end{aligned} \quad (2.4)$$

where  $E_k = \sqrt{\Delta^2 + (\epsilon_k^2 - \mu)}$ .

These two equations are solved simultaneously to yield the values of  $\Delta(U, T)$  and  $\mu(U, T)$ . In the BCS limit, the chemical potential is fixed at  $\epsilon_F$ , and one gets the characteristic  $T_c$  by solving the first equation alone.

### 2.1.3 Diagrammatic approaches

The partition function of the negative  $U$  Hubbard model can be written in the language of finite temperature many body theory as [105]

$$\mathcal{Z} = \int \mathcal{D}(\bar{\Psi}, \Psi) \exp\left(\int_0^\beta (\bar{\Psi} \partial_\tau \Psi + H)\right)$$

where  $H$  is the Hubbard Hamiltonian and  $\Psi$ s are Grassman variables. A standard way to treat interacting systems where the interaction term is weak is to expand the expressions for relevant observables in a perturbation series in  $U$ , keeping terms up to a specific order. However, in the case of the attractive Hubbard model, even in the weak coupling BCS limit, the non-analytic form  $T_c \sim \omega_D \exp(-1/(N(0)U))$  implies that the BCS state cannot be reached by considering any finite order in perturbation theory in the interaction  $U$ . This necessitates the summation of an entire class of diagrams.

#### Pairing fluctuations

The relevant summation process is best phrased in the language of the T-matrix [6]. For the attractive problem, the T-matrix can be written in the following form [106]:

$$T(q, i\omega_n) = -U/(1 - U\chi_0(q, i\omega_n))$$

Here,  $\chi_0(q, i\omega_n)$  is a ‘band’ susceptibility. For the superconducting case, the most important physical effects are contained in pairing fluctuations, where a pair of electrons are scattered repeatedly by the interaction potential  $U$ . This is given by the so called ‘pairing’ susceptibility [106]:

$$\chi_0(q, i\omega_n) = \frac{1}{\beta} \sum_{k, m} G_0(k, i\Omega_m) G_0(q - k, i\omega_n - i\Omega_m)$$

The superconducting instability is signalled by the divergence of the T-matrix at long wavelengths and low frequencies, and hence, we have:

$$(1 - U\chi_0(0, 0)) = 0$$

This equation amounts to the condition determining  $T_c$ , where the order parameter  $\Delta$  vanishes. On the other hand, the number equation is given by

$$n = \frac{2}{\beta} \sum_{k,n} G(k, i\omega_n)$$

Here, the Green's function  $G(k, i\omega_n)$  is given by the Dyson equation [105]

$$G(k, i\omega_n)^{-1} = G_0(k, i\omega_n)^{-1} - \Sigma(k, i\omega_n)^{-1}$$

where the self energy  $\Sigma(k, i\omega_n)$  can be expressed in terms of the T-matrix as [106]

$$\Sigma(k, i\omega_n) = \frac{1}{\beta} \sum_{q,m} T(q, i\Omega_m) G_0(q - k, i\Omega_m - i\omega_n)$$

With increasing coupling, the chemical potential shift becomes noticeable, and one has to include the effects of fluctuations. This was first considered by Nozieres and Schmitt-Rink (NSR) [107], who approximated the number equation by expanding the Green's function to first order in  $\Sigma$ :

$$G = G_0 + G_0 \Sigma G_0$$

They showed that the resultant equations implied a smooth crossover with coupling at finite temperature in the continuum case in three dimensions, and the transition point was still given by the divergence of the pairing susceptibility. On the other hand, the same procedure does not work for a lattice system, as the inclusion of fluctuations causes an unphysical negative compressibility [108] at low temperatures at strong coupling, even though a NSR like calculation starting from a Hartree shifted ground state manages to get reasonably correct results for  $T_c$  in three dimensions [108]. It is also not clear whether one can get pseudogaps correctly using such theories, even though feeding back pairing fluctuations in the single particle propagator can generate pseudogaps in the NSR scheme. Furthermore, this procedure is inapplicable in two dimensions, as it cannot capture the physics of the BKT transition. Even though this process can be extended by a more general treatment of the number equation above to provide more accurate results on the  $T > T_c$  state [109], the above limitations have given rise to alternative approaches that introduce self consistency into the equations. Some of these are described below.

### Self-consistent methods

The self consistent method replaces the unperturbed Green's functions  $G_0$  by the full  $G$  in the equations above. This leads to a self consistent 'loop' of equations which can be solved for the

Green's function  $G$  and the other relevant quantities. Fig.2.2 shows this self consistency loop schematically.

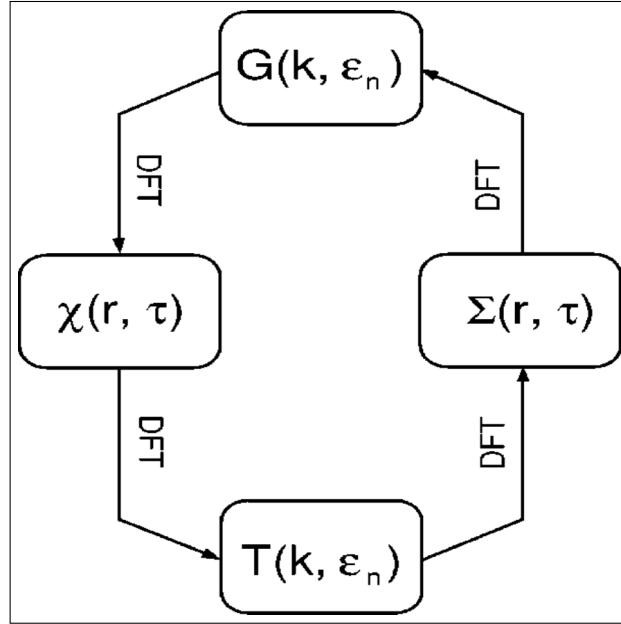


Figure 2.2: Schematic diagram of the self consistency loop [112]. An initial guess of the Green's function provides the susceptibility  $\chi$ , which is then used to calculate the T-matrix  $T$ , which leads to the self energy  $\Sigma$ , which is used to calculate the Green's function again, completing the loop. DFT is discrete Fourier transform.

The different ways to achieve this is primarily classified by the ansatz used for the susceptibility  $\chi$ . Apart from the original ansatz  $\chi = \chi_0 \sim G_0 G_0$  that we saw above, one can replace one [110] (the 'mixed' or Kadanoff-Martin approach) or both [106, 111] (the 'fluctuation exchange' approach) of the Green's functions  $G_0$  by  $G$ . The solutions of these equations provide more accurate results on some aspects of the BCS-BEC crossover. In particular, the fluctuation exchange method has been further generalized to include the effects of both particle-particle and particle-hole chain diagrams [112], and can capture the non-monotonic  $T_c$  with  $U$  in lattice systems even in 2 dimensions. Other non-perturbative methods not based on T-matrix approaches have also been developed [113]. For instance, Ref [113] develops a formalism which also incorporates vertex corrections that are neglected by standard T-matrix approaches. This successfully captures the behaviour of the spectral function above  $T_c$  to great accuracy, even though it becomes progressively less accurate as one moves closer to  $T_c$ . Fig.2.3 shows the  $T_c$  calculated using one such semi-analytic method [114] and the accurate density of states data from the method in Ref [113].

A more rigorous classification of the above methods can be done by examining whether they are 'conserving' or not, that is, whether, and to what extent, they satisfy the conservation laws in the system. Theories that are phi-derivable in the sense of Kadanoff-Baym satisfy all Ward identities

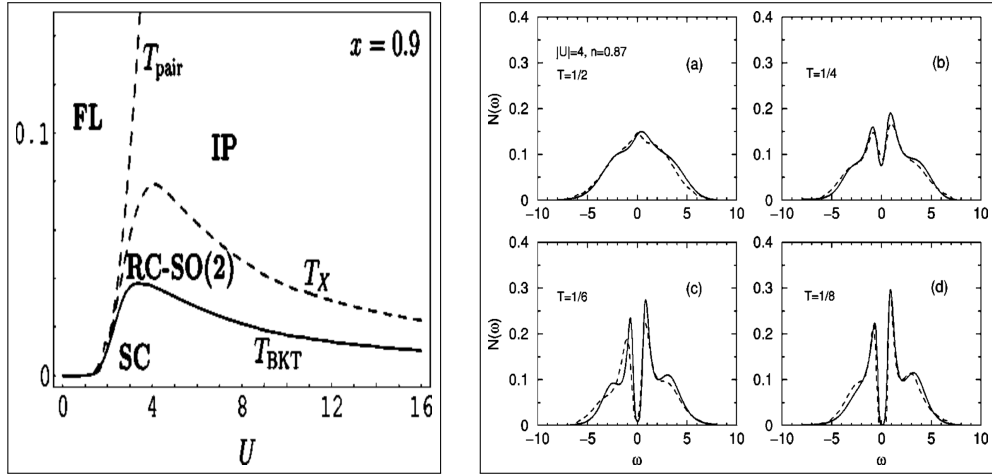


Figure 2.3: Left:  $T_c$  and other thermal scales calculated using the method of Ref [114]. in two dimensions. Right: Density of states data calculated using the method of Ref [113] , showing accurate match with QMC data (dashed lines).

and conservation laws in principle, while most T-matrix based methods generally do not [115]. Concrete examples of the second kind provided above include the Nozieres-Schmitt-Rink based theories (using  $G_0G_0$  in the susceptibility) and Kadanoff-Martin ( $G_0G$ ). On the other hand, the fluctuation exchange method (FLEX), which can also be set up in the T-matrix language with  $GG$  in the susceptibility, and the two particle self consistent method (2PSC) fall in the first category. However, instead of analysing the formal correctness of these theories, we use the indicators listed in Table 1 of Chapter 3 (that are more relevant to our analysis) for comparing the usefulness of different methods.

While these approaches provide much insight into the effect of fluctuations, functional methods, based on a systematic expansion of the partition function, provide an organized way of including the effects of fluctuations. The resultant models are also more amenable to numerical analysis in more generalized situations (such as involving disorder, etc.), and are intimately related to our numerical approach. We provide a description of the method below.

### 2.1.4 Functional methods

Functional methods provide an organized way of including the effect of fluctuations and allows one to compare the successive orders of approximation efficiently. There are two steps to accomplish this: first rewriting the Hubbard Hamiltonian by inserting ‘pairing’ fields  $\Delta_i(\tau)$  using the ‘Hubbard-Stratonovich’ transformation [116], and second, reorganizing the resultant action using the Nambu-Gorkov method [105]. We discuss this below.

## Hubbard-Stratonovich transformation

The Hubbard-Stratonovich transformation enables one to reformulate a problem with a quartic interacting term into a quadratic one by inserting additional fields into the problem. Starting with the expression for the partition function, we first insert the Gaussian identity relation

$$1 = \int \mathcal{D}(\Delta_i(\tau), \bar{\Delta}_i(\tau)) \exp\left(-\int_0^\beta \sum_i (|\Delta_i|^2/U)\right)$$

into the expression for the partition function  $\mathcal{Z}$ . Then, we make the substitution  $\Delta_i \rightarrow \Delta_i - U\Psi_{i\downarrow}\Psi_{i\uparrow}$ , and the quartic term in  $\Psi$  cancels the quartic interaction term of the original Hamiltonian, while we get new terms involving products of one  $\Delta$  and two  $\Psi$  operators. The new action is

$$S = \int_0^\beta \left( \sum_{i\sigma} \bar{\Psi}_{i\sigma} \partial_\tau \Psi_{i\sigma} - t \sum_{\langle ij \rangle \sigma} (\bar{\Psi}_{i\sigma} \Psi_{j\sigma} + h.c.) + \sum_i (\Delta_i(\tau) \bar{\Psi}_{i\uparrow} \bar{\Psi}_{i\downarrow} + \bar{\Delta}_i(\tau) \Psi_{i\downarrow} \Psi_{i\uparrow}) + |\Delta_i(\tau)|^2/U \right)$$

The final partition function is given by

$$\mathcal{Z} = \int \mathcal{D}(\bar{\Delta}, \Delta) \mathcal{D}(\bar{\Psi}, \Psi) \exp(-S)$$

This action is quadratic in the fermion operators and these can hence be integrated out to give an effective action containing only the  $\Delta$  fields [105]. This can be subjected to further approximations to yield effective models at the required level of accuracy. The various approximations can now be applied systematically starting from this. For instance, the mean field theory is given by the ‘saddle point’ of the corresponding action w.r.t. the variables  $\Delta$  and  $\mu$ :

$$\delta S / \delta \Delta = 0$$

$$\delta S / \delta \mu = 0$$

These yield the usual mean field equations. Expanding the action to quadratic order in the  $\Delta$  fields is equivalent [4] to the pairing fluctuations calculation of Nozieres and Schmitt-Rink. Further expansion to fourth and higher order in  $\Delta$  can be done to formulate an effective Landau-Ginzburg theory [4]. On the other hand, by integrating out further degrees of freedom (such as amplitude or phase of the  $\Delta$  fields), one can formulate effective XY models that are valid in a restricted parameter regime [114, 117]. These also manage to get the non-monotonicity in  $T_c$ , though their results are severely limited due to the approximations involved.

### 2.1.5 Summary and conclusions

In summary, we find that analytic methods that extend the mean field formalism to include the effects of fluctuations can get several aspects of the BCS-BEC crossover correctly. In particular, the continuum problem in three dimensions, where the  $T_c$  rises and then saturates with increasing coupling is captured by the Gaussian fluctuations of Nozieres and Schmitt-Rink. However, to access the pseudogap effects in the density of states correctly, as well as getting accurate results for  $T_c$  in lattice systems on two and three dimensions, one needed more sophisticated self consistent methods, both based on T-matrix approaches and without it. The reformulation of the problem in terms of functional integrals, on the other hand allowed a systematic expansion in fluctuation effects, capturing the mean field, NSR and effects beyond by successive approximations. It further enables the construction of effective Landau-Ginzburg functionals or XY models in restricted parameter regimes, which can also be used to study various aspects of the problem.

In spite of the reasonably accurate estimates of  $T_c$  and some aspects of the spectral functions that these methods provide, most of them have narrow regimes of validity. This has given rise to other approaches such as numerical QMC to gain a better understanding of the problem. We will discuss these issues in greater detail in the next chapter on the BCS-BEC crossover. For now, we move on to disordered superconductors.

## 2.2 Disordered superconductors

The rich experimental history of disordered superconductors has also led to a parallel development of theoretical and numerical methods to examine the problem in various ways and to understand the experimental results. This section will provide a review of these methods and their connection to experimental results. We start off with a discussion of methods that extend the BCS mean field theory to disordered systems. Then we look at the two paradigms for understanding the disorder induced superconductor-insulator transition: the so called ‘fermionic’ mechanism due to Finkelstein, and the bosonic mechanism, due to Fisher et. al. Finally, we review the numerical work done on this problem, and conclude by reviewing the overall situation in the field.

### 2.2.1 Extending BCS theory

As already discussed earlier, the first step in this direction was taken by Abrikosov and Gorkov, who showed using perturbation theory that weak disorder had little effect on the thermodynamic properties of a superconductor, including its  $T_c$ , which remained unchanged to  $\mathcal{O}(1/k_F l)$  [30]. This was followed up by the intuitive explanation of Anderson [31], as explained in the last chapter. Nevertheless, other properties such as the coherence length, penetration depth, critical magnetic

field, etc. are affected by disorder. Many of these were investigated using perturbative approaches, often using the Landau-Ginzburg formulation of superconductivity, managing to successfully describe the properties of many superconducting alloys. These results are collectively known as the classical theory of dirty superconductors [118], and are valid at weak disorder,  $k_F l \gg 1$ .

With increasing disorder, the eigenstates become localized, and the validity of the weak disorder theories become questionable. While it was originally thought that Anderson's arguments would cease to hold when the eigenstates of the disordered problem became localized, Ma and Lee [119] demonstrated that Anderson's pairing argument remains valid even beyond the mobility edge as long as  $(\rho L^d)^{-1} < \Delta_0$ , where  $\rho$ ,  $L$  and  $\Delta_0$  denote the averaged density of states at the Fermi energy, the localization length and the BCS order parameter respectively, and  $d$  is the number of dimensions, if the superconducting parameter  $\Delta$  is uniform over the whole system. In fact, within mean field theory, they showed that superconductivity existed all the way to site localization. However, one can expect that at high enough disorder, the  $\Delta$  themselves would become inhomogeneous, and the above arguments would no longer hold.

The BCS mean field theory can be generalized [81] to include such an inhomogeneous  $\Delta$  distribution in a disordered system, and self consistent solutions of the corresponding mean field equations can show considerable inhomogeneities at strong disorder. This method has often been applied numerically, and hence, we will discuss it in more detail when we review the numerical work. Below, we review the two primary analytic formulations of the SIT, the fermionic [82] and the bosonic [83] mechanisms.

### 2.2.2 The 'fermionic' mechanism

An important ingredient of all materials is the Coulomb interaction, which acts as a long range repulsive force between the electrons that make up the free carriers of the material. In a good metal, this repulsive interaction is screened considerably due to the surrounding electron cloud, and hence at comparatively long length scales (compared to  $\sim 1/k_F$ , for example) or low energy scales (compared to  $\epsilon_F$ , the effect is weakened. On the other hand, the indirect electron-electron interaction mediated by the lattice vibrations (as shown by Frohlich [18]) can provide an attractive interaction at a low energy scale  $\sim \omega_D$ . Due to the weakening effect of screening, the overall interaction can be negative in a small range of energy, which gives rise to superconductivity. In BCS theory and its extensions, the effect of the Coulomb repulsion is not considered explicitly, and it is assumed that the effective attractive interaction is not influenced significantly by disorder. Nevertheless, from the arguments provided above, we see that the overall nature of the interaction is sensitively dependent on the efficacy of the screening process. Fig.2.4 illustrates the basic physics [120, 121] of the competition of the two scales and their dependence on the energy scale.

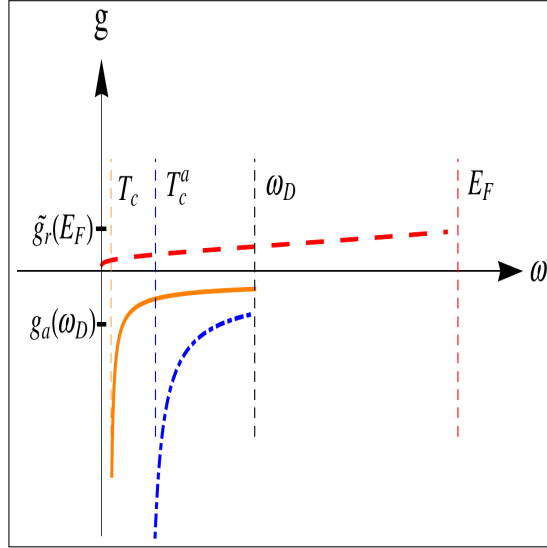


Figure 2.4: Schematic diagram [121] of the physics of the competition between the Coulomb repulsion and the attractive interaction induced by electron-phonon interactions in a clean superconductor. The repulsive interaction (red dashed line) is defined at the Fermi energy  $E_F$  and is renormalized down. The attractive interaction (blue dashed dotted line) is defined at the Debye energy  $\omega_D$  and its strength increases with decreasing energy, diverging at a nominal temperature  $T_c^a$ . The combined interaction (orange line), if attractive at  $\omega_D$ , becomes stronger under further renormalization until it diverges at the true  $T_c$  of the system. Disorder changes this physics, strengthening the Coulomb interaction, and hence decreases the overall attraction.

The ‘fermionic’ mechanism specifically includes the effect of disorder on the screening process of the material. The effect of screening is provided by a dielectric function  $\epsilon(q)$ , and the resultant screened potential is given by  $V_{eff} \sim V_0/\epsilon$ . If one investigates how disorder affects this screening process, one finds that it becomes weaker with increasing disorder, strongly renormalizing the effective Coulomb interaction. In particular, the repulsion of electrons with opposite momentum and spins (that is, those that form the most stable Cooper pairs) corresponding to low momentum transfer become enhanced. This leads to a decrease in the effective attractive interaction, and hence the  $T_c$ . The first comprehensive results were derived by Maekawa and Fukuyama [122]. Their perturbative calculations demonstrated that the  $T_c$  is suppressed by the following formula:

$$\ln(T_c/T_{c0}) = (e^2/3\pi^2\hbar)R_{\square}\ln(1/T_c\tau_0)^3$$

Here,  $R_{\square}$  is the square resistivity of the system, which increases as the disorder increases. While it matches the data at weak disorder, the rate of decrease is too fast at strong disorder, where this theory is inapplicable. However, it can be extended to strong disorder using renormalization group techniques [123, 124]. They demonstrated that at sufficiently large disorder,  $T_c$  can be suppressed all the way to zero, leading to a non-superconducting Fermi system where no superconducting

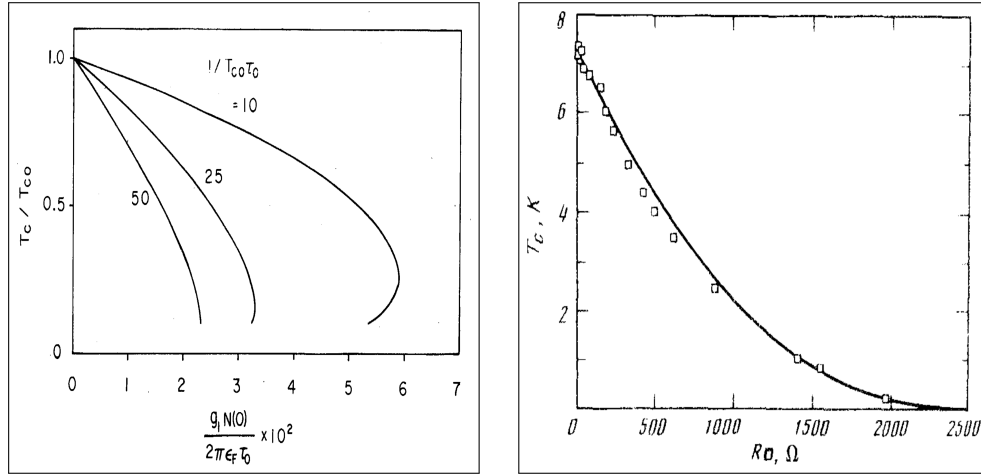


Figure 2.5: Left: Results from perturbation calculations in Ref. [122], showing the strong decrease at large disorder (x axis is proportional to  $R_{\square}$ ). Right: Renormalization group calculations of Ref. [123] compared to experimental data, showing a very good match. Note the slower fall at stronger disorder, contrary to the perturbation calculations.

pairs exist any more. Fig.2.5 shows the results from the Maekawa-Fukuyama theory and the renormalization group calculations compared to experimental data, clearly showing that the perturbative theory fails at strong disorder, whereas the renormalization group calculations show a very good match. We find that while the the initial decrease of  $T_c$  is linear with  $R_{\square}$ , it becomes slower at larger disorder, and eventually goes to zero when the effective attractive interaction vanishes.

Since the pairing correlations weaken with increasing disorder, this theory predicts the weakening of the  $T = 0$  gap as well as the  $T_c$  of the system. The final state after superconductivity is destroyed can be metallic or insulating depending on the localization properties of the system. Hence, depending on the dimensionality of the system and the disorder strength where the transition occurs, one can have a S-M-I transition (primarily in 3 dimensional systems) or a direct S-I transition. Nevertheless, the increasing disorder invariably increases the resistivity of the system, and hence the  $T_c$  and resistivity/resistance always follow an inverse relation.

To summarize, the fermionic mechanism achieves the following:

1. Provides a viable mechanism for the suppression of superconductivity where the single particle gap vanishes, and where the strong disorder state can be metallic or insulating.
2. Provides detailed relationships between the resistivity  $R_{\square}$  and the disorder with very few fitting parameters that can be easily extracted from experiments.

Fig.2.6 shows a schematic plot demonstrating the basic physics of the fermionic mechanism.

These predictions are seen to be in agreement with experimental results on some materials such as amorphous Pb and Sn [125] films, and alloys such as W-Re [126], Mo-Ge [127] and  $Nb_3Ge$

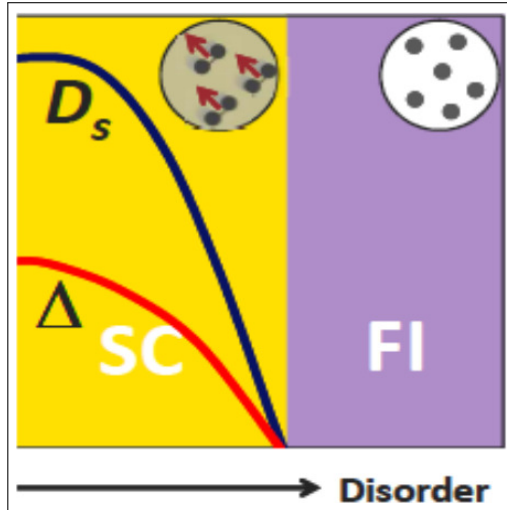


Figure 2.6: Schematic figure [131] of the evolution of superconductivity with increasing disorder as postulated by the fermionic mechanism. The superconductor consists of coherent pairs with finite order parameter  $\Delta$  and stiffness  $D_s$ . With increasing disorder both  $\Delta$  and  $D_s$  decrease due to increasing Coulomb repulsion, until they vanish at the critical point. Beyond this, all pairs are broken, and the system properties are determined by free fermions in a disordered system.

[128], whose  $T_c$  dependence on disorder and sheet resistance  $R_s$  are in good agreement with those from the theory. Three dimensional materials such as amorphous  $\text{Au}_x\text{Si}_{1-x}$  [129] or  $\text{Nb}_x\text{Si}_{1-x}$  [130] also show the expected S-M-I transitions. Nevertheless, from what we saw in the previous chapter, many materials including thin films of Be, NbN,  $\text{InO}_x$  and TiN, and three dimensional NbN show a direct S-I transition, alongwith a seemingly robust gap at  $T = 0$  in the single particle spectral function, and surviving pairing correlations even in the insulating state. This calls for a completely different theory, which brings us to the ‘bosonic’ mechanism.

### 2.2.3 The ‘bosonic’ mechanism

The bosonic mechanism provides an effective low energy description of the system where the temperature scale is much smaller than the typical pairing scale in the problem. Thus, it assumes the presence of pairs in the system, and investigates the effect of disorder on the effective bosonic degrees of freedom that the pairs represent.

In the clean system, the superfluid state is characterized by a finite stiffness to phase twists. The long range phase modes are gapless, corresponding to the Goldstone modes of the system. The presence of the long range electromagnetic field has far reaching consequences, however; the Goldstone mode couples with the electromagnetic degrees of freedom, and in 3D results in a massive transverse field corresponding to the exponential spatial decay inside the material, and a high frequency plasmon mode corresponding to long range density oscillations in the system. Thus

the long range phase modes acquire a gap of the order of the plasma frequency  $\omega_p$  in normal metals at  $T = 0$ . In 2D this plasmon mode has a dispersion  $\sim \sqrt{q}$  and is still gapless.

The first comprehensive theory of the disorder induced  $S - I$  transition was provided by Fisher et. al [83]. They considered a collection of bosons in two dimensions in a random potential with a repulsive Coulomb interaction between them. As the disorder is increased, or the boson number density is decreased, the system undergoes a transition from a superconducting state where the pairs are condensed to a disordered Bose glass state below a critical density  $n_c$ . In this state, the Cooper pairs are localized and there is no coherence between these localized pairs. Thus, the system is no longer superconducting, but since the pairs continue to exist, the single particle spectrum remains gapped.

Another way to understand this transition is from the dual of the bosonic representation, which is given by vortex configurations in the bosonic wave functions. In the superconducting state, the vortices are bound into pairs and hence do not move. On the other hand, beyond the transition these vortices are unbound and become mobile, and the resultant state can be interpreted as a condensed state of vortices instead of bosons. The movement of vortices traversing the system provides a mechanism for dissipation in the form of phase-slips. Right at the transition, where the theory is self dual in two dimensions, *both* bosons and vortices are about equally mobile, and this implies that there is a **finite, universal resistivity**  $R_{Qp} \sim \hbar^2/4e^2$  at the transition point. Thus, this theory provides the remarkable prediction that even in two dimensions, where all single particle eigenstates are localized, the resistivity can have a finite, universal value at the superconductor-insulator transition. Fig.2.7 shows a schematic figure of the resistivity as predicted by this theory, and the corresponding experimental results from Ref. [132].

Since the bosonic theory emphasizes phase fluctuations of the bosonic variables with no changes in their ‘amplitudes’, it falls in the same universality class as the quantum XY model. This simpler problem has thus been studied to expand our understanding of the results of the bosonic mechanism. A very recent QMC study [134] of the model concentrated on the low energy features of the optical conductivity.

In a disordered superconductor, there are two energy scales corresponding to the inverse of the mean free path  $\tau^{-1}$  and the superconducting single particle gap  $\Delta$ . Since the conductivity is infinite in the superconducting state, the conductivity  $\sigma(\omega)$  has a delta function at  $\omega = 0$  [1]. In a system with weak disorder such that  $\tau^{-1} \gg \Delta$ , one can use the BCS formalism to work out the conductivity, as was done by Mattis and Bardeen [135]. In the absence of superconductivity, the system shows a finite conductivity at  $\omega = 0$  that begins to fall off when  $\omega$  becomes comparable to the scattering rate,  $\sim \tau^{-1}$ . In a superconducting system, however, due to the absence of single particle excitations inside the gap, the conductivity is zero upto  $\omega = 2\Delta$ , except for the delta function. As with the normal metal, it drops off for  $\omega \gtrsim \tau^{-1}$ .

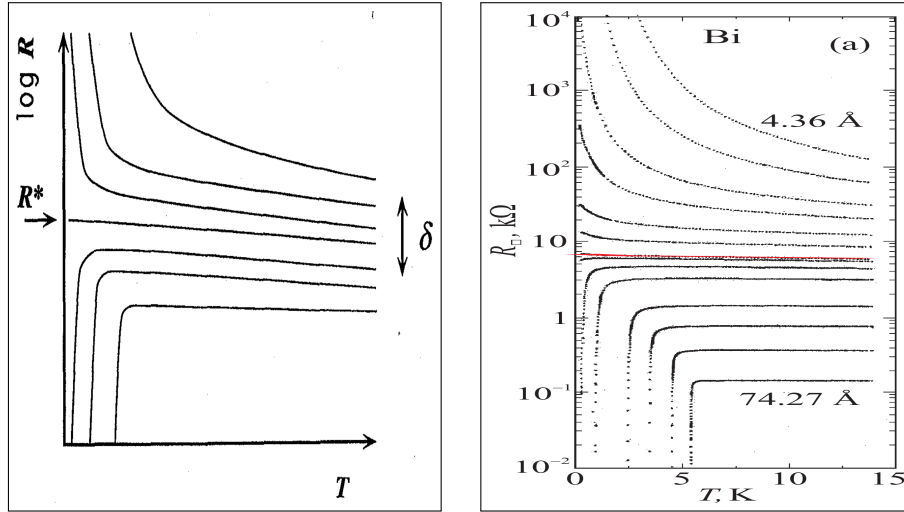


Figure 2.7: Left: Schematic resistivity from bosonic mechanism [133], showing the horizontal critical line, along with the universal value, and other resistivity lines diverging from it. Right: Experimental data from Ref. [132], in agreement with this theory.

Thus, mean field arguments imply that there can be no conduction for  $\omega \lesssim 2\Delta$  due to the presence of the single particle gap. However, phase degrees of freedom can result in low energy collective modes that lead to finite conductivity even inside this interval. The QMC study found that at strong disorder, these modes contribute to enhance the low frequency conductivity, contrary to expectations from naive mean field theory. In a realistic model with fermionic degrees of freedom (to be described in detail later in connection with QMC work done on the negative  $U$  Hubbard model) this behaviour can be explained from the presence of different energy scales for single particle and two particle correlation functions. Fig.2.8 shows the results that one expects from mean field theory contrasted with the QMC results, clearly demonstrating the presence of low energy weight near the transition.

To summarize, the bosonic mechanism provides the following results:

1. A viable theory of the SIT due to phase fluctuations, where the single particle gap does not close, in agreement with many recent experimental results.
2. The prediction of finite universal conductivity  $R_{Qp} \sim (\hbar^2/4e^2)$  at the critical disorder.
3. Enhanced low frequency conductivity at strong disorder, due to low energy phase modes.

Fig.2.9 shows a schematic figure depicting the evolution of the superconductor with disorder as predicted by the bosonic mechanism.

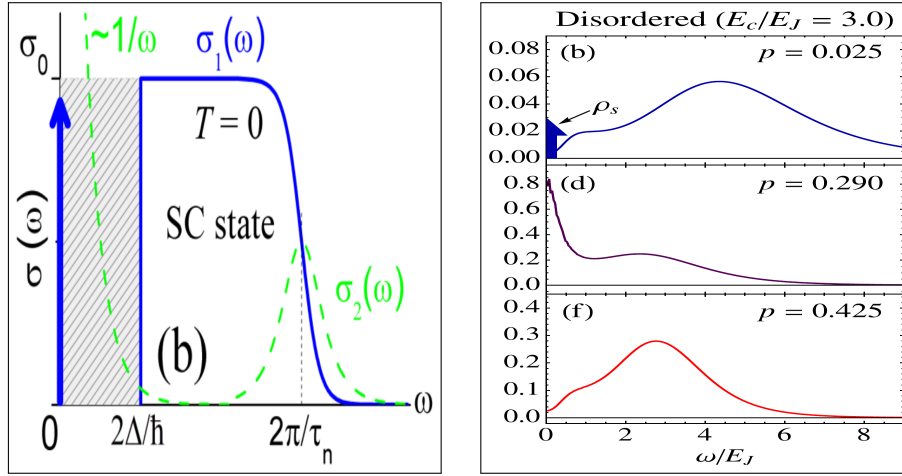


Figure 2.8: Schematic picture of optical conductivity calculated from Mattis-Bardeen theory (left) [136] and results from QMC calculation using the quantum XY model in Ref. [134] (right). Top right plot is at weak disorder, far from the critical region, middle right is near the critical region, clearly showing enhanced low frequency weight, which again decreases as one goes beyond it into the insulator (bottom right). This is in contrast to the mean field theory results, which show zero conductivity between  $\omega = 0$  and the single particle gap  $2\Delta$ .

## 2.2.4 Numerical methods

We have seen that the fermionic and bosonic mechanisms provide two different theoretical frameworks for understanding the superconductor insulator transition. While both of them successfully explain certain observations in different classes of materials, the bulk of results from recent experiments on materials like Be,  $\text{InO}_x$ , TiN and NbN (as mentioned above and reviewed in an earlier chapter) seems to be compatible with the bosonic scenario, at least at low temperatures. Nevertheless, there are certain features of real systems that the bosonic theory cannot successfully capture:

1. The bosonic formulation, being a low temperature effective theory, assumes that the single particle gap  $\rightarrow \infty$ , while real materials in the BCS limit have a small gap and a large coherence length. Thus, fermionic degrees of freedom are important in the thermal behaviour.
2. Experimental results do not seem to show a universal conductivity at the critical region, further emphasizing the role of fermionic degrees of freedom.
3. The inhomogeneous clusters and their specific dependence on the background disorder cannot be predicted by the theory.

These reasons have motivated the development and application of numerical techniques to this problem. Motivated by the experimental results in favour of the bosonic scenario, these approaches usually neglect the Coulomb repulsion between the fermions, and use simplified model Hamiltonians such as the negative  $U$  Hubbard model to investigate the physics. The applicability of such

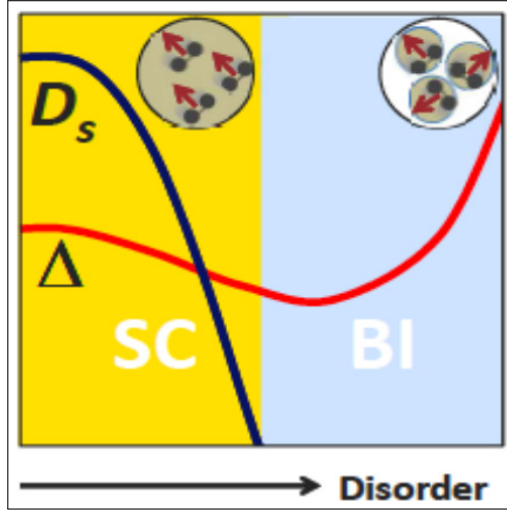


Figure 2.9: Schematic figure [131] of the evolution of superconductivity with increasing disorder as postulated by the bosonic mechanism. The superconductor consists of coherent pairs with finite order parameter  $\Delta$  and stiffness  $D_s$ . With increasing disorder, increasing phase fluctuations results in a decrease in  $D_s$ , while the gap parameter  $\Delta$  remains the same. The disorder causes the bosonic pairs to lose long range coherence, and increased phase fluctuations among these pairs drives the system insulating. In the insulating regime, the bosonic pairs are incoherent, but the single particle gap reimagines (the variation shown in the single particle gap is determined from calculations using fermionic models, see numerical methods section).

simple models to this problem will be discussed in more detail when we describe our model and methods.

### Inhomogeneous mean field theory

The first approach in this direction was taken by Ghosal et. al. [84, 85], who investigated the problem at  $T = 0$  using a mean field theory generalized to disordered systems. Their work differed from earlier mean field generalizations (like Ma-Lee as discussed earlier) in that they allowed for the variation of the local pairing amplitudes  $\Delta_i$ , which resulted in very important differences from the earlier theories, as described below.

They started with the negative  $U$  Hubbard model in a two dimensional lattice with disorder incorporated in the form of a random potential  $V_i$ . Their mean field model can be written as:

$$\mathcal{H} = \mathcal{H}_{kin} + \sum_i \Delta_i c_{i\uparrow}^\dagger c_{i\downarrow}^\dagger + \Delta_i^* c_{i\downarrow} c_{i\uparrow} + \sum_{i\sigma} (V_i - \mu_i) c_{i\sigma}^\dagger c_{i\sigma} \quad (2.5)$$

While the terms involving  $\Delta$  arise from a usual mean field decomposition in the pairing channel  $\sim \langle c_{i\downarrow} c_{i\uparrow} \rangle$ , Ghosal et. al. also considered the mean field decomposition in the ‘density’ channel

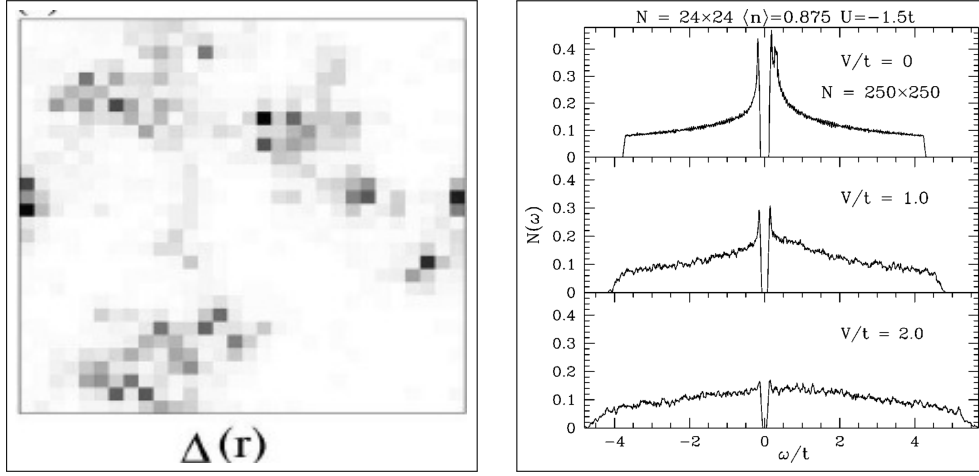


Figure 2.10: Left: Map of  $\Delta_i$  at strong disorder from BdG calculations [85], showing clusters with large  $\Delta_i$  embedded in regions with very small  $\Delta_i$ . Right: Density of states at  $T = 0$  at three different disorder strengths [85], showing the persisting gap even at high disorder, and decreasing coherence peaks with disorder.

$\sim \langle c_{i\sigma}^\dagger c_{i\sigma} \rangle$ , giving rise to a term  $(U/2)\langle n_i \rangle$  (the ‘Hartree’ term), which they absorbed into the chemical potential by defining  $\mu_i = \mu + (U/2)\langle n_i \rangle$ . This gives rise to the following self consistency relations:

$$\begin{aligned} \Delta_i &= U \langle c_{i\downarrow} c_{i\uparrow} \rangle \\ n_i &= \sum_{\sigma} \langle c_{i\sigma}^\dagger c_{i\sigma} \rangle \end{aligned} \quad (2.6)$$

This is known as the Hartree-Fock-Bogolyubov-de-Gennes (HFBdG) mean field theory. This Hamiltonian, being quadratic can be solved by a generalization of the Bogolyubov-Valatin ansatz described before, and these equations can then be solved self consistently. Ghoshal, *et. al.* [85] solved these for different values of disorder at  $U/t = 1.5$  in lattices upto size  $24 \times 24$ .

The resultant solutions showed an increasingly inhomogeneous distribution of both  $\Delta_i$  and  $n_i$  with increasing disorder. While the  $n_i$  variation essentially followed that of the random potential, becoming stronger with increasing disorder, the  $\Delta_i$  distribution showed large clusters where  $\Delta_i$  was comparatively large embedded in a background with  $\Delta \sim 0$  at strong disorder. This was the first explicit demonstration of superconducting clusters at strong disorder starting from a fermionic model. Additionally, they showed that the density of states remains gapped at arbitrarily strong disorder, since the low energy excitations are confined to the superconducting clusters. This lent further credence to the bosonic theory of the  $T = 0$  transition, where the gap persists, but independent quantum fluctuations between the clusters destroys the superconducting state. By using

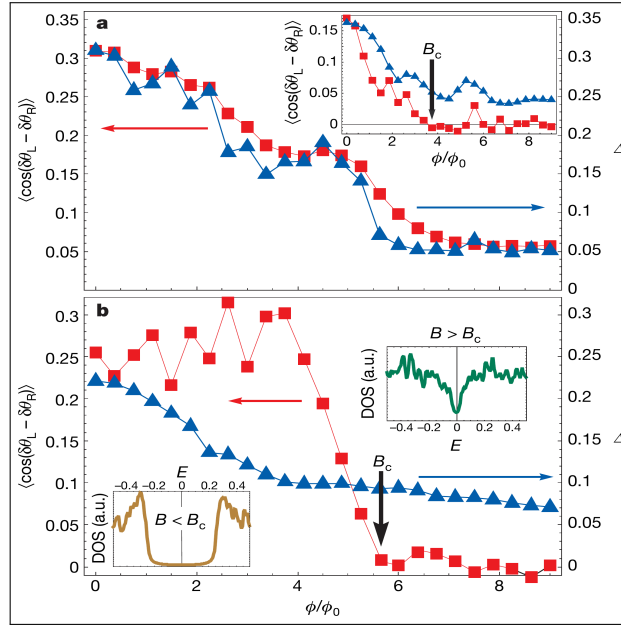


Figure 2.11: Phase correlation between edges (red) and order parameter  $\Delta$  with increasing magnetic flux  $\phi/\phi_0$  at weak disorder (top) and strong disorder (bottom) [87]. While the top shows a suppression of both the order parameter and phase correlation, both of which vanish at the transition point, the bottom one shows that the order parameter remains finite, but enhanced phase fluctuations drive the transition, causing the phase correlations to vanish.

a quantum XY model with coefficients extracted from the mean field calculation, the authors also provided an estimate of the critical disorder  $V_c$ . Fig.2.10 shows the clusters at strong disorder and the density of states from their BdG calculations.

### Including thermal fluctuations

The mean field method outlined above provides a single  $\Delta_i$  at each site, neglecting amplitude and phase fluctuations. Subsequent numerical techniques developed real space Monte Carlo methods to incorporate some of the effects of thermal fluctuations [86, 87, 137–139] in various calculations in the context of s-wave and d-wave superconductors. The effect of classical phase fluctuations in a disordered s-wave superconductor in the presence of a magnetic field was investigated by Dubi, et. al. [87]. They started with the disordered negative  $U$  Hubbard model in the presence of a magnetic field, which added site dependent phase factors to the Fermi operators. After a Hubbard-Stratonovich transformation in a single channel, they formulated a model with extra classical fields  $\Delta_i$  and numerically solved it (this mechanism will be discussed in greater detail in the model and methods section). They found that the suppression and destruction of superconducting order with increasing magnetic field followed completely different mechanisms at weak and strong disorder. At weak disorder, the destruction was accompanied by the destruction of  $\Delta_i$  everywhere. At strong

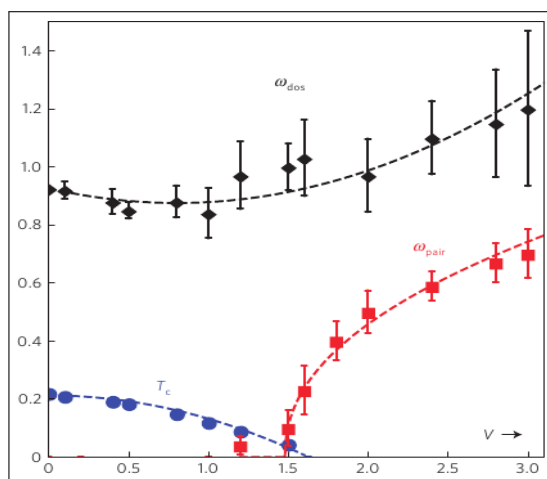


Figure 2.12: Phase diagram from QMC calculations [88]. Blue line shows the  $T_c$  degradation with disorder  $V$ , vanishing at  $V_c \sim 1.6t$ . Single particle gap  $\omega_{dos}$  persists through the transition, while a two particle correlation gap  $\omega_{pair}$  vanishes as one goes from the insulator to the superconductor.

disorder, on the other hand, increasing magnetic field caused the inhomogeneous superconducting clusters to shrink and disconnect, and the resultant loss of phase correlation destroyed the superconducting order. This also hinted towards a similar, phase fluctuation driven transition with increasing temperature at zero magnetic field, and provided an explanation for the initial rise in the non-monotonic behaviour of the magnetoresistance at strong disorder. Fig.2.11 shows their results for the destruction of superconductivity with increasing magnetic field at weak and strong disorder. Subsequent work [137–139] including both thermal phase and amplitude fluctuations have investigated the nature of the percolation transition at finite temperature [137], the resistivity near the BKT transition [138] and the non-monotonic magnetoresistance [139] at strong disorder. While the first implemented a single channel decomposition, the latter two [138, 139] used a double channel decomposition very similar to our methods to study the transport features.

## Quantum Monte Carlo

Quantum Monte Carlo (QMC) methods incorporate both dynamic and spatial fluctuations in the Hubbard-Stratonovich fields (though they decouple the quartic term in the ‘density’ channel, which incorporates the same physics as the full Hubbard model when all fluctuations are retained), and hence are free of approximations in principle. QMC calculations on the disordered negative  $U$  Hubbard model [88, 140, 141] have provided many benchmark results about the superconductor-insulator transition. Fig.2.12 summarizes these results from Ref. [88] in the form of a phase diagram at  $U/t = 4$ . It shows the disorder induced suppression of  $T_c$ , providing a benchmark for the critical disorder  $V_c$ . While the superconducting regime is characterized by a non-zero superfluid stiffness which vanishes at  $V_c$ , the insulating regime is characterized by a finite pair energy scale  $\omega_{pair}$ ,

corresponding to the decaying of a Cooper pair in the insulator. This is different from the single particle gap  $\omega_{dos}$ , which remains finite throughout the transition at  $T = 0$ .

The two particle scale vanishes at the transition, and the vanishing of a similar quantity is related to the anomalous behaviour of the optical conductivity as explained earlier in connection with the QMC of the quantum XY model [134]. Fig. 2.12 shows a phase diagram that describes the evolution of the various scales,  $T_c$ , the single particle gap  $\omega_{dos}$  and the two particle gap  $\omega_{pair}$  with increasing disorder.

These calculations also demonstrated a disorder induced pseudo-gap in the density of states at finite temperature. Thus, QMC calculations provide important benchmark results about the disorder dependent  $T_c$ , demonstrate different energy scales  $\omega_{dos}$  and  $\omega_{pair}$ , and show a disorder induced pseudo-gap in the spectral function at finite temperature.

## Summary and shortcomings

In summary, the numerical methods achieve the following:

1. Mean field methods successfully showed the  $T = 0$  inhomogeneity in the superconducting state at strong disorder, alongwith the persistence of the single particle gap for all disorder values.
2. Inclusion of classical phase fluctuations further demonstrated the contrasting effect of magnetic field at weak and strong disorder, providing an explanation for the non-monotonic magnetoresistance at strong disorder.
3. Recent generalizations of this method have included both amplitude and phase fluctuations and clarified certain aspects of the thermal transition and the corresponding transport behaviour, along with an explicit demonstration of non-monotonic magnetoresistance at strong disorder.
4. QMC methods, on the other hand, provided results on the  $T_c$  and its suppression, and different energy scales  $\omega_{dos}$  and  $\omega_{pair}$  for single particle and pair excitations, clarifying the physics of the transition further.

Together, these methods have thus explained several aspects of disordered superconductors.

There are, however, inherent shortcomings to all of these methods that limit their applicability to certain aspects of the problem, especially related to thermal behaviour and spatial resolution. These are:

1. Mean field theories are incapable of capturing the thermal behaviour at strong disorder, where the phase degrees of freedom are expected to play an important role.

2. While the inclusion of thermal phase fluctuations yields qualitatively correct results at low temperatures and moderate coupling, they ignore amplitude fluctuations, which are expected to be important at weak coupling and higher temperature, and hence cannot capture the correct physics of the system. Even when thermal amplitude fluctuations are incorporated, methods based on a single channel decomposition neglect the contribution of the density channel. Thus, they do not reproduce the HFBdG ground state. From the mean field results, we found that the extra inhomogeneous term  $(U/2)\langle n_i \rangle$  magnifies the effective disorder  $V_i - (U/2)\langle n_i \rangle$  considerably at strong disorder, where  $n_i$  is highly inhomogeneous. Thus, the results of such methods, though qualitatively correct, are expected to be quantitatively incorrect at strong disorder.
3. Recent work has incorporated both amplitude and phase fluctuations in both pairing and density channels, but have not yet studied the disordered problem exhaustively, in particular, the disorder induced transport crossover or the spatial and spectral characteristics relevant to the STM experiments.
4. QMC is computationally complex, limiting it to moderate coupling  $U/t \sim 4$  and small lattices  $\mathcal{O}(10 \times 10)$ . This prohibits their application to ‘weak’ coupling systems which are experimentally relevant. Furthermore, it provides data on variables in imaginary frequency, requiring complicated numerical analytic continuation techniques such as the Maximum Entropy Method to yield results in real frequency, potentially reducing the accuracy of the results, for example, on the single particle spectral functions and response functions like the resistivity. We shall discuss this aspect, particularly the difficulty in calculating transport properties using QMC, in more detail in Chapter.4, where we will describe our own results on the charge dynamics of our system. Finally, the size limitation prevents a spatially resolved picture of the system, providing no insight on the evolution of the inhomogeneities with temperature.

Hence, to overcome these limitations and provide a comprehensive method to study the disordered superconductor problem in detail, one requires a method with the following characteristics:

1. Inclusion of **all thermal fluctuations** necessary to capture the finite temperature behaviour of the system, especially to capture the complex interplay of disorder and thermal degrees of freedom at strong disorder.
2. Inclusion of **both the ‘pairing’ and the ‘density’ channels**, so that the  $T = 0$  state is identical to HFBdG, and the important effects of the feedback of the inhomogeneous number density at strong disorder is correctly incorporated in the physics.

3. Ability to access **larger lattice sizes**, and hence smaller coupling values to allow meaningful comparisons with experimental results done at weak coupling. This also reduces finite size effects and allows access to larger spatial scales that QMC cannot access due to its high computational cost. QMC is implemented in an imaginary time formulation and extracting dynamical information involves a difficult analytic continuation process. A method using **real frequencies** would avoid these problems.

As we remarked earlier, generalizations of mean field methods to include classical thermal fluctuations in such interacting models have been developed before [86, 87, 137, 138]. However, none of them incorporated all the factors listed above and applied that to the problem of disordered superconductors. Below, we will describe our method, which allows us to incorporate all the important features above, and explain the numerical protocol we follow for simulation and the recipe for calculating various observables from that.

## 2.3 Model and methods

In this section, we describe our model and the numerical methods and Monte Carlo protocol that we use to solve this model. We choose the negative U Hubbard model on a two dimensional lattice, which we have already come across earlier as a model used both in the context of the BCS-BEC crossover and numerical simulations of disordered superconductors. As is true with any model, this simplifies the complicated actual forces in play in the real materials, substituting them with a simplified constant attractive interaction. In this section, we discuss the appropriateness of this model for studying the problem of disordered superconductors.

### 2.3.1 Choice of model

In traditional s-wave superconducting materials, the effective attractive interaction between pairs arises from the competition between the repulsive Coulomb interaction and the indirect phonon-mediated retarded attractive interaction (which we will call the ‘Frohlich’ interaction). We saw from previous discussions that disorder can affect such superconductivity in two distinct ways, by either decreasing the effective attractive interaction (the fermionic mechanism) or by increasing inhomogeneities, which results in an increase of phase fluctuations (the ‘bosonic’ mechanism). As many of the experimental results seem to support the bosonic mechanism whereby these inhomogeneities increase phase fluctuations, any candidate model should be able to reproduce this. From the numerical results, we see that the negative U Hubbard model manages to capture this physics very successfully. Thus, to a first approximation, it seems possible to neglect the complex interplay of the Coulomb interaction with the Frohlich interaction. Even though there are visible signatures

of the Coulomb interaction in the detailed behaviour of certain observables such as the density of states, it does not seem to play an essential qualitative role in the basic physics.

With magnetic impurities, a model with an on-site interaction is relevant for studying its effects on s-wave superconductors as we saw in Chapter 1. The magnetic moments tend to destroy the singlet pairing in such materials, suppressing superconductivity. However, If the system has a finite range attractive interaction, an alternative is to form triplet pairing between neighbouring sites, thus resulting in the formation of p-wave superconductors. A well known example of p-wave superconductivity is He3 (though for a repulsive core rather than magnetic field). In the context of magnetic superconductors, similar p-wave pairing is found in a range of materials including UGe2, URhGe, UCoGe etc [142]. A model with on site interactions like the Hubbard model is clearly inadequate to study these cases.

Taking all these factors into account, we also choose the negative  $U$  Hubbard model as our starting model, neglecting the Coulomb effects and the retarded nature of the electron phonon induced attraction. As explained earlier, our emphasis would be on capturing the non-trivial effect of the interplay of thermal fluctuations and disorder on the electronic motion. Hence, in our formulation, we will make further approximations by neglecting the quantum fluctuations of our ‘auxiliary’ fields resulting in a considerable increase in computational efficiency compared to QMC, while being reasonably accurate in the regimes of interest.

As discussed before, there are two parameters in this model, namely,  $U/t$  and the filling fraction  $f$ , which determines the average number density  $n$ . As evident from the analysis on the BCS-BEC crossover, this model shows a superconducting ground state at all coupling values  $U$ , but for all  $n \neq 1$ . At that particular filling, both superconducting and charge density wave order co-exist, which implies that there is no order above  $T = 0$ . We will discuss these properties again with more emphasis in Chapter.3 while describing our results on the BCS-BEC crossover.

### 2.3.2 Auxiliary fields

We begin with the negative  $U$  Hubbard model in a two dimensional square lattice:

$$\mathcal{H} = (-t) \left( \sum_{\langle ij \rangle} c_{i\sigma}^\dagger c_{j\sigma} + h.c. \right) - U \sum_i n_{i\uparrow} n_{i\downarrow} \quad (2.7)$$

To incorporate the effect of both the pairing and the density channels (whose importance to the disorder problem has been discussed earlier), we do a multi-channel Hubbard-Stratonovich decomposition, as done in Ref. [143]. To begin with, we rewrite the interacting term as

$$-Un_{i\uparrow}n_{i\downarrow} = -(U/4)(n_i^2 - s_{iz}^2)$$

Here,  $s_{iz} = (n_{i\uparrow} - n_{i\downarrow})^2$ .

As in the Hubbard-Stratonovich transformation in one channel, we insert Gaussian identity integrals for three channels corresponding to the pairing operator  $c_{i\downarrow}c_{i\uparrow}$ , the density operator  $n_i$ , and the spin operator  $s_{iz}$  respectively. Let us call these fields  $\Delta_i(\tau)$ ,  $\phi_i(\tau)$  and  $\phi_{si}(\tau)$ . One can then make the substitutions  $\Delta_i \rightarrow \Delta_i + \alpha c_{i\downarrow}c_{i\uparrow}$ ,  $\phi_i \rightarrow \phi_i - \gamma n_i$  and  $\phi_{si} \rightarrow \phi_{si} - i\gamma s_{iz}$  respectively. The quartic fermionic terms that come from this exactly cancel the interaction term of the original model provided  $\alpha^2 + \gamma^2 = 1$ . The final action is

$$S_f = \int_0^\beta \sum_{i\sigma} \left( \bar{\Psi}_i \partial_\tau \Psi_i + H_{kin} + H_{cl} + H_{int} \right) \quad (2.8)$$

Here,  $H_{kin}$  is the kinetic energy term, and

$$\begin{aligned} H_{cl} &= \sum_i (|\Delta_i|^2/U) + (\phi_i^2/U) + (\phi_{is}^2/U) \\ H_{int} &= \sum_i \left( \alpha(\Delta_i c_{i\uparrow}^\dagger c_{i\downarrow}^\dagger + h.c.) + \gamma(\phi_i n_i + i\phi_{si} s_{iz}) \right) \end{aligned} \quad (2.9)$$

This is an exact result and is valid in principle for all sets of  $\alpha$  and  $\gamma$  satisfying the constraint. However, at the mean field level, this very clearly does not recover the HFBdG ground state [144]. To recover this, we put  $\alpha = \gamma = 1$ . As mentioned in Ref. [143], the spin channel fluctuations decouple from the rest of the system and are hence ignored. We neglect the quantum fluctuations in  $\Delta$  and  $\phi$ , assuming that for many thermal properties of interest, these quantum effects would not be important, as explained before. The resultant problem of interacting thermal classical fields coupled to quadratic fermionic operators is described by the Hamiltonian

$$H_{eff} = H_{kin} + \sum_i \left( (\Delta_i c_{i\uparrow}^\dagger c_{i\downarrow}^\dagger + h.c.) - (\mu + \phi_i) n_i + (|\Delta_i|^2/U) + (\phi_i^2/U) \right) \quad (2.10)$$

The assumption  $\alpha = \gamma = 1$ , while making the ground state identical to HFBdG, causes an over-counting of fluctuations, since this model does not integrate back to the original Hubbard model. However, we expect that in the relevant temperature range, such effects will be weak. We will discuss these issues in more detail later in the context of benchmarking our model.

To incorporate disorder in this Hamiltonian, we model potential disorder by a random on-site

potential  $V_i$ , and magnetic impurities by randomly positioned and oriented classical spins  $\vec{S}_\nu$  which couple to the fermion spin operator  $\vec{\sigma}_i$  with a strength  $J$ . Thus, our most general model is given by

$$H_{eff} = H_{kin} + \sum_i \left( (\Delta_i c_{i\uparrow}^\dagger c_{i\downarrow}^\dagger + h.c.) + (V_i - \mu - \phi_i) n_i + (|\Delta_i|^2/U) + (\phi_i^2/U) \right) + \sum_{i\nu} J \delta_{i\nu} \vec{S}_\nu \cdot \vec{\sigma}_i$$

### 2.3.3 Bogolyubov transformation

Our model reformulates the effect of the Hubbard electron-electron interaction in terms of classical auxiliary fields  $\Delta_i$  and  $\phi_i$  coupled to the ‘pairing’ and ‘density’ operators  $c_{i\downarrow} c_{i\uparrow}$  and  $n_i$  respectively. The partition function is given by

$$Z = \int \mathcal{D}(\Delta, \bar{\Delta}) \mathcal{D}\phi T r_{c, c^\dagger} e^{-\beta H_{eff}}$$

As  $T \rightarrow 0$ , it is obvious that  $Z$  will be dominated by the saddle point configuration, *i.e.*,  $\Delta_i, \phi_i$ , that minimise  $H_{eff}$ , giving the same self consistency conditions as HFBdG. On the other hand, at finite temperature, the problem will involve solving for the fermionic problem in a fluctuating  $\{\Delta, \phi\}$  background in contrast to HFBdG, which would involve solving the problem in a situation where electrons would see only the *average* background at any temperature.

At finite temperature, the Boltzmann weight of a given configuration  $\{\Delta, \phi\}$  is given by

$$P\{\Delta_i, \phi_i\} \propto T r_{c, c^\dagger} e^{-\beta H_{eff}} \quad (2.11)$$

This is related to the electron free energy in a particular  $\{\Delta_i, \phi_i\}$  background, given by

$$e^{-\beta F} \sim P\{\Delta_i, \phi_i\}$$

For an arbitrary configuration of the auxiliary fields, the trace cannot be analytically calculated. However, since the trace contains quadratic fermionic terms, it can be evaluated numerically by diagonalizing  $H_{eff}$  for a given  $\{\Delta_i, \phi_i\}$  background. Hence, with the effective classical free energy  $F$ , one can use classical Monte Carlo methods to simulate the system at a finite temperature.

### General formulation with magnetic impurities

The effective Hamiltonian  $H_{eff}$  can be diagonalized for a given configuration  $\{\Delta_i, \phi_i\}$ , via the following transformation:

$$\begin{aligned}
c_{i\uparrow} &= \sum_n \left( u_{n\uparrow}^i \gamma_n - v_{n\uparrow}^{*i} \gamma_n^\dagger \right) \\
c_{i\downarrow} &= \sum_n \left( u_{n\downarrow}^i \gamma_n - v_{n\downarrow}^{*i} \gamma_n^\dagger \right)
\end{aligned} \tag{2.12}$$

Here,  $n$  is a complete set of states,  $u_n$  and  $v_n$  are related to the eigenfunctions of  $H_{eff}$ , and the new fermionic operators  $\gamma_n$  are the quasiparticle operators. These are chosen such that in terms of new operators,

$$H_{eff} = E_0 + \sum_n \epsilon_n \gamma_n^\dagger \gamma_n$$

Hence, we have,

$$\begin{aligned}
[H_{eff}, \gamma_n] &= -\epsilon_n \gamma_n \\
[H_{eff}, \gamma_n^\dagger] &= \epsilon_n \gamma_n^\dagger
\end{aligned} \tag{2.13}$$

Using these, one can solve for the coefficients  $u_{n\sigma}^i$  and  $v_{n\sigma}^i$  by solving a matrix eigenvalue equation. Define the matrix  $A$  as:

$$A = \begin{pmatrix}
\hat{K} - JS \hat{\cos}(\theta) & \hat{\Delta} & -JS \sin(\hat{\theta}) e^{-i\phi} & \hat{0} \\
\hat{\Delta}^* & -\hat{K} - JS \hat{\cos}(\theta) & \hat{0} & -JS \sin(\hat{\theta}) e^{-i\phi} \\
-JS \sin(\hat{\theta}) e^{i\phi} & \hat{0} & \hat{K} + JS \hat{\cos}(\theta) & \hat{\Delta} \\
\hat{0} & -JS \sin(\hat{\theta}) e^{i\phi} & \hat{\Delta}^* & -\hat{K} + JS \hat{\cos}(\theta)
\end{pmatrix}$$

Here,  $\hat{K}$  denotes the kinetic energy matrix, with  $\hat{K}_{ij} = (V_i - (U/2)\phi_i - \mu)\delta_{ij} - (t)\delta_{i+n,j}$ , where the term  $\delta_{i+n,j}$  is non zero only when  $\langle ij \rangle$  are nearest neighbours,  $\hat{\Delta}_{ij} = \delta_{ij}\Delta_i$  and  $\hat{\Delta}$  is its hermitian conjugate,  $JS \hat{\cos}(\theta)_{ij} = \delta_{ij}\delta_{i\nu} JS_\nu \cos(\theta_\nu)$  etc, where  $\theta_\nu$  and  $\phi_\nu$  are the polar and azimuthal angles of the spin vector  $\vec{S}_\nu$ .

We further define the column vector  $\Psi$  as

$$\Psi = \begin{pmatrix}
\{u_{n\uparrow}\} \\
\{v_{n\downarrow}\} \\
\{u_{n\downarrow}\} \\
\{v_{n\uparrow}\}
\end{pmatrix}$$

Then, the eigenvalue equation is given by

$$A\Psi = \epsilon_n\Psi \quad (2.14)$$

If we start with a lattice of dimensions  $L \times L$ , then the dimension of each of the  $4 \times 4$  blocks in  $A$  is  $N \times N$ , where  $N = L^2$ . Hence, the total dimension of the matrix is  $4N \times 4N$ , and the integer  $n$  runs from 1 to  $4N$ . Physically this quadrupling of the degrees of freedom is caused by considering two different spin degrees of freedom and both electronic and its corresponding hole degrees of freedom, originating from the structure of the transformation which contains both electronic  $\gamma_n^\dagger$  and hole  $\gamma_n$  creation operators.

If there are no magnetic impurities, the matrix structure can be simplified considerably. This is relevant to the study of superconductors with potential disorder. Since our primary topic of interest in this thesis is investigating the effect of such disorder, we shall henceforth use this simplified scheme to describe our method further. The full calculations with the spins will be taken up in a later chapter, where we describe our work on magnetic impurities.

### Formulation with potential scattering

When there are no magnetic impurities, the Hamiltonian acquires a block structure, where the upper half and the lower half become decoupled. Thus, the matrix elements mix  $\{u_{n\uparrow}\}$  only with  $\{v_{n\downarrow}\}$  and  $\{v_{n\uparrow}\}$  only with  $\{u_{n\downarrow}\}$ .

This enables us to consider only the upper or lower blocks of the matrix, and brings down the degrees of freedom to  $2N$ . Considering, say, the upper block only, one can remove the spin indices from  $\{u_{n\uparrow}\}$  and  $\{v_{n\downarrow}\}$ , calling them simply  $\{u_n\}$  and  $\{v_n\}$ . The quasiparticle operators  $\gamma_n$  with  $n$  running from 1 to  $4N$  can now be reclassified as  $\gamma_{n\uparrow}$  and  $\gamma_{n\downarrow}$  respectively, with  $n$  now running from 1 to  $2N$ . This notation emphasizes the fact that in the absence of impurity magnetic moments changing the spin quantization axes, the character of the spins remains the same. Thus, in this new notation, the transformations can be rewritten as

$$\begin{aligned} c_{i\uparrow} &= \sum_n \left( u_n^i \gamma_{n\uparrow} - v_n^{*i} \gamma_{n\downarrow}^\dagger \right) \\ c_{i\downarrow} &= \sum_n \left( u_n^i \gamma_{n\downarrow} - v_n^{*i} \gamma_{n\uparrow}^\dagger \right) \end{aligned} \quad (2.15)$$

and  $A$  and  $\Psi$  can be redefined as

$$A = \begin{pmatrix} \hat{K} & \hat{\Delta} \\ \hat{\Delta} & -\hat{K} \end{pmatrix} \text{ and } \Psi = \begin{pmatrix} \{u_n\} \\ \{v_n\} \end{pmatrix}$$

From the structure of the matrix, one can see that if  $\epsilon_n > 0$  is an eigenvalue with eigenvector  $(u_n v_n)^T$ , then  $(-\epsilon_n)$  is an eigenvalue with vector  $(-v_n^* u_n^*)^T$ . Hence, the spectrum is symmetric about  $\epsilon = 0$ , and one can effectively use only the positive set of eigenvalues to calculate all averages and expectation values.

To calculate the expression for  $F(\{\Delta_i, \phi_i\})$ , we note that after the diagonalization, the Hamiltonian can be written as

$$H_{eff} = E_0 + \sum_{n\sigma, \epsilon_n > 0} \epsilon_n \gamma_{n\sigma}^\dagger \gamma_{n\sigma}$$

To calculate the energy  $E_0$ , we note that for the ground state  $\Psi_G$ , we have

$$\langle \Psi_G | H_{eff} | \Psi_G \rangle = E_0$$

Rewriting the terms in  $H_{eff}$  in terms of the operators  $\gamma_n$  and  $\gamma_n^\dagger$ , and applying the relations  $\langle \Psi_G | \gamma_n \gamma_n^\dagger | \Psi_G \rangle = 1$ , we get, for  $E_0$ :

$$E_0 = - \sum_{in, \epsilon_n > 0} 2\epsilon_n |v_n^i|^2$$

The second part of  $H_{eff}$  is simply a collection of free fermions and its trace can be easily calculated from elementary statistical mechanics. Thus, the free energy is given by

$$F(\{\Delta_i, \phi_i\}) = - \sum_{in, \epsilon_n > 0} 2\epsilon_n |v_n^i|^2 - (2/\beta) \sum_{n, \epsilon_n > 0} \ln(1 + \exp(-\beta\epsilon_n)) \quad (2.16)$$

### 2.3.4 Monte Carlo protocol

To simulate the thermal behaviour of the system, we use classical Monte Carlo methods. The thermal weight of a particular configuration is given by  $P(\{\Delta_i, \phi_i\}) \sim e^{-\beta F}$ . We use a Metropolis based update mechanism, where, starting with an arbitrary random configuration of the auxiliary fields at high temperature, we update their values at a given site ‘i’ randomly. We calculate the difference of free energies  $F_{final} - F_{initial}$  between the two configurations. The ratio of the thermal weights of the two configurations is given by  $r \sim e^{-\beta(F_{final} - F_{initial})}$ , and we would like the thermal statistics to obey this ratio. To accomplish that, we define a random number  $x$  and accept or reject

the update depending on whether  $x < / > r$ .

This update protocol, after being carried out on all sites of the lattice, provides one thermal configuration  $\{\Delta_i, \phi_i\}$ . This step is repeated for a large number of times at a given temperature, generating different thermal configurations of the auxiliary fields at that temperature. The same process is then repeated at the next, lower temperature, and so on, gradually letting the system anneal through to a suitably low temperature at the end. Typically, half of the total number of configurations at each temperature are disregarded to let the system equilibrate, and the rest are used to calculate various thermally averaged quantities of interest.

The costliest part of this simulation process is the diagonalization of the matrix to calculate the free energy  $F$ . For a given matrix  $N \times N$ , the computational cost to diagonalize it is  $\sim \mathcal{O}(N^3)$  per update, or  $\mathcal{O}(N^4)$  per lattice sweep. This limits the accessible lattice sizes to  $10 \times 10$ . To access larger lattice sizes in a reasonable amount of time, we use lattice based update methods [145], where, instead of the full lattice, we only diagonalize a lattice of size  $L_c \times L_c$  centred around the update site ‘i’. This reduces the cost per update to  $\sim \mathcal{O}(N_c^3)$  instead, where  $N_c = L_c^2$ , and the cost per sweep to  $\sim N \times \mathcal{O}(N_c^3)$ , which scales linearly with the lattice size  $N$ . This allows us to access larger lattice sizes  $\sim 30 \times 30$ , and hence coupling values as low as  $U/t = 2$ , that exact methods like QMC cannot.

In the next subsection, we describe in detail how we calculate thermally averaged values of observables from the configurations  $\{\Delta_i, \phi_i\}$  that our Monte Carlo simulation provides at each temperature.

### 2.3.5 Calculating thermal averages

The quantities of interest that can be calculated from such a simulation can be classified into two types, namely, quantities that depend on the auxiliary fields only, such as thermal averages of various combinations of fields  $\Delta$  and  $\phi$ , and quantities that depend on combinations of electronic operators  $c_{i\sigma}$  or  $c_{i\sigma}^\dagger$ . Calculating quantities of the first type is trivial, but for the second type, one is required to calculate a double average, first over the quantum degrees of freedom, and then, over the different classical thermal configurations.

At a given temperature, the expectation value of any electronic operator  $f(c_i, c_i^\dagger)$  is given symbolically by  $\langle f(c_i, c_i^\dagger) \rangle = \mathcal{Z}^{-1} \int \mathcal{D}(\bar{\Delta}, \Delta) \mathcal{D}\phi \text{Tr}_{c, c^\dagger} f(c_i, c_i^\dagger) e^{-\beta H_{eff}}$ . To compute this, we proceed as follows. For each configuration  $\{\Delta_i, \phi_i\}$ , the first step is to express the fermionic operators in terms of the quasiparticle operators  $(\gamma_{n\sigma}, \gamma_{n\sigma}^\dagger)$ , with the eigenvectors  $(u_n^i, v_n^i)$  as coefficients. The electronic trace over the resultant expressions in terms of the quasiparticle operators can then be evaluated from the statistical mechanics of free fermions. This result is then averaged over equilibrium configurations  $\{\Delta_i, \phi_i\}$  to give the final, thermally averaged result. For disordered systems,

we average this further over a number of disorder realizations (typically 10, but this will be described in detail in the relevant chapters) for global indicators, but typically choose a particular realization to investigate the specific local properties. The next subsection describes the relevant calculations in more detail.

### 2.3.6 Computing observables

The following are the quantities of interest that provide information on the properties of the system:

- Structure factor  $S(q)$  and correlation functions of the form  $\langle \Delta_i \Delta_j \rangle$ , which provide information about the local and global superconducting correlations in the system.
- Conductivity  $\sigma(T)$ , or in general, the optical conductivity  $\sigma(\omega, T)$ , providing information about the transport properties of the system, especially the effect of disorder.
- Spectral functions such as the global density of states  $N(\omega)$ , or the ‘site-resolved’/‘k-resolved’ spectral function  $N_i(\omega)/A_k(\omega)$ , which reveals the nature of the single particle excitations and provides information about the underlying state.

#### Structure factor

In the superconducting state, one expects that the pairs will be coherent throughout the system. This long range order implies that the correlation function  $M_{ij} = \langle (c_{i\downarrow} c_{i\uparrow})(c_{j\uparrow}^\dagger c_{j\downarrow}^\dagger) \rangle$  will be non-zero even at large distances  $|i - j|$ . Since the  $\Delta_i$  fields ‘mimic’ the behaviour of the electron operator ( $c_{i\downarrow} c_{i\uparrow}$ ) on the average, one can expect the corresponding  $\Delta - \Delta$  correlation function  $\langle \Delta_i \Delta_j \rangle$  to behave in a similar manner.

Using an analogy with spin systems, this implies that the  $\Delta$  values get aligned in the same direction, just like spins below a ferromagnetic transition. This will be indicated by the long range correlation function as  $q \rightarrow 0$ . To this end, we define the structure factor  $S(q) = (1/N^2) \sum_{ij} \langle \Delta_i \Delta_j^* \rangle e^{i\mathbf{q} \cdot (\mathbf{r}_i - \mathbf{r}_j)}$ . When  $S(q \rightarrow 0) \sim \mathcal{O}(1)$ , it implies that the pairing field has a non-zero spatial average and would in turn induce long range order (power law correlation in 2D) in the  $M_{ij}$ . Thus  $S(q = 0)$  provides information on the long range superconducting order. In our calculations, we plot  $S(q = 0, T)$  vs  $T$ , after duly averaging over different disorder realizations in the disordered problem, and determine the  $T_c$  from the rise of the curve.

On the other hand, the short range spatial correlation function  $\langle \Delta_i \Delta_j \rangle$  provides information about the short range superconducting correlation between the sites ‘i’ and ‘j’. This will be important in disordered systems, where superconducting regions break up into small clusters. Since these probe specific local properties depending on one particular realization, these will be calculated on specific disorder realizations.

## Spectral functions

The spectral functions are defined in general as the imaginary parts of corresponding correlation functions [74, 146]. This relation can be symbolically written as  $N \sim -(1/\pi)Im(G)$ , where  $G$  denotes the retarded single particle Green's function. The most fundamental Green's function is given by  $G_{ij}^\sigma(t - t')$ . The general definition of this is given by

$$G_{ij}^\sigma(t - t') = -i\Theta(t - t')\langle [c_{i\sigma}(t)c_{j\sigma}^\dagger(t') + c_{j\sigma}^\dagger(t')c_{i\sigma}(t)] \rangle$$

Here, the angular brackets indicate taking the thermodynamic average. Now, as shown in Ref. [146], by inserting complete sets of eigenstates  $|n\rangle, |m\rangle$  of the total interacting problem, one gets, for the time Fourier transformed function  $G_{ij}^\sigma(\omega)$ :

$$G_{ij}^\sigma(\omega) = \frac{1}{\mathcal{Z}} \sum_{n,m} \langle n|c_{i\sigma}|m\rangle \langle m|c_{j\sigma}^\dagger|n\rangle \frac{e^{-\beta E_n} + e^{-\beta E_m}}{\omega + E_n - E_m + i\delta}$$

Now, by utilizing the BdG equations Eq. 2.15, one can express this in terms of the eigenoperators of the problem,  $\gamma_{n\sigma}^\dagger$ . The exact multiparticle states are then just Slater determinants of these quasiparticle eigenstates, and one can reformulate the problem in terms of single particle levels  $n$ . Further, since this system is spin-symmetric,  $G_{ij}^\uparrow(\omega) = G_{ij}^\downarrow(\omega) = G_{ij}(\omega)$ , and one can extract the local density of states,  $N_i(\omega)$  from the imaginary part of  $G_{ii}(\omega)$ :

$$N_i(\omega) = \sum_n (|u_n^i|^2 \delta(\omega - \epsilon_n) + |v_n^i|^2 \delta(\omega + \epsilon_n)) \quad (2.17)$$

Similarly, from the Fourier transform  $G(\mathbf{k}, \omega)$ , one can extract the  $\mathbf{k}$ -resolved spectral fuction  $A_k(\omega)$ :

$$A(k, \omega) = \sum_n (|u_n^k|^2 \delta(\omega - \epsilon_n) + |v_n^{-k}|^2 \delta(\omega + \epsilon_n)) \quad (2.18)$$

Here,  $u_n^k$  and  $v_n^k$  are Fourier transforms of  $u_n^i$  and  $v_n^i$  respectively.

The total density of states is given by the sum

$$\sum_i N_i(\omega) = \sum_{in} (|u_n^i|^2 \delta(\omega - \epsilon_n) + |v_n^i|^2 \delta(\omega + \epsilon_n)) \quad (2.19)$$

Due to the finite size of our lattices, the eigenstates  $\epsilon_n$  are not dense, and have finite intervals

between them. Hence, we must resort to some approximations while incorporating the effect of the delta functions. Thus, we approximate the delta function by a box of some suitable size  $a$  spanning the energy values  $(\omega - a/2, \omega + a/2)$ , then add the contributions of all energy states  $\epsilon_n$  that lie in this interval to the value of  $N(\omega)$ , and finally divide by the interval width  $a$  to get  $N(\omega)$  per unit interval. As usual, we first calculate this for a particular configuration  $\{\Delta_i, \phi_i\}$ , and average over the auxiliary field configurations to get the final thermally averaged result at a given temperature. The final results are averaged over many disorder realizations for the global density of states, but for the local density of states, we investigate specific realizations of disorder.

### Optical conductivity $\sigma(\omega)$

The optical conductivity of a system is related to the linear response of the system to an externally applied electric field  $\vec{E}$ . The electric field induces a current density in the system given by  $\vec{J}$ , and the conductivity  $\sigma_{xx}(q, \omega)$  is defined as:

$$j_x(q, \omega) = \sigma_{xx}(q, \omega)E_x(q, \omega)$$

The long range transport properties of the system are given by  $\sigma_{xx}(q = 0, \omega)$ . Henceforth, we will simply call this  $\sigma(q, \omega)$ , which should always be taken to mean  $\sigma_{xx}(q = 0, \omega)$ . Using linear response theory, one can relate this to the current-current correlation function  $\Lambda_{xx}(q, \omega)$ , which gives [147]

$$\sigma(q = 0, \omega) = -\frac{\langle -k_x \rangle - \Lambda_{xx}(q = 0, \omega)}{i(\omega + i\delta)} \quad (2.20)$$

Here,  $\langle -k_x \rangle$  is the kinetic energy of the system in the x-direction, and  $\Lambda_{xx}(q = 0, \omega)$  is the fourier-frequency transform of a current current correlation function  $\sim \langle j_x(x_1, t_1)j_x(x_2, t_2) \rangle$ . The current operator  $j_x$  is given by

$$j_x = (-it) \sum_i (c_{i+x\sigma}^\dagger c_{i\sigma} - h.c.)$$

From Eq. 2.20, we see that the real part of  $\sigma(q = 0, \omega)$  consists of a singular part  $\sigma_s(q = 0, \omega)$  and a regular part  $\sigma_{reg}(q = 0, \omega)$  given by

$$\begin{aligned}
\sigma_s(q=0, \omega) &= D\delta(\omega), \text{ where, } D/\pi = \langle -k_x \rangle - \Lambda_{xx}(q=0, \omega), \text{ and} \\
\sigma_{reg}(q=0, \omega) &= \frac{\text{Im}(\Lambda_{xx}(q=0, \omega))}{\omega}
\end{aligned} \tag{2.21}$$

The superconducting state is characterized by a non-zero superfluid stiffness  $D_s$  which is given by

$$D_s/\pi = \Lambda_{xx}(q_x = 0, q_y \rightarrow 0, \omega = 0)$$

For gapped systems, one can generally show that  $D = D_s$  [147], and hence the non-zero superfluid stiffness shows up as the weight of the delta function in  $\sigma_s(q=0, \omega)$ . Since we determine the superconducting correlations in our systems from the structure factor  $S(q=0)$ , we neglect this part of  $\sigma(q=0, \omega)$  and concentrate on the regular part  $\sigma_{reg}(q=0, \omega)$ .

To proceed, we note that for any general bosonic operator  $\bar{B}(t)$ , the corresponding retarded correlation function  $\bar{B}_{ret}(\omega)$  is given by [146]:

$$\bar{B}_{ret}(\omega) = \frac{1}{\mathcal{Z}} \sum_{n,m} \langle n|B|m\rangle \langle m|B^\dagger|n\rangle \frac{e^{-\beta E_n} - e^{-\beta E_m}}{\omega + E_n - E_m + i\delta}$$

Utilizing this general expression, we can write the current-current correlation function  $\Lambda_{xx}(q=0, \omega)$  as

$$\Lambda_{xx}(q=0, \omega) = \frac{1}{\mathcal{Z}} \sum_{n,m} |\langle n|j_{xx}|m\rangle|^2 \frac{e^{-\beta E_n} - e^{-\beta E_m}}{\omega + E_n - E_m + i\delta}$$

where  $j_x = (-it) \sum_i (c_{i+x\sigma}^\dagger c_{i\sigma} - h.c.)$  is the current operator in the x direction,  $n$  and  $m$  represent exact multiparticle states of the system.

Now, similar to the spectral function case, we write these in terms of the eigenoperators  $\gamma_{n\sigma}$  and  $\gamma_{n\sigma}^\dagger$  and reformulate the problem in terms of single particle eigenstates. This gives

$$\begin{aligned}
\sigma_{reg}(\omega) &= \sum_{a,b} \left| \sum_i f_1(i, a, b) \right|^2 \frac{(n(e_a) + n(e_b) - 1)}{e_a + e_b} \delta(\omega - e_a - e_b) \\
&\quad + \sum_{a,b} \left| \sum_i f_2(i, a, b) \right|^2 \frac{(n(e_a) - n(e_b))}{e_a - e_b} \delta(\omega - e_b + e_a) \\
&\quad + \sum_{a,b} \left| \sum_i f_3(i, a, b) \right|^2 \frac{(n(e_a) - n(e_b))}{e_a - e_b} \delta(\omega - e_a + e_b) \tag{2.22}
\end{aligned}$$

Here,  $a, b$  label single particle eigenstates of the system such that  $\epsilon_a, \epsilon_b > 0$ , and  $f_1(i, a, b)$ ,  $f_2(i, a, b)$  and  $f_3(i, a, b)$  are given by

$$\begin{aligned}
f_1(i, a, b) &= (v_a^{i+x} u_b^i - v_a^i u_b^{i+x} + v_b^{i+x} u_a^i - v_b^i u_a^{i+x}) \\
f_2(i, a, b) &= (u_a^{*i+x} u_b^i - u_a^{*i} u_b^{i+x} - v_b^{i+x} v_a^{*i} + v_b^i v_a^{*i+x}) \\
f_3(i, a, b) &= (v_a^{i+x} v_b^{*i} - v_a^i v_b^{*i+x} - u_b^{*i+x} u_a^1 + u_b^{*i} u_a^{i+x})
\end{aligned}$$

Interchanging  $a$  and  $b$  in the second term in Eq. 2.22, and defining  $F_1(a, b) = |\sum_i f_1(i, a, b)|^2$  and  $F_2(a, b) = +|\sum_i f_2(i, a, b)|^2 + |\sum_i f_3(i, b, a)|^2$ , we get

$$\begin{aligned}
\sigma_{reg}(\omega) &= \sum_{a,b} F_1(a, b) \frac{(n(\epsilon_a) + n(\epsilon_b) - 1)}{\epsilon_a + \epsilon_b} \delta(\omega - \epsilon_a - \epsilon_b) \\
&\quad + \sum_{a,b} F_2(a, b) \frac{(n(\epsilon_a) - n(\epsilon_b))}{\epsilon_a - \epsilon_b} \delta(\omega - \epsilon_b + \epsilon_a) \tag{2.23}
\end{aligned}$$

The resistivity of the system is given by  $\rho(T) = \sigma(q = 0, \omega \rightarrow 0)^{-1}$ . To calculate the conductivity, we again approximate the delta functions by box functions as explained earlier. In particular, the  $\omega \rightarrow 0$  limit is taken by calculating the conductivity in an interval  $(0, \omega_a)$  and taking the average over that interval. The choice of these intervals and widths will be explained in more detail in the respective chapters.

### 2.3.7 Approximations, benchmarking

In this subsection, we briefly summarize the approximations used in our method and their primary consequences, and the observables and quantities that we use for benchmarking our results with respect to the system parameters that we have used, including system size, number density and

coupling strength. Detailed discussions, including specific data, are left to the relevant chapters.

## Consequences of approximations

The primary approximations that are employed in our model are:

### 1. **Static approximation in the auxiliary fields $\Delta$ :**

As seen before, these fields are time dependent in the most general case, but we approximate them as classical fields. In the context of disordered superconductors, the time dependence can be significant in the following regimes:

- (a) The vicinity of the  $T = 0$  SIT, where the dynamics of the bosonic fields provide low energy modes that can affect the transport and low frequency optics significantly.
- (b) Critical regime, close to  $T_c$ , where the Aslamazov-Larkin fluctuation corrections to the transport, which involve the dynamics of the fields, can be important. These are discussed in greater detail in Chapter 4, where we consider the transport and global spectral features of the disordered system.

### 2. **The neglect of Coulomb interactions:**

As discussed earlier, this does not seem to be the driving force behind the disorder driven SIT seen in many recently investigated materials. Nevertheless, Coulomb interaction can affect the system in the following manner:

- (a) Increase in phase fluctuations due to the long range nature of the Coulomb interactions, which will result in effects that are phenomenologically similar to the ones we have studied
- (b) Characteristic wide dip in the density of states, that are seen in experiments, but are absent from our results. More comprehensive discussions are found in Chapters 4 and 5.

### 3. **Presence of both auxiliary fields:** As mentioned earlier, the presence of both fields $\Delta$ and $\phi$ with coefficient of unity results in an overcounting. These extra fluctuations may have significant effects at large temperatures. However, in the parameter regimes that we have considered, they only result in a slight depression of $T_c$ , while other parameters such as transport and density of states are not changed significantly. A detailed discussion appears in Chapter 3, where we examine these in the context of the BCS-BEC crossover.

#### 4. System size:

The bulk of our results are at a system size of  $24 \times 24$ . This implies that we cannot access coupling values  $U \lesssim t$ , since the coherence length becomes comparable to system size. The effect of magnetic impurities is studied on lattices of size  $16 \times 16$ .

#### 5. Cluster approximation:

The cluster approximation implies that our method is not able to capture long range modulated phases. While this is not relevant in the systems we have investigated, it could be relevant for systems with population imbalance, as well as magnetic superconductors.

### Benchmarking

Our results are benchmarked to ensure that they are reliable in the parameter regimes we have used, including coupling, number density and system size. Most of our results are on lattices  $\sim 24 \times 24$  with coupling values ranging from  $U/t = 2$  to 10 and a number density of 0.9. To ensure their robustness, we compare our results at various system sizes, various averaging intervals to ensure that finite size effects are negligible and with results from single channel calculations to ensure that overcounting effects are negligible in our parameter regime. This ensures the internal consistency of our results. This is followed by comparisons, wherever possible, with established results from QMC and other methods, to verify that the correct physics is captured by our method. Leaving detailed discussion of the parameter regimes and numerical data and their comparison to other methods to the relevant chapters, we briefly describe the quantities that we examine to benchmark our results. These are

1. The structure factor  $S(q = 0)$ , from which we extract  $T_c$ , which we compare at various lattice sizes from  $8 \times 8$  upto  $32 \times 32$ , for coupling values ranging from  $U/t = 2$  to 10. Detailed discussion and results are shown in Chapter 3.
2. Resistivity, at  $U/t = 2$  for various lattice sizes, and various averaging intervals that we have used to mimic the delta functions, as well as the frequency interval  $\omega_a$  for calculating  $\sigma(q = 0, \omega \rightarrow 0)$ . We elaborate on this, with detailed results, in Chapter 4.
3. Density of states, especially the behaviour at low frequencies, which we compare for the single field and two fields cases respectively, in Chapter 3, to ensure that overcounting effects are negligible in the regime under consideration.

These benchmarks establish the essential correctness of our calculations, and hence lend credence to our results that go beyond those captured by other methods.

This concludes the experimental and theoretical summary of the literature, and the description of our model and methods. The following chapters will describe the results of our work on thermal fluctuations in superconductors in detail. We begin with an examination of the BCS-BEC crossover in the context of our model in Chapter.3, which helps us to benchmark our model thoroughly. We then shift our focus to disordered superconductors, the main topic of our thesis, in Chapters 4 and 5. Finally, we provide our results on magnetic impurities in superconductors in Chapter 6.



## THE BCS-BEC CROSSOVER

In this chapter we will describe our results on the BCS-BEC crossover in attractive fermion systems. Since this has been a topic of continued interest, our results and their comparisons with the various other theoretical and numerical methods will help in establishing the key strengths and limitations of our method. After benchmarking our method here, we will move on to consider the more complex case of disordered superconductors, where fewer methods are available, in the subsequent chapters.

The BCS to BEC crossover, describing the change in the properties of a Fermi system with increasing attractive interaction between the fermions, has been a topic of active research for the last few decades. With increasing interaction, the ground state of a weak coupling ‘BCS superconductor’ [2], with pair size  $\xi$  much larger than the interparticle separation  $k_F^{-1}$ , evolves smoothly [4, 89, 107, 148–150] into a ‘Bose-Einstein condensate’ (BEC) of preformed fermion pairs with  $\xi \lesssim k_F^{-1}$ .  $k_F$ , above, is the Fermi wavevector. The ‘high temperature’ normal state changes from a conventional Fermi liquid at weak coupling to a gapped phase at strong coupling. While the zero temperature pairing gap increases with coupling strength, the superconducting  $T_c$  in lattice systems reaches a maximum at intermediate coupling and falls thereafter. A striking consequence of the separation of pairing and superconducting scales is the emergence of a (pseudo)gapped normal phase, with preformed fermion pairs but no superconductivity due to strong phase fluctuations.

The early work of Leggett [89] and Nozieres and Schmitt-Rink [107] provided the intuitive basis for understanding this problem. It has since been followed up by powerful semi-analytic schemes [108, 151–155], extensive quantum Monte Carlo (QMC) work [156–165], and most recently dynamical mean field theory (DMFT) [166–171]. The efforts have established the non-monotonic  $T_c$ , and the presence of a pseudogap in the single particle spectrum beyond moderate coupling and temperature  $T > T_c$ .

While the success of multiple methods in capturing the crossover is remarkable, most of them depend on translation invariance in the underlying problem. They do not naturally generalise to

problems that involve the presence of disorder, or a confining potential, or the emergence of spontaneous modulation. These situations, for example, occur in the context of the disorder driven superconductor-insulator transition [5], trapped fermions in an optical lattice [96, 98], and Fulde-Ferrell-Larkin-Ovchinnikov (FFLO) states [173] in population imbalanced systems. Such problems, in general, require a real space approach. Our method provides such an implementation.

Our main results are the following:

1. We demonstrate the ability of our approach to quantitatively capture the  $T_c$  scale across the BCS-BEC crossover, confirming its usefulness at all interaction strengths.
2. We quantify the crossover from an amplitude fluctuation dominated regime to a phase fluctuation dominated regime, through the ‘high  $T_c$ ’ intermediate coupling window where both are important.
3. We present the thermal evolution of the single particle density of states with interaction and temperature, and, more importantly, the momentum resolved spectral function  $A(\mathbf{k}, \omega)$ . We compare our results to QMC data wherever available.

This chapter is organised as follows. In Sec.II we quickly compare the existing analytic and numerical methods used to study the BCS-BEC crossover in lattice models. Sec.III presents our model and describes the method used in detail. Sec.IV shows our results on thermodynamic indicators, the nature of fluctuations, density of states, and  $A(\mathbf{k}, \omega)$ . Sec.V discusses the limitations of our method and the scope for further work.

### 3.1 Earlier work

Since the BCS-BEC crossover is a prototype of weak to strong coupling evolution, several methods, of increasing sophistication, have been brought to bear on it. These include mean field theory (MFT) [89], MFT corrected by gaussian fluctuations [107], the self consistent T-matrix approach (SC-TMA) [151, 152], a two particle self consistent (2PSC) scheme [153], the mapping to XY models [154, 155], quantum Monte Carlo (QMC) [156–165], and recently dynamical mean field theory (DMFT) [166–171].

Detailed descriptions of these methods are available in the original literature so we just provide a table that compares the strengths and limitations of these methods in the light of a few crucial indicators such as (i) thermodynamics: the estimate of  $T_c(U)$ , (ii) single particle spectra, (iii) two particle properties, *e.g.* conductivity, and (iv) handling inhomogeneity, *e.g.* disorder or trapping.

Method	$T_c(U)$	Spectra at large $U/t$	Transport at large $U/t$	Handling inhomogeneity
MFT	Correct only when $U/t \lesssim 1$ .	No gap/pseudogap in the normal state.	No access to transport.	Real space MFT is reasonable at $T = 0$ , can access size $\sim 40 \times 40$ .
MFT+fluctuations	Leads to unphysical negative compressibility at large $U$ [108]	PG above mean field $T_c$ , incapable of capturing BKT physics in 2D. [149]	No results	Not systematically explored.
SC-TMA	Accurate upto intermediate coupling; captures non monotonic behaviour correctly to $U/t \sim 8$ . [151].	Shows a PG, but quantitatively inaccurate due to neglect of vertex corrections [149].	No results	Not generalised.
2PSC	Approach fails close to the BKT transition temperature and at strong coupling [153].	Accurate upto intermediate coupling [153].	No results	Not generalised.
XY models	Captures non monotonic $T_c(U)$ but not quantitatively accurate [154, 155].	PG inferred from different pairing and $T_c$ scales.	Not explored.	Disordered XY model needs to be derived from the Hubbard model.
QMC	Accurate, sets the benchmark [157, 165].	Accurate in principle but involves uncertainties due to analytic continuation from imaginary frequency [158, 162].	Contains the relevant physics but dynamical properties are difficult to extract due to analytic continuation.	Handles inhomogeneity [88] but sizes limited to $\sim 12 \times 12$ . Associated $U/t \gtrsim 4$ .
DMFT	Captures non monotonic $T_c(U)$ but quantitatively inaccurate when used in the 2D context [166].	Accurate [170].	Transport misses bosonic contribution.	Requires <i>ad hoc</i> real space generalisation.
SAF	Accurate, matches quantitatively with QMC.	Accurate, compares reasonably with QMC.	Transport misses bosonic contribution.	Handles inhomogeneity, $\mathcal{O}(N)$ method, readily accesses [174] size $\sim 30 \times 30$ .

Table 3.1: Comparison of available methods with our static auxiliary field approach for the two dimensional attractive Hubbard model. The expanded title for each method is given in the text.

## 3.2 Model and method

We briefly recap the model and methods that we use. We study the attractive two dimensional Hubbard model (A2DHM),

$$H = \sum_{ij,\sigma} (-t - \mu\delta_{ij}) c_{i\sigma}^\dagger c_{j\sigma} - |U| \sum_i n_{i\uparrow} n_{i\downarrow}$$

Here,  $t$  denotes the nearest neighbour tunneling amplitude on a square lattice.  $\mu$  is the chemical potential which fixes the average number density  $n$ . We set  $t = 1$  and measure all other energies in terms of it.  $U > 0$  is the strength of onsite Hubbard attraction. We will focus on the density  $n \sim 0.9$  which is close to half-filling but avoids the density wave features of  $n = 1$ .

The model is known to have a superconducting ground state for all  $n \neq 1$ , while at  $n = 1$  there is the coexistence of superconducting and density wave (DW) correlations in the ground state. For  $n \neq 1$  the ground state evolves from a BCS state at  $U/t \ll 1$  to a BEC of ‘molecular pairs’ at  $U/t \gg 1$ . The pairing amplitude and gap at  $T = 0$  can be reasonably accessed within mean field theory or a simple variational wavefunction.

Mean field theory, however, assumes that the electrons are subject to a *spatially uniform* self-consistent pairing amplitude  $\langle\langle c_{i\uparrow}^\dagger c_{i\downarrow}^\dagger \rangle\rangle$ . At small  $U/t$  this vanishes when  $k_B T \sim t e^{-t/U}$ , but at large  $U/t$  it vanishes only when  $k_B T \sim U$ . The actual  $T_c$  at large  $U$  is controlled by phase correlation of the local order parameter, rather than finite pairing amplitude, and occurs at  $k_B T_c \sim f(n)t^2/U$ , where  $f(n)$  is a function of the density. The wide temperature window, between the ‘pair formation’ scale  $k_B T_f \sim U$  and  $k_B T_c$  corresponds to equilibrium between unpaired fermions and hardcore bosons (paired fermions).

Our auxiliary field scheme applies a Hubbard-Stratonovich transformation in both the ‘pairing’ and the ‘density’ channels, as explained earlier. After the subsequent neglect of quantum fluctuations, we have

$$H_{eff} = H_{kin} + \sum_i (\Delta_i c_{i\uparrow}^\dagger c_{i\downarrow}^\dagger + h.c.) - \sum_i \phi_i n_i + \sum_i \frac{|\Delta_i|^2}{U} + \sum_i \frac{\phi_i^2}{U}$$

The mean field HFBdG equations are saddle points of this model w.r.t. the auxiliary fields.

$$\Delta_i = U \langle c_{i\uparrow} c_{i\downarrow} \rangle, \quad \phi_i = \frac{U}{2} \langle n_i \rangle$$

We will describe the indicators separately in detail in their respective sections.

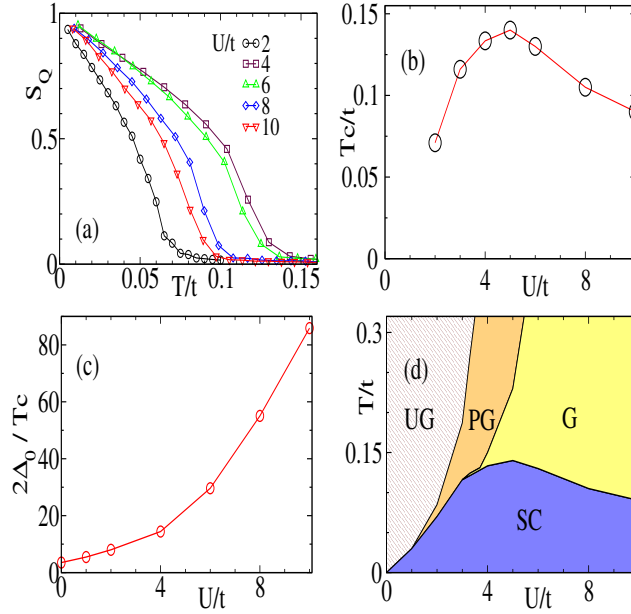


Figure 3.1: (a). Temperature dependence of the  $\mathbf{q} = \{0, 0\}$  component of the pairing field correlation for different  $U/t$ . The onset locates the superconducting  $T_c$ . (b). The  $T_c$  inferred from the structure factor result. This is compared to QMC results at the end of the paper. (c). Ratio of  $T = 0$  gap  $2\Delta_0$  to  $T_c$ . In the BCS limit the ratio would be  $\sim 3.5$ . (d). The ‘phase diagram’ in terms of the low frequency behaviour of the density of states. The high temperature normal state has three regimes, ungapped (UG), pseudogapped (PG) and gapped (G), while for  $T < T_c$  the system is a gapped superconductor (SC) exact definitions of these phases are given in the text.

### 3.3 Results

#### 3.3.1 Thermodynamic indicators

Fig. 3.1(a) shows our result for the structure factor corresponding to the growth of superconducting order. We compute the thermally averaged pairing field correlation  $S(\mathbf{q}) = \frac{1}{N^2} \sum_{ij} \langle \Delta_i \Delta_j^* \rangle e^{i\mathbf{q} \cdot (\mathbf{r}_i - \mathbf{r}_j)}$  at  $\mathbf{q} = \{0, 0\}$ . We locate the superconducting transition from the rise in  $S(0, T)$  as the system is cooled. The results are not reliable below  $U/t \lesssim 1$ , since the correlation length  $\xi$  becomes comparable to our system size, but compare very well with available QMC data for  $U/t \gtrsim 2$ . We will discuss the interpretation of the  $S(0, T)$  results in detail at the end of the paper.

Fig. 3.1(b) shows the result for  $T_c(U)$  showing the clear peak around  $U/t \sim 5$ . We will compare this to the result from QMC, and also discuss the system size dependence, at the end of the paper.

In Fig. 3.1(c) highlights the rapid rise in the ‘gap’ to  $T_c$  ratio with increasing interaction. In the weak coupling limit this value is 3.5, at  $U = 2t$  it is already  $\sim 7$ , quite beyond BCS, and grows roughly as  $(U/t)^2$  at large  $U$ . Needless to say, the  $T = 0$  gap is not an indicator of the robustness of the superconducting state once we go beyond weak coupling.

Fig. 3.1(d) shows the phase diagram, consisting of four distinct phases. When the density of

states has zero weight over a frequency window around  $\omega = 0$  we call the system gapped. When the weight is nonzero but depressed we call it pseudogapped. This feature typically has a strong  $T$  dependence. Due to size effects a weak  $T$  independent depression is visible even at  $U = 2t$ , we have not labelled this as a pseudogap. The large gap but low  $T_c$  leaves its imprint on several physical properties, as this diagram highlights. At weak coupling the vanishing of SC order also means the vanishing of the gap in the density of states. The high  $T$  regime at small  $U/t$  is ungapped (UG). The regime  $U/t \lesssim 2$  is a ‘renormalised BCS’ window, although the gap to  $T_c$  ratio is large. For  $2 \lesssim U/t \lesssim 4$  the  $T > T_c$  phase has a pseudogap (PG), while for  $U/t \gtrsim 4$  the  $T > T_c$  regime is gapped. Notice that the normal state gap appears before the peak  $T_c$  is reached, *i.e.*, on the ‘BCS’ side of the crossover.

### 3.3.2 Background fields

To understand the spatial behaviour of the system and its evolution with  $U$  and  $T$  we examine the variation of the background fields  $\Delta_i$  and  $\theta_i$ . Fig. 3.2 shows single snapshots of  $|\Delta_i|$  (upper row in each set), normalised by the  $T = 0$  mean field value, and the phase correlation  $\Phi_i = \cos(\theta_i - \theta_0)$  (lower row in each set), where  $\theta_0$  is the angle at fixed site  $R_0$  in the lattice.

Of the three sets in Fig. 3.2, the top set is for  $U/t = 2$ , which we will use as typical of ‘weak’ coupling, the middle set is for  $U/t = 6$ , typical of intermediate coupling, and the bottom set is for  $U/t = 10$ , strong coupling. The rows are for  $T/T_c(U) = 0.1, 1, 2$ .

At  $T = 0.1T_c$  all the snapshots show almost uniform  $|\Delta_i|$  and perfect phase locking at all  $U/t$ . This is almost the mean field ground state. As we move to higher  $T$ , however, we see a clear difference in the amplitude fluctuations of the three systems. While the  $U/t = 2$  plots show an increasing inhomogeneity and a steadily rising value of  $\Delta$  throughout the system, the  $U = 10t$  case hardly shows any change. The  $U = 6t$  behaviour is intermediate. This shows that with increasing  $U$ , the system moves smoothly from an amplitude fluctuation dominated regime to one in which amplitudes are effectively constant, the transition being driven by the phase fluctuations.

The phase maps, on the other hand, show how the system breaks up into correlated patches with temperature. The middle column corresponds to  $T_c$ , and show large correlated clusters, as expected for a system close to criticality. As  $T$  is increased, the correlation length decreases, as evident from the right column at  $2T_c$ .

While it is phase fluctuations that ultimately destroy order at all  $U/t$ , the amplitude fluctuations are quantitatively important at weak coupling. To highlight this, we plot the distribution of  $|\Delta|$  for the three  $U$  values at four temperatures  $T = 0.1T_c, 0.5T_c, T_c$  and  $2T_c$  in Fig. 3.3(a),(b) and (c). (d) shows the temperature dependence of the mean  $\langle |\Delta| \rangle$  and its variance for  $U = 2t, 6t$  and  $10t$ . We find that the distributions widen for each case with increasing  $T$ , but the increase is

much more pronounced at weak coupling, and decreases systematically with increasing coupling. The distribution is noticeably non gaussian at high temperature in the weak coupling case. The temperature dependence of the mean and width of  $P(|\Delta|)$  is shown in Fig. 3.3(d). A detailed discussion is postponed to the end of the paper.

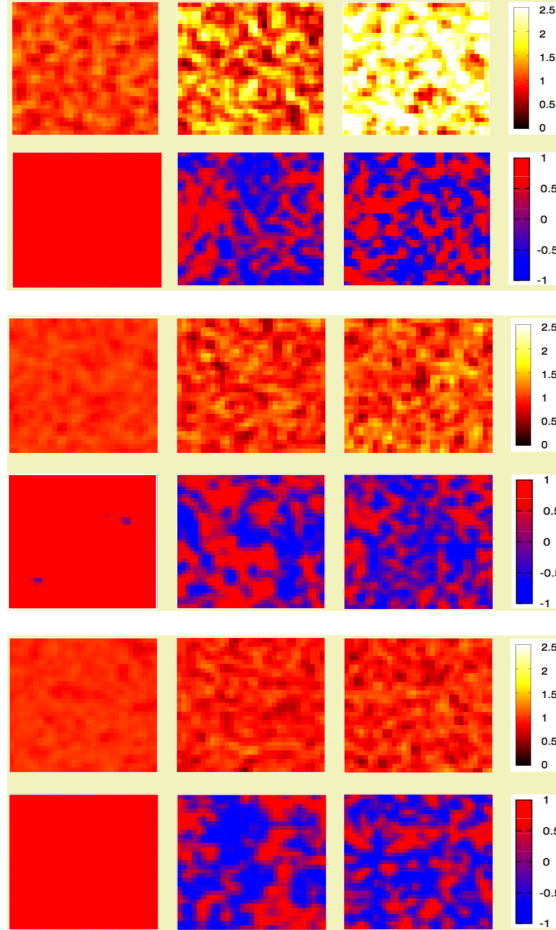


Figure 3.2: Maps of amplitude fluctuation and phase correlation for single configurations at  $U/t = 2$  (top),  $U/t = 6$  (middle) and  $U/t = 10$  (bottom) at three temperatures:  $T = 0.1T_c$ ,  $T = T_c$  and  $T = 2T_c$  (left to right). For each set, the upper row shows the amplitude  $|\Delta_i|$  (normalised by the  $T = 0$  mean field value  $\Delta_0$ ) for a MC configuration, while the lower row shows the phase correlation:  $\Phi_i = \cos(\theta_i - \theta_0)$ , where  $\theta_0$  is the phase at a site  $\mathbf{R}_0$  near the center.

### 3.3.3 Density of states

Fig. 3.4 highlights the behaviour of the single particle density of states (DOS). We show results at the ‘BCS end’ ( $U = 2t$ ), near the peak  $T_c$  ( $U = 6t$ ), and in the BEC regime ( $U = 10t$ ). The  $T = 0$  results in all cases are described by the canonical DOS,  $N(\omega) \sim 1/\sqrt{\omega^2 - |\Delta_0|^2}$ , where  $2\Delta_0$  is the full  $T = 0$  gap in the single particle spectrum. There is a gap in the spectrum at all  $U$ , a ‘coherence

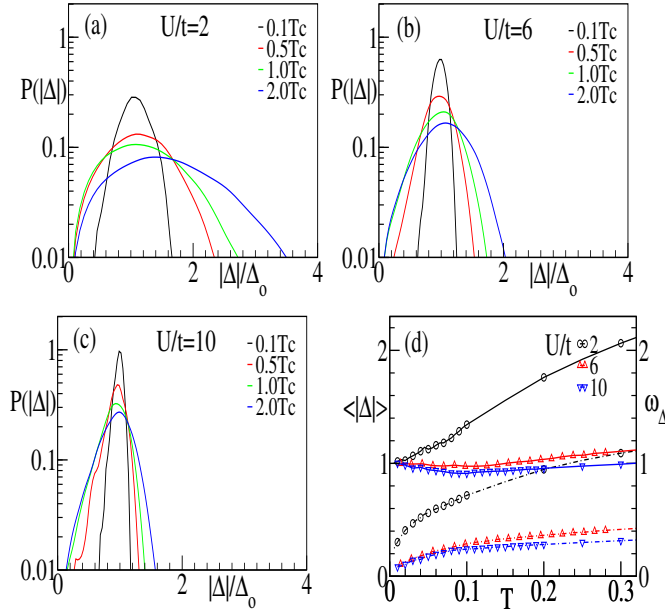


Figure 3.3: (a)-(c). The distribution  $P(|\Delta|)$  of the magnitude,  $|\Delta|$ , of the pairing field. The x-axis is normalised by the mean field value  $\Delta_0$  at  $T = 0$ . The results are for  $T = 0.1T_c, 0.5T_c, 1.0T_c, 2.0T_c$ . (a).  $U/t = 2$ , (b).  $U/t = 6$ , (c).  $U/t = 10$ . At  $U/t = 2$  there is a prominent increase in the mean and width of  $P(|\Delta|)$  with  $T$ . This  $T$  dependence weakens with growing  $U/t$ . (d). The growth of the mean value  $\langle|\Delta|\rangle$  and width  $\omega_\Delta$  with  $T$ . Both are normalized by the  $T = 0$  mean value of  $\Delta$ . The firm lines denote the mean  $|\Delta|$ , while the dot-dashed lines show the corresponding width.

peak' at the gap edges, arising from electron propagation in a perfectly pair correlated background, and a featureless fall at high energies. The oscillatory pattern in the DOS at  $T = 0$  for  $U = 2t$  is a consequence of finite size, showing up even on a  $24 \times 24$  lattice.

While the  $T = 0$  DOS is just a mean field result, and the  $T$  dependence at  $U = 2t$  is expected, the  $T$  dependence at  $U = 6t$  and  $U = 10t$  is not obvious. At  $U = 6t$ , the system has a 'hard gap' persisting to  $T \sim 3T_c \sim 0.5t$ . This is reflected in the phase diagram in Fig. 3.1. At both  $U = 6t$  and  $10t$  the transition to SC occurs from a gapped fermion state rather than a Fermi liquid. The DOS indicates that down to  $U$  values around peak  $T_c$  (and even somewhat below) the qualitative physics remains similar to the BEC end.

Another striking feature is the large transfer of spectral weight that occurs on a modest change of temperature. For the  $U = 10t$  case, for example, at  $T \sim T_c \sim 0.09t$  there is weight transfer over a scale  $\mathcal{O}(U)$ . The reason is fairly simple: the magnitude  $|\Delta_i|$  in this limit are almost  $T$  independent, but the phase correlation between them is destroyed at a temperature  $T \sim t^2/U$ . As a result, over a small  $T$  window the system evolves from a state with perfectly ordered  $\Delta_i$ , to one where these large amplitudes are randomly oriented. The strong 'disorder' in the  $\Delta_i$  lead to the broadening of the density of states.

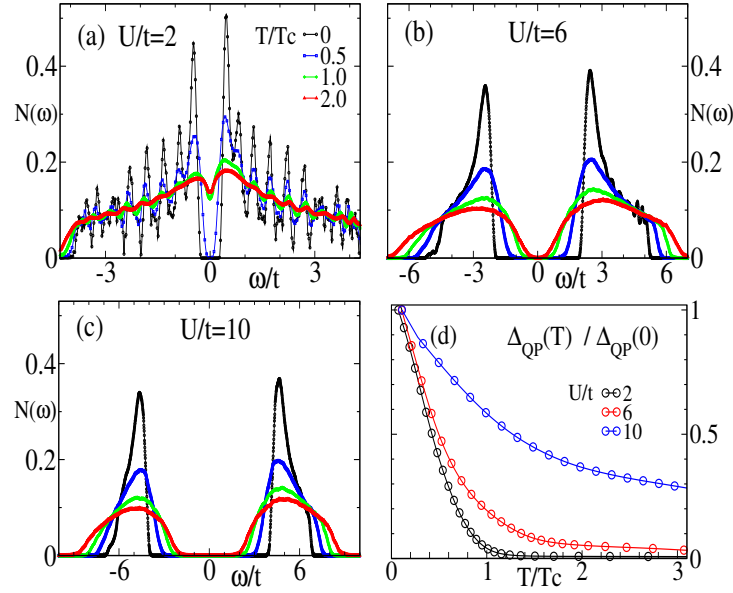


Figure 3.4: Temperature dependence of the DOS,  $N(\omega)$  at different couplings. Panels (a)-(c) have the same legends. (a).  $U/t = 2$ , (b).  $U/t = 6$ , and (c).  $U/t = 10$ . The oscillations in the DOS in panel (a) are finite size artifacts (even on a  $24 \times 24$  lattice). At  $U/t = 2$  the gap essentially vanishes at  $T \sim T_c$ , while at  $U/t = 6$  a small ‘hard gap’ persists to  $T_c$  and above, although lorentzian broadening gives the impression of a pseudogap at the highest  $T$ . For  $U/t = 10$  a ‘hard gap’ persists to  $T \sim 0.5$  although with a clear reduction with increasing temperature. (d). Variation in the single particle gap, normalised by its  $T = 0$  value.

The large size of  $|\Delta_i|$  even in the normal state preserves the gap feature, but the randomness smears the band edges.

### 3.3.4 Spectral functions

Now we turn to the spectral functions. Fig. 3.5 shows intensity plots of the spectral function  $A(\mathbf{k}, \omega)$  for  $U/t = 2, 6, 10$  (top to bottom) for  $T/T_c = 0.1, 1, 2$  (left to right). Let us start with the low temperature results, where mean field theory is a good starting point.

At density  $n \sim 0.9$  the non interacting Fermi surface is almost a square, rotated by  $45^\circ$  with respect to the Brillouin zone. The separation between the two branches of the mean field dispersion,  $\pm \sqrt{(\epsilon_{\mathbf{k}} - \mu)^2 + \Delta_0^2}$ , is smallest when  $\epsilon_{\mathbf{k}} = \mu$  and for the  $\mathbf{k}$  scan shown in Fig.5 it occurs for  $\mathbf{k}$  near  $(0, \pi)$  and  $(\pi/2, \pi/2)$ . Within MFT the spectral function is given by  $A(\mathbf{k}, \omega) = u_{\mathbf{k}}^2 \delta(\omega - E_{\mathbf{k}}) + v_{\mathbf{k}}^2 \delta(\omega + E_{\mathbf{k}})$ . In the BCS limit,  $v_{\mathbf{k}}^2$  is either one or zero for  $k < k_F$  or  $k > k_F$ , with a small region around  $k_F$  where it crosses from one to the other.

At  $U = 2t$ ,  $v_{\mathbf{k}}^2 \sim 1$  for  $\epsilon_{\mathbf{k}} \lesssim \mu$ , and  $u_{\mathbf{k}}^2 \sim 1$  for  $\epsilon_{\mathbf{k}} \gtrsim \mu$ , with significant mixing only near  $\mu$ . As a result  $A(\mathbf{k}, \omega)$  shows either a lower branch or an upper branch, but not both - except for  $\epsilon_{\mathbf{k}} \sim \mu$ .

The growing symmetry in the plots, about the horizontal  $\omega = 0$  line, with increasing  $U/t$  arises

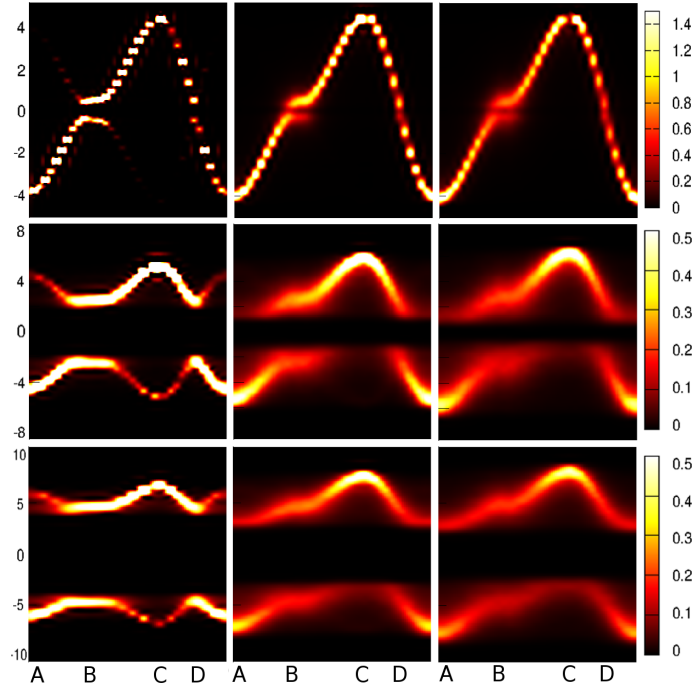


Figure 3.5: Plot of  $A(\mathbf{k}, \omega)$ . The rows, left to right, are for  $U/t = 2, 6$  and  $10$ . Columns, top to bottom, correspond to  $0.1T_c, T_c$  and  $2T_c$ . The momentum, on the x-axis, is scanned as  $(0,0) \rightarrow (0,\pi) \rightarrow (\pi,\pi)$  and back through  $(\pi/2,\pi/2)$  to  $(0,0)$  along the diagonal. These points are labelled as A, B, C and D respectively. The gaps are lowest around  $(\pi/2, \pi/2)$  and  $(\pi, 0)$ , where the Fermi-surface of the free system intersects our path in  $\mathbf{k}$ -space. Increasing temperature causes broadening and a decrease of the gaps, which close in the case of  $U = 2t$ . The increasing symmetry of the low  $T$  graphs with increasing  $U$  signals the participation of states far from the FS in pairing.

from the changing character of  $u_{\mathbf{k}}$  and  $v_{\mathbf{k}}$ . For  $U/t \gg 1$ ,  $u_{\mathbf{k}}^2$  and  $v_{\mathbf{k}}^2$  are both  $\sim 1/2$  all over the Brillouin zone, since ‘pairing’ is no longer limited to the vicinity of the non interacting Fermi surface (FS). The cases  $U = 6t$  and  $U = 10t$  are already in this regime although some residual asymmetry is visible. The large difference between weak and strong coupling in terms of the  $T = 0$  pairing amplitude decides the finite  $T$  state.

At finite  $T$ , thermal fluctuations broaden the delta functions and the detailed lineshapes for  $\mathbf{k} = \{\pi, \pi\}$  and  $\{\pi/2, \pi/2\}$  are shown in Fig. 3.6. As expected, the gap closes for  $U = 2t$ , while it does not for  $U = 6t$  and  $U = 10t$ , though there is a noticeable decrease in the former.

Quantum Monte Carlo work [162] had suggested the presence of non-trivial structure in the spectral function near the zone boundary  $(\pi, \pi)$ . The top row in Fig. 3.6 shows the spectral function at this  $\mathbf{k}$  point for  $U/t = 2, 6, 10$  at three temperatures,  $T = 0.5T_c, T_c, 2T_c$ . The energy is measured in units of the  $T = 0$  dispersion  $E_{\mathbf{k}}^0$ .

We start with the top row:  $\mathbf{k} = \{\pi, \pi\}$ . At high temperature the  $U = 2t$  case shows only a single broad peak at positive energy, whereas  $U/t = 6, 10$  show a second peak at a smaller

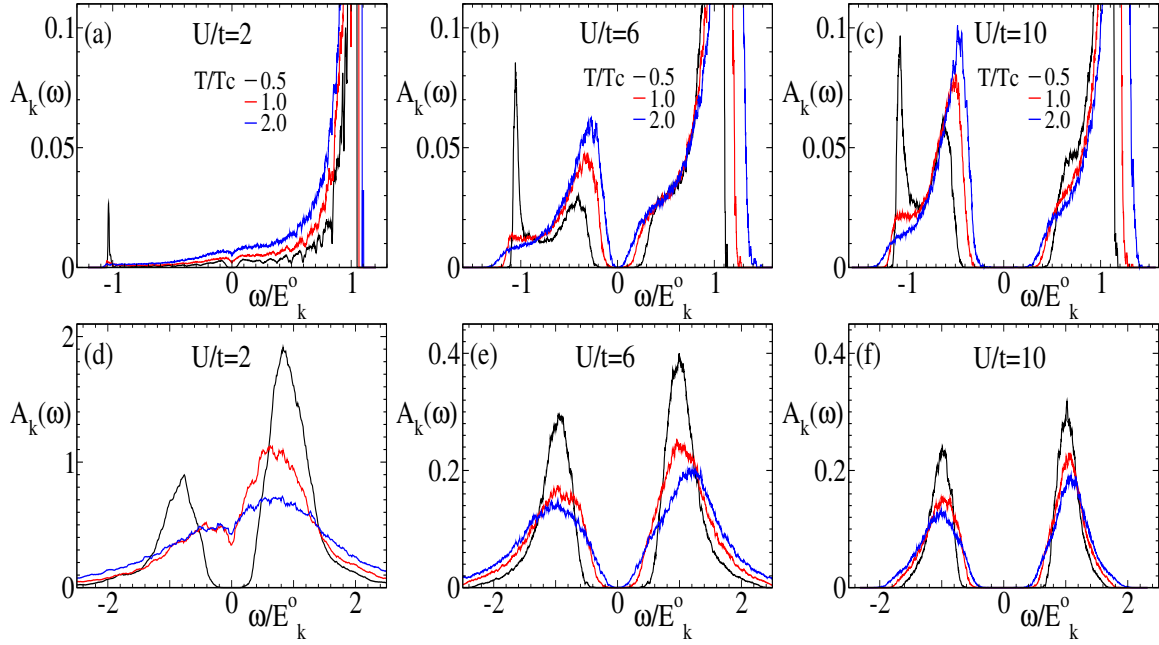


Figure 3.6: Spectral function  $A(\mathbf{k}, \omega)$ . The panels in the top row are for  $\mathbf{k} = \{\pi, \pi\}$ . (a).  $U/t = 2$ , (b).  $U/t = 6$ , (c).  $U/t = 10$ . Bottom row,  $\mathbf{k} = \{\pi/2, \pi/2\}$ , and interaction strengths: (d).  $U/t = 2$ , (e).  $U/t = 6$  and (f).  $U/t = 10$ . For each  $U$  we show data at  $T = 0.5T_c, T_c$  and  $2T_c$ . The frequency axis is normalised by the  $\mathbf{k}$  dependent mean field energy  $E_{\mathbf{k}}^0$  at  $T = 0$ . For  $\mathbf{k} = \{\pi, \pi\}$ , which is outside the non interacting Fermi surface, the basic structure consists of large peak at positive energies  $\omega \sim E_{\mathbf{k}}^0$ , a broad negative energy feature at  $\omega \gtrsim -E_{\mathbf{k}}^0$ , and for  $T < T_c$  a remnant of the quasiparticle peak at  $\omega = -E_{\mathbf{k}}^0$ . Beyond weak coupling the survival of a two peak structure even for  $T > T_c$  indicates ‘incoherent pairs’. For  $\mathbf{k} = \{\pi/2, \pi/2\}$  the features are similar to what we observe at  $\mathbf{k} = \{\pi, \pi\}$ , except the quasiparticle peak is no longer separately visible.

negative energy value. This two peak structure with a gap around  $\omega = 0$  is an indicator of pairing without global coherence. The complete absence at  $U = 2t$ , and the increase in peak height from  $U = 6t$  to  $10t$  bolsters this interpretation.

We do not find any peak near  $\omega \sim 0$  for medium to large  $U$ . However from  $T_c$  downwards, another peak becomes visible at negative energies, at  $\omega \sim -E_{\mathbf{k}}^0$ . This peak is indicative of the global coherence setting in below  $T_c$ . As  $T$  is decreased, this peak slowly gains weight while weight in the ‘pairing feature’ becomes smaller, with its maximum shifts to larger negative energies as the gap becomes larger.

Thus, we find some degree of consistency with the QMC work which mainly deals with temperatures larger than  $T_c$ , and also find another peak, indicative of global coherence, that starts to develop below  $T_c$ .

For  $\mathbf{k} = \{\pi/2, \pi/2\}$  and high temperature the spectral functions at  $U = 6t$  and  $U = 10t$  have a gap at  $T > T_c$ , as before, while the  $U = 2t$  result is gapless. In contrast to  $\mathbf{k} = \{\pi, \pi\}$  however we cannot disentangle the lower temperature coherence feature, at  $\omega = \pm E_{\mathbf{k}}^0$  from the overall broad

band.

## 3.4 Discussion

Our model has been set up with the explicit constraint that it reproduce the standard mean field (or HFBdG) result at  $T = 0$ . It ignores quantum fluctuations of the pairing field. The impact of these fluctuations have been discussed using DMFT by Garg et. al. [168] and Bauer and Hewson [169]. They find that the *qualitative* results at  $T = 0$  for the order parameter, spectral gap, occupation probability and superfluid stiffness are all given correctly by the mean field method, though it tends to overestimate the spectral gaps and order parameter values at intermediate coupling. For most of the  $U$  window, however, the mean field results are reasonable. The results from our method should get better at finite temperature as thermal fluctuations become more important than zero point quantum fluctuations. A comparison of our  $T_c$  with QMC estimate bears this out.

### 3.4.1 Accuracy of $T_c$ estimate

Fig. 3.7(a) compares our  $T_c$  with different methods. We find that our results compare well with QMC and sophisticated semi-analytic methods with a slight underestimate at medium to large coupling. Fig. 3.7(b) shows the size dependence of the  $T_c$  estimate with data for  $L = 8, 16, 24$ . We see that while the ‘critical temperature’ estimate decreases noticeably from  $L = 8$  to 16, it does not change significantly beyond  $L = 16$ . Thus, the estimate we obtain at  $L = 24$  should be a fair approximant to the bulk  $T_c$ .

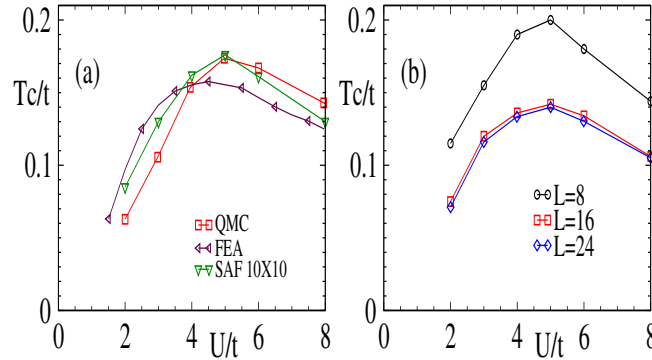


Figure 3.7: (a) Comparison of our  $T_c$  (labelled SAF) with QMC [165] on a  $10 \times 10$  lattice, and the semi-analytic method employing the fluctuation exchange approximation (FEA) [151]. DMFT results [166] overestimate the  $T_c$  significantly, and also the location of peak  $T_c$ , and have not been included in the same plot. (b) Size dependence of our result, showing that the  $T_c$  estimate is almost size independent beyond  $L = 16$ .

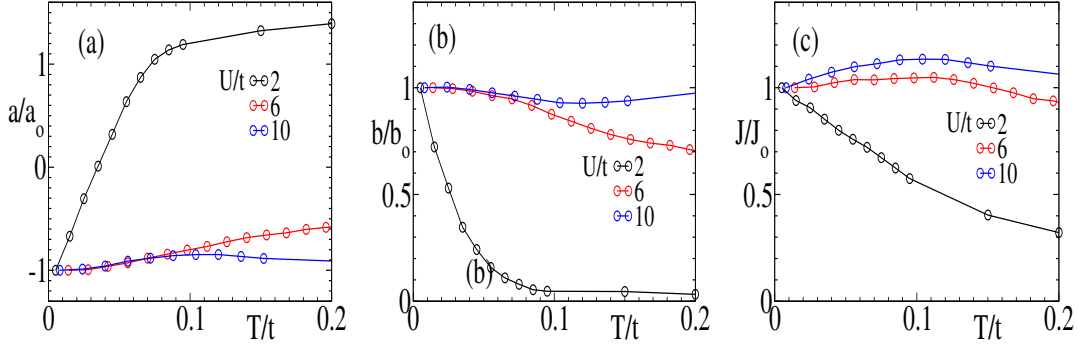


Figure 3.8: Parameters defining the phenomenological model. (a) The parameter  $a(T, U)$ , (b). the parameter  $b(T, u)$ , and (c). the stiffness  $J(T, U)$  of the effective XY model for the phase degrees of freedom.  $a$  and  $b$  are normalised to their  $T = 0$  values. Notice the essential flatness of  $a(T)$  and  $b(T)$  at  $U = 10t$ , the weak  $T$  dependence at  $U = 6t$ , and the dramatic variation with  $T$  at  $U = 2t$ .  $J$  similarly is only weakly  $T$  dependent for  $U \gtrsim 6t$  and varies strongly with  $T$  at weak coupling.

### 3.4.2 Effective classical functional

The BdG framework involves fermions coupled to the fields  $\Delta_i$  and  $\phi_i$ . For simplicity let us focus on the  $\Delta_i$  since the  $\phi_i$  do not play a crucial role in a translation invariant system.

The physics of fermions in an arbitrary  $\Delta_i$  background is not obvious. It is therefore helpful to have an explicit classical functional involving only the  $\Delta_i$  since the minimum and possible fluctuations in  $\Delta_i$  are easier to estimate.

If the  $\Delta_i$  are small compared to the kinetic energy, as would happen when  $U/t \ll 1$ , the functional,  $H_{eff}^0$ , can be obtained via a standard cumulant expansion:

$$H_{eff}^0\{\Delta_i\} = \sum_{ij} a_{ij} \Delta_i \Delta_j^* + \sum_{ijkl} b_{ijkl} \Delta_i \Delta_j^* \Delta_k \Delta_l^* + \mathcal{O}(\Delta^6)$$

The superscript in  $H_{eff}$  is to indicate  $U/t \ll 1$  character.  $a_{ij} = -\chi_{ij}^0/2 + (1/U)\delta_{ij}$ ,  $\chi_{ij}^0$  being the non-local pairing susceptibility of the free Fermi system, and  $b_{ijkl}$  can be computed from a convolution of four free Fermi Greens functions.

If we had  $U/t \gg 1$  then  $H_{eff}$  would have to be expanded to higher order in  $\Delta_i$ . In that situation it actually helps to extract the functional by expanding in powers of  $t/\Delta$ , leading to the strong coupling limit:

$$H_{eff}^\infty\{\Delta_i\} \approx -t^2/|\Delta| \sum_{\langle ij \rangle} \cos(\theta_i - \theta_j) + \sum_i H_{loc}(|\Delta_i|)$$

$H_{loc}(|\Delta_i|)$  can be obtained from the atomic problem. The leading intersite term is calculated perturbatively and connects only nearest neighbour sites.

While these BCS and BEC limits are easy, obtaining an usable functional at *arbitrary*  $U/t$  does not seem possible. We have therefore tried a parametrisation of the (local) amplitude fluctuation spectrum and the phase correlations in terms of the following phenomenological model. It is valid at all  $U/t$  and over the temperature window of interest.

$$H_{eff}^{phen} = - \sum_{\langle ij \rangle} J \cos(\theta_i - \theta_j) + \sum_i \{a|\Delta_i|^2 + b|\Delta_i|^4\}$$

The first term defines an effective XY model involving only the phases, but, as we will see, the  $J$  needs to be temperature dependent to incorporate the effect of amplitude fluctuations. The amplitude part of  $H_{eff}$  is purely local, and to that extent misses out on spatial correlation between amplitude fluctuations.

The parameters  $a$  and  $b$  are extracted from a fit to the  $P(|\Delta|)$  that we obtain from the full MC, see Fig.3. With the moments of  $|\Delta_i|$  fixed by  $a$  and  $b$ , the  $J(U, T)$  is obtained by imposing the following equality:

$$\langle \sum_{ij} |\Delta_i| |\Delta_j| \cos(\theta_i - \theta_j) \rangle_{MC} = \langle \sum_{ij} |\Delta|^2 \cos(\theta_i - \theta_j) \rangle_{phen}$$

The left hand side is the MC based order parameter, Fig. 3.1(a). The right hand side computes the same quantity within the phenomenological model (in which the  $|\Delta|$  and  $\theta$  averages factorise) by using a Monte Carlo estimate of  $\langle \cos(\theta_i - \theta_j) \rangle$  in the XY model.

Fig. 3.8(a)-(b) shows the  $T$  dependence of  $a$  and  $b$  for  $U = 2t$ ,  $U = 6t$  and  $U = 10t$ . Because of the large difference in scales between the weak and strong coupling we have normalized the parameters by their  $T = 0$  values.

The  $U = 2t$  parameters show large change with  $T$ . The normalized  $a$  quickly increases and becomes positive, while  $b$  rapidly decreases from its  $T = 0$ . Both parameters tend to saturate for  $T \gtrsim T_c \sim 0.07t$ . The 6th order term in the expansion would be necessary to describe the  $U = 2t$  case accurately.

With increasing  $U$ , the thermal change of the parameters slows down, and even at  $U = 6t$  the parameters show a much weaker dependence on  $T$ . By  $U = 10t$ , they are essentially constant at their  $T = 0$  values, indicating that only phase fluctuations are relevant in this regime.

To gain more insight, we consider an expansion of the distribution about its mean value,  $P(\Delta) = K_2(\Delta - \Delta_0)^2 + K_3(\Delta - \Delta_0)^3 + K_4(\Delta - \Delta_0)^4 \dots$ , where the first term represents the gaussian stiffness of the distribution and the other terms represent non gaussian contributions. At strong coupling, the physics is driven completely by the phase fluctuation term, and the magnitude of the amplitudes is almost fixed. Thus, the stiffness coefficient is very large. As the coupling decreases, amplitude fluctuations increase, hence signalling a decrease in the stiffness. Apart from

the increase in amplitude fluctuations, the mean value of  $\Delta$  also shows a remarkable increase with  $T$  at weak coupling, signalling the importance of the non gaussian terms in the expansion. We next turn to examine the phase stiffness which is the crucial coupling at large  $U$ .

Fig. 3.8(c) shows the  $T$  dependence of  $J$  for the three couplings, again normalized by their  $T = 0$  values,  $J_0(U)$ . The  $U = 2t$  case shows a pronounced decrease with  $T$ , while the other two are effectively constant. An XY description with a  $T$  independent coupling is reasonable for  $U = 6t$  and  $10t$  but inadequate at  $U = 2t$ .

### 3.4.3 Role of the ‘density’ field

An important addition in our model is the field  $\phi$ , coupling to the density operator. It serves a twofold purpose: first, it is indispensable in a disordered system since it provides a site dependent background field that renormalises the total disorder, and is crucial to get the correct scales; and second, it incorporates fluctuations in the charge sector, which play an important role for  $n \sim 1$ .

At  $n = 1$  the negative  $U$  Hubbard model can be mapped to its positive  $U$  counterpart, with the components of the magnetization field,  $\mathbf{m}_i$ , of the positive  $U$  model corresponding to the  $\Delta_i$  and  $\phi_i$ . The symmetry the model is increased from  $O(2)$  to  $O(3)$ , so there can be no superconducting order at finite temperature in 2D. At  $T = 0$ , the superconducting state is degenerate with the charge density wave state. This degeneracy is built into the structure of our model, and simulations at  $n \sim 1$  do actually show both superconductivity and charge density wave order at low  $T$ . The two field decomposition captures the correct ground state and relevant fluctuations in the model.

However, as discussed before, our way of incorporating the fluctuations in both fields can lead to overcounting effects. Fig. 3.9 shows how the  $T_c$  and density of states calculated with both fields compare with the single field results. Fig. 3.9(a) shows that while the fluctuations in both fields result in a decrease in the  $T_c$ , it actually brings the values in closer correspondence with corresponding QMC results [165], increasing its accuracy. Fig. 3.9 (b), (c) and (d) compare the density of states at three different coupling values, for three temperatures each, demonstrating that overcounting effects are negligible in this regime.

### 3.4.4 Handling inhomogeneity

As remarked earlier, this method is particularly well suited to dealing with inhomogeneous systems, including disordered systems and systems in a trap. We have extensively studied both of these, the former in the context of the disorder induced superconductor-insulator transition [174,175], and the latter in the context of superconductors in a harmonic trap [176]. In such inhomogeneous systems, the Hartree feedback plays a crucial role in modifying the effective potential that the electronic system sees. In the former, this is crucial in determining the correct critical disorder and moderate

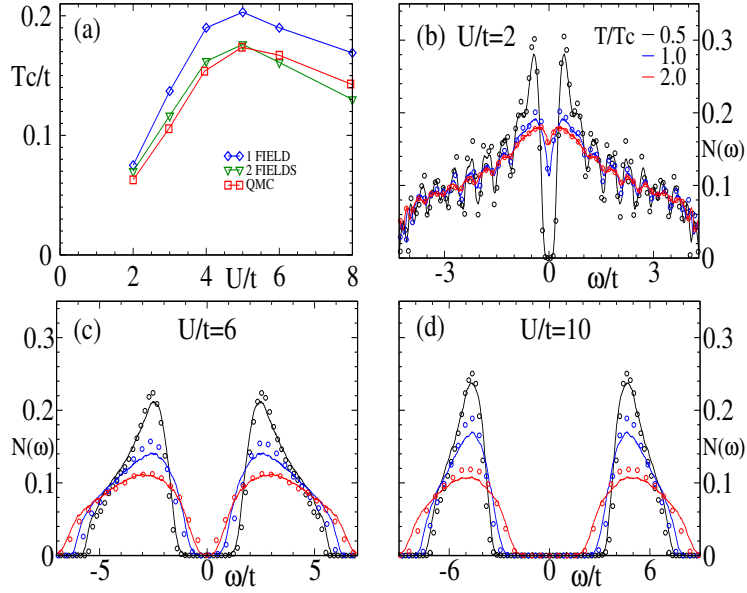


Figure 3.9: (a) Comparison of  $T_c$  with and without  $\phi$  fields and corresponding QMC results at size  $10 \times 10$  [165]. Inclusion of  $\phi$  fields brings  $T_c$  in closer correspondence with QMC. (b), (c) and (d) compare the density of states for the same two cases at  $U/t = 2, 6$  and  $10$  respectively, at  $T/T_c = 0, 1.0$  and  $2.0$  respectively. The firm lines show the two fields results, while the circles of same colour show the single field results. There are small differences, but on the whole, they are very similar to each other.

disorder charge transport properties [174], and plays a major role in the spatial fragmentation of the system [175]. In a harmonic trap, the resultant inhomogeneous density profile can drastically alter the spectral properties of the system [176], compared to a flat one. Similarly for FFLO phases in imbalanced Fermi systems the real space treatment on large lattices allow access to a wealth of non trivial modulated phases.

### 3.4.5 Quantum fluctuations

The major approximation in our model is the neglect of temporal fluctuations in the auxiliary fields. We have already seen that our method captures the non-monotonic  $T_c(U)$  in the BCS- BEC problem as well as the correct overall scale when compared with QMC, which, we believe, shows that the thermodynamic properties at these scales are well captured. There are some effects in the spectral function and optical conductivity that we miss as discussed below.

#### *a) Single particle spectrum:*

Our method neglects the interaction of the single particle propagator with dynamical particle-hole and particle-particle fluctuations. The DMFT results for the  $k$ -resolved spectral functions show that while the weak coupling results match with the mean field values, this interaction results in the formation of an incoherent background (forming what the authors term a peak-dip-hump

structure [169]) in addition to the quasiparticle peaks, which are also somewhat shifted from their mean field values. This effect is absent at  $T = 0$  in our approach. By the time  $T \sim T_c$ , however, classical fluctuations capture most of the spectral features.

*b) Optical conductivity:*

Our method misses the contribution of the collective modes in the optical conductivity. The contribution of these result in a finite contribution above the Higgs mass threshold  $m_H$ . (in two dimensions, the sub-Higgs mass weight is further suppressed to a weak  $\omega^5$  tail [177]). In a weak coupling superconductor,  $m_H \sim 2\Delta$ , hence the Higgs mode rapidly decays into particle-hole excitations and the normal Mattis-Bardeen results are valid. At strong coupling, however, we completely miss the contribution of the collective modes to the low frequency optical conductivity, which are also relevant for  $T > T_c$ .

### 3.5 Conclusions

We have presented results on the BCS-BEC crossover in an attractive Fermi system in the context of the two dimensional Hubbard model. We use an auxiliary field decomposition, treat these fields as classical, and solve the resulting problem through a real space Monte Carlo technique. The inclusion of all spatial thermal fluctuations allows us to capture the correct  $T_c$  all the way from the BCS to the BEC end. It allows conceptual clarity about the amplitude and phase fluctuation dominated asymptotes and the crucial intermediate coupling window where both these fluctuations are relevant. We provide a detailed characterisation of the auxiliary field behaviour that dictates fermion physics and access results on the density of states and angle resolved spectral features without any need for analytic continuation. We lay the groundwork for the study of disordered superconductors, trapping effects in superfluids, and spontaneous inhomogeneity in imbalanced systems.



# CHARGE DYNAMICS ACROSS THE SUPERCONDUCTOR-INSULATOR TRANSITION

This chapter will be the first of two describing our work on disordered superconductors. In this chapter we will study the *global* properties of the system, concentrating on the charge dynamics, which determines the transport and optical conductivity, on which surprisingly little theoretical work seems to exist in spite of extensive experimental results. This will be accompanied by results on the transition temperature  $T_c$  and the global density of states, leading to a phase diagram of the system in the disorder-temperature plane, as determined from these indicators. In the next chapter we will concentrate on the *local*, i.e., *spatial* properties of the system, concentrating on the disorder induced inhomogeneities and their effect on local indicators. Together, these results will provide a comprehensive picture of the disorder induced evolution of a superconducting system.

This chapter is structured in the following manner: we will begin with a short recap of the overall situation in the field, which has already been discussed in detail in the introductory chapters. This will be followed by a more detailed discussion on the global characteristics, such as the transport, optical conductivity and the density of states. Finally, we will describe our own work, detailing our results and discussing their relevance in the context of available experimental and theoretical results.

## 4.1 Background to the problem

While the historical background has already been reviewed in detail in Chapters 1 and 2, we provide a basic summary of the same below, emphasizing the salient observations. This will be followed by

a slightly more detailed discussion of the transport and optical data, along with the single particle density of states, before we move on to our results.

### 4.1.1 Summary of experiments

As already discussed earlier, the problem of the disorder driven superconductor-insulator transition (SIT) has been studied for a long time in condensed matter physics. Although early theoretical work by Anderson [31] suggested that superconductivity (SC) should be insensitive to non-magnetic disorder, a large number of experiments over the last couple of decades [5] have revealed that superconductivity is actually suppressed and finally destroyed by increasing disorder. Simultaneously, the normal state resistivity changes from metallic to insulating, and a pseudogap (PG) appears in the single particle density of states.

The availability of high resolution scanning tunneling spectroscopy (STS) tools in recent times has led to a significant advance in the field, as we have already described in detail in the context of materials like Be, NbN, InO<sub>x</sub> and TiN in Chapter.1. The salient observations are:

1. The increasing fragmentation of the SC state with disorder [38, 47, 55, 56, 58–61].
2. Survival of an apparent (pseudo)gap in the disorder driven normal state [47, 55, 56, 60].
3. A change in the temperature dependence of the normal state resistivity from metallic to insulating, without necessarily any universal temperature independent value at critical disorder [44, 52], and, additionally,
4. Observations of non monotonic magnetoresistance [34, 52, 53], and finite frequency superfluid stiffness at large disorder [43, 62], well past the SIT.

On the theoretical front, the fully self-consistent Hartree-Fock-Bogoliubov-de Gennes (HFBdG) approach [84, 85] had already revealed that the strong disorder SC ground state is fragmented in an essential way, and predicted the survival of a single particle gap across the SIT. Thermal effects have been probed using quantum Monte Carlo (QMC) [88, 140, 141], providing an estimate of  $T_c$  and the global density of states, as we saw before. Nevertheless, surprisingly, apart from an early estimate [141] using the fermionic Hubbard model, and a very recent study using the quantum XY model [134], there seem to be no results on the charge dynamics, *i.e.*, the resistivity and optical features, across what is essentially a transport transition. The limitation stems from the inability of QMC methods to handle thermal fluctuations on a large spatial scale, and access real frequency information. This makes it particularly difficult to treat the full problem with fermionic degrees of freedom. Below, we elaborate on this in more detail.

## 4.1.2 Summary of current theory

As we know, even without the attractive interaction, the disordered fermion problem is affected by disorder induced scattering, leading to a nominally localized state at any disorder in two dimensions, and a delocalization to localization crossover at a critical disorder in three dimensions, which is accompanied by a metal to insulator transition. The addition of superconducting correlations on top can lead to very interesting phenomena related to the interplay of the disorder induced scattering with that induced by the attractive interaction. The non-trivial behaviour can come from the following physical effects:

1. The attractive interaction induces both elastic and inelastic scattering. The inelastic scattering implies a finite length  $L_{in}$  beyond which interference effects causing Anderson localization are cut off. Thus, this can lead to a weakening of localization effects with significant impact at weak disorder.
2. At strong disorder, the disorder induced pseudo-gap and the inhomogeneous structure of superconducting clusters above  $T_c$  can affect the transport properties in the *fermionic* channel, i.e., transport caused by the thermally activated fermionic quasiparticles in the system.
3. On the other hand, at low temperatures close to the transition, the *bosonic* degrees of freedom can contribute, as we found from the bosonic mechanism, leading to the universal finite value at the transition.
4. Coulomb interactions can also affect the transport properties by contributing a negative correction similar to the quantum weak localization correction.

Thus, we see that the transport properties of the interacting disordered system are determined by a complex set of physical effects. The inherent complexities of the problem and the number of factors involved has resulted in very little theoretical work being done on the subject. As mentioned before, we know of only one calculation using QMC (starting from a fermionic model) [141] that has dealt with this problem in an approximate manner. Below, we describe their results quickly.

The QMC calculations were done on two dimensional lattices using the negative U Hubbard model at coupling values  $U/t = (3 - 6)$  and density  $n \sim 0.875$  with varying disorder. Starting with the current current correlation function (see methods in Chapter.2) the authors applied an approximate scheme to calculate the transport. Fig.4.1 shows their main results. They found that the resistivity  $\rho$  showed a transition from metallic to insulating for all coupling values used, with  $d\rho/dt$  changing sign at the critical disorder where superconductivity is destroyed. While this established the presence of the SIT and a concurrent metallic-insulating crossover in the transport, their calculations were not accurate enough to reproduce the complex behaviour of the resistivity, especially

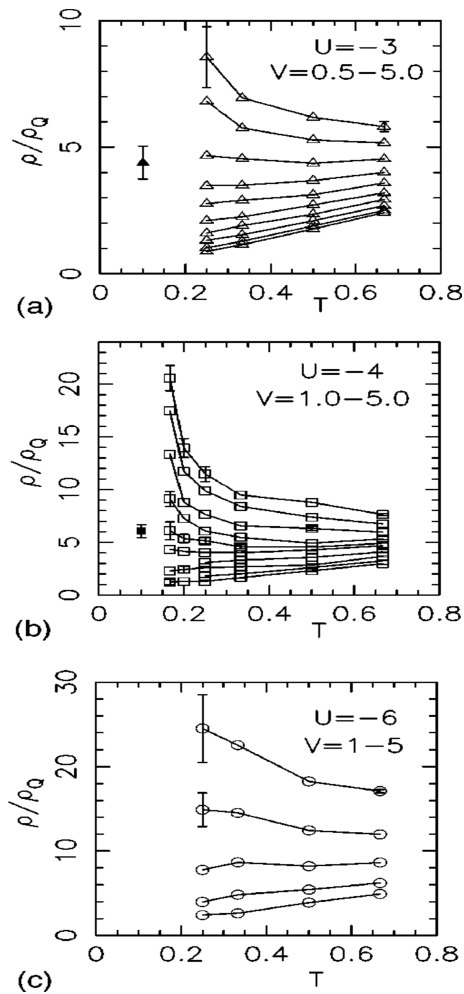


Figure 4.1: The disorder dependence of resistivity calculated using QMC [141] for  $U/t = 3, 4$  and  $6$ . Shows that  $d\rho/dt$  changes sign at the critical disorder  $V_c$  at all coupling values, going from metallic ( $d\rho/dt > 0$ ) to insulating ( $d\rho/dt < 0$ ). Does not manage to capture the interesting behaviour at intermediate disorder seen in experiments.

at intermediate temperatures found in experiments, that were described in detail in Chapter.1. To remind ourselves of these, we list them below:

1. In most cases, the metallic-insulating crossover happens much before the transition, i.e., the resistivity is weakly insulating over much of the phase diagram.
2. The critical curve is also insulating instead of horizontal as expected from the bosonic mechanism, without necessarily any universal temperature independent value at critical disorder.
3. The low temperature resistivity in the insulating regime is activated.

Thus, QMC results do not reproduce 1 and 2 at all, and are not accurate enough to ascertain whether their strong disorder results follow 3. On the one hand, these shortcomings, as already

mentioned before, stem from its inability to handle thermal fluctuations on a large spatial scale, and access real frequency information. On the other hand, as discussed before and speculated in some experimental papers, the Coulomb interaction might also play an important role in determining the exact behaviour of the transport.

Hence, there has been no theoretical work that has successfully captured the basic transport results in detail, especially the interesting behaviour at intermediate disorder. Similarly, there are no results on the optical conductivity starting from a fermionic model like QMC, whose low frequency behaviour is expected to show similar effects to the resistivity. While the existing QMC results using the XY model [134] elucidate the predictions of the bosonic model close to the transition, predicting non-trivial behaviour at low frequencies, we expect the fermionic degrees to be important over much of the phase window away from the critical point. Thus, one needs an approach starting with fermionic degrees of freedom to examine many of these questions. Furthermore, while the exact treatment would also incorporate Coulomb interactions, it also makes this problem a very hard one. Thus, in view of the lack of substantial results *even without considering Coulomb interactions*, we feel that it is quite important to study such a model in detail, especially since it manages to reproduce much of the phenomenology of strongly disordered superconductors correctly.

In this chapter we describe our approach to this problem using our method, that captures the HFBdG ground state, fully retains the thermal amplitude and phase fluctuations, and locates the correct disorder scale,  $V_c$ , for the zero temperature SIT.

## 4.2 Model, parameters, and main results

In this section, we will briefly describe our model and methods, and then explain the parameters we have chosen and the reasons for that and finally summarize the main results of our work.

### 4.2.1 Recapitulation of method

Our model has already been discussed before in detail. We begin with the negative U Hubbard model, with disorder incorporated in the form of a random potential  $V_i$  at each site. The Hubbard Stratonovich transformation in both pairing and density channels, and the neglect of the temporal fluctuations in the corresponding auxiliary fields  $\Delta$  and  $\Phi$  leaves us with the following model:

$$H_{eff} = H_{kin} + \sum_{i\sigma} (V_i - \mu) n_{i\sigma} + H_{coup} + H_{cl} \quad (4.1)$$

where

$$\begin{aligned}
H_{kin} &= -t \sum_{\langle ij \rangle \sigma} c_{i\sigma}^\dagger c_{j\sigma} \\
H_{coup} &= \sum_i (\Delta_i c_{i\uparrow}^\dagger c_{i\downarrow}^\dagger + h.c.) + \sum_i \phi_i n_i \\
H_{cl} &= \frac{1}{U} \sum_i (|\Delta_i|^2 + \phi_i^2)
\end{aligned} \tag{4.2}$$

As mentioned earlier, the presence of the ‘density’ field  $\phi$  is important, especially in disordered systems, since it captures the enhancement of disorder due to interaction effects.

We use a Metropolis algorithm to solve this model at various disorder, using a cluster based approach that allows access to lattice sizes  $\sim 24 \times 24$ . The disorder  $V_i$  is chosen from a box normalised distribution between  $\pm V$ , which sets the scale for the magnitude of disorder. Quantities calculated at finite disorder are averaged over at least  $\sim 10$  different realisations at the same magnitude. Below, we describe the parameters we choose for these calculations in more detail.

## 4.2.2 Parameters

The main parameters in the model that dictate the physical behaviour are the coupling  $U/t$ , the chemical potential  $\mu$  which determines the average density  $n$  and the range of disorder values used, characterised by the range of  $V$ .

Since the experimental materials we have considered all lie in the weak coupling BCS limit, we want the coupling values to be as small as possible in order to make meaningful comparisons. Since our lattice size  $\sim 24 \times 24$ , this fixes our lowest coupling value at  $U/t \sim 2$ , below which the clean coherence length  $\xi_0$  becomes comparable to the system size. Here, as we saw from the previous chapter, even though the clean  $\Delta_0/T_c$  values  $\sim 8$ , much higher than the BCS value, the system shows BCS like characteristics such as a vanishing gap above  $T_c$ , with a practically non-existent pseudogap. Hence, even though this is ‘intermediate’ coupling in strict terms, one can expect to make some meaningful comparisons at this coupling value (nevertheless, there are also differences that will be highlighted later), and thus we adopt  $U/t = 2$  for our calculations.

On the other hand, we choose our  $\mu$  such that  $n \sim 0.9$ . This facilitates comparisons with QMC which are done at similar densities, and ensures a high clean transition temperature  $T_c$  while avoiding the charge density order at  $n = 1$ . We vary our disorder strength  $V/t$  from 0 – 3, which allows us to access our nominal critical point  $V_c$  as well as points well inside the insulating regime. As remarked earlier, we average our results over at least  $\sim 10$  disorder copies at each disorder strength which seems to be good enough to provide robust answers.

### 4.2.3 Summary of main results

Our main results, at intermediate coupling, are the following:

1. For  $V \ll V_c$  the single particle gap closes at  $T_c$ , but beyond  $V \sim 0.25V_c$  there emerges a pseudogap window above  $T_c$ , and when  $V > 0.75V_c$  a *hard gap* persists for  $T > T_c$ .
2. The normal state resistivity  $\rho(T)$  is ‘insulating’, with  $d\rho/dT < 0$ , already at  $V \sim 0.5V_c$  so, for  $0.5V_c < V < V_c$  one actually observes an *insulator to superconductor* transition on cooling the system.
3. Increasing temperature leads to a growth in the low frequency single particle and optical weight across  $T_c$ , over a window  $\delta T \ll T_c$  at weak disorder and  $\delta T \gtrsim T_c$  at strong disorder. The  $T \gg T_c$  weight correlates closely with the ‘superconducting fraction’ in the ground state.
4. Increasing disorder leads to *non monotonic* behaviour of the low frequency single particle and optical weight, with a peak around  $V_c(T)$ .

There is already experimental evidence for 1 and 2. The other predictions can be tested experimentally and correlated with spatial data where available. Now, the detailed results.

## 4.3 Results

This section will describe our results on the transport, the density of states and the optical conductivity in detail. After describing these results over the whole disorder window  $[0, V_c]$ , we will compare the single particle spectral characteristics and the two particle ones and try to understand the connections between them as dictated by our model. We will also remark upon the connections of these results to experiments and compare them with well known limits, such as the weak disorder BCS limit. More comprehensive discussion on the specific features of our model that lead to these results and their usefulness and limitations in the light of results from real systems will be left for the Discussion section following this.

### 4.3.1 Phase diagram

We begin with the  $V-T$  phase diagram in Fig.4.2(a), detailing the degradation of  $T_c$  with increasing disorder, and the different phases in terms of transport and spectral character. As discussed before, we use the structure factor  $S(q=0)$  to determine the transition temperature  $T_c$  from the rise of the curve. The detailed behaviour of  $S(q=0)$  with increasing disorder is plotted in Fig.4.2(b), which

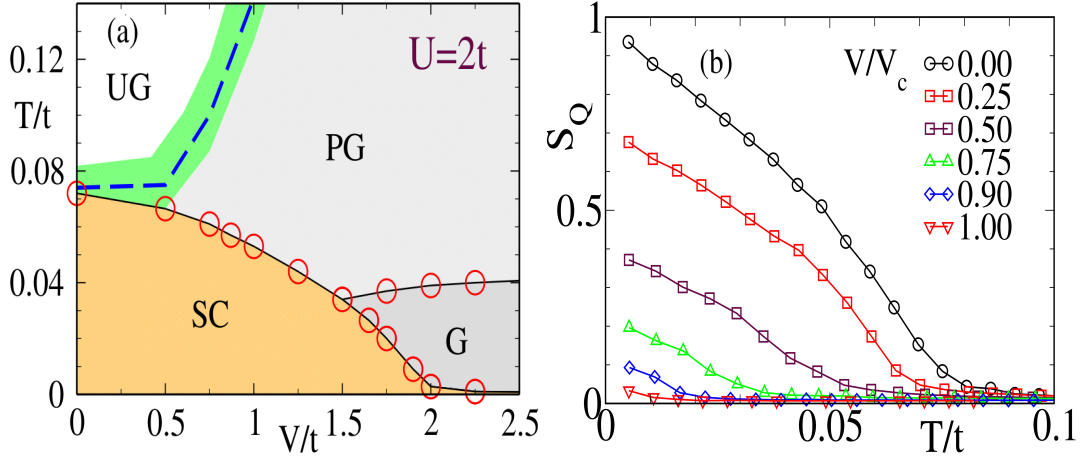


Figure 4.2: (a): Phase diagram for  $U = 2t$  showing the superconducting (SC), and the following non superconducting phases: gapped (G), ungapped (UG) and pseudogapped (PG). The SC  $T_c$  is determined from the behaviour of  $S(q = 0)$ , whose temperature dependence at various disorder is shown in (b). We take the critical disorder  $V_c \sim 2t$ . The tail shows the exponentially small superconducting  $T_c$  surviving beyond  $V_c$ . A normal state pseudogap shows up for  $V \gtrsim 0.25V_c$  and for  $V \gtrsim 0.75V_c$  the  $T \gtrsim T_c$  phase actually has a hard gap. The crossover between pseudogapped and notionally ungapped phase is shown by the green area. The blue dashed line shows the transition from an ‘insulating’ ( $d\rho/dT < 0$ ) to ‘metallic’ regime, which lies within the broad crossover.

clearly shows how the superconducting  $T_c$  is suppressed. In the absence of disorder SC order is lost at  $T_c = T_c^0 \sim 0.07t$ , benchmarked with QMC results [165]. Increasing disorder leads initially to a slow suppression of  $T_c$  which accelerates for  $V > 1.5t$ . Our method reduces to HFBdG at  $T = 0$  so the ground state within our scheme is in principle always superconducting. However, the phase stiffness of the HFBdG state reduces quickly with increasing disorder and for  $V \gtrsim 2t$  we do not observe a transition down to  $\sim 0.05T_c^0$ . We indicate the disorder scale associated with this resolution limit on  $T_c$  as  $V_c$ . Fig.4.2(a) also indicates the exponentially small  $T_c$  that survives in principle beyond our  $V_c$ . This would be pushed to zero by quantum phase fluctuations in the  $\Delta_i$ .  $T_c^0$  and  $V_c$  set the natural scales of temperature and disorder for us. Our observations are:

1. At weak disorder the fractional suppression of  $T_c$  is small, *e.g.*, at  $V = 0.25V_c$ ,  $T_c$  falls less than 10% from  $T_c^0$ . This is qualitatively consistent with the ‘insensitivity’ to disorder predicted by Anderson [31], but that approach fails to be useful beyond weak disorder. We are not aware of analytic results on the suppression of  $T_c$  in this coupling regime, although there are numerical results on the reduction of the phase stiffness [85]. Overall, the weak disorder regime,  $0 < V < 0.25V_c$ , corresponds to almost homogeneous  $|\Delta_i|$  in the ground state, metallic resistivity above  $T_c$ , and no significant anomaly in the normal state density of states (DOS).

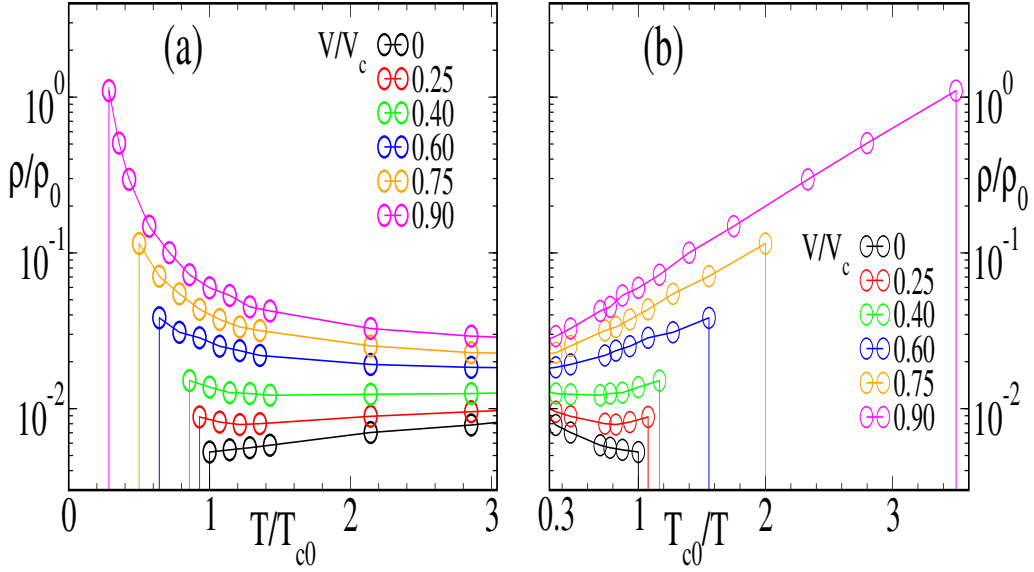


Figure 4.3: (a) The resistivity,  $\rho(T)$ , measured in units of  $\rho_0 = \hbar/(\pi e^2)$ , evolving from metallic to insulating behaviour in the normal state with growing disorder. For  $V \lesssim 0.25V_c$ , it is metallic, between  $0.25V_c \lesssim V \lesssim 0.75V_c$ , it is mixed, showing a thermal transition from ‘insulating’ at low  $T$  to weakly ‘metallic’ at larger  $T$ . Beyond  $V = 0.75V_c$ , the low  $T$  behaviour is exponential  $\rho(T) \propto e^{\Delta_g/T}$ , with  $\Delta_g$  increasing with  $V$ . This is highlighted in (b), where we see that such a fit ceases to be valid below  $V \sim 0.75V_c$ .

2. The intermediate disorder window,  $0.25V_c < V < 0.75V_c$ , resists easy characterisation.  $|\Delta_i|$  in the ground state shows increasing fragmentation [84, 85, 175]. The resistivity is ‘insulating’ near  $T_c$  and crosses over to metallic behaviour at high  $T$ , while the  $T > T_c$  density of states shows a pseudogap.
3. At strong disorder,  $V \gtrsim 0.75V_c$ , the pairing amplitude  $|\Delta_i|$  is very inhomogeneous in the ground state, a hard gap survives in the DOS even above  $T_c$ , and the resistivity shows activated behaviour. This is a regime where the low  $T$  superconducting state emerges from a high  $T$  *insulating* phase, suggesting that the  $T_c$  is no longer controlled by the low energy DOS.

The different phase boundaries would depend on  $U/t$ . Apart from the change in  $T_c^0$  and  $V_c(T = 0)$ , increasing  $U/t$  would lead to an increase in the ‘gapped’ region, while decreasing  $U/t$  would decrease the gapped window in favour of the PG (and the UG to PG crossover could be pushed to larger  $V/V_c$ ). We will present some results in the next chapter on the dependence of the phase boundaries and their evolution with coupling.

### 4.3.2 Resistivity

We have described the method that we employ for calculating the resistivity and optical conductivity in Sec.2.3.6. Here, we recount them briefly before moving on to the main results.

$\rho(T)$  is computed using the Kubo formula, via the low frequency limit of the optical conductivity  $\sigma(\omega)$ . Formally  $\sigma(\omega) = -\omega^{-1} \text{Im}(\Lambda_{xx}(q=0, \omega))$  where the current-current correlation function is defined by

$$\Lambda_{xx}(q=0, \omega) = \frac{1}{\mathcal{Z}} \sum_{n,m} |\langle n | j_{xx} | m \rangle|^2 \frac{e^{-\beta E_n} - e^{-\beta E_m}}{\omega + E_n - E_m + i\delta}$$

The  $|n\rangle, |m\rangle$  are many particle eigenstates of the system,  $j_{xx}$  is the current operator. For the regular part,  $\sigma_{reg}(\omega)$ , *i.e.*, excluding the superfluid response, it simplifies within our static auxiliary field theory to:

$$\begin{aligned} \sigma_{reg}(\omega) = & \sum_{a,b} F_1(a,b) \frac{(n(\epsilon_a) + n(\epsilon_b) - 1)}{\epsilon_a + \epsilon_b} \delta(\omega - \epsilon_a - \epsilon_b) \\ & + \sum_{a,b} F_2(a,b) \frac{(n(\epsilon_a) - n(\epsilon_b))}{\epsilon_a - \epsilon_b} \delta(\omega - \epsilon_b + \epsilon_a) \end{aligned}$$

where, now, the  $\epsilon_a, \epsilon_b > 0$ , *etc.*, are *single particle eigenvalues* of the BdG equations, the  $n(\epsilon_a)$ , *etc.*, are Fermi functions, and the  $F$ 's are current matrix elements computed from the BdG eigenfunctions. The dc resistivity is defined for  $T > T_c$  via  $\rho^{-1} = \omega_0^{-1} \int_0^{\omega_0} \sigma_{reg}(\omega) d\omega$ , where  $\omega_0 \sim 0.1t$ .

Fig.4.3(a) shows  $\rho(T)$  for different  $V$ . We use  $d\rho/dT > 0$  to indicate a metal and  $d\rho/dT < 0$  to indicate an insulator. Upto  $V \sim 0.25V_c$  the resistivity is metallic at all  $T$ , except very near  $T_c$ . For  $0.25V_c < V < 0.75V_c$ , however, the behaviour is mixed, with ‘metallic’ character at high  $T$  and an ‘insulating’ window below. As the companion plot, Fig.4.3(b), shows the weakly insulating behaviour cannot be characterised by a  $T$  independent gap in the DOS. Beyond  $0.75V_c$  the resistivity is insulating at all  $T$ , we have checked it upto  $T = 0.3t$ . The log plot in Fig.4.3(b) shows that the resistivity can be modeled as  $\rho(T) \propto e^{\Delta_g/T}$ , with a weakly disorder dependent coefficient  $A$  and an activation scale  $\Delta_g \sim 2.5(V - 0.75V_c)$ .

The large disorder regime admits a simple explanation in terms of the current paths. The low energy excitations are localised in the superconducting clusters that form at  $T = 0$ . Since the SC regions are ‘disconnected’ at  $T > T_c$  all current paths have to pass partly through the insulating matrix, leading to an activation factor in the conductance. At weaker disorder the SC clusters have a tenuous connection and the detailed frequency dependence of the DOS is important.

Overall, we observe that for our chosen  $U = 2t$ , superconductivity can arise out of a metallic or an insulating normal state. Our calculation does not hint at any ‘universal’ temperature independent

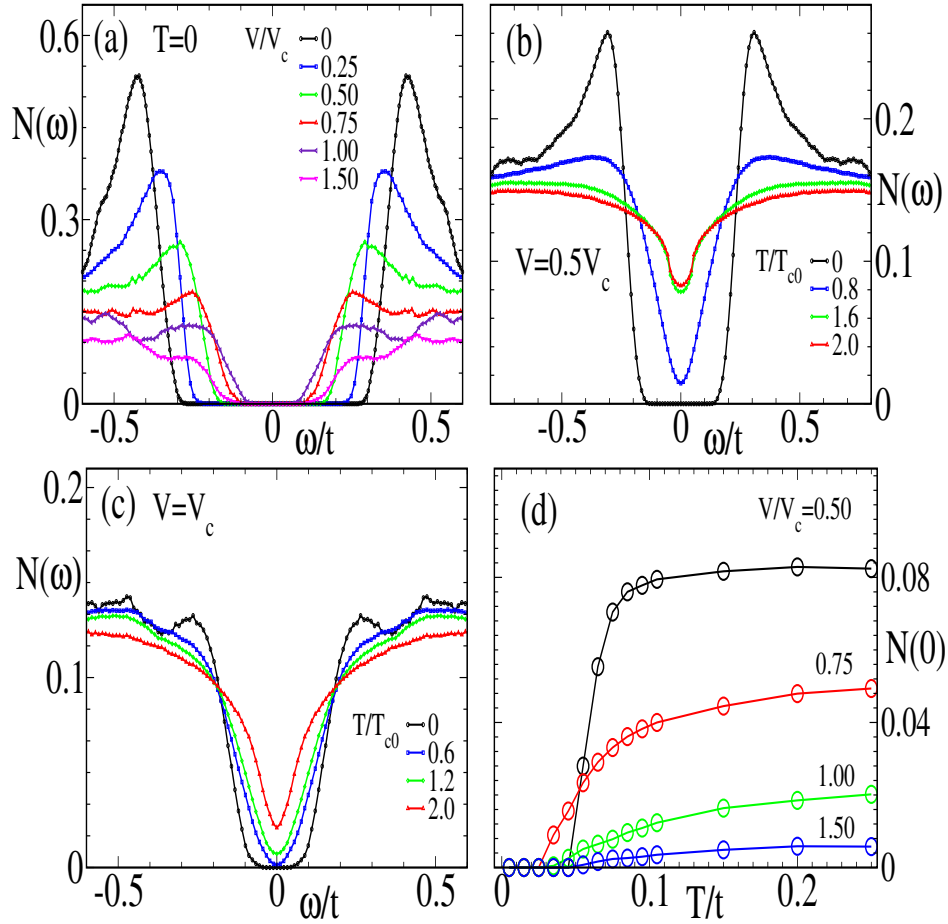


Figure 4.4: Density of states at  $U = 2$ . (a) The DOS at low temperature, showing the persistence of a gap at all  $V$ , while the coherence peaks are difficult to discern beyond  $V \sim 0.75V_c$ . (b) Temperature dependence of the DOS for  $V = 0.5V_c$ , already showing a noticeable pseudogap for  $T > T_c$ . (c) Same as (b) but for  $V \sim V_c$ , where the system is insulating at all temperature. (d) Temperature dependence of  $N(0)$ , the DOS at the Fermi level, for different disorder.

resistance at  $V = V_c$ , apparently consistent with recent experimental analysis [53].

### 4.3.3 Density of states

Fig.4.4 shows the variation in the single particle DOS with disorder and temperature. If  $\epsilon_n$  and  $\{u_n^i, v_n^i\}$  are the positive BdG eigenvalues and eigenvectors, respectively, in some equilibrium configuration, the DOS is computed as

$$N(\omega) = \left\langle \sum_{i,n} (|u_n^i|^2 \delta(\omega - \epsilon_n) + |v_n^i|^2 \delta(\omega + \epsilon_n)) \right\rangle$$

where the angular brackets indicate thermal average.

In Fig.4.4(a) we show the DOS plots at  $T = 0$  for varying disorder, from  $V = 0$  to  $V = 1.5V_c$ . The following features are noteworthy.

1. The system is gapped for all  $V$ . The ‘gap’ shows a non-monotonic character, decreasing upto  $V \sim V_c$  and increasing from thereon. These results match well with previous BdG [85] and QMC [88] benchmarks.
2. The coherence peaks decrease with increasing  $V$ , and beyond  $V \sim 0.75V_c$  they are hard to discern in the DOS. The ‘rise’ of the DOS at the gap edge is ideally sharp in the clean limit, corresponding to the square root BCS singularity, but for  $V \gtrsim 0.75V_c$  the rise is much gentler.

Fig.4.4(b) shows the thermal evolution at  $V = 0.5V_c$ , intermediate disorder, while Fig.4.4(c) shows the same at  $V = V_c$ . For  $V = 0.5V_c$  the coherence peak at the gap edge vanishes at  $T \sim T_c \approx 0.8T_c^0$ , the low frequency DOS grows steadily with increasing temperature, but a pseudogap feature survives upto  $T \sim 2.5T_c$ . Fig.4.4 shows the result at  $V = V_c$ , where the system retains a hard gap with increasing temperature till  $T \sim 0.5T_c^0$  and a deep pseudogap thereafter.

Figure Fig.4.4(d) shows the temperature dependence of  $N(0)$ , the DOS at the Fermi level, for a few  $V$ . At  $V = 0.5V_c$ ,  $N(0)$  is essentially zero till  $T \sim T_c$  and then rises quickly and saturates to a high  $T$  asymptote. With growing disorder the temperature interval  $\delta T(V)$  over which the rise occurs increases and the ‘asymptotic’ high temperature value reduces. We find that this high temperature value at a given disorder roughly corresponds to the superconducting fraction in the ground state [175] at that disorder.

### 4.3.4 Optical conductivity

Fig.4.5(a)-(c) shows aspects of the optical conductivity at two representative temperatures for various  $V$ , while Fig.4.5(d) shows the integrated low frequency weight as increasing disorder drives the SIT.

In a disordered superconductor, the real part of the optical conductivity consists of a delta function at  $\omega = 0$  (signifying dissipationless transport) and a ‘regular’ part  $\sigma_{reg}(\omega)$ . Within a mean field picture,  $\sigma_{reg}(\omega)$  at  $T = 0$  is suppressed for  $\omega \lesssim 2\Delta$ , the gap scale. Beyond this  $\sigma_{reg}$  rises to a peak and for  $\omega \gg \Delta$  tends to the disordered metal limit,  $\Gamma/(\omega^2 + \Gamma^2)$ , where  $\Gamma$  is the scattering rate. Fig.4.5(a) shows the low  $T$  result at different  $V$ , consistent with this general expectation. The low  $V$  curves have a gap, rise to a relatively sharp maximum and then fall off. Increasing  $V$  increases  $\Gamma$  making the fall off broader. In what follows we use just  $\sigma(\omega)$  rather than  $\sigma_{reg}(\omega)$  to denote the regular part.

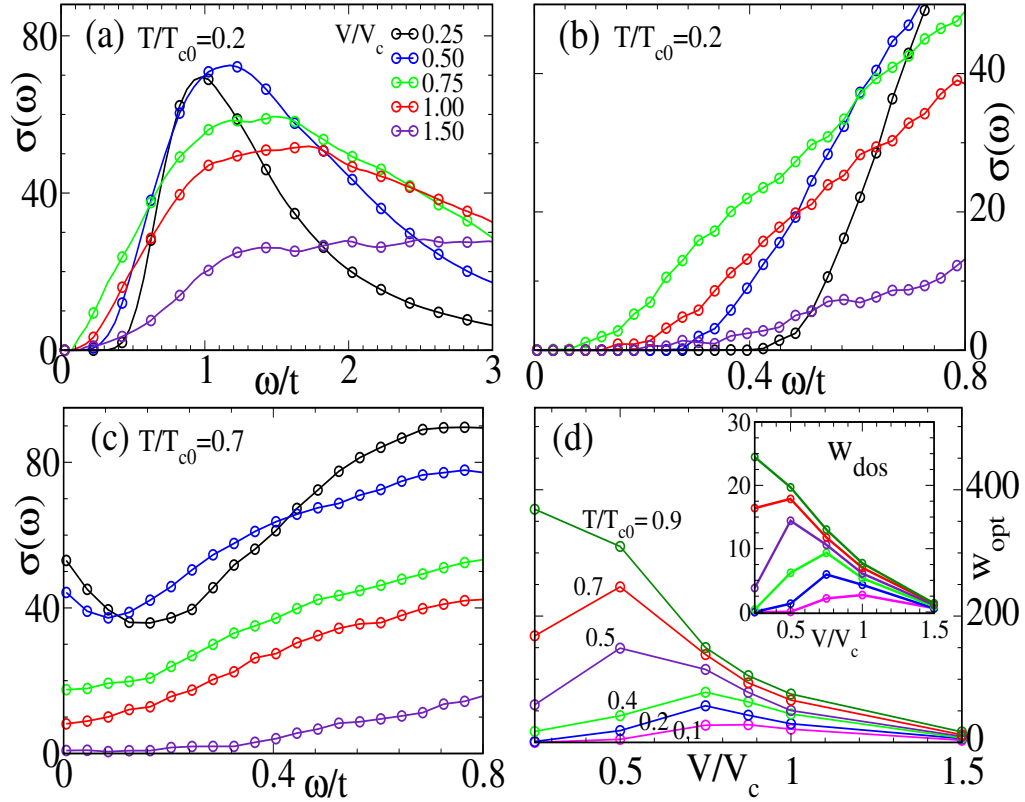


Figure 4.5: Optical conductivity and low frequency optical spectral weight. (a) The behaviour of  $\sigma(\omega)$ , measured in units of  $\sigma_0 = \pi e^2/\hbar$ , over a wide frequency range for disorder varying across the SIT. The temperature is  $T = 0.2T_c^0$ . (b) The low frequency behaviour of  $\sigma(\omega)$  for varying  $V$  (same legends as in panel (a)), at  $T = 0.2T_c^0$ . (c) Same as in (b), now at  $T = 0.7T_c^0$ . Notice the absence of any gap, and the low frequency upturn, in samples with  $V = 0.25V_c$  and  $V = 0.5V_c$  which are still below their respective  $T_c$ . (d) Disorder dependence of the low frequency optical spectral weight,  $w(V, \Omega)$ , see text, at different  $T$ . Inset shows low frequency weight of the single particle spectrum.

It is useful to compare these results with that of Mattis-Bardeen (MB) theory [135], which is formulated in the weak coupling limit. Qualitatively, within MB theory the thermal excitation of quasiparticles to the gap edge, with a probability  $\sim e^{-\Delta(T)/T}$ , leads to a ‘subgap’ feature in  $\sigma(\omega)$  at finite  $T$ . Due to the large DOS at the gap edge this contribution to  $\sigma(\omega)$  is large at low  $\omega$ . Disorder broadens the coherence peaks and makes this subgap  $\omega$  dependence flatter.

Fig.4.5(b) shows the low frequency results for  $\omega \lesssim 2\Delta_0$  at  $T = 0.2T_c^0$ . In this frequency range,  $\sigma(\omega)$  decreases monotonically with decreasing frequency, forming a hard gap at a disorder dependent frequency  $\omega_g(V)$ .  $\omega_g$  is lowest between  $0.75V_c$  and  $V_c$ , which seems to match with the critical disorder  $V_c(T)$  at this  $T$ , see Fig.1. We do not find any discernible subgap feature at this temperature. The thermal factor  $e^{-\Delta/T} \sim e^{-4T_c^0/0.2T_c^0}$  is too small.

At  $T = 0.7T_c^0$ , Fig.4.5(c), the cleaner samples do show an upturn reminiscent of MB theory.

However, even here for  $V \gtrsim 0.5V_c$  the low frequency peak is absent due to the disorder and temperature induced broadening of the coherence peak.

In Fig.4.5(d), we show the the low frequency optical weight  $w_{opt}(V, T, \Omega) = \int_0^\Omega d\omega \sigma(\omega, V, T)$  with  $\Omega = 0.2t$ . We find that the maximum in  $w_{opt}(V, T)$  at a given  $T$  occurs at a disorder  $V_{max}(T)$  that tracks the critical disorder  $V_c(T)$ . The inset shows the low frequency single particle weight  $w_{dos}(V, T) = \int_0^{\Omega/2} d\omega N(\omega, V, T)$  and its strong correspondence with  $w_{opt}(V, T)$ . At  $T = 0$  the behaviour of  $w_{dos}$  is consistent with earlier observation [85] that the gap is minimum close to  $V_c$ . The resulting maximum in  $w_{dos}$  persists, surprisingly, at finite  $T$  as well and also shows up in the behaviour of  $w_{opt}$ .

Since the weights are readily measurable, a qualitative explanation may be useful. Within our scheme the optical spectrum arises as a convolution over the single particle Greens function, so understanding  $w_{dos}(V, T)$  can shed light on  $w_{opt}$  as well. Fig.4.4(d) provides a hint, where, crudely,  $N(0, V, T)$  rises from zero at  $T \ll T_c$  to its high  $T$  asymptote,  $N_\infty(V)$ , say, across  $T_c$ .  $N_\infty(V)$  reduces monotonically with  $V$ . If we ignore the ‘width’  $\delta T$  of the low to high temperature transition, then  $N(0, V, T) \approx 0$  for  $T < T_c(V)$  and  $N(0, V, T) = N_\infty(V) \propto f_{SC}(V)$ , the superconducting fraction, for  $T > T_c$ . If we approximate  $w_{dos} \propto N(0)$ , then at a given  $T < T_c^0$ , the  $V < V_c(T)$  samples have  $w_{dos} \sim 0$ , and the  $V > V_c(T)$  samples have  $w_{dos} \sim N_\infty(V)$ , with  $dN_\infty(V)/dV < 0$ . The peak would be obviously at  $V \sim V_c(T)$ . The real  $V$  dependence is of course smoother than what the crude argument above suggests.

This observation ties together *independent measurements* on density of states, optical weight, and the spatial character of the superconducting state over the complete disorder-temperature window.

## 4.4 Discussion

In this section, we discuss and clarify some aspects of our model and results which may not be apparent from the description of our data that has been provided so far. We first begin by clarifying some numerical aspects, examining the robustness of our transport results with system size and frequency intervals used for averaging. Then, we shift our focus to some issues involving the physics of the system as captured by our model, concentrating on:

1. The microscopic basis of our results, which are determined by the detailed behaviour of the auxiliary fields  $\Delta_i$  and  $\phi_i$  in the disordered background.
2. The effect of the attractive interaction on Anderson localization, and its subsequent modification of transport properties.

3. The nature of the superconductor thermal transition at  $T_c$ , which is expected to be in the BKT class, and its indicators such as vortex physics, and finally,
4. Expanded discussion on previous observations on the limitations of our approach and the connection of our results to experimental data.

#### 4.4.1 Numerical checks on transport

The transport in our system is calculated on finite lattice systems of size  $\sim 24 \times 24$ . Since our system is finite, the energy eigenvalues are also separated by finite intervals, and this further forces us to choose some arbitrary parameters, such as the averaging interval  $\Delta\omega$  mentioned earlier to approximate the limit  $\sigma(\omega \rightarrow 0)$ . To examine the robustness of our results w.r.t. the size and the interval choice, we show, in Fig.4.6 the dependence of the resistivity on lattice size and frequency interval. Fig.4.6(a) shows that beyond  $L = 16$ , the resistivity shows no further change with increasing lattice size. Figs.4.6(b), (c) and (d) show the dependence on the averaging interval at weak ( $V = 0.25V_c$ ), moderate ( $V = 0.5V_c$ ) and strong ( $V = 0.75V_c$ ) disorder respectively. We find that as long as the interval is much larger than the finite size gap and much smaller than the other electronic scales in the problem, the results do not depend significantly on the particular value of  $\Delta\omega$ .

#### 4.4.2 The microscopic picture

Within our approach the thermal properties are controlled by the mean value and thermal fluctuations of the ‘pairing’ field  $\Delta_i$  and the ‘density’ field  $\phi_i$ . Disorder creates inhomogeneities in  $n_i$  which are fed back via the Hartree shift  $\phi_i$  leading to an amplified effective disorder  $V_{eff}^i = V_i - \phi_i$ . This is shown in Fig.4.7. For  $V/t \rightarrow 0$  the bare and effective disorder are similar, while for  $V \sim V_c \sim 2t$ ,  $V_{eff} \sim 1.7V$ .

Transport and spectral features are determined by the combined effect of  $V_{eff}^i$  and scattering from the  $\Delta_i$ . While the detailed local behaviour of these quantities will be taken up in the next chapter, here we briefly borrow some of these results to explain our observations on the global properties.

1. At weak disorder,  $V \lesssim 0.25V_c$ , the ground state has almost homogeneous  $n_i$  and  $|\Delta_i|$ , with perfect phase correlation. With increasing  $T$ , the  $\langle |\Delta_i| \rangle$  increase and the  $\theta_i$  randomise. The growing amplitude and phase disorder lead to increased scattering and  $d\rho/dT > 0$  for  $T > T_c$ . The  $n_i$  remain roughly homogeneous over the relevant  $T$  window and the potential scattering just adds a constant contribution to the overall resistivity.

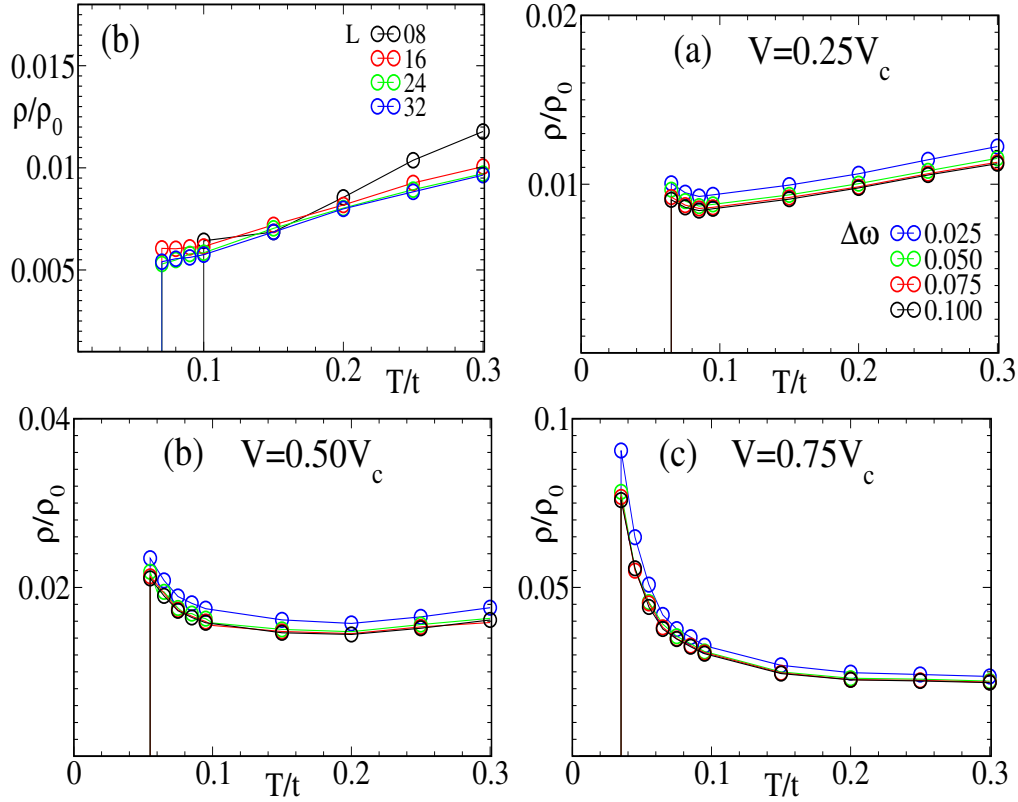


Figure 4.6: (a): Size dependence of clean resistivity. (b), (c) and (d): Dependence on the averaging interval  $\Delta\omega$  at weak ( $V = 0.25V_c$ ), moderate ( $V = 0.5V_c$ ) and strong ( $V = 0.75V_c$ ) respectively.

- At intermediate disorder,  $0.25V_c \lesssim V \lesssim 0.75V_c$ ,  $n_i$  is noticeably inhomogeneous in the ground state, leading to a large  $V_{eff}^i$ , but homogenize with increasing  $T$ . The  $|\Delta_i|$ , on the other hand, grow with increasing  $T$  in the high temperature regime. The result is a crossover in the resistivity with increasing  $T$ , with the  $T \gtrsim T_c$  region showing  $d\rho/dT < 0$  due to weakening  $V_{eff}^i$ , and the  $T \gg T_c$  region showing  $d\rho/dT > 0$  due to growing scattering from the  $\Delta_i$ . A prominent pseudogap starts to form below  $T_{corr} \lesssim T_c^0$ , where strong local correlations appear among  $\Delta_i$ , and deepens with decreasing  $T$  until  $T_c$ , where the bulk superconducting transition takes place and a hard gap is formed.
- At large disorder,  $V \gtrsim 0.75V_c$ , the  $n_i$  inhomogeneity is very large in the ground state and SC clusters form only in ‘favourable’ regions [175] of this landscape. The insulating regions have a larger effective gap than the SC clusters. The  $n_i$  inhomogeneity, and the large  $V_{eff}^i$  survives to  $T \gg T_c$  and leads to the activated resistivity.

While this explains our results in terms of the behaviour of the auxiliary fields  $\Delta_i$  and  $\phi_i$ , one would still want to understand these in the context of the  $U = 0$  problem, where Anderson localization effects should be visible even at weak disorder in two dimensions. It seems, however, that

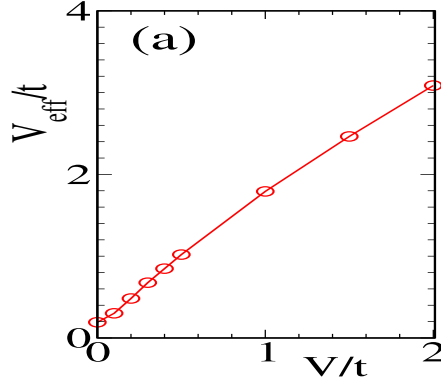


Figure 4.7: Effective disorder  $V_i^{eff} = V_i - \phi_i$  with increasing disorder.

the interaction effects (encoded in the behaviour of the  $\Delta_i$  and  $\phi_i$ ) alter the localization behaviour of the system considerably. Below, we consider this aspect in greater detail.

### 4.4.3 Interaction effects on localization

In view of the finite lattice size of our system, weak localization effects probably cannot be incorporated satisfactorily in our results. While the discussion above hinted at the substantial effect of interactions on the behaviour of the observables, one can still ask whether our system size manages to capture all the effects satisfactorily. Below, we attempt to answer this question and justify our results.

We have already seen how the ‘density’ field  $\phi_i$  amplifies the effective disorder and affects the system properties. We found that for  $V/t \rightarrow 0$ , the bare and effective disorder are similar, while for  $V \sim V_c \sim 2t$ ,  $V_{eff} \sim 1.7V$ . At weak disorder the localisation length  $\xi_{loc}$  in this 2D system (at the band center) would be exponentially large. At  $V \sim V_c$  the  $\xi_{loc}$  is still larger than  $L = 24$  that we use [178], but these lengths are not relevant for the  $T > T_c$  transport due to the effect of electron electron interactions.

Electron-electron interactions give rise to inelastic scattering at finite  $T$ , mimicked by the disorder in the  $\Delta_i$  in our model. The presence of a finite inelastic scattering length  $L_{in}$  would cut off quantum interference effects, as we already discussed at the beginning of this chapter. A heuristic estimate of the effective localization length can be made in the following way.

The perturbative scattering rate is  $\Gamma_{inel} \sim U^2 N(\epsilon_F) \langle |\Delta^2| \rangle$ , where we assume the phases  $\theta_i$  to be uncorrelated. The associated lengthscale is  $v_F/\Gamma_{inel}$ . Using  $U = 2t$ ,  $N(\epsilon_F) \sim 1/8t$  and  $\langle |\Delta^2| \rangle \sim 0.16$ ,  $\Gamma_{inel} \sim 0.08t$ . The associated lengthscale is  $\sim 12$  lattice spacings, well within system size.

The temperature dependence of the  $T > T_c$  resistivity at weak disorder is, thus, controlled not by weak localization but by the ‘phase randomness’ in the  $\Delta_i$ . At stronger disorder the pseudogap

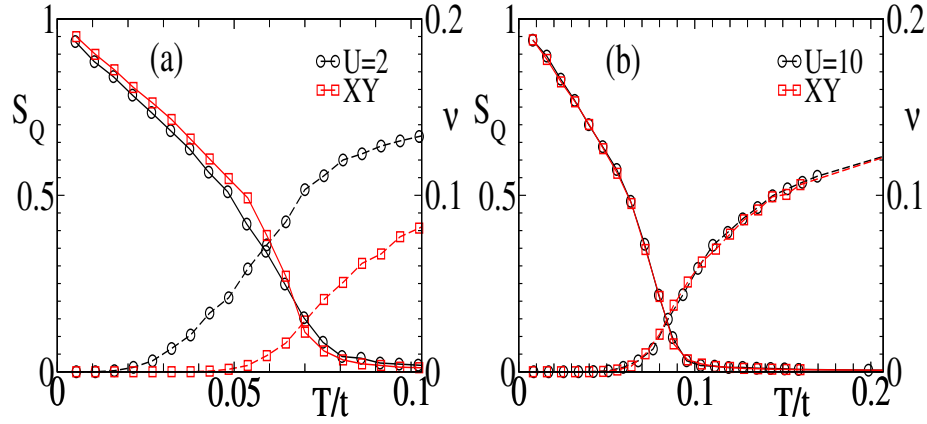


Figure 4.8: Vortex density and structure factor with temperature for (a):  $U/t = 2$  and (b):  $U/t = 10$ . The black lines denote the results from our calculations while the red lines denote corresponding XY model results with the same  $T_c$ .

induced by the pairing fields persists to  $T > T_c$ . This spectral weight suppression is only weakly size dependent, as is the resulting fermionic contribution to conductivity.

Overall, the conductivity at  $U = 2t$  within our static approximation seems to be adequately captured by a  $24 \times 24$  lattice as a result of the effect of interactions. Thus, the weak disorder results, especially the metallic regime (which probably should not exist in the  $U = 0$  problem in two dimensions) display the effects of interactions, and are not due to the failure to include localization effects due to finite size restrictions.

#### 4.4.4 Thermal transition and vortex physics

In two dimensions, the thermal transition from a superconducting to a metallic/insulating state is a BKT transition, driven by the unbinding of vortex and antivortex pairs, since conventional long range order is forbidden by the Mermin-Wagner theorem. While our finite size system doesn't allow us to directly confirm the algebraic scaling properties below  $T_c$  or to visualize individual vortices above  $T_c$ , it nevertheless seems to capture the basic vortex physics correctly. To demonstrate this, we calculate a vortex density by using the 'site-vortex' measure calculated in Erez, *et. al.* [137].

Fig.4.8 shows the vortex density in the clean limit at  $U/t = 2$  and 10, comparing them with the corresponding XY models (which undergo a BKT transition in two dimensions) that give the same  $T_c$ . The proliferation of vortices before  $T_c$  and their subsequent saturation above the same demonstrates that our model captures the basic aspects of vortex physics correctly. The deviation of the detailed behaviour from the XY model at  $U/t = 2$  is, of course, due to the fact that the weak coupling transition, though in the XY class, is not identical to the XY model due to substantial amplitude fluctuations, as discussed in the previous chapter.

### 4.4.5 Limitations of our method

The primary approximations in our model has already been noted in Chapter.2. Out of these, the effect of using both auxiliary fields has already been discussed in detail in the previous chapter. On the other hand, the limitations of the cluster approximation are not valid in this case, since there are no modulated phases. Hence, we consider the other three, namely, the static approximation in the auxiliary fields, the finite size effects and the absence of Coulomb interactions, and describe their effects in greater detail below.

1. The static approximation: the auxiliary fields are in principle time dependent and their temporal (quantum) fluctuations can be significant in the following two regimes:
  - (a) The vicinity of the  $T = 0$  SIT. As the electronic DOS becomes gapped due to pair formation, the dynamics of these bosonic pairs can play a significant role in transport and low frequency optics. In particular, the Higgs mode becomes soft and one can presumably see its signatures in the optical conductivity [179] This has been emphasized in some theoretical studies that we have discussed before [134, 177]. However, for the  $U/t = 2$  that we have used, Fig.4.2(a) shows that the finite temperature SIT, for  $V \lesssim 0.75V_c$ , occurs in the presence of a finite DOS at the fermi level. So, at weak to moderate coupling, and across the finite temperature SIT, our approach should be useful.
  - (b) In the critical regime, close to  $T_c$ , where fluctuation corrections (Aslamazov-Larkin and Maki-Thompson) [180] are important. These also involve the dynamics of the pairing fields, which are absent in our scheme. However, away from the immediate vicinity of  $T_c$  the effects that we highlight, arising from a combination of the disorder and Hubbard interaction, would dominate.
2. System size: weaker coupling,  $U/t \lesssim 1$ , is relevant experimentally, but difficult to access with current size limitations since the coherence length grows as  $1/\Delta_0$ . Our system size,  $\sim 24 \times 24$ , is significantly larger than what is accessible within QMC but still much smaller than the inhomogeneity scales observed experimentally. As a result, some of the predictions we make are only of qualitative value in the experimental context. We discuss these in greater detail when we compare our results with experimental data in the next subsection.
3. Coulomb effects: Coulomb interactions can affect superconductivity in two ways:
  - (a) weakening of the effective pairing interaction [181], and,
  - (b) an increase in phase fluctuations [182].

The first effect can lead to an SIT driven by a vanishing gap. However, most recent experiments suggest that the SIT is driven by phase fluctuations in a fragmented ground state, and not so much by a vanishing gap. In this sense, our model captures the correct phenomenology.

#### 4.4.6 Comparison to experiments

When comparing with experiments, it must be kept in mind that  $U = 2t$  is already beyond the weak coupling BCS regime, with  $2\Delta/kT_c^0 \sim 8$  instead of 3.5. Most real materials, explored in the SIT context are however in the BCS window, so the relevant  $U_{eff}/t \lesssim 1$ . This is also borne out by the rather low  $T_c^0 \sim 10\text{K}$  of these materials [56, 60]. Additionally, Coulomb effects are neglected in our model. For the different indicators that we have calculated, a comparison to experiments reveal the following:

1. Resistivity: While our observation of a metal to insulator crossover in the normal state transport is consistent with experiments, experimental resistivities are less insulating than we observe [44, 52, 60]. For instance, at  $V = 0.75V_c$ , with  $T_c = 0.4T_c^0$ , our resistivity already shows insulating behaviour, falling to one-fourth of its maximum value by  $T = 3T_c^0$ , while the two dimensional TiN sample in [56] only falls to 60% of its maximum value even though  $T_c \sim 0.1T_c^0$  for that sample. Similar behaviour is seen in three dimensional NbN samples [60].
2. Density of states: Pseudogap effects are more pronounced in our case, extending to larger temperatures. For instance, at  $V = 0.5V_c$ , this scale is around  $T = 2.5T_c^0$ , and by  $V = V_c$ , it extends beyond  $T = 4T_c^0$ . In contrast, experiments on three dimensional systems [60] indicate that the pseudogap vanishes at a temperature  $T^*$  that decreases initially with increasing disorder, and finally becomes constant at  $T^* \sim 0.5T_c^0$  at large disorder. Two dimensional systems [55], on the other hand, do seem to show a qualitatively similar increase as ours, though their relevant scales are much smaller (for instance at  $T_c = 0.1T_c^0$ ,  $T^* \sim 1.4T_c^0$ , whereas our scale is greater than  $4T_c^0$ .)
3. Optics: Low frequency features are sharply depressed, at low  $T$ , in our model at large disorder, whereas there is a much more modest effect in experiments. Furthermore, some recent experiments have shown signatures of collective modes close to the critical point. [43, 62].
4. Spatial character: Our results for local indicators reveal significant similarity, but also points of difference, in terms of spatial dependence and thermal variation, with recent experiments [61]. They will be discussed in greater detail in the next chapter.

5. Coulomb effects: Coulomb effects cause a characteristic wide dip in the DOS [183], which is absent from our results. They also lead to a contribution similar to the weak localisation correction to the conductivity [183, 184]. As noted earlier, this has led to proposals that the moderate disorder weakly insulating behaviour is caused by Coulomb interactions. However, we have shown an alternative way in which one can get the same qualitative effect from the interplay of the disorder and attractive interaction alone.

## 4.5 Conclusions

We have studied the transport and spectral characteristics of a disordered s-wave superconductor over the complete disorder and temperature window relevant for the superconductor-insulator transition. We have identified the metal to insulator crossover in the normal state with increasing disorder and demonstrate a disorder window where the superconductor arises out of a high temperature ‘insulating’ state. We map out the disorder and temperature dependence of the single particle and optical spectra, discover that their low frequency weight is non monotonic with disorder, and relate the weight to the superconducting spatial fraction in the disordered ground state.



# TUNNELING SPECTROSCOPY ACROSS THE SUPERCONDUCTOR-INSULATOR TRANSITION

This chapter will describe our work on the local properties of disordered superconductors and their evolution with disorder and temperature. As we have described before, recent advances in scanning tunneling spectroscopy reveal the presence of superconducting nanoregions well past the bulk thermal transition in strongly disordered superconductors. The analysis of the thermal evolution of this highly inhomogeneous state requires the inclusion of thermal fluctuations and high spatial resolution to track the local properties. Our Monte Carlo tool allows us to capture the spatially differentiated amplitude and phase fluctuations in such a material and establish spatial maps of the coherence peak as the superconductor is driven through the thermal transition. Through our analysis of the local density of states we provide a comprehensive description of the evolution of these nanoregions, detailing how they shrink and fragment with increasing temperature, but survive in small clusters to a temperature  $T_{clust} \gg T_c$ . The gap (or pseudogap) in the spectrum, on the other hand, survives in general to another independent scale,  $T_g$ , depending on the strength of interaction. This multiple scale description is consistent with recent measurements, and together with the global results that we presented in the previous chapter, defines the framework for analysing strongly disordered superconductors.

This chapter will be structured in the following way. First, we provide a brief summary of the background work, focussing on the new insight provided by the STM results, and how our approach overcomes these limitations. Then, we briefly recap the model and methods and the parameters we have used, and summarize the main results. The next section describes our work on the spatial characteristics and their evolution, focussing on the local DOS and gap, and their connection to the

superconducting state. This is followed by a discussion section where we describe several aspects of the problem, including the physics of cluster formation, understanding the physics using simple models, and comparisons with experiments. Finally, we conclude.

## 5.1 Background to the problem

As we know, the bulk features of the superconductor-insulator transition (SIT) have been explored experimentally for several decades. However, [39, 50, 53, 132], the recent use of high resolution scanning tunneling spectroscopy (STS) [38, 47, 48, 55, 56, 59–61] has generated new questions about the superconducting state near the SIT. These experiments allow two major advances.

1. They confirm the essentially inhomogeneous nature [38, 47, 48, 55, 56, 59–61] of the superconducting (SC) state, affirming that one does not have a homogeneous suppression of SC order with disorder and temperature.
2. They highlight the presence of *additional temperature scales* in the problem, for example, a cluster formation scale,  $T_{clust}$ , a pseudogap formation scale,  $T_{pg}$ , and, at strong disorder, a possible gap formation scale  $T_g$  - all distinct from  $T_c$ .
3. In addition, STS measurements quantify the detailed behaviour of the local density of states (LDOS) with disorder and increasing temperature [38, 47, 48, 56, 60, 61] - posing a challenge for theories that address only average properties.

Addressing these issues requires an approach that captures the increasing fragmentation in the ground state and retains the crucial phase and amplitude fluctuations that dictate thermal properties. Neither the mean field Hartree-Fock-Bogoliubov-de-Gennes (HFBdG) theory [84, 85], which reasonably describes the ground state but ignores phase fluctuations, nor quantum Monte Carlo (QMC) [88, 140, 141] calculations, which retains all fluctuations but lacks spatial resolution, can address these issues adequately. On the other hand, our auxiliary field scheme, which captures the HFBdG ground state, and the correct  $T_c$  and critical disorder ( $V_c$ ), incorporates these thermal fluctuations. It allows a spatially resolved description of the thermal transition and an estimate of the emergent scales in a strongly disordered superconductor.

## 5.2 Model, methods and main results

In this section, we briefly recap the model and methods and the parameters that we have used, and summarize the main results of our work.

## 5.2.1 Methods and parameters

The model methods and parameters have been described in Chapter.4. Here we restate them quickly for completeness.

We study the attractive two dimensional Hubbard model (A2DHM) in the presence of a random potential picked from a normalised flat distribution between  $\pm V$ .  $\mu$  is the chemical potential which we fix so that the electron density  $n \sim 0.9$  We choose the coupling value  $U/t = 2$  for reasons we have described before. A Hubbard-Stratonovich transformation in the ‘pairing’ and ‘density’ fields, and subsequent neglect of their quantum fluctuations leads to our model.

$$H_{eff} = H_{kin} + \sum_{i\sigma} (V_i - \mu) n_{i\sigma} + H_{coup} + H_{cl} \quad (5.1)$$

where  $H_{coup} = \sum_i (\Delta_i c_{i\uparrow}^\dagger c_{i\downarrow}^\dagger + h.c) - \sum_i \phi_i n_i$  and  $H_{cl} = \frac{1}{U} \sum_i (|\Delta_i|^2 + \phi_i^2)$ .

We solve the coupled fermion-auxiliary field problem through a Monte Carlo [86, 87, 145] for various disorder and temperature values. At finite  $T$  this allows us to consider electron propagation in an amplitude and phase fluctuating background, affording a dramatic improvement in the handling of thermal physics.

## 5.2.2 Main results

Working at our ‘moderate’ coupling value  $U = 2t$ , we confirm the fragmentation of the superconducting ground state with increasing disorder, with SC islands surviving in an ‘insulating’ background. Our key results on thermal behaviour of the LDOS are the following:

1. At weak disorder increasing temperature ( $T$ ) leads to spatially homogeneous closure of the gap at  $T_c$ . For  $V \rightarrow V_c$  the  $T = 0$  gaps are lower in the SC regions than in the insulator, increasing  $T$  reduces all gaps but they survive to a scale  $T_g \gg T_c$ , and a pseudogap is observed to  $T_{pg} \gg T_g$ .
2. In the weakly disordered system the coherence peak in the LDOS vanishes throughout the system at  $T = T_c$ . At strong disorder it survives on isolated clusters to a scale  $T_{clust} \gg T_c$ .
3. The scales  $T_g$ ,  $T_{clust}$ , *etc*, have distinct physical origin. We establish their variation with disorder and interaction strength. Finally, (iv) we suggest a simple lattice Ginzburg-Landau model, with parameters extracted from the electronic problem, that reasonably describes the complex thermal behaviour.

In the next section, we describe these results in detail.

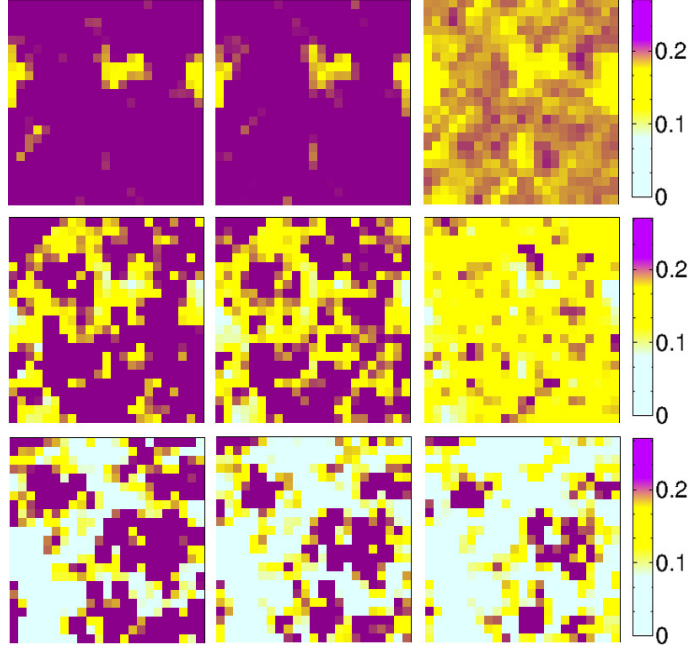


Figure 5.1: Maps of the tunneling conductance integrated over a narrow frequency window around the coherence peak feature in the LDOS (see text). Rows, top to bottom,  $V = 0.2V_c, 0.5V_c, 0.9V_c$ . Columns, left to right,  $T/T_c(V) = 0, 0.5, 1.0$ . Thermal average over 100 configurations.

## 5.3 Results

This section will describe the main results of our work in detail.

### 5.3.1 Tunneling maps

The ‘clean  $T_c$ ’ at  $U = 2t$  is  $T_c^0 \approx 0.07t$ . Increasing disorder pushes our  $T_c$  below measurement resolution ( $\sim 0.005t$ ) at  $V \approx 2t$ . We set this as  $V_c$  [186]. Based on the bulk transport and spectral properties, we characterise [174]  $V \lesssim 0.25V_c$  as ‘weak’ disorder,  $0.25V_c \lesssim V \lesssim 0.75V_c$  as intermediate, and  $V \gtrsim 0.75V_c$  as strong disorder. The weak disorder regime is characterised by a featureless DOS and metallic transport for  $T > T_c$ , intermediate disorder involves a pseudo-gap (PG) for  $T > T_c$  and a thermal crossover from insulating to metallic resistivity, while strong disorder involves a hard gap over a window  $T_g > T > T_c$  and activated transport at high  $T$ .

Fig.5.1 presents a summary of the thermal evolution of the coherence peak map at weak, moderate, and strong disorder. Our data shows the integrated tunneling conductance (TC) over the window  $[\omega_c^-, \omega_c^+]$ , defined by  $T_i^{coh} = \langle \int_{\omega_c^-}^{\omega_c^+} d\omega N_{ii}(\omega) \rangle$ , where  $N_{ii}(\omega)$  is the local density of states at site  $\mathbf{R}_i$ .  $\omega_c^- = 0.2t$  and  $\omega_c^+ = 0.45t$  are chosen so that they cover the coherence peaks in the global density of state, and hence gives information about the local phase correlations in the system.

We make the following observations:

1. At weak disorder the pattern remains almost homogeneous at all  $T$ , except for a few isolated regions. Coherence peaks get suppressed with increasing temperature, and vanish by  $T = T_c$ .
2. At intermediate disorder the ground state is noticeably inhomogeneous and increasing  $T$  causes further fragmentation. However, by the time  $T = T_c$  hardly any coherence peaks are visible anywhere.
3. The high disorder regime shows tenuously connected clusters at  $T = 0$ , which shrink as  $T$  is increased, but have a prominently visible but disconnected pattern at  $T = T_c$ . In fact at  $V = 0.9V_c$  the clusters are visible to  $T \sim 2T_c$ . The ‘cluster survival scale’ at  $V_c$  is  $\sim 0.6T_c^0$  and drops slowly with increasing disorder.

### 5.3.2 Spatial character at strong disorder

Fig.5.2 shows spatial maps of the pairing field and the tunneling conductance, averaged over 100 thermal configurations, at strong disorder ( $V = 0.9V_c$ ) for a single realisation of disorder. The next subsection below shows results at weaker disorder,  $V = 0.5V_c$ . The top row shows  $\langle |\Delta_i| \rangle$ , normalised by the clean  $T = 0$  value  $\Delta_0$ . Next row: nearest neighbour averaged phase correlation  $\Phi_i = \langle \frac{1}{4} \sum_{\delta} \cos(\theta_i - \theta_{i+\delta}) \rangle$ , where  $\delta$  refer to the four nearest neighbours of a site. Third row:  $T_i^{gap} = \langle \int_{\omega_g^-}^{\omega_g^+} d\omega N_{ii}(\omega) \rangle$ , the local tunneling conductance probed at subgap frequencies. Fourth row:  $T_i^{coh}$ . We set  $\omega_g^- = 0$ ,  $\omega_g^+ = 0.2t$ . Columns, left to right, correspond to  $T = 0$ ,  $T_c$ ,  $2T_c$ .

Let us start with the patterns at  $T = 0$ , left column.

1. We see a pattern of regions with large  $\Delta \sim 0.7\Delta_0$  (coloured yellow) surrounded by sites whose values decrease with increasing distance from these centres. Our chosen colour scheme defines  $\Delta \sim 0.4\Delta_0$  as the periphery of these regions. A different choice will change the periphery somewhat, but keep the overall pattern the same.
2. The large  $\Delta$  regions are phase correlated:  $\Phi_i$  is large in regions where  $\langle |\Delta_i| \rangle$  is large. These regions are the SC clusters.
3.  $T_i^{gap}$  shows that the large  $\langle |\Delta_i| \rangle$  phase correlated regions have *large* subgap TC, while regions with poor SC correlation have virtually zero TC. This suggests a smaller local gap in the SC clusters, as we will confirm later, and a larger gap in the non SC regions. The behaviour is in contrast to homogeneous systems where larger  $\langle |\Delta_i| \rangle$  would have meant a larger gap and a *smaller* TC.
4. The map for  $T_i^{coh}$  shows that the SC clusters in the ground state have a modest coherence peak, while there is no CP in the larger gap non SC regions. Overall, at  $T = 0$  the non

SC regions have no noticeable spectral weight from  $\omega = 0$  to frequencies well beyond the average CP location.

Now we come to the thermal evolution. By  $T = T_c$ , middle column, we observe the following.

1. There is significant homogenisation of  $\langle |\Delta_i| \rangle$ . Non SC regions generate a strikingly large  $\langle |\Delta_i| \rangle$  while the SC clusters see a more modest growth from the  $T = 0$  value. Temperature leads to strong spatially differentiated amplitude fluctuation in the system.
2.  $\Phi_i$  shows thermal shrinking of the correlated regions. It is still large in parts of the regions which had the large  $\langle |\Delta_i| \rangle$  at  $T = 0$ . The clusters are internally correlated but disconnected. The independent fluctuation of the phase of the different clusters leads to loss of global SC order.
3. There is no noticeable change in  $T_i^{gap}$  with  $T$  for regions that were non SC at  $T = 0$ . For SC regions there is an increase in intensity. (d) For  $T_i^{coh}$ , as we have already seen in Fig.1, areas with strong CP feature shrink but are still clearly visible. Non SC regions do not respond to temperature.

By  $T = 2T_c$ , 3rd column, we find that

1. The mean magnitude has homogenised, with traces of clustering apparently lost, and,
2.  $\Phi_i$  is virtually zero everywhere. The homogenisation of amplitude and phase variables may suggest that any imprint of the  $T = 0$  cluster pattern would be lost. However,
3. The subgap TC is still very inhomogeneous, but now uniformly large over regions that were SC at  $T = 0$ . So, even at this “high temperature” the subgap TC reveals the granularity of the ground state. Finally,
4. The high intensity regions in  $T_i^{coh}$  shrink and the pattern tends towards a homogeneous intermediate intensity with only small remnants of the high CP regions.

Below, we show the results at weaker disorder,  $V = 0.5V_c$ , which, in contrast to strong disorder, shows much weaker correspondence of  $T_{gap}^i$  with the background superconducting pattern.

### 5.3.3 Spatial character at moderate disorder

In the previous subsection, we discussed the strong disorder regime where the cluster pattern is quite prominent. In this section, we show the same results at weaker disorder,  $V = 0.5V_c$ , where we find that the correspondence of  $T_{gap}^i$  with the background superconducting pattern is much

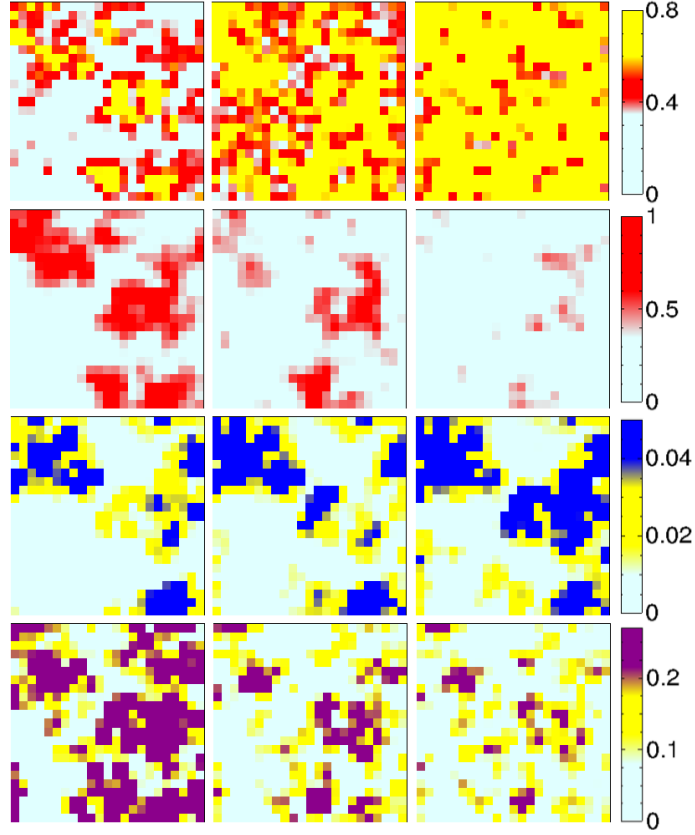


Figure 5.2: Spatial maps at  $V = 0.9V_c$ . 1st row:  $\langle |\Delta_i| \rangle$ , 2nd row: phase correlation  $\Phi_i$ , 3rd row: tunneling conductance  $T_i^{gap}$ , 4th row:  $T_i^{coh}$ . The notation is explained in the text. Columns, from left to right, are for  $T = 0, T_c, 2T_c$ . The interpretation of these patterns is discussed in the text.

weaker.  $T_{coh}^i$ , however, continues to roughly track the superconducting order, both in the ground state and at finite  $T$ , down to low disorder.

*Ground state:* The top left panel in Fig.5.3 is the  $T = 0$  pattern of  $\langle |\Delta_i| \rangle$ . In contrast to  $0.9V_c$  in the main text this has only small regions with suppressed amplitude, scattered in a background with moderate to large  $\langle |\Delta_i| \rangle$ . The corresponding nearest neighbour phase correlation  $\Phi_i$  is almost saturated over the system, except for small regions which correlate with the small  $\langle |\Delta_i| \rangle$  patches.

The subgap tunneling *does not* follow the trend observed at  $0.9V_c$ :  $T_i^{gap}$  seems to be larger where  $\langle |\Delta_i| \rangle$  is either weak or only moderately large. There is no direct correspondence with the correlated regions. Local gaps in the correlated region can be larger as well as smaller than gaps in poorly correlated regions, but we observe a partial recovery of the ‘large  $\Delta \equiv$  large gap’ rule.  $T_i^{coh}$  is large over most of the system, with larger intensity corresponding, roughly, to larger values of  $\langle |\Delta_i| \rangle$ .

*Thermal evolution:* The middle column in the right set of panels is for  $T \approx 0.5T_c$  and the right column for  $T \approx T_c$ . The  $\langle |\Delta_i| \rangle$  increase on an average with  $T$  and is uniform by  $T \approx T_c$ . The loss

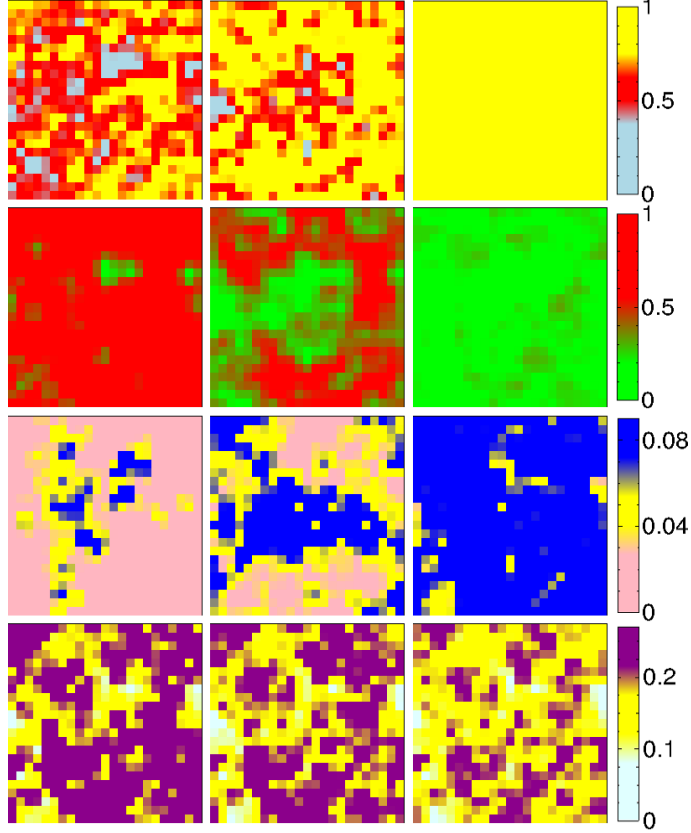


Figure 5.3: Spatial maps at  $U = 2$  and  $V = 0.5V_c$ . First row:  $\langle |\Delta_i| \rangle$ , second row: phase correlation  $\Phi_i$  (see text), third and fourth rows show the tunneling conductance averaged over two frequency (or bias) windows  $\omega_{gap}$  and  $\omega_{coh}$ . Along the row: temperatures  $T = 0, 0.4T_{c0}$  and  $0.8T_{c0}$ .  $\langle |\Delta_i| \rangle$  at low  $T$  forms phase correlated clusters, which shrink in size as  $T$  is increased.  $\langle |\Delta_i| \rangle$  is weakly inhomogeneous at low  $T$ , and smoothens with increasing  $T$ .  $\Phi_i$  decrease with  $T$  and vanishes almost homogeneously at  $T_c$  (not shown, but between  $0.5T_{c0}$  and  $T_{c0}$ .) The subgap region lights up with increasing  $T$ , due to the transfer of spectral weight to low frequency, while the plot for  $\omega_{coh}$  loses intensity.

of phase correlation is spatially differentiated, stronger phase correlation survives in regions where the  $\langle |\Delta_i| \rangle$  is larger. By  $T_c$  the  $\langle |\Delta_i| \rangle$  has homogenised and phase correlations are lost throughout, unlike the strong disorder case where correlated patches survived to  $\sim 1.3T_c$ .

The subgap tunneling does not have a forceful correspondence with the profile of  $\langle |\Delta_i| \rangle$  or  $\Phi_i$ . At  $T = 0.5T_c$  it seems to show low intensity (hence larger ‘gap’) roughly in regions which have larger  $\langle |\Delta_i| \rangle$  and stronger  $\Phi_i$  (roughly the ring like region excluding the center). At  $T \sim T_c$  the intensity is large almost everywhere and no signature of any cluster can be seen. Large intensity in  $T_i^{coh}$  at  $T = 0.5T_c$  similarly has a rough correspondence with large  $\langle |\Delta_i| \rangle$  and phase correlation and only a tentative match with  $\Phi_i$  at  $T \sim T_c$ .

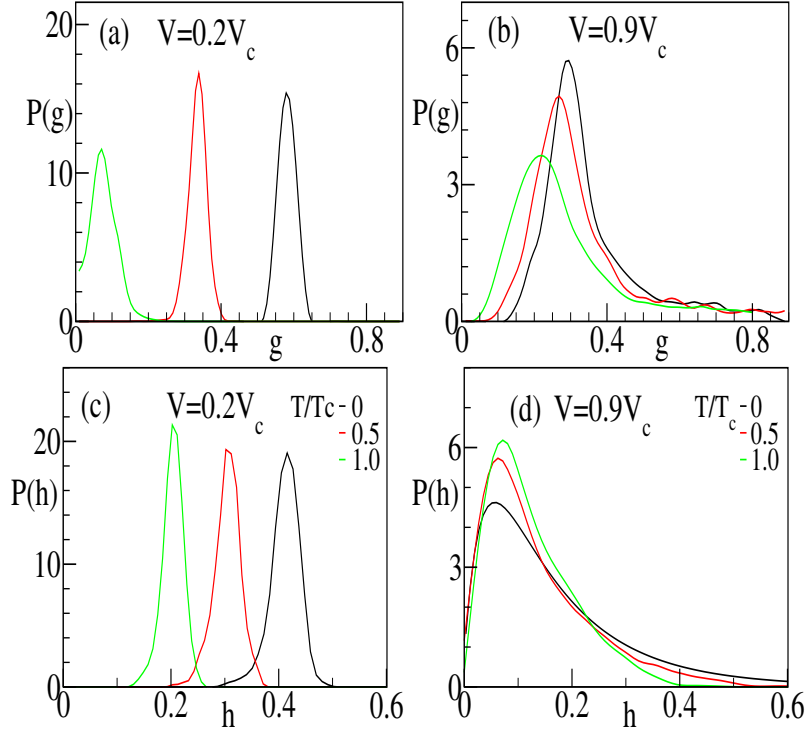


Figure 5.4: Thermal evolution of the gap and coherence peak height distribution. Top: Gap distribution for  $V = 0.2V_c$  (left) and  $0.9V_c$  (right). Bottom: Coherence peak height distribution at same  $V$ .  $T/T_c(V) = 0, 0.5, 1.0$ .

### 5.3.4 Gap and coherence peak distributions

After analysing the spatial maps, we now consider the statistics of the gap and coherence peak height and their evolution with disorder and temperature. This provides a slightly different way of looking at the data and is often calculated by other researchers in the field. Fig.5.4 shows the distributions of the coherence peak height  $\mathcal{P}(h)$  and gap  $\mathcal{P}(g)$  with temperature and disorder. In practice, it was difficult to measure the heights, so we used the same measure as  $T_i^{coh}$  to extract  $\mathcal{P}(h)$ . The ‘gap’ is extracted from the local density of states plots by a suitable cutoff ( $N_i(\omega) < 0.005$ ). The distributions are averaged over all sites and all thermal configurations, in contrast to the spatial maps which were thermal averages at a given site. The results are for  $V = 0.2V_c$  and  $0.9V_c$ , and  $T/T_c(V) = 0, 0.5, 1.0$ . At  $0.2V_c$  the  $P(g)$  has a mean  $\approx 2\Delta_0$  at  $T = 0$ , with a narrow width around it. With increasing  $T$  the mean ‘gap’ shifts to lower values while the width shows a small increase. This suggests a homogeneous decrease throughout the system. At  $0.9V_c$   $P(g)$  is wide at  $T = 0$  with a large gap tail arising from sites with large positive or negative effective potential (we call these hill and valley sites). Increasing  $T$  leads to shift in weight to lower  $g$  from intermediate values while  $P(g)$  at large  $g$  remains unaffected.

Coming to  $P(h)$ , panel (c) shows that the coherence peak distribution is also roughly uniform at

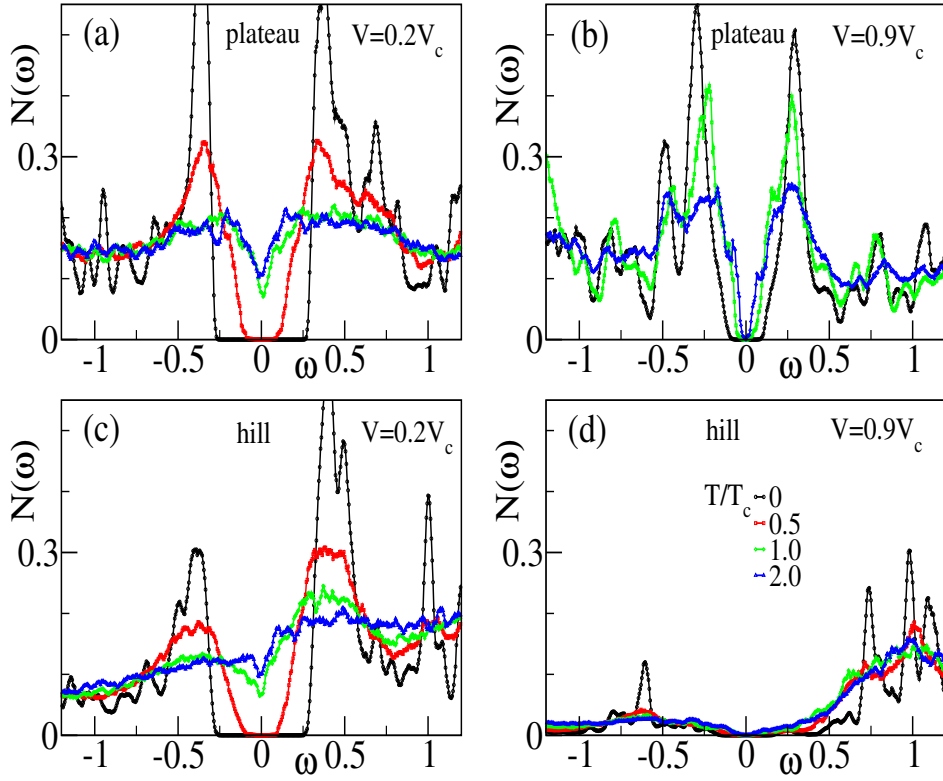


Figure 5.5: Local DOS on a typical ‘plateau’ site (top) and ‘hill’ site (bottom). The left panels (a) & (c) are at  $V = 0.2V_c$ , the right panels (b) & (d) are for  $V = 0.9V_c$ . In each panel the low energy DOS is shown for four temperatures  $T \approx 0, 0.5T_c, T_c, 2.0T_c$ . The curve at  $0.5T_c$  has been omitted in (b) for clarity.

$0.2V_c$  at all  $T$ . The peak at  $h \gtrsim 0.4$  at  $T = 0$  narrows slightly and moves to lower values at higher  $T$  but the mean remains finite since we have not subtracted the high  $T$  background. At  $0.9V_c$ , however, most sites have poor coherence features, defining the trunk of the distribution, except for the tail with  $h \gtrsim 0.4$  arising from sites in the superconducting clusters. With increasing  $T$  as the SC regions shrink the weight in this  $h \gtrsim 0.4$  region is lost.

### 5.3.5 Hills, valleys and LDOS

Fig.5.5 correlates the low energy features of local gap and coherence peak to spectral weight distribution over a wider frequency window. We plot the LDOS at two representative sites (‘plateau’ and ‘hill’) at low and high disorder. The plateau site involves an effective potential  $V_i - \phi_i$  close to the mean value, and a local density  $n_i$  close to the average,  $n_{av} \sim 0.9$ , while the hill site has a large positive effective potential and  $n_i \ll n_{av}$ . At low disorder, Fig.5.5(a)-(b), both sites show coherence peaks and similar gaps, with the hill site naturally having larger weight at  $\omega > 0$ . The thermal evolution is also similar, with both gaps decreasing and closing at  $T \lesssim T_c$ .

At high disorder, Fig.5.5(c)-(d), the LDOS at the plateau site (part of a SC cluster) shows a narrow gap at low  $T$ , moderate coherence peaks, and expected thermal behaviour. The hill site, by contrast, shows a large gap (strongly suppressed low frequency spectral weight), no coherence peaks, and is virtually insensitive to  $T$ .

## 5.4 Discussion

In this section, we expand on and clarify several aspects of our results. We first remark on the relation between the clusters and the background disorder. Then we elaborate on the physics of the multiple scales that emerge, and try to understand that using the framework of a simple Landau-Ginzburg theory. This is followed by a comparison of our methods with experiments, highlighting the similarities and differences. Finally, we examine the dependence of our results on coupling, and discuss how some of the differences with experiments can be explained from them.

### 5.4.1 $T = 0$ cluster pattern

Fig.5.6 shows ‘gap-maps’ for a particular disorder realisation at  $V = 0.9V_c$  for three different cases: (a) actual ground state, (b) ground state obtained with  $V_i^{eff} = V_i - \phi_i$  and (c) with  $V_i$ , but the potential scaled to lie between  $(V - (U/2)n_{min}, -V - (U/2)n_{max})$ , with  $n_{min} = 0$  and  $n_{max} = 2$ . The ‘gap’ at a site ‘i’ is defined as the difference between the smallest energy  $\omega_+ > 0$  at which the LDOS  $N_{ii}(\omega) \gtrsim N_{cut}$  and the corresponding  $\omega_- < 0$ , where  $N_{cut}$  is a suitably defined cutoff.

All three show the same pattern of low gap areas (coloured red) even though the overall scales change. Thus, superconducting clusters form in areas that are already defined by a small local gap at the Fermi level. The Hartree field magnifies this effect, further increasing the local gaps in the insulating regions, while the  $\Delta$  open up a smaller gap on sites within the superconducting clusters.

Since regions with low local gap *around the chemical potential* decide the cluster pattern, this pattern depends sensitively on the overall electron density in the system.

To understand the density distribution in the system we define ‘hill’ sites as those with  $n_i \lesssim 0.4$ , valley sites as those with  $n_i \gtrsim 1.6$ , and ‘plateau’ sites where  $n_i$  is within 10% of  $n_{avg} \sim 0.9$ . The rest are ‘moderate’ sites. Fig.5.7 shows the distribution of ‘plateau’ sites inside the SC clusters (with  $\Delta \gtrsim 0.4\Delta_0$ ) as well as outside at high disorder  $V = 0.9V_c$ . The plots clearly show that a majority of the plateau sites lie inside the SC cluster region, providing a backbone for the formation of the clusters.

These only account for 13% of the total number of sites, but combined with the 40% ‘moderate’ sites, they allow enough particle-hole mixing to favour the formation of SC clusters. The fact that

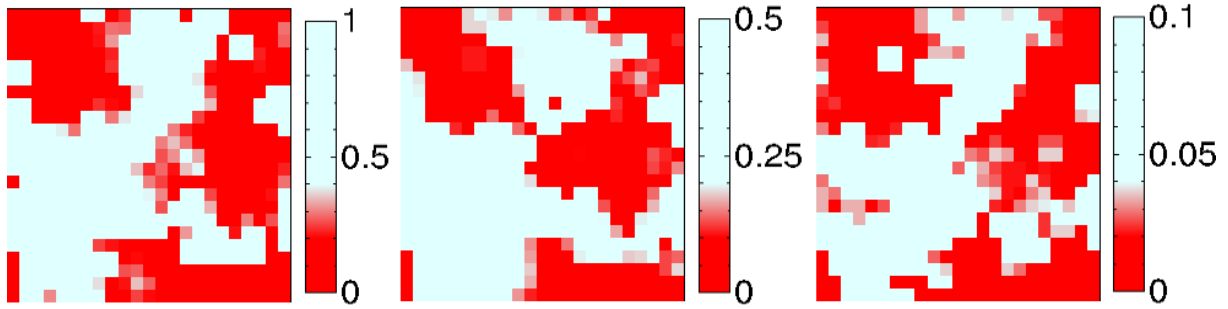


Figure 5.6: Gap maps for 3 cases,  $T = 0$ . Left: Original calculation, showing patches with low gaps, identical to the correlated patches. Middle: With  $V_{bare}$ , scaled to lie between  $(-V - 2, V)$ , showing low gap patches with same basic structure; Right: with  $V_{eff}$ , increasing the contrast of the original  $V$ , gives similar map, with gaps of the insulating regions raised substantially.

47% of sites within the SC clusters are of the ‘hill/valley’ type shows that the SC regions are far from being ‘flat’. On the other hand, in the insulating regions, 80% of the sites are of the ‘hill/valley’ type, surrounding the few isolated ‘plateau’ site.

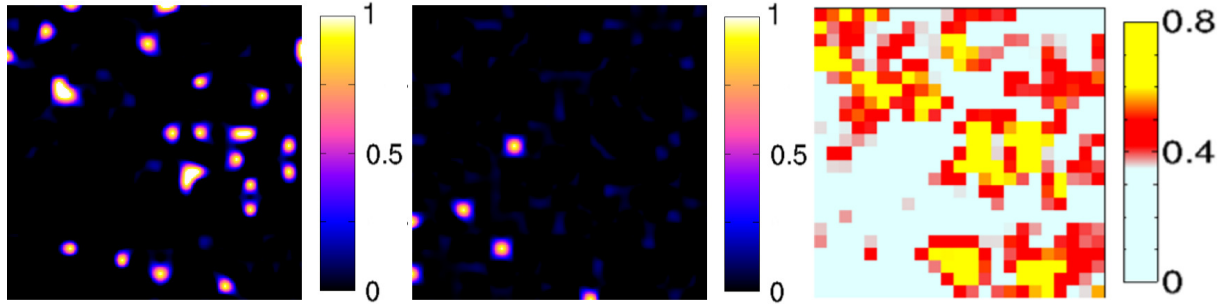


Figure 5.7: Comparison of location of ‘plateau’ sites (see text) inside superconducting clusters (left) with the same outside clusters (middle) at  $V = 0.9V_c$ ,  $T = 0$ . Right figure shows the spatial plot of  $|\Delta_i|$  for reference. ‘Plateau’ sites form a backbone over which the superconducting clusters are formed. In the insulating area, ‘hill’ or ‘valley’ sites (see text) predominate, ruling out the formation of SC clusters.

## 5.4.2 Multiple scales

In the clean limit, weak coupling SC is characterised by only one scale,  $T_c^0(U)$ , while strong coupling brings into play two additional [187] scales  $T_g^0(U) > T_c^0(U)$  and  $T_{pg}^0(U) > T_g^0(U)$ . This paper focuses on the weak coupling end where there is no gap/PG above  $T_c$  at  $V = 0$  but disorder *generates* such scales. These scales emerge due to the fragmentation of the SC ground state with increasing disorder (the nature of the patterns was discussed above, and also in [85]). The inhomogeneous state leads to a spatially varying phase and amplitude stiffness, whose distribution and spatial correlation dictates the thermal response.

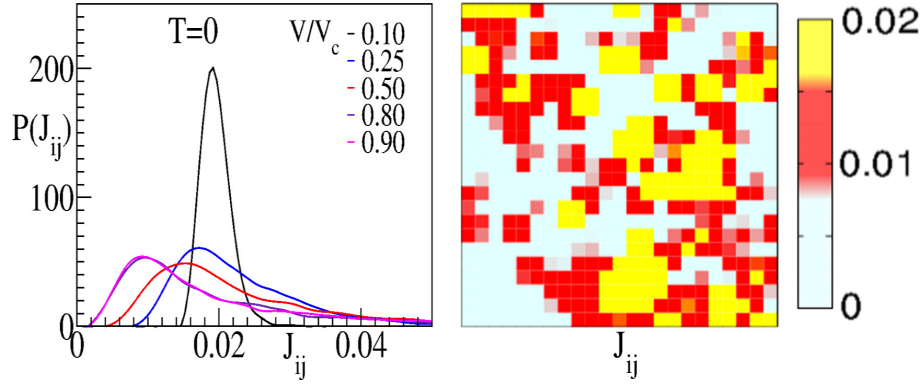


Figure 5.8: Left: Distribution of nearest neighbour  $J_{ij}$  at different disorder, showing successive broadening with disorder, but even at strong disorder, a finite number of sites have  $J \sim O(J_0)$ . Right: Spatial map of  $J_{ij}$ , at  $V = 0.9V_c$ , showing that the large values of  $J_{ij}$  correspond to the centres of the SC clusters.

In the next subsection, we describe a method to extract a bond resolved phase stiffness,  $J_{ij}$ , from the non local pairing susceptibility in the disordered ground state. Leaving the details of the calculations to the corresponding subsection, we focus on the result. Fig.5.8 shows plots of the distribution  $P(J_{ij}, V)$  for various disorder  $V$ , and a spatial map of  $J_{ij}$  for nearest neighbour bonds  $\langle ij \rangle$  at strong disorder,  $V = 0.9V_c$ .

We find that at small  $V$  the  $J_{ij}$  are ‘large’, homogeneous, and  $\sim \mathcal{O}(J_0) \sim 0.023$ , the clean value. The distributions broaden with increasing disorder, and their means shift to lower values, and at large  $V$  they are strongly inhomogeneous, with a smaller mean value  $\langle J \rangle \ll J_0$ . Nevertheless, a finite proportion of sites have  $J \sim J_0$ . While  $\langle J \rangle$  (on the percolative backbone) decides  $T_c(V)$ , the presence of bonds with  $J \sim J_0 \gg \langle J \rangle$ , near the center of the SC clusters, leads to survival of local SC correlations to  $T_{clust} \gg T_c$  as  $V \rightarrow V_c$ .

Although phase fluctuations destroy global order, the  $|\Delta_i|$  survive to  $T \gg T_c$ . At  $U = 2t$  this sustains a gap to  $T_g > T_c$  and then a PG to a scale  $T_{pg} > T_g$ , ultimately closing due to amplitude fluctuations. We will examine the dependence of these scales on the coupling later, showing results at  $U = 2t$ , and  $U = 4t$  to allow extrapolation over a wider interaction window, allowing us to compare our results more fruitfully with experiments and explain some of the differences between the two (this will be discussed in greater detail in a separate subsection).

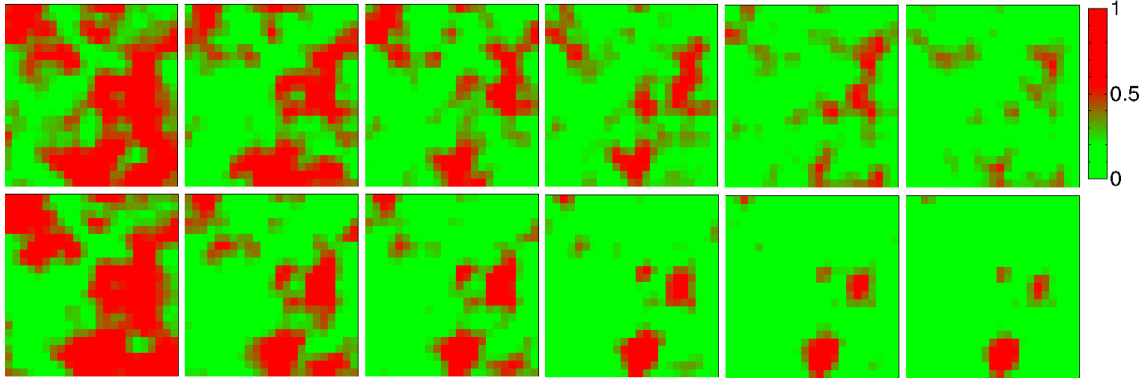


Figure 5.9: Comparison of correlated patches for  $V = 0.8V_c$  for successive  $T$  points using the full Monte Carlo (top) and the simplified XY model (bottom). The basic phenomenon of an island pattern at low  $T$ , and shrinkage of these clusters with increasing temperature is well captured by the simplified model.

### 5.4.3 Effective Landau-Ginzburg functional

The interplay of ‘amplitude’ and ‘phase’ fluctuations in our model is best understood in terms of a simple lattice Landau-Ginzburg model:

$$\mathcal{F}(\Delta) = \sum_{i \neq j} J_{ij} \Delta_i \Delta_j^* + \sum_i (a_i |\Delta_i|^2 + b_i |\Delta_i|^4) \quad (5.2)$$

The  $a_i$  and  $b_i$ , crudely, control the  $|\Delta_i|$  while  $J_{ij}$  determine a bond coupling between the ‘i’ and ‘j’ sites (not necessarily nearest neighbours). These parameters are in general temperature dependent, and the clean problem at  $U = 2t$  involves renormalisation of all these parameters with temperature. We focus here on understanding the strong disorder regime  $V \gtrsim 0.75V_c$  and the thermal evolution of the superconducting clusters only over a small temperature window above the ground state (the  $T_c$  here is small). Such a situation allows us to ignore the thermal renormalisation of the GL parameters as a first approximation.

We calculate  $J_{ij}$  via a perturbative expansion of the energy in  $\Delta_i$  around the disordered ground state. This leads to:

$$J_{ij} \sim \frac{1}{\beta} \sum_n G_{ij}(i\omega_n) G_{ij}(-i\omega_n) \quad (5.3)$$

where  $G_{ij}(i\omega_n)$  is the electronic Greens function computed in the background defined by  $V_i$  and  $\phi_i$ . We compute  $G_{ij}$  exactly in the  $\{V_i + \phi_i\}$  background. The  $a_i$  and  $b_i$  can be found by fitting the local amplitude distributions to the given form, but we concentrate on  $J_{ij}$  here.

Fig.5.9 compares the phase correlations obtained from the bond disordered XY model, above, with that from the full Monte Carlo at  $V = 0.8V_c$ . We find a reasonable match, demonstrating the usefulness of this crude model.

#### 5.4.4 Estimating the new scales

Fig.5.10 shows the phase diagrams for  $U = 2$  and 4. The tails emphasize the fact that in principle, the  $T = 0$  state is always superconducting within our scheme. At  $U = 2t$ , while  $T_c \rightarrow 0$  as  $V \rightarrow V_c$ ,  $T_{clust}$  remains roughly constant at  $\sim 0.5T_c^0$ , as does  $T_g$ . On the other hand,  $T_{pg}$  is much larger than these scales. At  $U = 4t$ , the increased Hartree field increases the effective disorder  $V_i - \phi_i$ , leading to a smaller  $V_c$ . This also leads to a faster fragmentation with disorder, and a more differentiated  $J_{ij}$  distribution, which results in a faster decline in  $T_{clust}$  compared to that at  $U = 2$ . The gap vanishing scale  $T_g$ , on the other hand, increases considerably with coupling and is greater than the clean  $T_c^0$  at all disorder values considered here. Thus, at  $U = 4t$ ,  $T_g \gg T_{clust}$ , so their coincidence at  $U = 2t$  is accidental. Extrapolating downward we expect that when  $U \ll t$ ,  $T_{clust}$  will continue to be a finite fraction of  $T_c^0$ , with  $T_{pg} \sim T_{clust}$ . We will elaborate on this further when we compare our results with experiments.

#### 5.4.5 Comparison with experiments

Our main results, *i.e.*, the emergence of a  $T_{clust}$ ,  $T_g$ , *etc.*, in addition to  $T_c$ , the shrinkage and fragmentation of the SC pattern with increasing temperature, and the distinct thermal evolution of the STS spectra in the SC and insulating regions, are all in agreement with recent experiments. However, there are also important differences, arising from (a) our parameter choice, (b) our approximation, and (c) the neglect of Coulomb interactions. We discuss each of them below.

1. Experimental spectra indicates a pseudogap [60], rather than a hard gap above  $T_c$  for  $V \rightarrow V_c$ . Our exploration of the  $U$  dependence suggests that at weaker coupling such a result would emerge from our method as well. Another effect of the relatively ‘large’ coupling that we use is the larger variation of local gaps between the SC and insulating regions, experimentally these gaps are comparable [47].
2. The neglect of quantum fluctuations in our treatment of the attractive Hubbard model prevents access to the correct asymptotic low temperature behaviour for  $V \rightarrow V_c$ . However, apart from the immediate vicinity of  $V_c$  the thermal fluctuations seem to capture most of the qualitative experimental features.
3. The recent observation [61] of enhanced zero-bias conductance in the insulating regions is probably caused by additional interactions that are absent in our model. Also, the broad V-

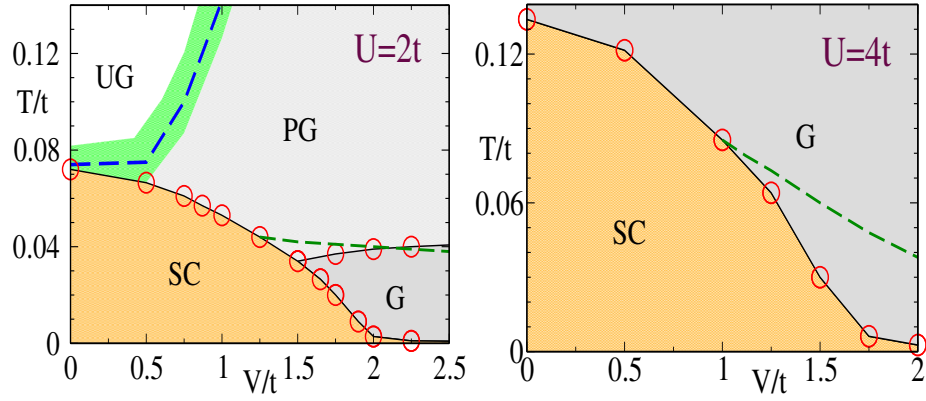


Figure 5.10: Phase diagrams showing superconducting (SC), gapped (G), pseudogapped (PG) and ungapped (UG) phases, and the cluster vanishing scale  $T_{clust}$  (green dashed lines) at  $U = 2$  and 4 (see text).

shaped background observed in the STS spectra possibly arises from Coulomb interactions, and is absent in our results.

## 5.5 Conclusions

We have studied the spatial signatures of the thermal transition in a disordered s-wave superconductor as probed by tunneling spectroscopy. Our detailed spatial maps of the coherence and subgap features in the local DOS allow us to identify the distinct evolution of the superconducting and ‘insulating’ regions with temperature. We point out new thermal scales,  $T_{clust}$ ,  $T_{pg}$  and  $T_g$  that come into existence at strong disorder, identify their physical origin, and quantify their dependence on disorder and interaction strength. Recent experiments have already indicated the existence of such scales in 2D films, our results provide the broader framework within which these results can be analysed.

# DENSE MAGNETIC IMPURITIES IN A *S*-WAVE SUPERCONDUCTOR

This chapter describes our work on the effect of magnetic impurities in superconductors. We will consider these impurities in an s-wave superconductor on a lattice at moderate coupling, for various values of impurity concentration and impurity-electron coupling. Our primary aim will be to study the thermal and strong impurity coupling effects beyond those provided by the benchmark Abrikosov-Gorkov (AG) theory. In particular, we will study the transition temperature  $T_c$ , the global density of states, and local properties. We examine the thermal behaviour to construct phase diagrams at different impurity coupling strengths showing the superconducting (gapped and gapless) phases. We compare and contrast our results to AG theory and explain how the increased impurity coupling modifies the physics of the system.

This chapter is structured as follows. In the first section we provide a brief summary of the problem and our model and methods (already reviewed in detail in Chapter 2). Section 2 considers the single impurity case, benchmarking our results against existing results. In the next section we present our main results for multiple magnetic impurities. We describe our phase diagrams at various values of impurity coupling, and discuss the different phases with reference to AG theory. Then we present our results on the global and local indicators, at  $T = 0$  and finite temperature respectively. The final section provides a discussion of these results and further explanation of the deviations from AG theory in terms of the spatial location of the low lying eigenfunctions of the system.

## 6.1 Background and model

### 6.1.1 Earlier work and limitations

As we have already discussed before, the problem of magnetic impurities in a superconductor has been studied for a long time now. The absence of time reversal symmetry in the problem invalidates Anderson's theorem in this case, and hence superconductivity can be greatly suppressed and eventually completely destroyed by a relatively low concentration of such impurities.

The perturbative mean field treatment of Abrikosov and Gorkov [75] provided an estimate of the critical concentration  $\eta_c$  and the striking prediction of the presence of a gapless superconducting phase for  $\eta_c > \eta > \eta_g \sim 0.91\eta_c$ . However, the AG results are valid only in the perturbative regime and more sophisticated methods [67, 68, 78] demonstrated deviations from the AG theory, in particular, an increase in the gapless regime. These semi analytic methods, however, have the following limitations:

1. They are all derived in the limit of weak attractive coupling, that is the BCS regime, and do not incorporate the non-BCS effect of stronger coupling on the system; further, most assume the order parameter to be homogeneous, though their methods allow it to be spatially varying.
2. These (T-matrix) methods neglect complex interference effects from different impurities and are strictly valid only at low impurity concentration.
3. They cannot provide any insight into the spatial nature of the system, especially at strong impurity coupling, where there could be inhomogeneities.
4. They cannot incorporate the effect of thermal fluctuations, which can be non-trivial at large  $U/t$  and impurity coupling.

Thus, these methods cannot provide a satisfactory picture of the system at strong attraction and impurity coupling, where the possibility of spatial inhomogeneities and thermal fluctuations can give rise to interesting effects and change the phase diagram non-trivially.

Numerical studies can overcome many of these limitations, but there has been little work on this subject. Using a mean field BdG method, Nanguneri et.al. [79] considered spin dependent disorder and investigated the resulting gapless phase and deviations from AG theory. Some other work has been done [80] on the related and interesting problem of magnetic order in superconducting materials, where they considered the stability of various one dimensional magnetic domains in a superconductor. However, none have considered the full thermal problem of magnetic impurities in a superconductor.

An important reason for this is the inability of standard determinantal QMC methods to include spin dependent disorder. QMC calculations incorporating non magnetic disorder in the negative  $U$  Hubbard model are free of the sign problem, and hence such methods have been used extensively to study the disorder induced SIT. However, these run into problems when spin dependent disorder is included, and the determinant becomes negative. Hence, QMC methods cannot be applied to this problem.

Our real space method can be easily generalized to include magnetic disorder at arbitrary concentration, and can be used on comparatively large lattices to provide global as well as spatially resolved information at both zero and finite temperature. Below, we quickly summarize the model, method, and parameters before going on to describe the results of our work.

### 6.1.2 Model and parameter space

Our model, as already described in detail in Chapter 2, is given by

$$H_{eff} = H_{kin} + \sum_i \left( (\Delta_i c_{i\uparrow}^\dagger c_{i\downarrow}^\dagger + h.c.) + (V_i - \mu - \phi_i) n_i \right) + \sum_{i\nu} J \delta_{i\nu} \vec{S}_\nu \cdot \vec{\sigma}_i + H_{cl} \quad (6.1)$$

Here,  $t$  denotes the hopping matrix element,  $U$  the attractive coupling,  $\mu$  the chemical potential,  $\Delta$  and  $\phi$  the pairing and density channel auxiliary fields respectively, and  $J$  the impurity coupling strength.  $\vec{S}_\nu$  denotes the impurity spins situated at random sites  $R_\nu$ , that are coupled to the electronic spins by the usual exchange coupling term. We neglect the quantum nature of our spins, modelling them as classical vectors of length unity and random orientation  $(\theta, \phi)$ . The neglect of the quantum nature of  $\mathbf{S}_\nu$  loses the effect of spin flip on these moments, and in particular the Kondo effect at low temperature below the Kondo scale  $T_K$ . Furthermore, the impurities are assumed to be frozen, and thus, we do not consider the possibility of simultaneous magnetic and superconducting order. The chemical potential  $\mu$  is fixed so that the average density  $n \sim 0.9$ . We consider a moderately strong regime of attractive coupling,  $U/t = 2$ , with a clean transition temperature  $T_{c0} \sim 0.07t$ . In the ground state, the ratio  $2\Delta_0/kT_c \sim 8$ , much greater than the BCS value of 3.53 (however, note that in the context of non-magnetic superconductors, we classified this value as ‘weak’ in the sense that in the clean problem, the gap vanished at  $T_c$  and there was no appreciable pseudogap window, just like a BCS system. Our reason for calling this ‘strong’ in this context will be explained in more detail below.) We vary the impurity coupling  $J$  from 0.25, which we term ‘weak’, to 1.0, which we call ‘strong’. These names will be justified below, where we consider the effect of a single impurity of varying strength in the superconducting system. As discussed in Chapter 2, this Hamiltonian is annealed using classical Monte Carlo methods [86, 87, 137–139, 174, 175, 185] by employing a

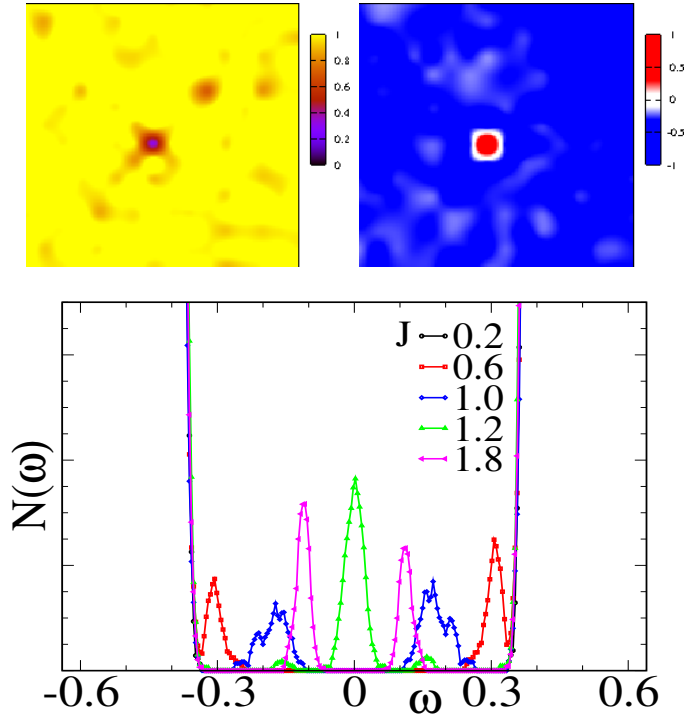


Figure 6.1: Top row: Spatial maps of left:  $|\Delta|$  and right: Phase correlation  $P_i$  (see text) at  $J = J_c = 1.2$ . Below  $J_c$  both are uniform, while after the phase transition has taken place,  $|\Delta|$  at the impurity site decreases in magnitude and changes phase by  $\pi$ . Bottom row shows the density of states for different  $J$ . As  $J$  increases, impurity level moves from edge of gap inwards, crossing  $\omega = 0$  at  $J_c$ .

cluster approximation [145]. The primary cost of the calculation lies in diagonalizing a modified BdG matrix, whose dimensions are increased from  $2N \times 2N$  to  $4N \times 4N$ , where  $N$  is the number of sites, to incorporate the extra spin degrees into the problem. Our calculations are done in two dimensions on lattices  $16 \times 16$ .

## 6.2 Single impurity

We begin with the effect of a single magnetic impurity on a superconductor at low temperature. As remarked at the beginning, this allows us to benchmark our system in terms of the values of the impurity coupling  $J$ , helping us define ‘weak’ and ‘strong’ impurity coupling regimes. The evolution of a BCS superconductor with increasing  $J$  is a well studied problem [6]. At low  $J$ , the impurity induced level lies at the gap edge, but with increasing  $J$ , it moves inwards. At a critical value  $J_c$ , the impurity level touches zero, and the system undergoes a quantum phase transition, where the impurity captures an electron from the condensate, resulting in a condensate with a non-zero total spin equal to that of a single electron.

In Fig.6.1, we show the spatial indicators and the spectral functions at low temperature. The top

row shows  $|\Delta_i|$  and the phase correlation  $P_i = (\Delta_i \cdot \Delta_0) / (|\Delta_i| |\Delta_0|)$  (where 0 is a reference site chosen judiciously) respectively, averaged over 100 configurations, at the critical impurity coupling value  $J = J_c = 1.2$ . We find a noticeable decrease in  $|\Delta|$  at the impurity position and a corresponding phase change by  $\pi$ , as found in the literature [6]. The origin of the phase change is still not completely understood, but it seems to be reproducible in our model. The bottom row shows the evolution of the single particle density of states with increasing  $J$ . For  $J \sim 0.2$ , the impurity level is at the gap edge and indistinguishable from the other levels. By  $J \sim 0.6$ , however, the level is clearly recognizable, though it is still at the gap edge. Increasing  $J$  further, we find that the level moves inwards, and crosses the zero mark by  $J \sim 1.2$ , where the QPT takes place. We roughly identify the regime  $J \sim 0.2$  as ‘weak’, while  $J \gtrsim 1$  is in the very strong scattering regime. Hence, we pick four  $J$  values, viz.,  $J = 0.25$ ,  $J = 0.5$ ,  $J = 0.75$  and  $J = 1.0$  to investigate the effect of multiple impurities on the superconducting system. These results, presented below, form the core of our work.

### 6.3 Multiple impurities

Increasing the number of impurities increases the corresponding subgap impurity levels, and for finite impurity concentration in a thermodynamic system these levels form an impurity band. Many of the assumptions employed by semi-analytic methods, such as weak attractive coupling, homogeneous order parameter, weak concentration, and neglect of thermal fluctuations are, however, suspect in the regime of strong scattering at large impurity concentration. In such a situation strong local changes due to the impurity can cause considerable inhomogeneity in the system, and the short inter-impurity distance can increase the interference effects between scattering from different impurities. Our numerics allows us to explore this regime in detail, while simultaneously visualizing the physics in the weak scattering regime.

In the Abrikosov-Gorkov theory, superconductivity is destroyed when the scattering rate  $\alpha \sim \eta J^2 \mathcal{N}_0$  is equal to the gap parameter  $\Delta_0$ , where  $\mathcal{N}_0$  is the normal density of states at the Fermi level. In our theory, this translates to the condition  $\eta J^2 / t \sim \Delta_0$ . Pure BCS superconductors have a  $2\Delta_0 / T_c$  ratio of around 3.52. In this respect, the system with  $U/t = 2$ , having a ratio of  $\sim 8$ , is already much outside the BCS window. As mentioned above, though, it lies to the left of the BCS-BEC crossover [185] and the gap vanishes at  $T_c$  with no appreciable pseudogap window above it. We may therefore think of it as within a ‘renormalized’ BCS regime, and we have treated it, in some sense, as a ‘weak’ coupling point in our study of non-magnetic disorder. However, in the current problem, where the critical concentration  $\eta_{sc}$  is linearly dependent on the superconducting order parameter  $\Delta_0$ , such a system would require a much larger concentration of impurities to suppress superconductivity compared to experiments, since the gap is much larger than in the experimental

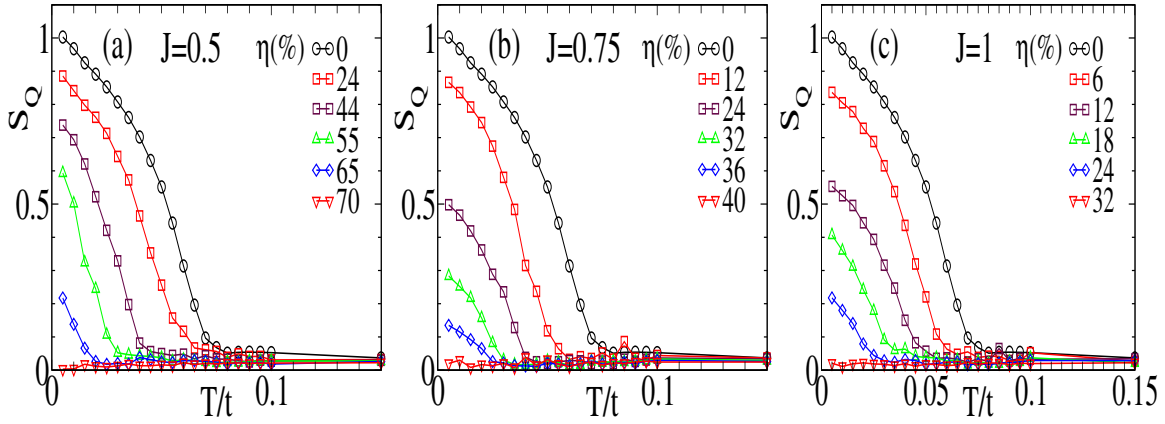


Figure 6.2: Superconducting order parameter  $S(q = 0)$  -vs-  $T$  at  $J = 0.5, 0.75$  and  $1.0$  at various concentrations  $\eta$ , demonstrating the suppression and eventual destruction of superconductivity. The critical concentration  $\eta_{sc}(\%)$  is  $\sim 70, 40$  and  $30$  for the three  $J$  values respectively.

materials that are in the BCS regime. So, multiple impurity and interference physics would be vital for our  $U/t$  choice.

Below, we first show our phase diagrams at various  $J$  values, summarizing our results on the gapped, gapless and non-superconducting phases of the system, and discuss their significance in the context of existing results. We then consider our global and local signatures in detail to understand and explain these observations.

### 6.3.1 Phase diagrams

This subsection shows the summary of our results in terms of phase diagrams in the  $\eta - T$  plane for various impurity coupling values  $J$ , detailing the positions of the gapped, gapless and non-superconducting phases as functions of these parameters. As has been described earlier, the superconducting  $T_c$  is determined from the rise of the structure factor  $S(q = 0)$  curve vs.  $T$ . Fig.6.2 shows the corresponding  $S(q = 0)$  curves for different concentrations  $\eta$  at three values of  $J$ , viz.,  $0.5, 0.75$  and  $1.0$ .

We find that superconductivity is suppressed and destroyed by increasing concentration of impurities. The critical concentration decreases with increasing impurity coupling  $J$ , as is expected from the single impurity picture generalized to that of a band. Thus, while even  $\eta = 100\%$  fails to destroy superconductivity at  $J = 0.25$  (not shown here), at strong coupling  $J = 1$  only  $30\%$  impurities destroy superconductivity completely.

Fig.6.3 shows the overall phase diagrams summarizing our results. Here, we show the gapped and gapless superconducting phases for  $J = 0.5, 0.75$  and  $1$  respectively. At  $J = 0.5$ , we find that the gapless phase is quite narrow, with  $\eta_g/\eta_c \sim 0.83$ , even though this is already beyond the AG regime. As  $J$  is increased, the gapless phase increases steadily, and by  $J = 1$ , the ratio is only

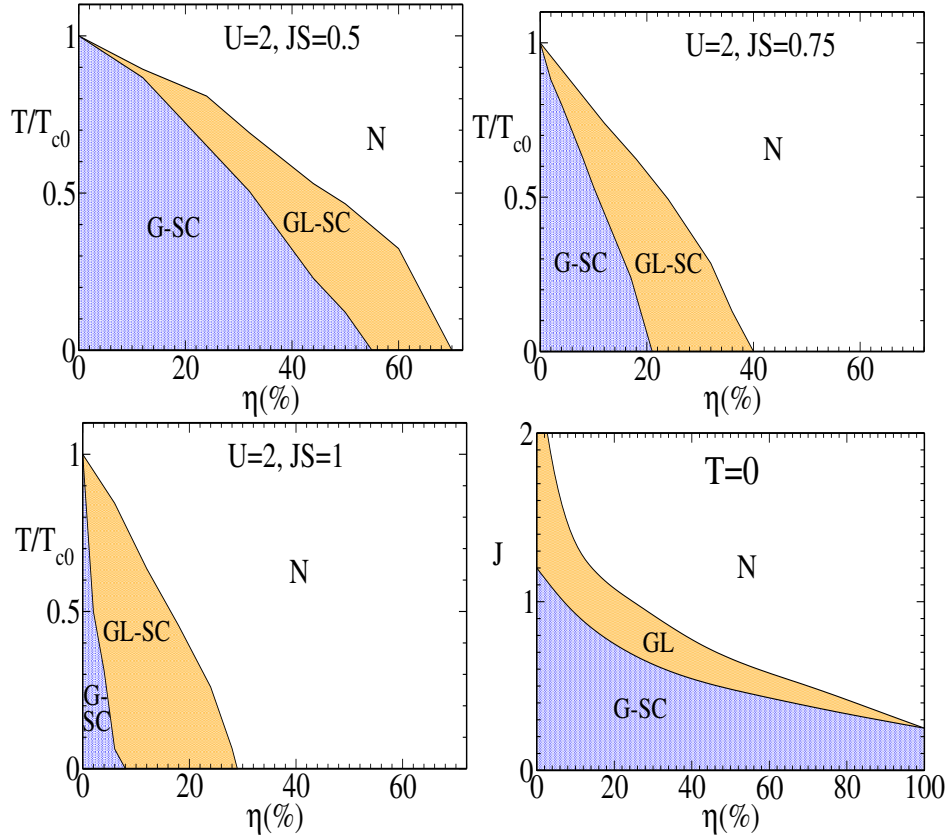


Figure 6.3:  $\eta - T$  phase diagrams for  $J = 0.5, 0.75$  and  $1$ . G-SC, GL-SC/GL and N denote the gapped superconducting, gapless superconducting and normal phases respectively. As we increase  $J$ ,  $\eta_c$  decreases from around 80% for  $J \sim 0.5$  to 30% for  $J \sim 1$ . The gapless fraction increases substantially from  $\eta_g/\eta_c \sim 0.83$  for  $J = 0.5$  to 0.25 at  $J = 1$ . Bottom right shows a  $J$  vs.  $\eta$  phase diagram at low  $T$ , using data from the three  $J$  points and extrapolating them to the limits  $J \rightarrow \infty$  and  $\eta \rightarrow 100$  respectively.

0.25. As expected,  $\eta_c$  also decreases, going from 70% to only 30%. Thus, for all points in the data, we are in a regime far away from the true AG regime, where we would have expected the gapless phase to exist only in a tiny sliver in the phase diagram.

The ground state and its variation with  $J$  is summarized in the bottom right panel as a phase diagram in the  $J - \eta_c$  space. There are two limits to be considered here, namely the  $\eta_c \rightarrow 100\%$  and the very strong scattering limit corresponding to  $J \rightarrow \infty$ . These correspond to the right and the left ends of the phase diagram respectively. Let us consider the right hand side first, i.e., the  $\eta \rightarrow 100\%$  limit. As argued before, our coupling value dictates that we can never truly be in the AG regime, corresponding to both weak concentration  $\eta$  and weak impurity coupling  $J$ . In our case, at weak  $J$ , we would require a very large  $\eta_c$  to kill off superconductivity, and a dense concentration would invalidate self-consistent T-matrix methods in principle, bringing in complex effects of interference between scattering from different impurities. However, we expect the basic

mechanism behind the formation of intra gap impurity levels to remain valid for arbitrarily weak  $J$ , and hence, the presence of a tiny gapless phase all the way up to  $\eta_c = 100\%$ . This is shown as the narrowing orange sliver in the diagram. As  $J$  is increased,  $\eta_c$  and  $\eta_g$  both decrease, but  $\eta_g$  decreases faster, and the gapless regime increases. As we move towards the strong scattering limit, the intra gap levels move closer to zero and hence, using the single impurity results, we expect the system to be gapless beyond  $J \sim 1.2$  for any  $\eta$ . The destruction of superconductivity, on the other hand, can never be accomplished with a vanishingly small concentration of impurities, however strong, and hence the GL-N boundary is an asymptote to the y-axis.

Having summarized the key results in terms of the phase diagrams, we now consider the detailed indicators such as the spectral function and the local behaviour and study their behaviour at  $T = 0$  and their thermal evolution.

### 6.3.2 $T = 0$ results

This section will describe the global and spatial indicators at  $T = 0$ . We first begin with the global density of states.

#### Density of states

We had already described the general formulation with magnetic impurities in Section 2.3.3. The density of states for the case with non-magnetic disorder was calculated in Section 2.3.6. In a very similar way, one can easily calculate the density of states for the case with magnetic disorder, from the general spin dependent Green's functions  $G_{ij}^\sigma(\omega)$ . The resultant expression is simply the spin dependent generalization of Eq. 2.17:

$$N(\omega) = \sum_{ni\sigma, \epsilon_n > 0} (|u_{n\sigma}^i|^2 \delta(\omega - \epsilon_n) + |v_{n\sigma}^i|^2 \delta(\omega + \epsilon_n)) \quad (6.2)$$

Fig.6.4 shows the density of states at  $T = 0$  with increasing concentration  $\eta$  at  $J = 0.25, 0.5, 0.75$  and  $1.0$  respectively. The density of states preserves all the usual characteristics at large frequencies and the impurity only affects the low frequency behaviour by forming intra-gap states. At  $J = 0.25$ , we are truly in the 'weak' scattering regime, where the impurity induced levels are right at the gap edge, and impossible to make out separately, as expected from the AG theory. As  $\eta$  is increased, the gap narrows slightly, but the system remains a gapped superconductor even at  $\eta = 100\%$ . At  $J = 0.5$ , we first see a superconductor-metal transition at  $\eta \sim 70\%$ , and the gap closes at  $\sim 60\%$ . By  $J = 1$ , in the strong scattering regime, the impurity levels are isolated from the gap edge at  $\eta = 2\%$  and close the gap at  $\sim 8\%$ , though it is difficult to ascertain whether they

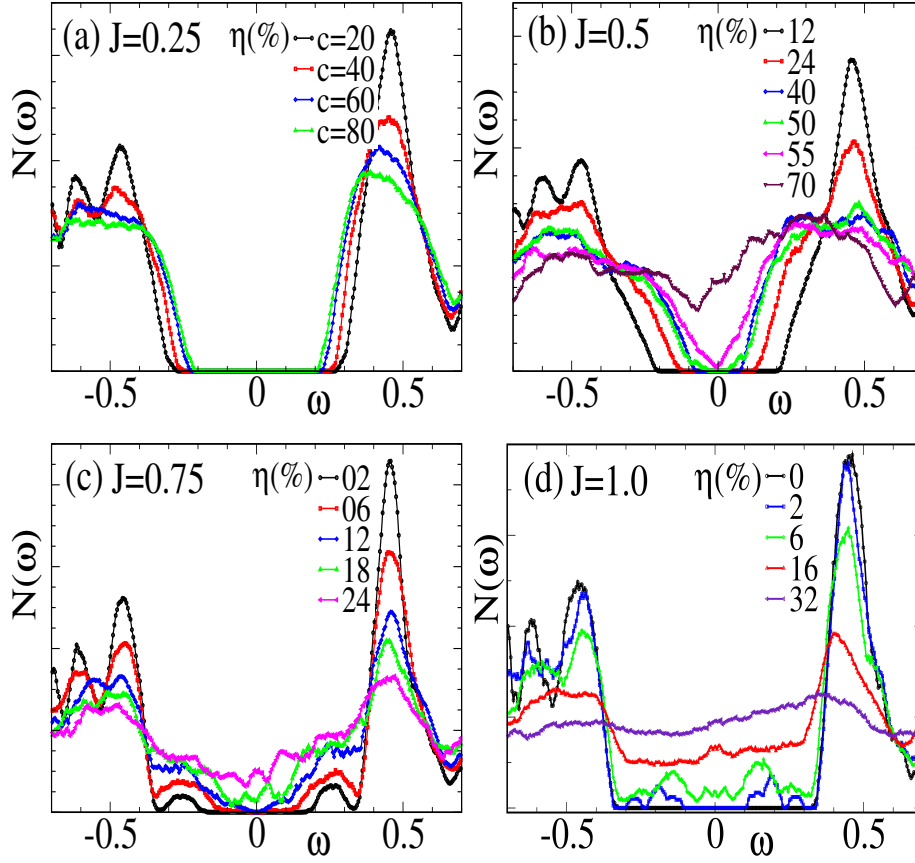


Figure 6.4: Density of states for  $J = 0.25, 0.5, 0.75$  and  $1$  at various concentrations  $\eta$  at  $T = 0$ . At  $J = 0.25$ , there is a very small narrowing of the gap with increasing  $\eta$ , impurity levels are at the edge. As  $J$  increases, impurity levels move inwards and with increasing  $\eta$ , close the gap at some  $\eta_g(J)$  to form a gapless superconducting phase.  $\eta_g$  decreases from 60% at  $J = 0.5$  to only 8% at  $J = 1$ .

are still disconnected from the gap edge when that happens.

### Spatial Plots

Figs.6.5 and 6.6 shows the spatial plots at  $T = 0$  for two different coupling strengths,  $J = 1.0$  and  $0.5$  respectively.

The top panels show the impurity positions. In the middle panels, we show  $|\Delta_i|$  averaged over 100 configurations. The bottom panels show the phase correlation  $\mathcal{P}_i = (\Delta_i \cdot \Delta_0) / (|\Delta_i| |\Delta_0|)$ .

First, we focus on Fig.6.5. We find that as expected from the single impurity case, a very dilute concentration of impurities ( $\eta = 2\%$ ) behaves similarly to a non-interacting combination of single impurities. Thus this case shows a completely uniform  $\Delta_i$  and phase correlation throughout. As we increase the concentration, however, multiple scattering effects from the different impurities change the character of the problem, and we find that at  $\eta \sim 12\%$ ,  $\Delta_i$  is depressed significantly at

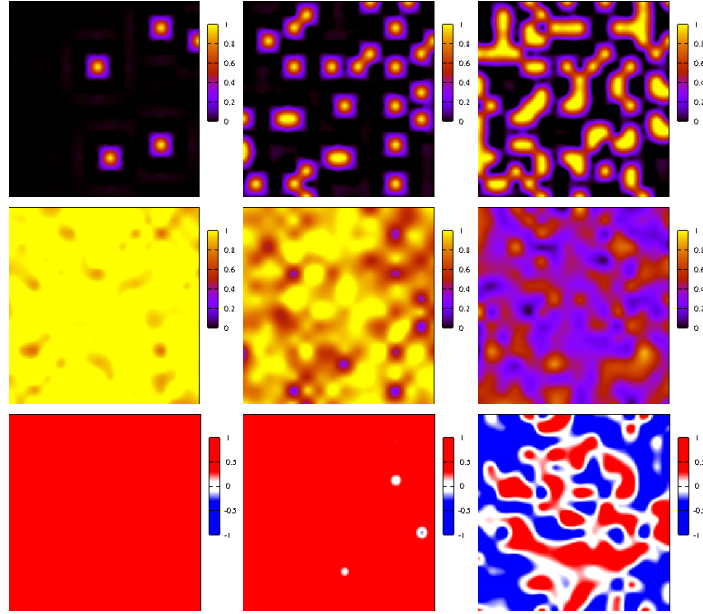


Figure 6.5: Spatial plots for for  $J = 1$  at  $\eta = 2\%, 12\%$  and  $30\%$  at  $T = 0$ . Upper panel shows the impurity positions. Middle panels show the thermally averaged  $|\Delta_i|$ , while bottom panels show the phase correlation (see text). At  $\eta = 2\%$ , the system is a uniform superconductor. At  $12\%$ ,  $\Delta_i$  are depressed in many impurity positions, however, the phase correlation seems uniform except for three sites. At  $\eta = 30\% \sim \eta_c$ ,  $\Delta_i$  is small at most sites, while the phases are randomly oriented, signalling the transition to a non superconducting metal.

many impurity sites, even though the reduction is negligible in the case of a single impurity at the same coupling. The phase correlation, on the other hand, shows a much more uniform behaviour and only three particular sites (seen as white) seem to have low values. Both the reduction in  $\Delta_i$  values and their phase correlations seem to be very local and limited mostly to the corresponding impurity sites.

As the concentration is increased further, more and more sites show a reduction of  $\Delta_i$ , and correspondingly, the number of sites showing reduced phase correlation is increased as well. As a reference, we have shown the case  $\eta = 30\%$  corresponding to the concentration where superconductivity vanishes, in the right column. We find that by this time, most sites have very low pairing fields, and the phase correlations are broken up into random patches, thereby signalling complete loss of superconductivity. The gapped to gapless transition, happening at  $\eta \sim 8\%$  for this  $J$  value, has no remarkable spatial signatures, and hence cannot be inferred from spatial plots like these.

The plots at  $J = 0.5$ , on the other hand, show uniform phase correlation and  $\Delta_i$  values for a much larger fraction of concentration values before superconductivity is destroyed at  $\eta = 70\%$  where  $\Delta_i$  becomes very low everywhere just like at  $J = 1$ , and the corresponding phases are also randomized.

Thus, we find that the increased local effect of larger impurities creates inhomogeneities in  $\Delta_i$

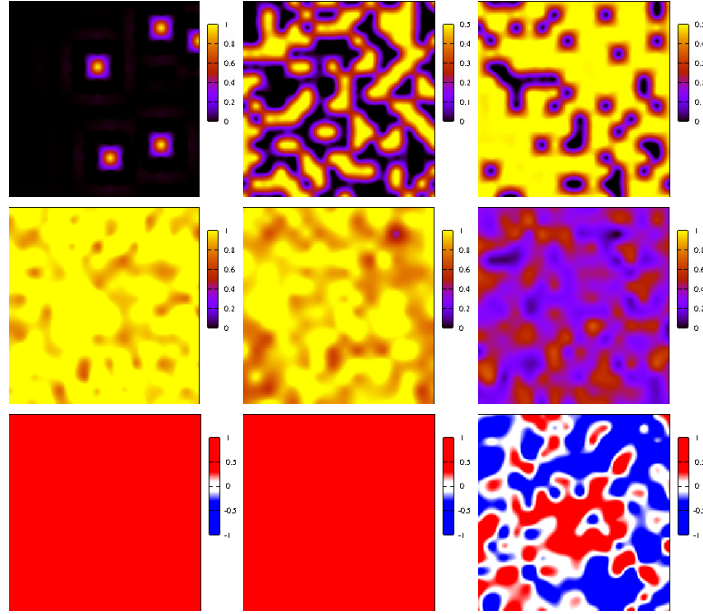


Figure 6.6: Spatial plots for for  $J = 0.5$  at  $\eta = 12\%, 44\%$  and  $70\%$  at  $T = 0$ . Panels same as Fig.6.6. Shows much more homogeneous behaviour than  $J = 1$ , with the system being largely homogeneous and phase coherent even around  $\eta \sim 60\%$ , where the system becomes gapless. However, the eventual destruction at  $\eta = 70\%$  is brought about by almost complete suppression of all  $\Delta_i$ , just like at  $J = 1$ .

with increasing concentration, until they are depressed everywhere, destroying superconductivity. The phases of these sites also seem to show weaker local stiffness, as in the non-magnetic disorder case, and hence, we expect the thermal evolution to be affected by this inhomogeneity. As the impurity coupling value  $J$  is decreased, the corresponding regime of inhomogeneity also decreases, approaching the weak  $J$  limit, where inhomogeneities are practically absent unless very close to the critical value. In the next section, we examine the thermal evolution of the system and its signatures on the spectral and spatial properties.

## 6.4 Thermal properties

In this section, we study the thermal properties of the system. We found that at large values of  $J \sim 1$ , the system became inhomogeneous with increasing concentration  $\eta$ . It is interesting to study the effect of this on the thermal evolution, and how the system smoothly interpolates to the more homogeneous behaviour at weaker  $J$ .

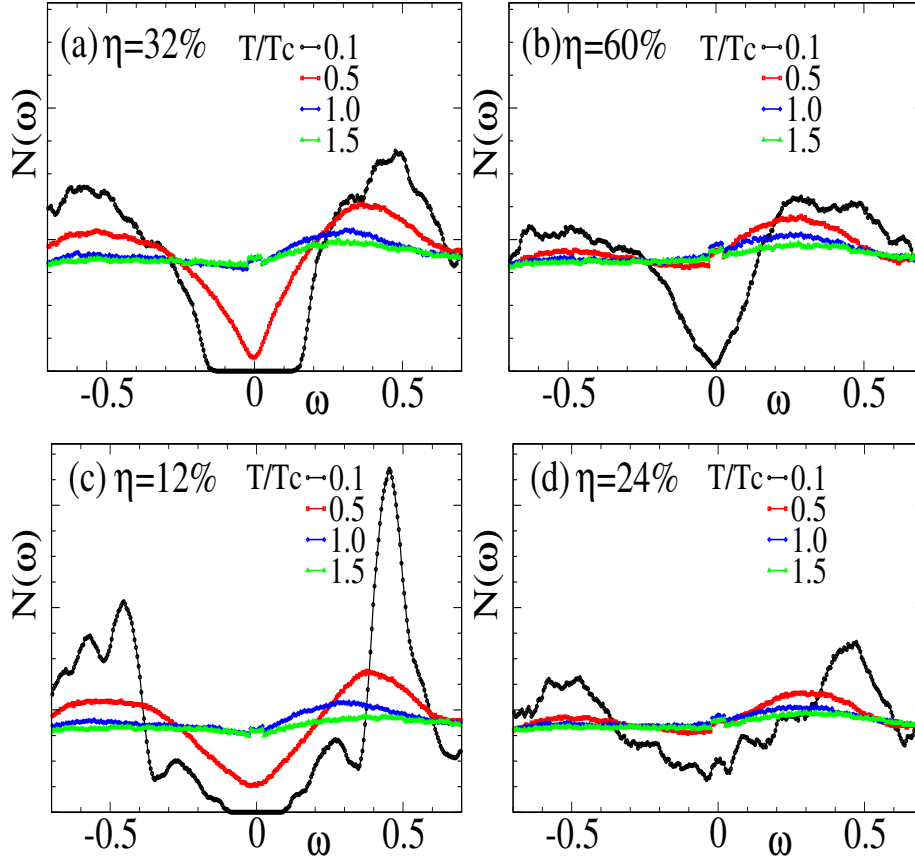


Figure 6.7: Density of states for  $J = 0.5$  and  $0.75$ , at two values of  $\eta$ , 32% and 60%, and 12% and 24% respectively. Four temperature values are given by  $0.1T_{c0}$ ,  $0.5T_{c0}$ ,  $T_{c0}$  and  $1.5T_{c0}$ , where  $T_{c0} \sim 0.07t$  is the clean transition temperature. The evolution is along expected lines starting from the  $T = 0$  values, with no outstanding features.

### 6.4.1 Density of states

Fig.6.7 shows the thermal evolution of the density of states at  $J = 0.5$  and  $0.75$  for two values of  $\eta$ , corresponding to the gapped and the gapless regimes respectively. Data is shown for four  $T$  values,  $0.1T_{c0}$ ,  $0.5T_{c0}$ ,  $T_{c0}$  and  $1.5T_{c0}$  respectively. In all the cases, starting from the  $T = 0$  states, the thermal evolution is quite standard, as the gap fills up and the low energy DOS becomes uniform. At a larger value of  $\eta$ , where the  $T = 0$  gap is smaller or has been closed, the density of states becomes flatter at a smaller temperature, as expected. Thus, we find that the density of states does not show any unexpected behaviour with increasing temperature. Thus, we direct our attention to the spatial evolution next.

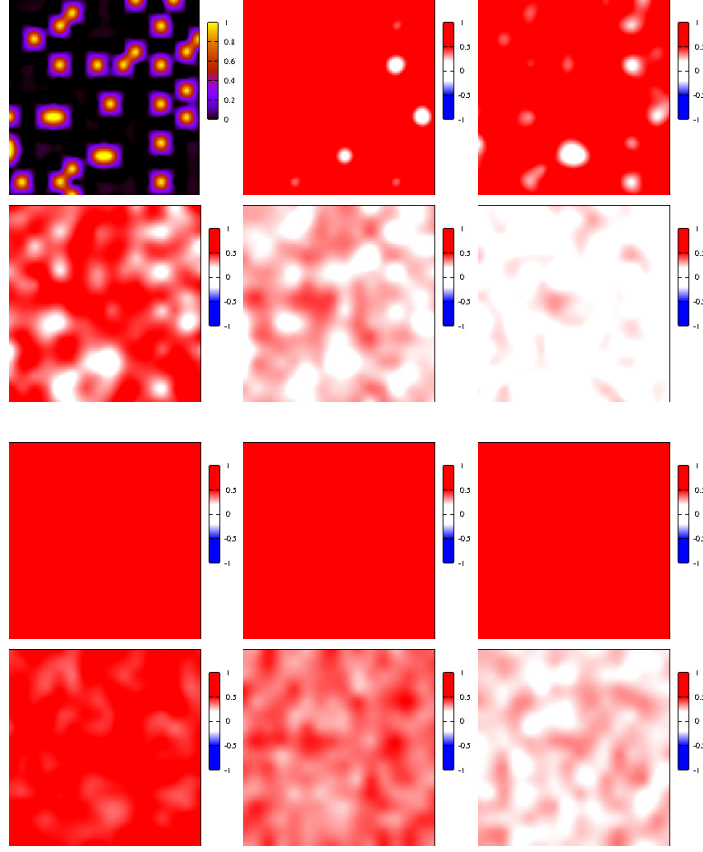


Figure 6.8: Spatial signatures of thermal evolution for  $J = 1$  (top two rows) and  $J = 0.5$  (bottom two rows) at  $\eta = 12\%$ . The first snapshot shows the impurity positions. Next 5 snaps show the nearest neighbour phase correlation (see text) in steps of  $T = 0.01$  starting at  $T_{min} = 0.005$ . Shows low correlations at a few sites to begin with, which become larger with increasing  $T$ , while the correlations weaken at other impurity sites as well. Last 6 snaps show the correlations for  $J = 0.5$ , starting at  $T_{min}$  with steps of  $T = 0.01$ . Show negligible effects on phase correlation till  $T \sim 0.35$ , and even after that, the correlation is lost much more homogeneously.

## 6.4.2 Spatial character

Fig.6.8 shows the thermal evolution of the system in terms of the nearest neighbour phase correlation  $\mathcal{N}_i$ , which is defined as  $\mathcal{N}_i = (1/4) \sum_j (\Delta_i \cdot \Delta_j^*) / (|\Delta_i| |\Delta_j|)$ , where  $j$  sums over the 4 nearest neighbours of  $i$ . To contrast the behaviour of the system at strong and weak coupling, we have shown two  $J$  values, viz. 1 and 0.5.

At  $J = 1$ , the  $T = 0$  state consists of a phase correlated superconductor except for three sites, where the correlation is particularly low, as evident from the white spots in the figures. As  $T$  is increased, these regions grow, and simultaneously, other impurity sites begin to lose phase correlation as well. This continues until the global correlation is lost at  $T_c \sim 0.7T_{c0}$ , where  $T_{c0} = 0.07t$  is the transition temperature for the pure superconductor. However, it is difficult to make out

whether the transition is a percolative one, since the correlation at all sites become quite weak close to  $T_c$ . Thus, this system is characterized by an extremely inhomogeneous thermal evolution, where impurity sites act as ‘nucleation’ centres for loss of phase correlation. The presence of impurities lowers the local phase stiffness at those sites, making them more susceptible to phase fluctuations. There is also a large variation even among impurity sites, with some (for example the three sites at low  $T$ ) sites clearly having much lower stiffnesses than others. In contrast, the evolution of the  $J = 0.5$  system shows negligible loss of phase correlations till  $T \sim 0.65T_{c0}$ , and a much more homogeneous loss of coherence after that.

To gain more insight into this, we can try to formulate an effective model of the form  $\mathcal{H}_{eff} = \sum_{\langle ij \rangle} \mathcal{K}_{ij} \Delta_i \cdot \Delta_j^*$ , where the effect of the impurities is incorporated in  $\mathcal{K}_{ij}$ . At present, we do not try and derive this from our starting Hamiltonian, but simply use it as a phenomenological construct to attempt to understand our results in terms of simpler quantities.

In this model, the pure superconducting system has a uniform negative  $\mathcal{K}_{ij}$  at  $T = 0$ . As we put magnetic impurities, they become scattering centres for the electrons and hence change the local values of  $\mathcal{K}_{ij}$ . For large impurity coupling, especially, there is a large reduction in the  $\mathcal{K}_{ij}$  value locally, and as we have seen in the single particle case, beyond a critical  $J$ , the impurity sites may even develop positive values of  $\mathcal{K}_{ij}$ , resulting in the  $\pi$  phase change. The zero temperature  $\Delta_i$  value at each site is determined by a stiffness term with higher powers, resulting in a locally reduced value of  $\Delta$  at the impurity positions.

The picture of a spatially varying  $\mathcal{K}_{ij}$  and  $\Delta_i$  helps us understand the contrasting thermal evolutions in the  $J = 1$  and  $J = 0.5$  case. At large impurity coupling, the system consists of an extremely inhomogeneous distribution of  $\mathcal{K}_{ij}$  values, with the impurity sites generally having lower values than the normal sites. As  $T$  is increased, the sites with lowest  $\mathcal{K}_{ij}$  values lose phase coherence first, followed by the others. Thus, these sites act as nucleation centres for phase correlation, as seen in the snaps. At weaker impurity coupling,  $J = 0.5$ , on the other hand,  $\mathcal{K}_{ij}$  are much more uniform, resulting in a more homogeneous thermal evolution.

## 6.5 Discussion

We now discuss several aspects of these results, relating the large  $J$  spatial inhomogeneities with the deviations in the phase diagrams compared to the AG results, the effect of increased attractive coupling on the thermal transition, the possibility of including an auxiliary field in the spin channel due to the broken spin symmetry in the problem, and, finally, possible extensions of this problem.

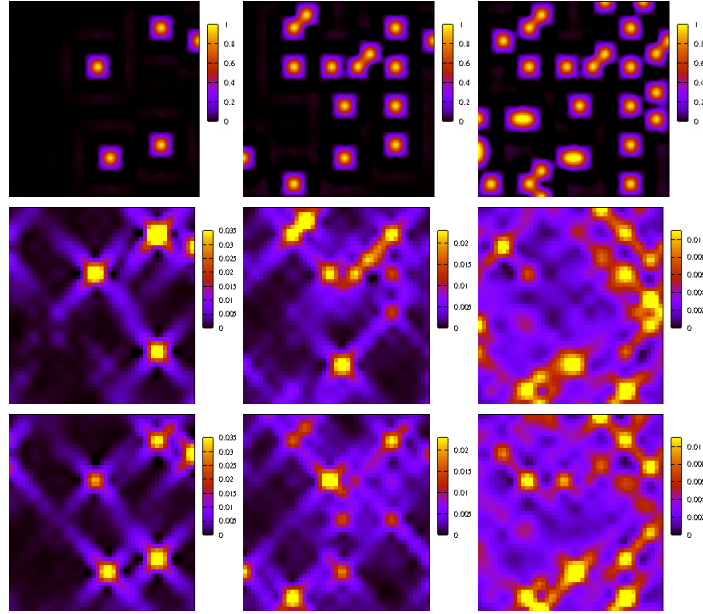


Figure 6.9: Low temperature wavefunctions for  $J = 1$  at  $\eta = 2\%, 6\%$  and  $12\%$  respectively. Top row shows spatial impurity distribution at these concentrations. Middle and bottom rows show wavefunctions corresponding to the first and third excited states. Have large overlaps with impurity positions, avoiding regions with large  $\Delta_i$  (see text).

### 6.5.1 Inhomogeneities and gapless phase

We have seen how increased impurity coupling  $J$  causes spatial inhomogeneities in the system on the one hand, and an increased gapless regime on the other. Here, we try to understand the connection of these two. To facilitate this, we show, in Fig.6.9 the wavefunctions of the first and second excited states for  $\eta = 2, 6$  and  $12\%$  at  $J = 1$  at  $T = 0$ . Quite clearly, these are concentrated at the impurity positions. Thus, the impurity induced low energy states that eventually make the system gapless live on the impurity positions, which are also regions where the pairing field  $\Delta_i$  is small. This explains the crucial role of spatial inhomogeneity in systems with strong scattering: the availability of low  $\Delta$  regions makes it much easier to form low energy excitations, thus creating a much larger gapless phase compared to superconductors where spatial inhomogeneities are weak, as in systems with weak scattering.

### 6.5.2 Nature of thermal transition

Strong impurity coupling caused an increased inhomogeneity in the superconducting state, resulting in an inhomogeneous thermal evolution, where the low  $\Delta_i$  sites seemed to act as nucleation centres for the loss of phase correlation. However, at  $T_c$  most of the sites seemed to have lost phase correlation and it is not clear whether the transition is percolative, as the simple  $\mathcal{K}_{ij}$  picture would

suggest. The thermal evolution, in general, would renormalize the  $\mathcal{K}_{ij}$  values, and it seems that at the parameter point  $U/t = 2$ , this renormalization is large enough to effectively homogenize these values for  $T \sim T_c$ , which weakens the percolative nature of the transition. It is possible that with a larger value of  $U/t$ , such that the effect of phase fluctuations are greater, one can see such a percolative transition much more clearly.

### 6.5.3 Effect of spin dependent auxiliary fields

In this work, we have utilized the same two field decomposition in the pairing and density channels that we had used to treat non-magnetic disorder. While most of our results seem to be qualitatively correct, it is possible that in view of the broken spin symmetry of the system, a further decomposition in the spin channel, resulting in the inclusion of the spin auxiliary fields  $\phi_{si}$  that couple to the spin density would provide better results. In Sec. 2.3.2, we found that such a decomposition in the spin channel comes with an extra imaginary factor multiplied to it, and hence it is not clear how one can incorporate the effect of thermal fluctuations at finite temperature in such a setup. However, one can include such effects at the mean field level. In such a theory, the resultant auxiliary field, along with the impurity spins, will renormalize the effective exchange interaction with the local electron spins in a way that is similar to the effect of the density field with non-magnetic disorder. This can shift the positions of the different phases and it would be interesting to study the resultant physics of such a system.

### 6.5.4 Extensions

An important extension of the present work would be to start with a periodic arrangement of these magnetic moments and consider fluctuations in their orientations as well. The resultant ‘magnetic’ superconductors, interacting via the intermediate electrons, can show simultaneous superconducting as well as magnetic order, and depending on the coupling, the impurity strengths and the specific arrangement of the moments, give rise to an array of complicated phases, including a spin glass at low temperatures [188]. One can also consider additional interactions among these moments to complicate the problem further, with the possibility of competing interactions and a further array of rich phases. A range of real materials, such as the pnictides [189], show complicated effects due to the presence of both superconducting as well as magnetic correlations.

## 6.6 Conclusions

In conclusion, we have studied the effects of magnetic impurities on s-wave superconductors over a large coupling and temperature window. We have demarcated the gapped and gapless supercon-

ducting phases, and tracked the evolution of the critical concentration  $\eta_{sc}$  with coupling. We have studied the spectral and spatial signatures, enabling us to create a comprehensive picture of the thermal evolution of the system.



# BIBLIOGRAPHY

- [1] M. Tinkham, *Introduction to Superconductivity*, Dover Publications; J. R. Schrieffer, *Theory of Superconductivity*, Westview Press
- [2] J. Bardeen, L. N. Cooper, and J. R. Schrieffer, Phys. Rev. **108**, 1175 (1957).
- [3] Q. Chen, J. Stajic, S. Tan and K. Levin, Phys. Repts. **412**, 1 (2005).
- [4] M. Randeria in *Bose-Einstein Condensation*, Cambridge University Press.
- [5] A. M. Goldman and N. Markovic, Phys. Today **51**, No 11, 39 (1998); V. F. Gantmakher and V. T. Dolgoplov, Phys. Usp. **53**, 3-53 (2010); M. Sadovsikii, Phys. Rep. **282**, 225 (1997); D. Belitz and T. Kirkpatrick, Rev. Mod. Phys. **66**, 261 (1994).
- [6] A. V. Balatsky, *et al.*, Rev. Mod. Phys. **78**, 373 (2006).
- [7] I. Giaever, Phys. Rev. Lett. **5**, 147 (1960); Phys. Rev. Lett. **5**, 464 (1960); Rev. Mod. Phys. **46**, 245 (1974).
- [8] H. Kamerlingh Onnes, Leiden Comm. 120b, 122b, 124c (1911).
- [9] W. Meissner, R. Ochsenfeld, Naturwissenschaften **21**, 787 (1933).
- [10] [en.wikipedia.org/wiki/Meissner\\_effect](http://en.wikipedia.org/wiki/Meissner_effect)
- [11] F. London and H. London, Proc. Roy. Soc. (London) **A149**, 71 (1935).
- [12] [physics.aalto.fi/en/midcom-serveattachmentguid-1e5725c9d5eefc2725c11e588d9e797bcfa46ea46ea/critical300x127.jpg](http://physics.aalto.fi/en/midcom-serveattachmentguid-1e5725c9d5eefc2725c11e588d9e797bcfa46ea46ea/critical300x127.jpg)
- [13] A. B.Pippard, Proc. Royal Soc. (London) **A216**, 547 (1953).
- [14] [www.doitpoms.ac.uk/tlplib/superconductivity/type.php](http://www.doitpoms.ac.uk/tlplib/superconductivity/type.php)

- [15] V.L. Ginzburg and L.D. Landau, Zh. Eksp. Teor. Fiz. **20**, 1064 (1950).
- [16] A.A. Abrikosov, Sov. Phys. JETP **5**, 1174 (1957). A. A. Abrikosov, Journal of Physics and Chemistry of Solids **2**, 199 (1957).
- [17] E. Maxwell, Phys. Rev. **78**, 477 (1950); **79**, 173 (1950); C. A. Reynolds, *et. al.*, Phys. Rev. **78**, 487 (1950); B. Serin, C. A. Reynolds, and L. B. Nesbitt, Phys. Rev. **78**, 813 (1950); **80**, 761 (1950).
- [18] H. Frohlich, Phys.Rev. **79**, 845 (1950); Proc. Roy. Soc. (London) **A215**, 291 (1952)
- [19] W. S. Corak, *et. al.*, Phys. Rev. **96**, 1442 (1954).
- [20] M.A. Biondi, M. P. Garfunkel and A. O. MacCubrey, Phys. Rev. **101**, 1427 (1956).
- [21] Joerg Schmalian, arxiv:1008.0447.
- [22] N. N. Bogoliubov, Nuovo Cimento **7**, 794 (1958); Soviet Phys. JETP **7**, 41 (1958); J. G. Valatin, Nuovo Cimento **7** 843 (1958).
- [23] P. Drude, Annalen der Physik 306 (3) (1900).
- [24] N. Ashcroft and N. D. Mermin, Solid State Physics, Saunders College Publishing.
- [25] P. W. Anderson, Phys. Rev. **109**, 1492 (1958).
- [26] Patrick A. Lee and T. V. Ramakrishnan, Rev. Mod. Phys. **57**, 287 (1985).
- [27] D. C. Licciardello and D. J. Thouless, J. Phys. C. **8**, 4157 (1975).
- [28] E. Abrahams, *et. al.*, Phys. Rev. Lett. **42**, 673 (1979).
- [29] A. M. Goldman and N. Markovic, Phys. Today **51**, No 11, 39 (1998).
- [30] A. A. Abrikosov and L. P. Gorkov, Zh. Eksp. Teor. Fiz. **36**, 319 (1959)
- [31] P. W. Anderson, J. Phys. Chem. Solids **11**, 26 (1959).
- [32] W. Wu and E. Bielejec, cond-mat/0511121.
- [33] E. Bielejec, J. Ruan, W. Wu, Phys. Rev. Lett. **87**, 036801 (2001);
- [34] V. Yu. Butko, P.W. Adams, Nature **409** 161 (2001).
- [35] E. Bielejec, J. Ruan, and Wenhao Wu, Phys. Rev. B **63**, 100502 (2001).

- [36] E. Bielejec and Wenhao Wu, Phys. Rev. Lett. **88**, 206802 (2002).
- [37] Wenhao Wu and E. Bielejec, Advanced Research Workshop Meso-06, Chernogolovka, Russia (2006); Wenhao Wu, AIP Conference Proceeding (LT24) 850, 995 (2006).
- [38] Y. Noat, *et al.*, Phys. Rev. B **88**, 014503 (2013).
- [39] D. Shahar, Z. Ovadyahu, Phys. Rev. B **46**, 10917 (1992).
- [40] D. Koval and Z. Ovadyahu, Solid State Comm. **90**, 783 (1994).
- [41] G. Sambandamurthy, *et al.*, Phys. Rev. Lett. **92**, 107005 (2004).
- [42] G. Sambandamurthy, *et al.*, Phys. Rev. Lett. **94**, 017003 (2005).
- [43] R.W. Crane, *et. al.*, Phys. Rev. B, **75**, 184530 (2007).
- [44] M.A. Steiner, N.P. Breznay, A. Kapitulnik, Phys. Rev. B **77** 212501 (2008).
- [45] M. Steiner and A. Kapitulnik, Physica C **422**, 16 (2005).
- [46] M. A. Steiner, G. Boebinger, and A. Kapitulnik, Phys. Rev. Lett. **94**, 107008 (2005).
- [47] B. Sacepe, *et al.*, Nature Phys. **7**, 239 (2011).
- [48] D. Sherman, *et al.*, Phys. Rev. Lett. **108**, 177006 (2012).
- [49] J.H. Kang and K.J. Kim, J. Appl. Phys. **86**, 346 (1999); N. Hadacek, M. Sanquer, and J. C. Villegier, Phys. Rev. B **69**, 024505 (2004).
- [50] W. Escoffier, *et al.*, Phys. Rev. Lett. **93**, 217005 (2004).
- [51] T. I. Baturina, *et. al.*, Physica C **468**, 316 (2008).
- [52] T.I. Baturina, *et al.*, Phys. Rev. Lett. **98** 127003 (2007).
- [53] T.I. Baturina, *et al.*, Phys. Rev. Lett. **99**, 257003 (2007).
- [54] T.I. Baturina, *et al.*, JETP Lett. **79**, 337 (2004).
- [55] B. Sacepe, *et al.*, Nature Commun. **1**, 140 (2010).
- [56] B. Sacepe, *et al.*, Phys. Rev. Lett. **101**, 157006 (2008).
- [57] Madhavi Chand, *et al.*, Phys. Rev. B **80**, 134514 (2009).

- [58] S. P. Chockalingam, *et al.*, Phys. Rev. B **79**, 094509 (2009).
- [59] M. Mondal, *et al.*, Phys. Rev. Lett. **106**, 047001 (2011).
- [60] Madhavi Chand, *et al.*, Phys. Rev. B **85**, 014508 (2012).
- [61] Anand Kamlapure, *et al.*, Scientific Reports **3**, 2979 (2013).
- [62] Mintu Mondal, *et al.*, Sci. Rep. **3**, 1357 (2013);
- [63] P. M. Chaikin and T. C. Lubensky, *Principles of condensed matter physics*, Cambridge University Press.
- [64] V. L. Berezinskii, Sov. Phys. JETP **34**, 610 (1972); J. M. Kosterlitz and D. J. Thouless, J. Phys. C **6**, 1181 (1973).
- [65] A. C. Hewson, *The Kondo Problem to Heavy Fermions*, Cambridge University Press.
- [66] A. I. Rusinov, Sov. Phys. JETP Lett. **9**, 85 (1969)
- [67] A. I. Rusinov, Sov. Phys. JETP **29**, 1101 (1969).
- [68] H. Shiba, Prog. Theor. Phys. **40**, 435 (1968).
- [69] L. Yu, Acta Phys. Sin. **21**, 75 (1965).
- [70] L. Dumoulin, , E. Guyon, and P. Nedellec, Phys. Rev. Lett. **34**, 264 (1975). L. Dumoulin, E. Guyon, and P. Nedellec, Phys. Rev. B **16**, 1086 (1977).
- [71] A. Yazdani, *et. al.*, Science **275**, 1767 (1997).
- [72] A. Sakurai, Prog. Theor. Phys. **44**, 1472 (1970). M. I. Salkola, A. V. Balatsky, and J. R. Schrieffer, Phys. Rev. B **55**, 12648 (1997).
- [73] A. I. Buzdin, Rev. Mod. Phys. **77**, 935 (2005).
- [74] A. A. Abrikosov, L. P. Gorkov, and I. E. Dzyaloshinski, *Methods of Quantum Field Theory in Statistical Physics*, Dover Publications.
- [75] A. A. Abrikosov, and L. P. Gorkov, Sov. Phys. JETP **12**, 1243 (1961).
- [76] J. S. Parker, *et. al.*, Europhys. Lett., **75** 950 (2006).
- [77] S. Skalski, O. Betbeder-Matibet, and P. R. Weiss, Phys. Rev. **136**, A1500 (1964). V. Ambegaokar and A. Griffin, Phys. Rev. **137**, A1151 (1965). C. D. Gong, and J.-H. Cai, J. Phys., (China) **22**, 381 (1966).

- [78] A. N. Chaba, and A. D. S. Nagi, *Can. J. Phys.* **50**, 1736 (1972).
- [79] R. Nanguneri et. al, *Phys. Rev. B* **85**, 134596 (2012).
- [80] P. D. Sacramento, V. K. Dugaev and V. R. Vieira *Phys. Rev. B* **76**, 014512 (2007).
- [81] P. G. de Gennes, *Superconductivity of metals and alloys*, Addison Wesley (1989).
- [82] A. M. Finkelstein, *Physica B* **197** (1994).
- [83] M.P.A. Fisher, *et al.*, *Phys. Rev. B* **40**, 546 (1989).
- [84] A. Ghoshal, M. Randeria and N. Trivedi, *Phys. Rev. Lett.* **81**, 3940 (1998).
- [85] A. Ghoshal, M. Randeria and N. Trivedi, *Phys. Rev. B* **65**, 014501 (2001).
- [86] M. Mayr, *et. al.*, *Phys. Rev. Lett.* **94**, 217001 (2005).
- [87] Y. Dubi, *et al.*, *Nature*, **449**, 876 (2007).
- [88] K. Bouadim, *et. al.*, *Nat. Phys.* **7**, 884 (2011).
- [89] A. J. Leggett in *Modern Trends in the Theory of Condensed Matter*, Springer-Verlag, Berlin.
- [90] M.H. Anderson, *et. al.*, *Science* **269**, 198 (1995)
- [91] K.B. Davis, *et. al.*, *Phys. Rev. Lett.* **75**, 3969 (1995).
- [92] E.A. Cornell and C.E. Wieman, *Rev. Mod. Phys.* **74**, 875 (2002).
- [93] C. A. Regal, *et. al.*, *Phys. Rev. Lett.*, **92**, 040403, (2004)
- [94] M.W. Zwierlein, *et. al.*, *Phys. Rev. Lett.*, **92**, 120403 (2004).
- [95] T. Bourdel, *et. al.*, *Phys. Rev. Lett.*, **93**, 050401 (2004).
- [96] I. Bloch, *et. al.*, *Rev. Mod. Phys.* **80**, 885 (2008).
- [97] M. Randeria and E. Taylor, *Ann Rev of Condensed Matter Physics*, Vol. **5**, 209-232 (2014)
- [98] I. Bloch, *et. al.*, *Nature Physics* **1**, 23 - 30 (2005)
- [99] T. Paiva, *et. al.*, *Phys. Rev. Lett.* **104**, 066406 (2010)
- [100] T. Schulte, *et. al.*, *Acta Physica Polonica A*, Vol. **109**, 89 (2006)
- [101] Juliette Billy, *et. al.*, *Nature* **453**, 891 (2008)

- [102] S. S. Kondov, *et. al.*, Science **334**, 66 (2011)
- [103] S. S. Kondov, *et. al.*, Phys. Rev. Lett. **114**, 083002 (2015)
- [104] J. Hubbard Proc. R. Soc. London Ser. **A276**, 238 (1963).
- [105] A. Altland and B. D. Simons, *Condensed Matter Field Theory*, Cambridge University Press.
- [106] R. Micnas, *et. al.*, Phys. Rev. B **52**, 16223 (1995).
- [107] P. Nozieres and S. Schmitt-Rink, J. Low. Temp. Phys. **59**, 195 (1985).
- [108] Parag Ghosh, arxiv:1107.3626
- [109] B. Jank, J. Maly and K. Levin, Phys. Rev. B **56** R11407 (1997). P. Pieri, L. Pisani and G. C. Strinati, Phys. Rev. Lett. **92**, 110401 (2004).
- [110] Q.J. Chen, *et. al.*, Phys. Rev. Lett. **81**, 4708 (1998). B. Giovannini and C. Berthod, Phys. Rev. B **63**, 144516 (2001).
- [111] R. Haussmann, Z. Phys. B **91**, 291 (1993); O. Tchernyshyov, Phys. Rev. B **56**, 3372 (1997); Y. Yanase, *et. al.*, Phys. Rep. **387** (14), 1 (2003).
- [112] J. J. Deisz, D. W. Hess, and J. W. Serene, Phys. Rev. **B66**, 014539 (2002).
- [113] B. Kyung, S. Allen, and A.-M. S. Tremblay, Phys. Rev. **B64**, 075116 (2001).
- [114] N. Dupuis, Phys. Rev. B **70**, 134502 (2004).
- [115] Yan He and K. Levin, Phys. Rev. B **89**, 035106 (2014).
- [116] R. L. Stratonovich, Sov. Phys. Doklady **2**, 416 (1958), J. Hubbard, *Phys. Rev. Lett.* **3**, 77 (1959), H. J. Schulz, *Phys. Rev. Lett.* **65**, 2462 (1990).
- [117] T. K. Kopec, Phys. Rev. B **65**, 054509 (2002).
- [118] K. Maki, *Physics* **1**, 21 (1964); P. G. de Gennes, *Phys. Kondens. Mater.* **3**, 79 (1964); E. Helfand and N. R. Werthamer, *Phys. Rev. Lett.* **13**, 686 (1964); *Phys. Rev.* **147**, 288 (1966). N. R. Werthamer, E. Helfand, and P. D. Hohenberg, *Phys. Rev.* **147**, 295 (1966).
- [119] Michael Ma and Patrick A. Lee, *Phys. Rev. B* **32**, 5658 (1985).
- [120] P. Morel and P. W. Anderson, *Phys. Rev.* **125**, 1263 (1962).
- [121] H. Bary-Soroker, *et. al.*, *Phys. Rev. Lett.* **110**, 056801 (2013).

- [122] S. Maekawa and H. Fukuyama, J. Phys. Soc. Jpn. **51** 1380 (1982); S. Maekawa, H. Ebisawa and H. Fukuyama, J. Phys. Soc. Jpn. **52** 1352 (1983).
- [123] A.M. Finkel'stein, Z. Phys. B **56** 189 (1984).
- [124] C. Castellani, *et. al.*, Solid State Commun. **52** 261 (1984).
- [125] A.E. White, R.C. Dynes and J.P. Garno, Phys. Rev. B, **33**, 3549 (1986); R.C. Dynes, *et. al.*, Phys. Rev. Lett. **57**, 2195 (1986); J.M. Valles Jr., R.C. Dynes and J.P. Garno, Phys. Rev. B **40**, 6680 (1989).
- [126] H.R. Raffy, *et. al.*, Phys. Rev. B **26**, 6607 (1983).
- [127] J.M. Graybeal and M.R. Beasley, Phys. Rev. B **29**, 4167 (1984); J.M. Graybeal, M.R. Beasley and R.L. Green, Physica B + C, **126**, 731 (1984).
- [128] P.H. Kes, C.C. Chi and C.C. Tsuei, in: Proc. Int. Conf. on Localization, Interaction and Transport Phenomena in Impure Metals (PT-8), eds. L. Schweitzer and B. Kramer (Braunschweig, 1984) p. 181
- [129] T. Furubayashi, *et. al.*, Solid State Commun. **55**, 513 (1985).
- [130] B.J. Bishop, E.G. Spencer and R.C. Dynes, Solid State Electron. **28**, 73 (1985); G. Hertel, *et. al.*, Phys. Rev. Lett. **50** 743 (1983).
- [131] [discor2013.files.wordpress.com/2013/12/castellani.pdf](http://discor2013.files.wordpress.com/2013/12/castellani.pdf)
- [132] D. B. Haviland, Y. Liu and A. M. Goldman, Phys. Rev. Lett. **62**, 2180 (1989).
- [133] S. M. Girvin, *et. al.*, Prog. Theor. Phys. Suppl., **107**, 135 (1992).
- [134] M. Swanson, Y. Lee Loh, M. Randeria, N. Trivedi, arXiv:1310.1073.
- [135] D. C. Mattis and J. Bardeen, Phys. Rev., **111**, 412 (1958).
- [136] Mintu Mondal, Ph.D. thesis, Tata Institute of Fundamental Research, Mumbai, arxiv:1303.7396.
- [137] A. Erez and Y. Meir, Europhys. Lett. **91**, 47003 (2010).
- [138] G. J. Conduit and Y. Meir, Phys. Rev. B **84**, 064513 (2011).
- [139] G. J. Conduit and Y. Meir, arxiv:1111.2941
- [140] C. Huscroft and R.T. Scalettar, Phys. Rev. Lett. **81**, 2775 (1998).

- [141] R. Scalettar, N. Trivedi and C. Huscroft, Phys. Rev. B **59**, 4364 (1999).
- [142] Andrew D. Huxley, Physica C **514**, 368 (2015).
- [143] S. De Palo, *et al.*, Phys. Rev. B. **60**, 564 (1999).
- [144] F. Solms, H. G. Miller and R. M. Quick, Phys. Rev. **B49**, 15945 (1994).
- [145] S. Kumar and P. Majumdar, Eur. Phys. J. B, **50**, 571 (2006).
- [146] G. D. Mahan, *Many-Particle Physics*, Springer.
- [147] D. J. Scalapino, S. R. White and S. C. Zhang, Phys. Rev. Lett. **68**, 2830 (1992); D. J. Scalapino, S. R. White and S. C. Zhang, Phys. Rev. B **47**, 7995 (1993).
- [148] D. M. Eagles, Phys. Rev. **186**, 456 (1969).
- [149] Daniel Rohe and Walter Metzner, Phys. Rev. B **63**, 224509 (2001).
- [150] For an early review, see R. Micnas, J. Ranninger and S. Robaszkiewicz, Rev. Mod. Phys. **62**, 113 (1990).
- [151] J. J. Deisz, D. W. Hess, and J. W. Serene, Phys. Rev. **B66**, 014539 (2002).
- [152] H. Tamaki, Y. Ohashi and K. Miyake, Phys. Rev. **A77**, 063616 (2008).
- [153] B. Kyung, S. Allen, and A.-M. S. Tremblay, Phys. Rev. **B64**, 075116 (2001).
- [154] N. Dupuis, Phys. Rev. B **70**, 134502 (2004).
- [155] T. K. Kopec, Phys. Rev. B **65**, 054509 (2002).
- [156] R. T. Scalettar, *et. al.*, Phys. Rev. Lett. **62**, 1407 (1989).
- [157] A. Moreo and D. J. Scalapino, Phys. Rev. Lett. **66**, 946 (1991).
- [158] A. Moreo, D. J. Scalapino and S. R. White, Phys. Rev. **B45**, 7544 (1992).
- [159] M. Randeria, *et. al.*, Phys. Rev. Lett. **69**, 2001 (1992).
- [160] N. Trivedi and M. Randeria, Phys. Rev. Lett. **75**, 312 (1995).
- [161] S. Allen, *et. al.*, Phys. Rev. Lett. **83**, 4128 (1999).
- [162] J. M. Singer, T. Schneider and P. F. Meier, EPJB **7**, 37 (1999).

- [163] A. Sewer, X. Zotos and H. Beck, Phys. Rev. B **66**, 140504 (2002).
- [164] T. Paiva, *et. al.*, Phys. Rev. B. **69**, 184501 (2004).
- [165] T. Paiva, *et. al.*, Phys. Rev. Lett. **104**, 066406 (2010).
- [166] M. Keller, W. Metzner and U. Schwoollwock, Phys. Rev. Lett. **86**, 4612 (2001).
- [167] M. Capone, C. Castellani and M. Grilli, Phys. Rev. Lett. **88**, 126403 (2002).
- [168] A. Garg, H. R. Krishnamurthy and M. Randeria, Phys. Rev. B **72**, 024517 (2005).
- [169] J. Bauer and A. C. Hewson, Europhys. Lett. **85** 27001 (2009).
- [170] J. Bauer, A. C. Hewson and N. Dupuis, Phys. Rev. B **79**, 214518 (2009).
- [171] A. Koga and P. Werner, Phys. Rev. A **84**, 023638 (2011).
- [172] I. Bloch, Nat. Phys. 1, **23** (2005), I. Bloch, *et. al.*, Rev. Mod. Phys. 80, **885** (2008).
- [173] S. Giorgini, *et. al.*, Rev. Mod. Phys. 80, **80**, 1215 (2008), R. Casalbouni, *et. al.*, Rev. Mod. Phys. **76**, 263 (2004), X-Wen Guan, *et. al.*, Rev. Mod. Phys. **85**, 1633 (2013)
- [174] S. Tarat and P. Majumdar, Europhys. Lett. 105 (2014) 67002.
- [175] S. Tarat and P. Majumdar, arxiv:1406.5423
- [176] Sanjoy Datta, Viveka Nand Singh and Pinaki Majumdar, arxiv:1312.5761
- [177] Daniel Podolsky, Assa Auerbach and Daniel P. Arovas, Phys. Rev. B **84**, 174522 (2011)
- [178] E. N. Economou, *et al.*, Phys. Rev. B **30** 1686 (1984).
- [179] Daniel Sherman, *et. al.*, Nature Physics **11**, 188 (2015).
- [180] A. Larkin and A. Varlamov in Theory Of Fluctuations In Superconductors (Clarendon Press, Oxford 2005).
- [181] A. M. Finkelstein, Physica B **197** (1994).
- [182] V. J. Emery and S. A. Kivelson, Phys. Rev. Lett. **74**, 3253 (1995).
- [183] B. L. Altshuler and A. G. Aronov in *Electron-Electron Interactions in Disordered Systems*, A. L. Efros, M. Pollak, Eds. (North-Holland, Amsterdam, 1985).
- [184] B. L. Altshuler, A. G. Aronov and P. A. Lee, Phys. Rev. B **44**, 1288 (1980).

[185] S. Tarat and P. Majumdar, arXiv:1402.0817.

[186] There is no SIT in the ground state strictly within HFBdG theory. However at any finite  $T$  phase fluctuations lead to a finite  $V_c(T)$ . Our  $V_c$  is an extrapolation of this quantity [174].

[187] Note that unlike  $T_c$ , the gap and pseudogap vanishing scales are more ambiguous, particularly the later. Nevertheless, they are useful constructs, and at least in the present case can be reasonably estimated.

[188] V. M. Galitskii and A. I. Larkin, Phys. Rev. B **66**, 064526 (2002).

[189] G. R. Stewart, Rev. Mod. Phys. **83**, 1589 (2011).